

PROCEEDINGS OF SPIE



SPIE—The International Society for Optical Engineering

Laser Optics 2000 **Solid State Lasers**

Vladimir I. Ustugov

Editor

**26–30 June 2000
St. Petersburg, Russia**

Organized by

Institute for Laser Physics (Russia)

All-Russia Scientific Center, S.I. Vavilov State Optical Institute

General Physics Institute, Russian Academy of Sciences

P.N. Lebedev Physical Institute, Russian Academy of Sciences

A.F. Ioffe Physico-Technical Institute, Russian Academy of Sciences

Russian National Center of Laser Physics, St. Petersburg State University

St. Petersburg Institute of Fine Mechanics and Optics (Russia)

Scientific Council on Coherent and Nonlinear Optics, Russian Academy of Sciences

SPIE—The International Society for Optical Engineering

SPIE Russia Chapter

OSA—Optical Society of America

ROS—Rozhdestvensky Optical Society (Russia)

Government of St. Petersburg (Russia)

ISTC—International Scientific and Technological Center

20010927 024

DISTRIBUTION STATEMENT A
Approved for Public Release
Distribution Unlimited



Volume 4350

REPORT DOCUMENTATION PAGE

Form Approved OMB No. 0704-0188

Public reporting burden for this collection of information is estimated to average 1 hour per response, including the time for reviewing instructions, searching existing data sources, gathering and maintaining the data needed, and completing and reviewing the collection of information. Send comments regarding this burden estimate or any other aspect of this collection of information, including suggestions for reducing this burden to Washington Headquarters Services, Directorate for Information Operations and Reports, 1215 Jefferson Davis Highway, Suite 1204, Arlington, VA 22202-4302, and to the Office of Management and Budget, Paperwork Reduction Project (0704-0188), Washington, DC 20503.

1. AGENCY USE ONLY (Leave blank)	2. REPORT DATE	3. REPORT TYPE AND DATES COVERED	
	14 September 2001	Conference Proceedings	
4. TITLE AND SUBTITLE			5. FUNDING NUMBERS
Laser Optics 2000: Solid State Lasers (Volume 4350)			F61775-00-WF
6. AUTHOR(S)			8. Performing Organization Report Number N/A
Conference Committee			
7. PERFORMING ORGANIZATION NAME(S) AND ADDRESS(ES)			10. SPONSORING/MONITORING AGENCY REPORT NUMBER
Institute for Laser Physics 12 Birzhevaya line St. Petersburg 199034 Russia			CSP 00-5049
9. SPONSORING/MONITORING AGENCY NAME(S) AND ADDRESS(ES)			
EOARD PSC 802 Box 14 FPO 09499-0200			
11. SUPPLEMENTARY NOTES			
Conference Proceedings in five volumes. Proceedings of SPIE – The International Society for Optical Engineering, 26-30 June 2000, St. Petersburg, Russia. Volumes 4350 (Solid State Lasers), 4351 (High-Power Gas Lasers), 4352 (Ultrafast Optics and Superstrong Laser Fields), 4353 (Control of Laser Beam Characteristics and Nonlinear Methods for Wavefront Control), and 4354 (Semiconductor Lasers and Optical Communication), ISSN 0277-786X			
12a. DISTRIBUTION/AVAILABILITY STATEMENT		12b. DISTRIBUTION CODE	
Approved for public release; distribution is unlimited.		A	
ABSTRACT (Maximum 200 words)			
The Final Proceedings for the Tenth Conference on Laser Optics, 26-30 June 2000. This is an interdisciplinary conference. Topics include generation of ultrashort light pulses, application of nonlinear correction techniques in adaptive optics and lasers, advanced methods of beam control and pointing; diode-pumped solid state lasers; high average power gas and solid-state lasers; and lasers in medicine and medical applications.			
14. SUBJECT TERMS			15. NUMBER OF PAGES
EOARD, Adaptive optics, Gas lasers, Solid state lasers, Aberration correction			Five bound volumes
			16. PRICE CODE
17. SECURITY CLASSIFICATION OF REPORT	18. SECURITY CLASSIFICATION OF THIS PAGE	19. SECURITY CLASSIFICATION OF ABSTRACT	20. LIMITATION OF ABSTRACT
UNCLASSIFIED	UNCLASSIFIED	UNCLASSIFIED	UL

NSN 7540-01-280-5500

Standard Form 298 (Rev. 2-89)
Prescribed by ANSI Std. Z39-18
298-102

PROCEEDINGS OF SPIE



SPIE—The International Society for Optical Engineering

Laser Optics 2000

Solid State Lasers

Vladimir I. Ustugov

Editor

26–30 June 2000

St. Petersburg, Russia

Organized by

Institute for Laser Physics (Russia) • All-Russia Scientific Center, S.I. Vavilov State Optical Institute • General Physics Institute, RAS • P.N. Lebedev Physical Institute, RAS • A.F. Ioffe Physico-Technical Institute, RAS • Russian National Center of Laser Physics, St. Petersburg State University • St. Petersburg Institute of Fine Mechanics and Optics (Russia) • Scientific Council on Coherent and Nonlinear Optics, RAS • SPIE—The International Society for Optical Engineering • SPIE Russia Chapter • OSA—Optical Society of America • ROS—Rozhdestvensky Optical Society (Russia) • Government of St. Petersburg (Russia) • ITC—International Scientific and Technological Center

Supported by

Ministry of Science and Technical Policy of the Russian Federation • Ministry for Economics of the Russian Federation • Ministry of Education of the Russian Federation • Federal Agency for Conventional Weapons (Russia) • Russian National Foundation for Basic Research • SPIE—The International Society for Optical Engineering • Lawrence Livermore National Laboratory (USA) • European Office of Aerospace Research and Development (USA) • OSA—Optical Society of America • ITC—International Scientific and Technological Center • Amada Corporation (Japan) • Jenoptic GmbH (Germany) • Corning Inc. (USA) • IRE-Polus Group (Germany)



Published by

SPIE—The International Society for Optical Engineering

Volume 4350

SPIE is an international technical society dedicated to advancing engineering and scientific applications of optical, photonic, imaging, electronic, and optoelectronic technologies.

AQ F01-12-2758



The papers appearing in this book compose the proceedings of the technical conference cited on the cover and title page of this volume. They reflect the authors' opinions and are published as presented, in the interests of timely dissemination. Their inclusion in this publication does not necessarily constitute endorsement by the editors or by SPIE. Papers were selected by the conference program committee to be presented in oral or poster format, and were subject to review by volume editors or program committees.

Please use the following format to cite material from this book:

Author(s), "Title of paper," in *Laser Optics 2000: Solid State Lasers*, Vladimir I. Ustugov, Editor, Proceedings of SPIE Vol. 4350, page numbers (2001).

ISSN 0277-786X
ISBN 0-8194-4040-X

Published by
SPIE—The International Society for Optical Engineering
P.O. Box 10, Bellingham, Washington 98227-0010 USA
Telephone 1 360/676-3290 (Pacific Time) • Fax 1 360/647-1445
<http://www.spie.org/>

Copyright© 2001, The Society of Photo-Optical Instrumentation Engineers.

Copying of material in this book for internal or personal use, or for the internal or personal use of specific clients, beyond the fair use provisions granted by the U.S. Copyright Law is authorized by SPIE subject to payment of copying fees. The Transactional Reporting Service base fee for this volume is \$15.00 per article (or portion thereof), which should be paid directly to the Copyright Clearance Center (CCC), 222 Rosewood Drive, Danvers, MA 01923 USA. Payment may also be made electronically through CCC Online at <http://www.directory.net/copyright/>. Other copying for republication, resale, advertising or promotion, or any form of systematic or multiple reproduction of any material in this book is prohibited except with permission in writing from the publisher. The CCC fee code is 0277-786X/01/\$15.00.

Printed in the United States of America.

Contents

vii *Laser Optics 2000 Program Committee*

SECTION 1 DPSS LASERS, LASERS WITH HIGH BEAM QUALITY, AND EYE-SAFE LASERS

- 1 **Novel adaptive resonators and thermal lensing** [4350-01]
T. Graf, H. P. Weber, Univ. of Bern (Switzerland)
- 9 **200-W-average-power Nd:YAG laser with self-adaptive cavity completed by dynamic refractive-index gratings** [4350-02]
O. L. Antipov, A. S. Kuzhelev, D. V. Chausov, A. P. Zinov'ev, Institute of Applied Physics (Russia)
- 17 **Low- and mid-power diode-pumped lasers and their application** [4350-03]
G. M. Zverev, Polyus Research and Development Institute (Russia); I. I. Kuratev, Laser Compact Co. Ltd. (Russia)
- 25 **Pulsed Nd:YAG laser with diode-laser bar side-pumped rod geometry** [4350-04]
A. J. Abazadze, J. M. Kolbatskov, V. L. Pavlovitch, G. M. Zverev, Polyus Research and Development Institute (Russia)
- 32 **Passive Q-switch operation of PbSe-doped glass at 2.1 μ m** [4350-05]
A. M. Malyarevich, V. G. Savitski, P. V. Prokoshin, K. V. Yumashev, International Laser Ctr. (Belarus); A. A. Lipovskii, St. Petersburg State Technical Univ. (Russia)
- 36 **SRS lasers with self-conversion of radiation frequency based on NaLa(MoO₄)₂:Nd³⁺ and KGd(WO₄)₂:Nd³⁺ crystals** [4350-06]
A. V. Gulin, V. A. Pashkov, N. S. Ustimenko, Polyus Research and Development Institute (Russia)
- 39 **1.53- μ m lasing by SRS in barium nitrate in focused beams and in resonator** [4350-07]
S. N. Karpukhin, S.I. Vavilov State Optical Institute (Russia)
- 50 **Single-mode beam amplification in a multimode pump field during SRS in a barium nitrate crystal** [4350-08]
S. N. Karpukhin, V. A. Berenberg, S.I. Vavilov State Optical Institute (Russia)

SECTION 2 LASER MATERIALS

- 62 **Family of highly efficient erbium-doped phosphate glasses** [4350-09]
A. A. Izyneev, P. I. Sadovski, Institute of Radio Engineering and Electronics (Russia)
- 68 **Spectroscopic and laser properties of BeLaAl₁₁O₁₉ single crystals doped with Cr³⁺, Ti³⁺, and Nd³⁺ ions** [4350-10]
E. V. Pstryakov, V. V. Petrov, V. I. Trunov, A. V. Kirpichnikov, Institute of Laser Physics (Russia); A. I. Alimpiev, Technological Institute of Monocrystals (Russia)

75 **Concentration and power dependencies of level population of 2.8- μm laser transition in YLF:Er crystals under cw laser diode pumping** [4350-11]
A. M. Tkachuk, I. K. Razumova, S.I. Vavilov State Optical Institute (Russia); A. A. Mirzaeva, G. E. Novikov, O. A. Orlov, Institute of Laser Physics (Russia); A. V. Malyshev, A.I. Ioffe Physico-Technical Institute (Russia); V. P. Gapontsev, IPG Laser GmbH (Germany)

81 **Upconversion processes, luminescence kinetics, and cw diode-pumped 2.8- μm laser action in Er-doped double-fluoride crystals** [4350-12]
A. M. Tkachuk, I. A. Mironov, V. M. Reiterov, S.I. Vavilov State Optical Institute (Russia); G. E. Novikov, O. A. Orlov, Institute of Laser Physics (Russia); H.-J. Pohl, Vitcon (Germany); R. W. Steiner, M. Edelmann, Univ. of Ulm (Germany); V. P. Gapontsev, IPG Laser GmbH (Germany)

90 **First-principle calculation for absorption spectrum of Cr⁴⁺:Ca₂MgSi₂O₇ (åkermanite)** [4350-13]
T. Ishii, K. Fujimura, K. Ogasawara, I. Tanaka, H. Adachi, Kyoto Univ. (Japan)

99 **Mechanisms of slow bleaching in YAG:Cr⁴⁺ under cw pumping** [4350-14]
I. T. Sorokina, S. Naumov, E. Sorokin, Technische Univ. Wien (Austria); A. G. Okhrimchuk, General Physics Institute (Russia)

SECTION 3 LASER COMPONENTS

106 **New Co-containing glass ceramics saturable absorbers for 1.5- μm solid state lasers** [4350-15]
A. M. Malyarevich, I. A. Denisov, K. V. Yumashev, International Laser Ctr. (Belarus); T. I. Chuvayeva, O. S. Dymshits, A. A. Onushchenko, A. A. Zhilin, S.I. Vavilov State Optical Institute (Russia)

112 **Kerr-lens mode-locking ability of Cr²⁺:ZnSe solid state laser** [4350-16]
V. L. Kalashnikov, I. G. Poloyko, International Laser Ctr. (Belarus)

117 **KTiOPO₄ electro-optical devices with extinction ratio up to 1:1000** [4350-17]
V. A. Rusov, Institute of Laser Physics (Russia); A. V. Gorchakov, A. L. Belostotsky, V. K. Sapojnikov, Institute of Semiconductor Physics (Russia); A. B. Kaplun, A. B. Meshalkin, Institute of Thermophysics (Russia); V. N. Shapovalov, SciMed Life Systems, Inc. (USA)

120 **Ion beam optical coatings for visible and near-IR lasers** [4350-18]
G. Kolodnyi, Yu. D. Golyaev, V. V. Azarova, M. Rasyov, N. Tikhmenev, Polyus Research and Development Institute (Russia)

SECTION 4 NONLINEAR FREQUENCY CONVERSION

126 **Miniature optical parametric 1064/1573-nm converter** [4350-19]
V. L. Naumov, A. M. Onischenko, A. S. Podstavkin, A. V. Shestakov, Polyus Research and Development Institute (Russia)

129 **Features of noncollinear parametric generation light in LiNbO₃ crystal pumped by the fundamental radiation of Nd:YAG laser** [4350-20]
N. V. Kondratyuk, Belarussian Technical Academy; A. A. Shagov, SC Solar LS (Belarus); V. N. Belyi, A. Mashchenko, Institute of Physics (Belarus); Yu. A. Bakhirkin, P. Philippow, NII Gazekonomika (Russia)

136 **Gain saturation effects in BBO parametric amplifier** [4350-21]
W. Hogervorst, Vrije Univ. (Netherlands); N. Kondratyuk, A. A. Shagov, SC Solar LS (Belarus);
V. N. Belyi, Institute of Physics (Belarus)

140 **Optical quality and efficiency of nonlinear laser crystals** [4350-22]
P. N. Afanasyev, Baltic State Technical Univ. (Russia); N. D. Baiborodova, A. A. Dashtoyan,
E. M. Dianov, V. F. Lebedev, General Physics Institute (Russia); V. V. Lobachev, Baltic State
Technical Univ. (Russia); M. Ya. Shchelev, General Physics Institute (Russia)

144 **General properties of harmonic generation susceptibilities** [4350-23]
F. Bassani, V. Lucarini, Scuola Normale Superiore (Italy) and INFM (Italy)

154 **Frequency doubling in the Čerenkov regime utilizing an abnormal reflecting mirror structure**
[4350-24]
I. F. Salakhutdinov, General Physics Institute (Russia) and Univ. of Twente (Netherlands);
L. Kotáčka, Institute of Radio Engineering and Electronics (Czech Republic) and Univ. of
Twente (Netherlands); H. J. W. M. Hoekstra, Univ. of Twente (Netherlands); J. Čtyroký,
Institute of Radio Engineering and Electronics (Czech Republic); H. van Wolferen, Univ. of
Twente (Netherlands); V. A. Sychugov, General Physics Institute (Russia); O. M. Parriaux,
Univ. Jean Monnet de Saint-Etienne (France)

SECTION 5 LASER APPLICATIONS FOR PRECISION MEASUREMENTS

161 **Laser detection of the parameters of small solid particles located in air** [4350-25]
A. A. Andreev, Yokogawa Electric Corp. (Japan) and Institute of Laser Physics (Russia);
T. Ueda, M. Wakamatsu, Yokogawa Electric Corp. (Japan); A. Golub, Institute of Laser
Physics (Russia)

171 **Application of femtosecond lasers for the frequency synthesis in radio-optical ranges
and for the creation of an optical clock** [4350-26]
S. N. Bagayev, S. V. Chepurov, V. M. Klementyev, D. B. Kolker, S. A. Kuznetsov,
Yu. A. Matyugin, V. S. Pivtsov, V. F. Zakharyash, Institute of Laser Physics (Russia)

175 **Doubled YAG laser stabilized on iodine as length/frequency standard at 532 nm** [4350-27]
Y. P. Millerioux, P. Juncar, Institute National de Metrologie/CNAM (France)

178 **Large-scale laser gravitational interferometer with suspended mirrors for fundamental
geodynamics** [4350-28]
V. N. Rudenko, V. V. Kulagin, S. L. Pasynok, A. V. Serdobolskii, M.V. Lomonosov Moscow
State Univ. (Russia)

190 **Optical fiber characterization by use of laser scanning microscopy** [4350-29]
H. Fatemi, Shahid Bahonar Univ. of Kerman (Iran)

194 **Theoretical backgrounds of methods of angle-resolved and total integral scattering for precise
dielectric surfaces** [4350-30]
K. Malitski, Moscow Institute of Physics and Technology (Russia)

203 *Author Index*

Laser Optics 2000 Program Committee

Chair

Artur A. Mak, Institute for Laser Physics (Russia)

Vice-Chairs

Alexander A. Andreev, Institute for Laser Physics (Russia)

Vladimir Yu. Venediktorov, Institute for Laser Physics (Russia)

Scientific Secretary

A. F. Vassil'yev, Institute for Laser Physics (Russia)

Members

Zhores I. Alferov, A.F. Ioffe Physico-Technical Institute (Russia)

Pavel A. Apanasevich, B.I. Stepanov Institute of Physics (Belarus)

Sergey N. Bagaev, Institute for Laser Physics (Russia)

Nikolai G. Basov, P.N. Lebedev Physical Institute (Russia)

Yuri D. Berezin, Institute for Laser Physics (Russia)

Viktor I. Bespalov, Institute of Applied Physics (Russia)

Ernest V. Boiko, Military Medical Academy (Russia)

F. V. Bunkin, General Physics Institute (Russia)

Oleg B. Danilov, Institute for Laser Physics (Russia)

Eugeni M. Dianov, General Physics Institute (Russia)

Sergei A. Dimakov, Institute for Laser Physics (Russia)

Alexander V. Dotsenko, Corning Scientific Center (Russia)

Valentin Gapontsev, IPG Laser GmbH (Germany)

Yu. D. Golyaev, Research and Development Institute Polyus (Russia)

Vyacheslav M. Gordienko, M.V. Lomonosov Moscow State University (Russia)

Serguei A. Gurevich, A.F. Ioffe Physico-Technical Institute (Russia)

Valerii P. Kandidov, M.V. Lomonosov Moscow State University (Russia)

Yakov I. Khanin, Institute of Applied Physics (Russia)

I. V. Kovsh, Laser Association (Russia)

O. N. Krohin, P.N. Lebedev Physical Institute (Russia)

Vladimir V. Lyubimov, Institute for Laser Physics (Russia)

Alexander A. Manenkov, General Physics Institute (Russia)

Yuri T. Mazurenko, S.I. Vavilov State Optical Institute (USA)

Anatoly P. Napartovich, Troitsk Institute for Innovation and Fusion Research (Russia)

Anatoly N. Oraevsky, P.N. Lebedev Physics Institute (Russia)

Vladislav Ya. Panchenko, Scientific Research Center for Technological Lasers (Russia)

Pavel P. Pashinin, General Physics Institute (Russia)

G. T. Petrovskiy, S.I. Vavilov State Optical Institute (Russia)

N. N. Rozanov, Institute for Laser Physics (Russia)

Alexander S. Rubanov, B.I. Stepanov Institute of Physics (Belarus)

Marat S. Soskin, Institute of Physics (Ukraine)

Victor A. Serebryakov, Institute for Laser Physics (Russia)
Ivan A. Shcherbakov, General Physics Institute (Russia)
Vladimir E. Sherstobitov, Institute for Laser Physics (Russia)
Leonid N. Soms, Institute for Laser Physics (Russia)
V. B. Smirnov, St. Petersburg State University (Russia)
Anatoli P. Sukhorukov, M.V. Lomonosov Moscow State University (Russia)
Vladimir I. Ustugov, Institute for Laser Physics (Russia)
V. V. Valuev, GPO Almaz (Russia)
V. N. Vasilev, St. Petersburg State Institute of Fine Mechanics and Optics (Russia)
Evgeny A. Viktorov, Institute for Laser Physics (Russia)
Vadim P. Veiko, St. Petersburg State Institute of Fine Mechanics and Optics (Russia)
Vladimir E. Yashin, Institute for Laser Physics (Russia)
Georgii M. Zverev, Research and Development Institute Polyus (Russia)

Novel Adaptive Resonators and Thermal Lensing

Thomas Graf* and Heinz P. Weber

University of Berne, Institute of Applied Physics, Sidlerstrasse 5, CH-3012 Berne, Switzerland

ABSTRACT

We present different approaches to improve the beam quality of solid-state lasers. The original dual- or variable-configuration resonator was improved to emit completely polarised output. This was achieved by enforcing unidirectional operation due to the polarisation dependence of the thermal lenses and of the gain in Nd:YVO₄ crystals. Single-frequency operation was obtained in a miniaturised version of this resonator based on a polarising beam splitter made of Nd:YAG. Our transversally pumped high-power lasers feature output powers exceeding 600 W. In order to compensate for the power dependent thermal lenses we investigate the use of self-adaptive compensating thermo-optical elements which generate thermally induced lenses with the opposite sign as the lens in the gain medium. Furthermore, to speed up the optimisation processes we have derived a general analytical solution of the heat conduction equation for arbitrary heating distributions with cylindrical symmetry.

Keywords: thermal lens, thermal effects, adaptive optics, laser resonators, resonator stability

1. INTRODUCTION

Thermally induced optical distortions are currently by far the most critical issue in the development of high-power solid-state lasers with good beam quality. The heating of the gain medium is an inherent consequence of the laser process itself and cannot be avoided except maybe with novel concepts such as radiation balance.¹ Hence, detailed investigations on the thermal effects to either alleviate or to exploit their influence on optical resonators are of major importance. In the following we present different ways to exploit thermal effects with the aim to improve the performance of solid-state lasers.

A novel folded dual-configuration resonator (or variable-configuration resonator)²⁻⁴ that emits polarised output was developed. This adds the feature of polarised output to the reputed advantages of this particular resonator which are compactness, scalability, simple repetitive end-pumping, unique stability properties, configuration Q-switching and efficient fundamental-mode operation. The improvement was achieved with unidirectional operation caused by the fact that the thermal lenses as well as the gain are different for the two propagation directions due to the anisotropy of the used Nd:YVO₄ crystals.

In another approach we present the latest results of our efforts to balance the thermally induced lenses in the gain medium with a self-adaptive lens in a compensating thermo-optical element. The compensating element absorbs a little bit of the circulating intra-cavity laser radiation and generates a thermally induced (negative) lens which balances the (positive) thermal lens in the laser medium.⁶

The optimisations of the thermal effects in solid-state lasers require an accurate and fast method to model the temperature and the stress distributions to subsequently calculate the thermo-optical and elasto-optical distortions. Until now solutions of the heat conduction equation were only known for the cases of homogeneous (incl. top-hat shaped) heating or Gaussian heating distributions in laser rods.⁷⁻⁹ The mathematical treatment of the thermally induced birefringence has been published only for homogeneous (or top-hat shaped) heating. However, thermal effects such as birefringence and thermal lenses strongly depend on the actual heating distributions.¹⁰ In section 4 we present a general analytical solution of the heat conduction equation for arbitrary heating distributions with cylindrical symmetry.¹¹

2. THE UNIDIRECTIONAL DUAL-CONFIGURATION RESONATOR

The variable-configuration resonator was originally developed to scale the output power of end-pumped fundamental-mode lasers.² It uses a scaleable folded-cavity design incorporating one (or more) polarising beam splitter(s) to allow for easy and efficient longitudinal pumping. The basic set-up includes three end-pumped laser rods, it is similar to the resonator shown in

* Correspondence: Email: thomas.graf@iap.unibe.ch, WWW: <http://www.iap.unibe.ch/>

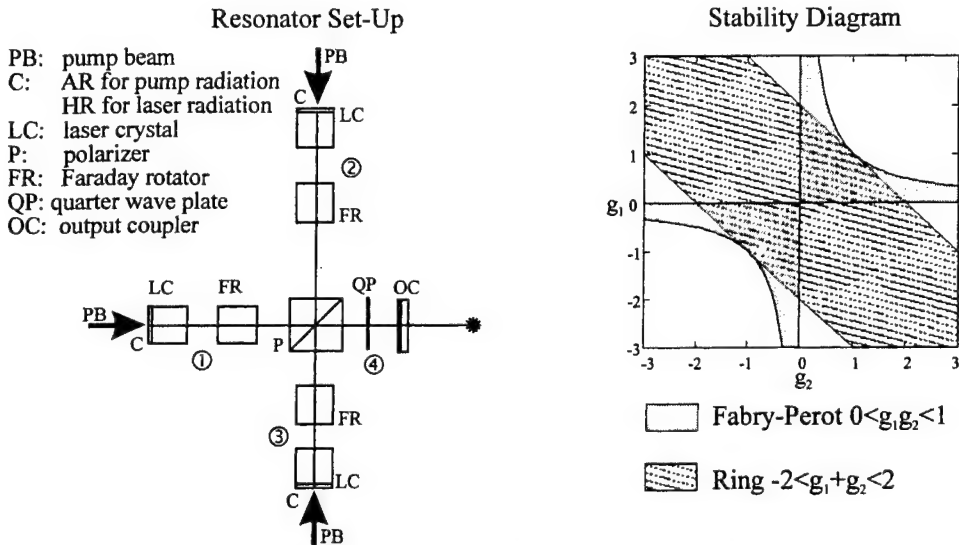


Figure 1. The three-rod dual-configuration resonator (left) and the corresponding stability diagram (right).

figure 1 except that quarter-wave plates were used instead of Faraday rotators. With every additional polariser, the number of rods can be increased by two. This resonator can either operate as a Fabry-Perot cavity or as a ring resonator. It features unique stability properties which are different for the two configurations (ring and Fabry-Perot), as shown in figure 1 (right). The stability condition for the ring configuration is particularly suitable for symmetric multirod resonators since the confocal point ($g_1=0$ and $g_2=0$) is in midst of the ring stability region.² Furthermore, the different stability conditions allow for the so-called configuration Q-switching technique.³ With the original set-up and three composite YAG/Nd:YAG rods, 16 W of fundamental-mode continuous-wave output with an excellent optical efficiency of 42% were obtained (limited by available pump power).⁴

In spite of the polariser in the cavity, the original resonator emits non-polarised radiation in both configurations.⁵ Polarised fundamental-mode output was now achieved by using birefringent laser crystals to enforce unidirectional operation in the ring configuration as explained in the following. The set-up of the new resonator is shown in figure 1. The only difference to the original set-up is the use of Nd:YVO₄ instead of Nd:YAG and that the quarter-wave plates in the arms with the laser crystals are replaced with Faraday rotators (FR). The a-cut Nd:YVO₄ crystals (1% Nd, 3x3x5 mm³) were oriented with the optical axis at 45° with respect to the drawing plane. To describe the path followed by the light through the resonator, it is useful to consider what happens in one arm of the crossed structure of the cavity. Light coming from the polarising beam splitter is reflected at the mirror at the end of the arm (HR-coating on crystal end faces, or output coupling mirror) and returns to the polariser. Because it has made a double pass of a FR or the quarter-wave plate in the process, it has its polarisation rotated by 90°. This means that light, if originally transmitted through the polarising beam splitter, on its return to the polariser is reflected and vice versa. Hence, whenever there is a FR or a quarter-wave plate in place the light is forced to progress on to the next arm of the resonator rather than returning to where it came from. With all the FRs and the quarter-wave plate in place, the resonator is in its ring configuration. Starting in arm 4, the light travels to the crystals 1, 2, and 3, returns to arm 4 and starts the roundtrip again with crystal 1. In principle, this roundtrip is also possible in the opposite direction, the only difference being the polarisation at the output coupler (and everywhere in the cavity). Hence if the (ring) laser operates in both directions, the output consists of a superposition of modes with different polarisations. Analogue arguments also apply to the laser in Fabry-Perot configuration. If one FR or the quarter-wave plate is removed, the resonator is in its Fabry-Perot configuration. A round-trip with the quarter-wave plate removed reads 4, 1, 2, 3, 4, 3, 2, 1, 4.

In the original dual-configuration resonator there is no mechanism that prevents the light from traversing the ring cavity in both directions and the polarisation of the modes is not defined in spite of the polariser P. In fact, an interesting feature of the original set-up is the existence of modes with circular polarisation at the linear polariser P.⁵ The key to polarised output is the use of birefringent laser crystals such as Nd:YVO₄ instead of the previously used isotropic Nd:YAG. In order to have a linearly polarised EM field for the propagation in the a-cut Nd:YVO₄ crystals, the quarter-wave plates of the original set-up had to be replaced by FRs, despite the higher intra-cavity losses caused by their reduced transmittance. The optical axes of the crystals are oriented such that the circulating light has always extraordinary polarisation in all crystals for one propagation direction and ordinary polarisation for the other propagation direction. Since for extraordinary beams in

Nd:YVO₄ the gain is higher (by a factor of more than three) and the thermal lens is weaker (by a factor of almost 3) than for ordinary beams, the laser only operates in the direction with the extraordinary polarisation and the laser output is perfectly polarised.

Despite unidirectional operation, single-frequency operation cannot be expected and was not aimed for with this set-up. The light entering the crystals from the AR-coated face interferes with the light that is reflected at the HR-coated face leading to spatial hole burning.

For the experiments the resonator was set-up with a distance of 158 mm between the end face of crystal 1 and the output coupler (to ensure fundamental-mode operation with a pump spot diameter of 600 μm). The other dimensions were adjusted to ensure symmetry (equidistant crystals along the laser beam). The crystals were pumped with fibre-coupled diode lasers. At a pump power of 9.0 W per crystal, the fundamental-mode output power at 1064 nm was 9.5 W, with a slope efficiency of 43%. The output has circular polarisation that can be converted to pure linear polarisation with a quarter-wave plate outside the resonator. At total pumping powers above about 30 W the resonator is unstable because of the thermal lenses in the crystals. We have recently shown that the stability range can be increased significantly by the use of composite rods thanks to weakened thermal lenses.⁴

Due to the different thermal lenses for the two propagation directions, the Fabry-Perot configuration of the set-up with a-cut Nd:YVO₄ crystals is always highly asymmetric even if the resonator is set-up for ideal symmetry in the ring configuration. This fact is very convenient for configuration Q-switching, since no additional asymmetry needs to be introduced by changing the set-up.³

In order to miniaturise the set-up we have recently reduced the dual-configuration resonator to the essential as shown in figure 2. The polarising beam splitter made of two Nd:YAG crystals separated by a dielectric polariser (coated on crystal) itself acts as the amplifying gain medium which is pumped by fibre-coupled diode lasers. The propagation distance from the pumped face to the polarising face is 11 mm. The crystals were originally used as amplifiers.^{12, 13} The quarter-wave plates are placed at the outer side of the laser crystals. Their rear faces are coated as HR mirrors for the laser wavelength. With the quarter-wave plates at this location the polarisation of the light reflected at the end of each arm is rotated with respect to the incident light and the beam of one single propagation direction does not form a standing wave in the gain medium. However, if both propagation directions are allowed to oscillate in the ring configuration, the counterpropagating modes lead to spatial hole burning. Single-frequency operation of this miniaturised laser was achieved by enforcing unidirectional operation by means of an additional polariser and a FR to prevent spatial hole burning as shown in the right-hand side of figure 2.

When the distance between laser crystal and output coupler was set to 15 mm in the left set-up of figure 2, 10.5 W of continuous-wave output at a total pump power of 27 W were obtained. The beam propagation factor was measured to be $M^2 = 3.2$ and the slope efficiency was 51%. To obtain fundamental-mode output, the distance between laser crystal and output coupler had to be increased to 130 mm. In this case the output power was 8 W at a total pump power of 24 W and a slope efficiency of 43%. In single-frequency operation (right set-up in figure 2) the output power was 4.5 W at a total pump power of 24 W. When the single-frequency set-up was Q-switched in preliminary experiments with an additional Pockels cell at a repetition rate of 500 Hz, the 0.3-mJ output pulses had a duration of 47 ns at a total pump power of 19 W.

In conclusion we have demonstrated that the dual- or variable-configuration resonator is an extremely interesting cavity for the efficient generation of continuous-wave or pulsed fundamental-mode laser output. The original set-up was improved to provide polarised and even single-frequency output radiation.

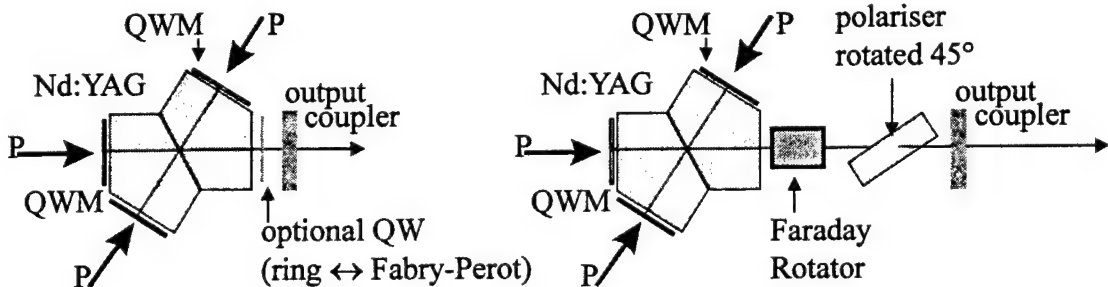


Figure 2. Left: miniaturised dual-configuration resonator. Right: single-frequency version. The arrows marked P represent the pumping beams. QW is a quarter-wave plate. QWM are quarter-wave plates that are HR-coated on the rear (outer) side.

3. RESONATORS WITH ADAPTIVE THERMAL LENS BALANCE

Due to the fast growing interest in high-power solid-state lasers for more and more industrial applications such as cutting, drilling, and welding a good solution of the thermally induced problems becomes indispensable. While schemes to compensate for the thermally induced birefringence were demonstrated successfully, the compensation of the phase front distortions resulting from the temperature dependence of the refractive index and the expansion of the material was addressed in alternative active medium designs but is not yet satisfying. With the thin-disk laser, for instance, laser output with $M^2 \approx 10$ is limited to powers below about 300 W.¹⁴ At the higher output powers of 529 W and 1070 W the M^2 values were reported to be approximately 50 and 80, respectively. For many applications the beam quality should not only have an acceptable value, it should also not vary with changing pump power. In our transversally pumped Nd:YAG laser based on the TransDuct pumping optics shown in figure 3 (left), the beam propagation factor varies significantly with increasing power and reaches a value of about 40 at an output power around 600 W (4 mm rod diameter). This performance is shown in the graph of figure 3. Higher powers but with lower beam quality were attained with rods of 5 mm in diameter.

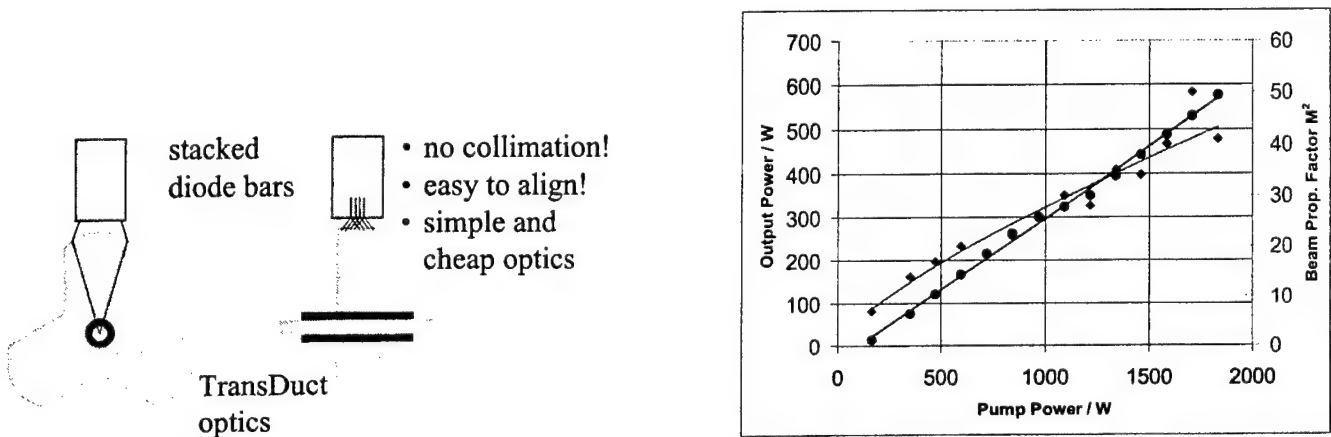


Figure 3. Left: TransDuct pumping optics: the laser rod is placed in a cooling water channel at the centre of the monolithic optics. The slow axis of the radiation emitted by the stacked diode-laser bars is focussed into the laser rod. In the fast axis the radiation is guided by total internal reflection inside the TransDuct glass. Right: performance of a laser with two TransDuct pumping heads (two 70 mm long Nd:YAG rods with a diameter of 4 mm pumped over a length of 44 mm) and a total resonator length of about 24 cm. The output power (dots) is shown on the left scale, the M^2 values (diamonds) on the right scale.

In order to get constant beam properties with varying power, the resonator parameters have to be adapted to account for the changing thermal lenses. Although active mirrors,^{15, 16} moving lenses,¹⁷ or resonator length adjustments¹⁸ are possible means, they require involved mechanical set-ups and/or electronic control. Another possibility to compensate for the thermally induced lens is to take advantage of the effect itself by using heated optical elements. In contrast to the use of a longitudinal pump source to generate mirror deformations or compensating lenses in appropriate optical elements,¹⁹ we have recently started to investigate a compensation scheme that is more suitable for transversally pumped high-power lasers.^{6, 20} The concept is sketched in figure 4. The rod-shaped compensating element in the resonator labelled B is heated by a weak absorption of the circulating intra-cavity laser radiation. Due to cooling at its barrel surface it generates a power-dependent thermal lens which is optically superimposed with the thermal lens of the laser rod. With appropriate values for sign and magnitude of the thermal dispersion dn/dT , absorption coefficient, and geometry the compensating element, above laser threshold, will always ideally compensate for changes of the thermal lens in the laser rod when the laser power is changed. This behaviour is illustrated by the solid line in the graph of figure 4, where the beam radius above threshold does not change anymore with varying power. The dashed line shows the fundamental-mode radius at the location of the thermal lens in the laser rod as a function of the pump power for a typical, transversally pumped Nd:YAG laser with the uncompensated resonator labelled A. It makes clear that without the self-adaptive compensating element, the power range for stable operation is limited and the beam properties change significantly with varying power.

In order to work in practice the amount of absorption in the compensating element needed to balance the thermal lenses should not exceed about 1%. It can be shown that the total absorption loss L introduced by the compensating element is given by the relation⁶

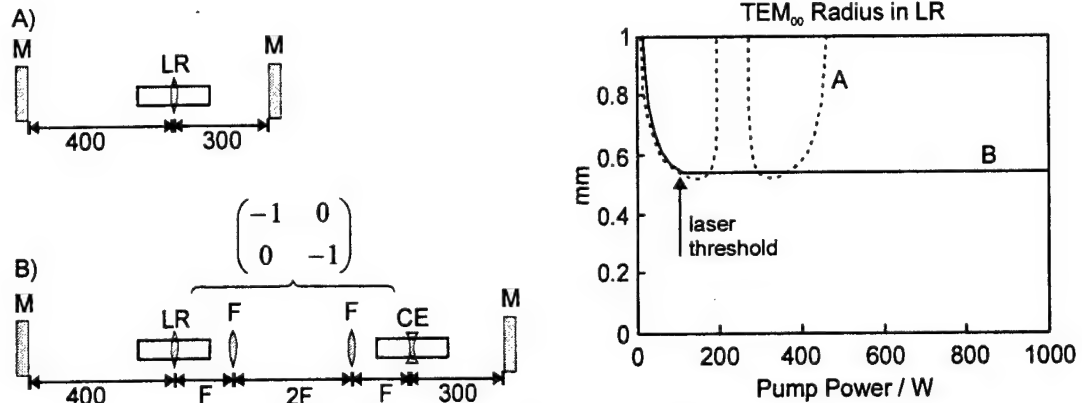


Figure 4. Self adaptive compensation scheme for high-power lasers. Above threshold the (negative) thermal lens in the compensating element (CE) balances the power-dependent changes of the thermal lens in the laser rod (LR). The lenses F are needed to optically superimpose the two thermal lenses. F is the focal length of the lenses marked F. Distances are given in mm.

$$L \approx \frac{dn/dT_{LR}}{-dn/dT_{CE}} \cdot \frac{k_{CE}}{k_{LR}} T_{OC}, \quad (1)$$

where T_{OC} is the transmittance of the output coupler, and k the heat conductivity. CE and LR stays for compensating element and laser rod, respectively. A suitable compensating material therefore has a strong thermal dispersion and a low heat conductivity. Technical glasses with dn/dT values of the order of that from Nd:YAG (but with negative sign) are available (Schott PK 51, PSK 54, and others) and typically have heat conductivities which are an order of magnitude lower than the heat conductivity of Nd:YAG. With a typical output coupling transmittance of $T_{OC} = 10\%$ the total absorption loss L required for an ideal compensation is about 1%, which is a very promising result.

The difficulty at the moment is to find glasses which, in addition to suitable thermal dispersion and low heat conductivity, also exhibit enough absorption at a wavelength of 1064 nm. Since the absorption of available technical glasses is too weak we made some tests with custom glass melts of PSK 54 were Cu was added in various concentrations (1%, 0.5%, and 0.2%) to tailor the absorption. The absorption at 1064 nm was unexpectedly strong. At a Cu concentration of only 0.2% the absorption in a 5 mm thick sample was found to be 91 % of the incident power. Further attempts with much lower Cu concentrations or tests with other dopants will have to be performed to get a suitable glass. It is noted that the absorbed power should also be distributed on a comparatively long compensating element (> 1 cm) to prevent stress induced fracture.

As an alternative to the development of novel glasses we have investigated the suitability of available Nd-doped laser glasses such as LG-760. The thermal dispersion ($dn/dT = -6.8 \cdot 10^{-6} \text{K}^{-1}$) and the heat conductivity ($0.67 \text{ Wm}^{-1}\text{K}^{-1}$) are well suited for the proposed compensation scheme. An interesting feature of Nd-doped laser glasses is their temperature-dependent absorption coefficient due to the thermal Nd^{3+} population on the lower laser level. The total absorption in a 45 mm long 8% Nd-doped LG-760 was measured to exponentially increase with increasing rod temperature reaching about 6% at a temperature of 140°C . On the one hand this means that the required absorption can be set by controlling the temperature of the cooling liquid around the compensating rod. On the other hand this temperature-dependent absorption leads to a dangerous feed back mechanism since an elevated temperature increases the absorption and the increased absorption on its turn leads to further heating. We have investigated this behaviour in extensive time- and spatially resolved finite-difference simulations. Since many parameters such as the exact energy levels, the fraction of absorbed power converted to heat etc. are not known with adequate accuracy, the results agree only within a factor of 2 with the experimental data. The qualitative results nevertheless give valuable information and explain the effects observed during the experiments. If the compensating element rod made of LG-760 is not cooled efficiently (e.g. air cooling with a heat transfer coefficient of $0.025 \text{ Wcm}^{-2}\text{K}^{-1}$), the temperature in the rod grows at increasing rate due to the above-mentioned feed-back mechanism, eventually leading to the stress-induced fracture of the rod. With the good heat transfer coefficient in the case of direct water cooling ($2 \text{ Wcm}^{-2}\text{K}^{-1}$) the temperature inside the rod reaches a stable distribution within seconds depending on cooling temperature and incident laser power. For a heat-sink temperature of about 50°C this stable behaviour is limited to approximately 1 kW of incident laser power. If the incident laser power exceeds this stability limit only slightly, the temperature in the rod first reaches what looks like a stationary distribution for a duration of the order of a minute and then all of a sudden growth exponentially with time before the rod is cracked. This was observed several times during the

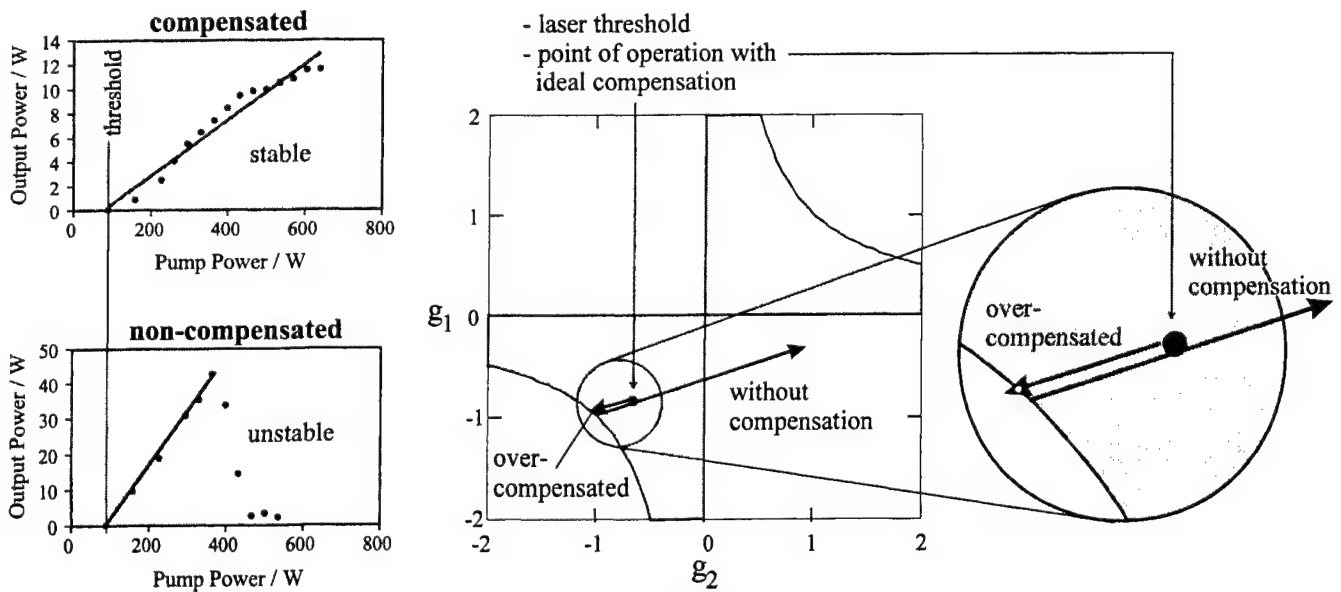


Figure 5. First demonstration of the thermo-optical compensation scheme. The compensated laser is stable up to the maximum available pump power, whereas the laser without compensation is unstable for pump powers exceeding 365 W. Since the compensating lens was too strong, the laser operates right on the edge of the stability region (white dot).

experiments. In conclusion we found that the temporally stable thermal lenses achieved with a 45 mm long LG-760 rod (8% doping) are not strong enough to compensate for the lens in the Nd:YAG laser rod. Unpractical long rods (about 10 cm) will have to be used for a good compensation with this material. Further extensive investigations are required to optimise the proposed thermo-optical compensation scheme.

With the aim to demonstrate the principle of the proposed compensation scheme, we set up a resonator similar to the one labelled B in figure 4. The parameters of the compensating element were far from being optimised but the experiment proved the scheme to work in principle. The optical distance from the plane output coupler to the thermal lens in the laser rod was 90 mm and the distance between the compensating lens and the other plane mirror was 270 mm. As shown in figure 5, the thermo-optically compensated laser is stable up to the maximum available pump power of 640 W. If the compensating element is removed, the laser is only stable up to a pump power of 365 W, which proofs that the negative lens of the compensating element balances the positive lens of the thermal lens in the Nd:YAG rod. Compared to the non-compensated case, the output power of the compensated resonator was however significantly reduced. Since in both cases the threshold was almost the same, this cannot be attributed to absorption or other losses introduced by the compensating element. The power reduction may be explained by the fact that the compensating thermal lens was far too strong. As shown in the stability diagram of figure 5 (right), with increasing pump power the non-compensated resonator starts at the point $g_1 = g_2 = -1$ and moves on a straight line before it becomes unstable with $g_2 = 0$. The laser starts to oscillate at threshold as marked with the black dot in the diagram. If the compensating element is in the cavity, this is the point where the compensating thermal lens sets in. In the case of ideal compensation every increase of the dioptric power of the thermal lens in the laser rod is compensated for with a change of the compensating lens and the laser does not move any further in the stability diagram. If however the compensating lens is too strong, the laser moves back towards the point $g_1 = g_2 = -1$. If the negative compensating lens became stronger than the positive lens in the laser rod, the resonator would even go beyond this point and become unstable. This however leads to a significant drop in power and consequently to a significantly weaker negative thermal lens in the compensating element so that the laser would move back into the stability region. Because of this process, the resonator is locked to the point right at the edge of the stability as marked with the white dot. This means that in this case of over-compensation at all pump powers above threshold the intra-cavity power drops to a level were the compensating thermal lens caused by the absorption of the intra-cavity laser radiation in the compensating element is not stronger than the thermal lens induced by the absorbed pump power in the laser rod.

Although the compensating lens was much too strong, this preliminary experiment proofs the proposed scheme to work in principle. Further investigations and developments will be needed to optimise the compensating elements. Good analytical and numerical models to describe and analyse the thermal processes in heated materials and their effects on optics are

required for this purpose. As a valuable complement to numerical simulations we have derived the general analytical solution of the cylindrically symmetric heat conduction equation as presented in the following section.

4. GENERAL ANALYTICAL MODEL FOR THE THERMAL EFFECTS IN LASER RODS

As the power of solid-state lasers increases a good understanding of the thermal effects is indispensable. Numerical simulations can handle the most general situations but optimisations of several parameters still need rather time consuming simulation series. Analytical models give the most comprehensive insight to the physical processes such as heat conduction, thermal dispersion and thermally induced birefringence. But so far, explicit expressions for thermally induced aberrations including birefringence were only known for the simple case of homogeneously heated rods or for rods with top-hat shaped heating distributions.^{7, 8} With these models it is impossible to optimise parameters such as pumping light distribution and active ion distributions or to calculate the exact phase aberrations of arbitrarily given heating distributions. In the following short summary we present a general analytical solution of the stationary heat conduction equation, where the only condition is the cylindrical symmetry of the heating distribution. The detailed derivations and discussions are published elsewhere.¹¹

In cylindrical symmetry the stationary heat conduction equation reads⁷

$$\frac{\partial^2}{\partial r^2} T(r) + \frac{1}{r} \frac{\partial}{\partial r} T(r) = -\frac{Q(r)}{k}, \quad (2)$$

where $Q(r)$ is an arbitrary heating distribution (power per unit volume), T is the temperature, k the heat conductivity and r the distance from the laser rod axis. The solution was found by exploiting the mathematical properties of this ordinary linear differentiation equation, whereupon the sum (or the integral) of solutions of several equations is the solution of the sum (or the integral) of the different equations. With this, the general solution of eq. (2) can be shown to be

$$T(r) = T_F + \frac{1}{2hr_{rod}} \int_{r_{rod}}^0 q(r_p) r_p^2 dr_p + \frac{Q(r_{rod})}{4k} (r_{rod}^2 - r^2) - \frac{\ln\left(\frac{r}{r_{rod}}\right)}{2k} \int_r^0 q(r_p) r_p^2 dr_p - \frac{1}{2k} \int_{r_{rod}}^r q(r_p) r_p^2 \ln\left(\frac{r_p}{r_{rod}}\right) dr_p + \frac{1}{4k} \int_{r_{rod}}^r q(r_p) r_p^2 dr_p - \frac{r^2}{4k} \int_{r_{rod}}^r q(r_p) dr_p \quad (3)$$

where T_F is the temperature of the cooling fluid, r_{rod} the rod radius and h the heat transfer coefficient between laser rod and cooling liquid. The function $q(r_p)$ is the differential heating distribution defined as

$$q(r_p) = \left. \frac{dQ(r)}{dr} \right|_{r=r_p} \quad (4)$$

With this solution and a given heating distribution $Q(r)$ explicit expressions for the temperature distribution and the optical distortions can be found. In most practical cases the real heating distribution measured in the experiment can easily be approximated with a polynomial fit of the form

$$Q(r) = \sum_{i=0}^n c_i r^i. \quad (5)$$

In this case the solution for the temperature distribution simplifies to

$$T(r) = T_F + \frac{1}{h} \sum_{i=1}^n \frac{c_i}{i+2} r_{rod}^{i+1} + \frac{1}{k} \sum_{i=0}^n \frac{c_i}{(i+2)^2} (r_{rod}^{i+2} - r^{i+2}). \quad (6)$$

With the equations (3) or (6), the thermally induced optical distortions such as lensing, birefringence and bifocussing are found by further straight-forward calculations. For these distortions, an excellent agreement to measurements and to numerical simulations was found, showing that we have developed a reliable and useful tool to optimise high-power lasers. The major importance of this analytical solution is that it leads to explicit expressions where the effects of various parameters such as pumping distribution, doping concentration distribution, etc. can be seen directly without the need of involved and time consuming numerical simulations. Compared to numerical finite-elements simulations, the use of our analytical model for the calculation of the thermally induced birefringence in laser rods is faster by three orders of magnitude (on the same PC) at even higher accuracy. Instead of 1½ hours the calculation takes just a few seconds.

5. CONCLUSIONS AND OUTLOOK

Some additional interesting properties of the dual-configuration resonator have been demonstrated in further experiments showing its potential in very varied operation regimes. From very efficient fundamental-mode continuous-wave or Q-switched operation this unique laser was improved to emit fully polarised and even single-frequency radiation in unidirectional ring operation.

The proposed scheme to compensate for the thermally induced lenses in the laser rod with an additional self-adaptive thermo-optical element has been demonstrated in a first experimental test. Further extensive investigations to optimise the performance of the compensating elements and the balance of the thermal lenses in high-power laser resonators are indispensable.

A novel analytical model for the thermal effects in cylindrically symmetric situations has been derived as a valuable tool for the required optimisations of high-power solid-state lasers.

6. REFERENCES

1. S. T. Bowman, "Lasers without internal heat generation", *IEEE J. Quantum Electron.* **35** (1), 115-122, 1999
2. Th. Graf, M. P. MacDonald, J. E. Balmer, R. Weber, and H. P. Weber, "Variable-configuration resonator (VCR) with three diode-laser end-pumped Nd:YAG rods", *OSA Trends in Optics and Photonics (TOPS)* **10**, 370-375, 1997
3. M. P. MacDonald, Th. Graf, J. E. Balmer and H. P. Weber, "Configuration Q-switching in a diode-pumped multirod variable-configuration resonator", *IEEE J. Quantum Electron.* **34**, 366-371, 1998
4. M. P. MacDonald, Th. Graf, J. E. Balmer and H. P. Weber, "Reduction of the thermal lens in a multiple-crystal, composite-Nd:YAG-rod laser", accepted for publication in *Opt. Comm.*, 2000
5. M. P. MacDonald, Th. Graf, J. E. Balmer, and H. P. Weber, "Efficient polarised output from end-pumped multirod resonators", *Opt. Comm.* **160**, 354-363, 1999
6. R. Weber, Th. Graf, M. Schmid, and H. P. Weber, "Self-adjusting compensating thermal lens to balance the thermally induced lens in solid-state lasers", accepted for publication in *IEEE J. Quantum Electron.* 2000
7. W. Köchner, "Solid-state laser engineering", 350-353, second edition, Springer 1988.
8. S. C. Tidwell, J. F. Seamans, M. S. Bowers, and A. K. Cousins, "Scaling CW diode-end-pumped Nd:YAG lasers to high average powers", *IEEE J. Quantum Electron.* **28**, 997-1009, 1992
9. M. E. Innocenzi, H. T. Yura, C. L. Fincher, and R. A. Fields, "Thermal modelling of continuous-wave end-pumped solid-state lasers", *Appl. Phys. Lett.* **56** (19), 1831-1833, 1990
10. M. Schmid, A. Lucianetti, R. Weber, Th. Graf, M. Roos, and H. P. Weber, "Numerical simulation and analytical description of the thermally induced birefringence in laser rods", accepted for publication in *IEEE J. Quantum Electron.*, 2000.
11. M. Schmid, Th. Graf, and H. P. Weber, "Analytical model of the temperature distribution and the thermally induced birefringence in laser rods with cylindrically symmetric heating" accepted for publication in *J. Opt Soc Am B*, 2000.
12. Th. Graf, U. Roth, M. Schmid, J. E. Balmer, H. P. Weber, "Diode-pumped Nd:YAG amplifier for intersatellite optical communication", *Opt. Comm.* **152**, 302-306, 1998
13. U. Roth, Th. Graf, E. Rochat, K. Haroud, J. E. Balmer, and H. P. Weber, "Saturation, Gain, and Noise Properties of a Multipass Diode-Laser-Pumped Nd:YAG CW Amplifier", *IEEE J. Quantum Electron.* **34**, 1987-1992, 1998
14. Chr. Stewen, M. Larionov, A. Giesen, and K. Contag, "Yb:YAG thin disk laser with 1 kW output power", Technical Digest of the conference on Advanced Solid-State Lasers, Davos, 13-16 February 2000, Davos, paper MA5
15. U. J. Greiner, H. H. Klinbenberg, "Thermal lens correction of a diode-pumped Nd:YAG laser of high TEM₀₀ power by an adjustable-curvature mirror", *Opt. Lett.* **19**, 1207-1209, 1994
16. A. V. Kudryashov, "Intracavity laser beam control", *SPIE proceedings* **3611**, 32-41, 1999
17. S. Jackel, I. Moshe, and R. Lavi, "High performance oscillators employing adaptive optics comprised of discrete elements", *SPIE proceedings* **3611**, 42-49, 1999
18. D. C. Hanna, C. G. Sawyers, M. A. Yuratich, "Telescopic resonators for large-volume TEM₀₀-mode operation", *Optical and Quantum Electron.* **13**, 493-507, 1981
19. R. Koch, "Self-adaptive elements for compensation of thermal lensing effects in diode end-pumped solid-state lasers - proposals and preliminary experiments", *Optics Communications* **140**, 158-164, 1997
20. Th. Graf, M. Schmid, R. Weber, and H. P. Weber, "Reduction of the thermal lens in solid-state lasers with compensating optical materials", proceedings of the 2nd International Workshop on Adaptive Optics for Industry and Medicine, 12th-16th July 1999, Durham, 175-180

200W-average-power Nd:YAG laser with self-adaptive cavity completed by dynamic refractive-index gratings

O.L. Antipov⁺, A.S. Kuzhelev, D.V. Chausov, A.P. Zinov'ev

Institute of Applied Physics of the Russian Academy of Science

603600, 46 Uljanov St., Nizhny Novgorod, Russia

Tel.: +7(8312)384547; Fax: +7(8312)363792;

⁺e-mail: antipov@appl.sci-nnov.ru

ABSTRACT

A high average power laser oscillator with a cavity completed by refractive index gratings that accompany population gratings induced in Nd:YAG laser crystals by generating beams themselves is investigated experimentally. The spatio-temporal self-adaptation of the cavity formed by nonlinear dynamic mirrors is studied. The possibility of compensating polarization distortions inside laser crystals is also investigated. The generation of beams with average power up to 250W, near-diffraction-limited divergence, and long coherence length is demonstrated.

1. INTRODUCTION

The holographic gratings of refractive index and gain induced in active laser media by generating optical beams themselves can complete the cavity of laser oscillators. Such kind of self-starting laser oscillator based on laser crystals has been demonstrated recently [1-8]. An important advantage of the lasers of a new class is the self-adaptive property of their cavity provided by a nonlinear dynamic mirror, which is a self-pumped phase conjugate mirror. This adaptive property is attractive for creation of high average power lasers with good beam quality.

Self-starting laser oscillators with dynamic cavity of two types have been recently demonstrated. The first type of the oscillator based on laser crystals (LaCs) such as Nd:YAG and Ti:S incorporates a nonreciprocal transmission element in the cavity formed by a gain grating (GG) [2,4,5]. Another laser oscillator with reciprocal cavity was reported to be formed by a moving resonant refractive index grating (RIG) which accompanies the population grating (PG) induced in a Nd:YAG crystal by generating beams [6-9]. The latter type of laser has demonstrated the capability for generating beams with high average power (up to 100W) and near-diffraction-limited quality [7,8].

In this paper we present new results of our experimental investigations of the self-starting lasers based on Nd:YAG crystals with a reciprocal cavity completed by the dynamic holographic grating. We also demonstrate the capability of these lasers to generate beams with an average power of 200-250 W and good quality.

2. PRINCIPLE OF THE SELF-STARTING LASER ON POPULATION GRATINGS

The general idea of the laser oscillator with a cavity completed by holographic gratings of population inversion induced in a LaC can be described for the simplest example of a laser scheme consisting of a Nd:YAG amplifier and a loop feedback formed with mirrors M₁-M₃ (Fig. 1).

Four optical waves (starting initially from amplified spontaneous emission (ASE)) with complex amplitudes E₁,...,E₄ can interfere with each other. The interference fields will induce the PG's. The gratings of population inversion in the laser crystals are accompanied by both GG's and RIG's. The latters are caused in the Nd:YAG amplifier by the difference in polarizability of excited and unexcited Nd³⁺ ions [10,11]. These gratings complete the cavity of the laser-oscillator.

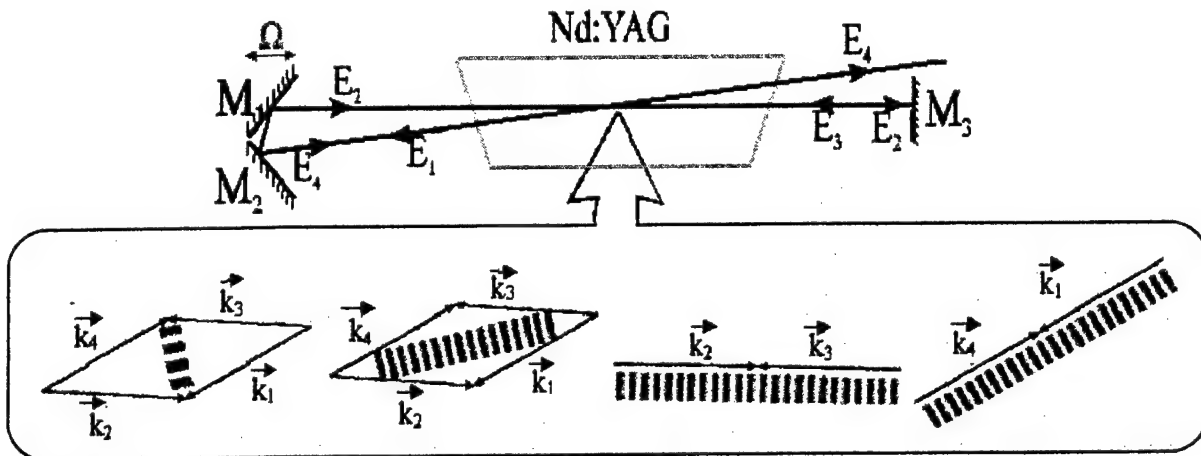


Fig. 1. Schematic of a self-starting generator with a loop cavity. M_1 is the vibrating mirror that gives the frequency shift Ω to reflected waves; M_2 and M_3 are linear mirrors; k_1, \dots, k_4 are wave vectors of the interacting optical waves E_1, \dots, E_4 in the cavity; the dashed area indicates PG's inside the LaC.

3. EXPERIMENTAL SCHEME OF THE LASER ON POPULATION GRATINGS

Our previous study of the self-starting laser with cavity completed by holographic gratings has shown the possibility of generation of 100W-average-power beams with near-diffraction quality [3,7-9]. Our new experiments were carried out to investigate the ways of increasing the output power of lasing beams

- in a scheme comprising amplifiers with larger Nd:YAG rods ($\varnothing 10 \text{ mm} \times 135 \text{ mm}$);
- adding one more pass of the generated beam through an amplifier;
- using different geometry of the cavity and mirrors with curvature.

The self-adaptive property of such kind of laser was studied additionally by using an intracavity phase plate.

3.1. The scheme comprising two amplifiers with large Nd:YAG rods

Laser rods of large size ($\varnothing 10 \text{ mm} \times 135 \text{ mm}$) with the concentration of Nd^{3+} ions of about 1.1% were used. These standard-quality laser rods were produced by the Chokhralskii method in Laser Material Corporation (USA).

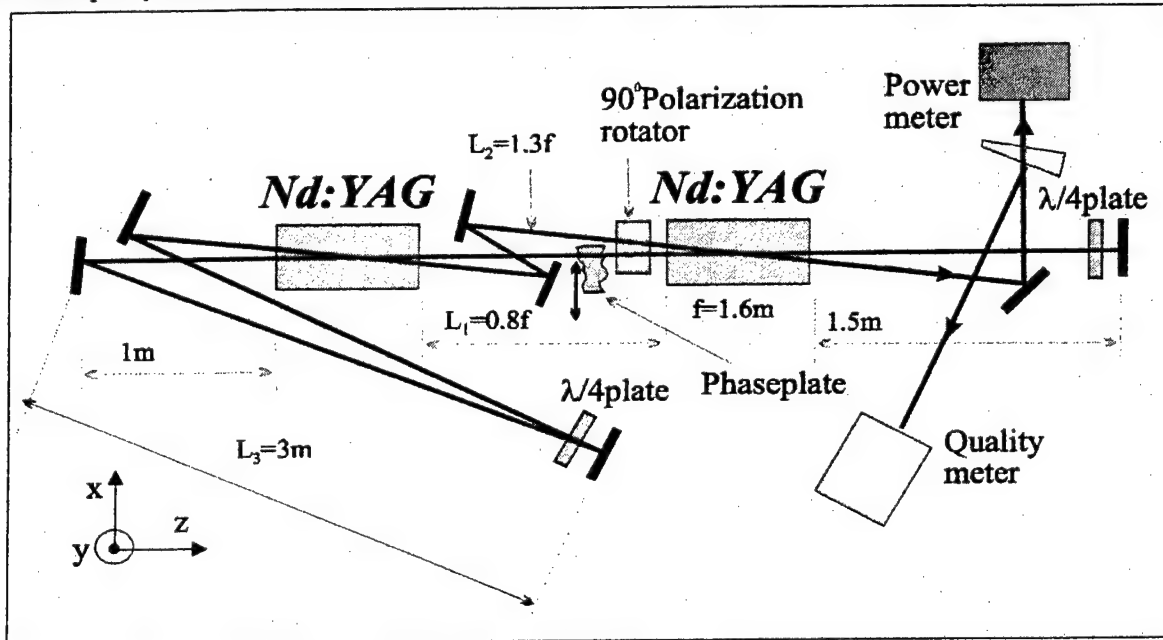


Fig. 2. The experimental setup of self-starting scheme based on two amplifiers (Nd:YAG rods with sizes $\varnothing 10 \times 135 \text{ mm}$).

The scheme comprising two amplifiers with these Nd:YAG rods was studied (Fig. 2). The amplifiers provided double flash lamp pumping to each rod with maximum pump pulse energy up to 200 J at a repetition rate of 30 Hz. Strong thermal lenses were induced in laser crystals under this pumping. The focal distances of the lenses depended on pump pulse energy, repetition rate and temperature of cooling water. We investigated the effect of focal distances on optimal distances between the amplifiers and mirrors required to achieve maximum output beam power and good quality. It was found that an increase in the focal distances by 1.5 times (due to improved cooling) leads to a necessity to have the same increase in the distances between the amplifiers and mirrors in order to achieve the same average power of the beam and the same beam quality (Fig. 3). The normalized distances between the amplifiers and mirrors determined from the focal distance of the lens thermally induced in the amplifiers are shown in Fig. 2.

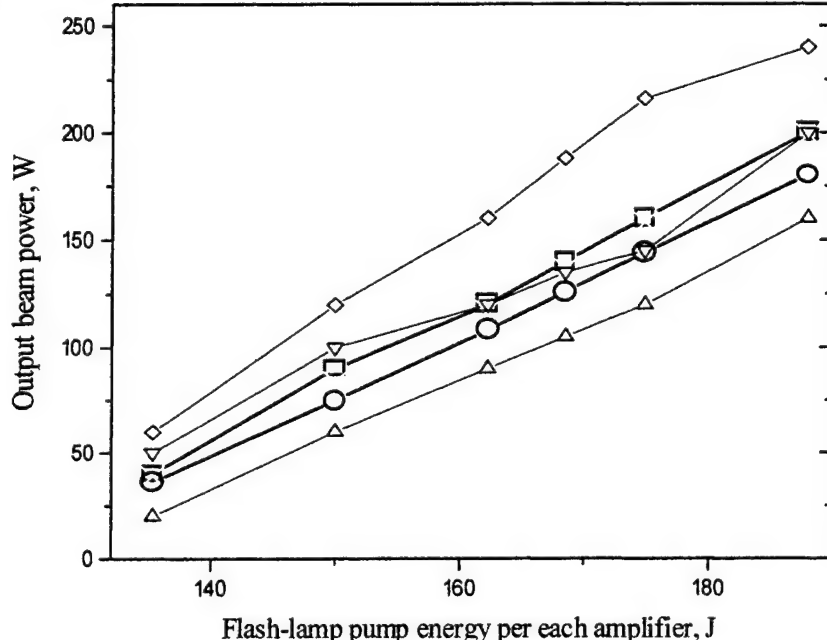


Fig. 3. Average power of the generated beam as a function of pump pulse energy of each amplifier in the scheme with two Nd:YAG amplifiers (circles – scheme of Fig. 2 without polarization elements with $L_3=0$, crosses – scheme of Fig. 2 without polarization elements, with $L_3=3$ m and without phase plate, squares – scheme of Fig. 2 with polarization elements, with $L_3=3$ m and without phase plate, down-triangles – scheme of Fig. 4 with plane mirror and polarization elements, diamonds – scheme of Fig. 4 comprising a mirror with curvature and polarization elements, up-triangles – scheme of Fig. 4 with polarization elements, with $L_3=3$ m and with phase plate). The repetition rate is 30 Hz.

The key property of the new laser is the quality of the beam it generates. The self-adaptive property of the cavity with the nonlinear phase-conjugate mirror allows us to expect an improvement in the quality of the generated beam [12,13]. To study the beam quality, we measured the M^2 parameter which characterizes the difference between an ideal gaussian beam and the real one [14]. We used a method for testing laser beam parameters (such as beam widths, divergence angle, and beam propagation factor) in accordance with standards of the International Organization for Standardization [14].

To decrease polarization distortions, we used a $\lambda/4$ plate and a quartz polarization rotator. These elements allowed for rotation of the generated wave polarization by 90° after passage through each amplifier. Therefore the polarization distortions that appeared during one passage through the amplifier were compensated during the next passage. This method for compensating polarization distortions has been used in design of solid-state lasers [15]. It can be seen that the average power of the generation beam did not depend on the presence of polarization elements. At the same time, the beam quality is strongly dependent on the pump power, the presence of polarization elements, and the scheme length (see Table 1).

3.2. The scheme of the self-starting laser with additional passes through the amplifier

We studied the possibility of increasing the output power of the generating beam by adding one more pass of the generated beam through an amplifier (Fig. 3).

Table 1.

Scheme	Maximum average power achieved	$M_{x,y}^2$ -parameter at maximal power	Beam profile in focal plane of the lens
Fig.8 L1=1.3 m L2=2.1 m L3=0 Without polarisation rotation	180 W	$M_x^2=11$ $M_y^2=14$	
Fig.8 L1=1.3 m L2=2.1 m L3=3 m Without polarisation rotation	200 W	$M_x^2=5.1$ $M_y^2=4.4$	
Fig.8 L1=1.3 m L2=2.1 m L3=3 m With polarisation rotation	200 W	$M_x^2=1.7$ $M_y^2=2.2$	
Fig.10 L1=1.3 m L2=2.1 m With polarisation rotation, with plane mirror.	200 W	$M_x^2=2.6$ $M_y^2=3.1$	
Fig.10 L1=1.3 m L2=2.1 m With polarisation rotation, with mirror having curvature.	250 W	$M_x^2=3.5$ $M_y^2=2.7$	
Fig.8 L1=1.3 m L2=2.1 m L3=4 m With polarisation rotation, with phase plate	160 W	$M_x^2=1.5$ $M_y^2=3.6$	

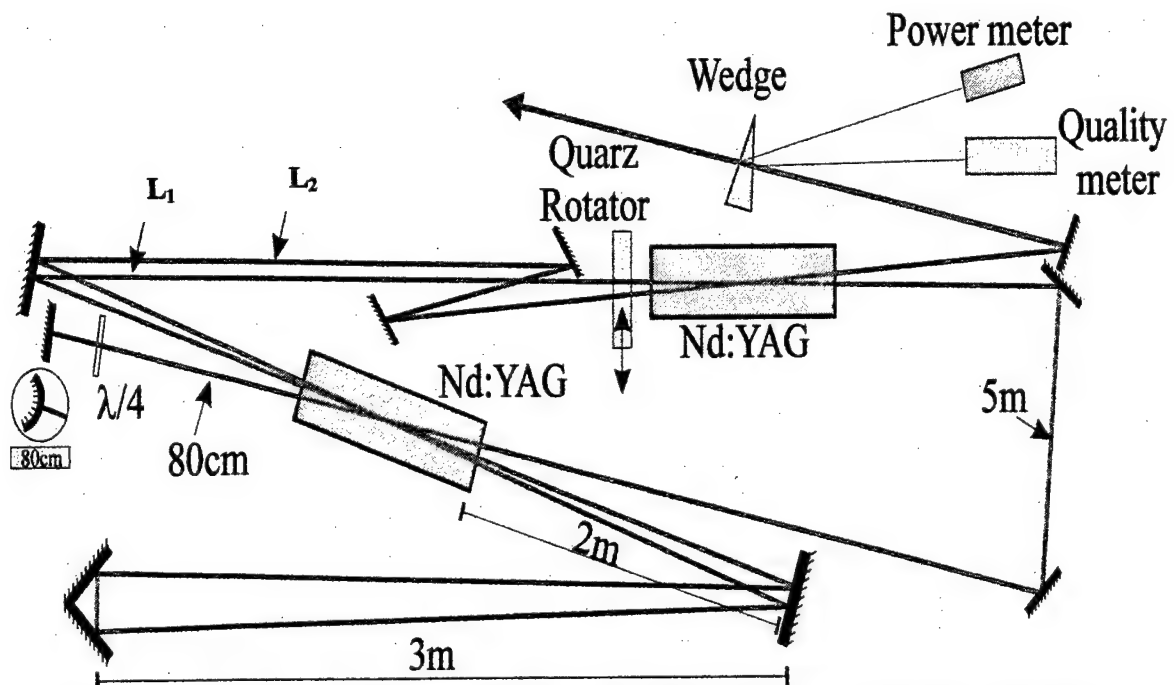


Fig. 4. The experimental setup of the self-starting scheme with two amplifiers (Nd:YAG rods $\varnothing 10 \times 135$ mm) with an additional pass of the generated beam through one amplifier. Two variants of the scheme: with a plane mirror and a mirror with the curvature radius of 80 cm.

It was found that in this case the average power of the output beam did not change (Fig. 3). However, the quality of the beam became worse; the M^2 parameter was 2.6 in the x direction and 3.1 in the y direction. An increase in the average power of the output beam was observed when a mirror with curvature was used to compensate thermal focusing in the additional pass (Fig. 4). The average power achieved 240 W (Fig. 3), but the quality of the beam decreased. The M^2 parameter was 3.5 in the x direction and 2.7 in the y direction. The results are summarized in Table 1.

It can be seen from Table 1 that the best results were observed in the scheme (Fig. 4) with large lengths and polarization rotation elements (a $\lambda/4$ plate and a quartz polarization rotator). The average power of the generation beam in the near field was 200 W. The transformation of the output beam profile during its propagation was studied. The profiles of the beam in the near and far field generated in the optimal scheme are shown in Fig. 5. The average power of the beam core within $\varnothing 13$ mm in the far field was 100W. The difference is caused by the large-angle components, and the power of the core indicates the ability of the generated beam to provide large-distance energy transfer. This result is in good accord with measurements of the beam-quality M^2 parameter.

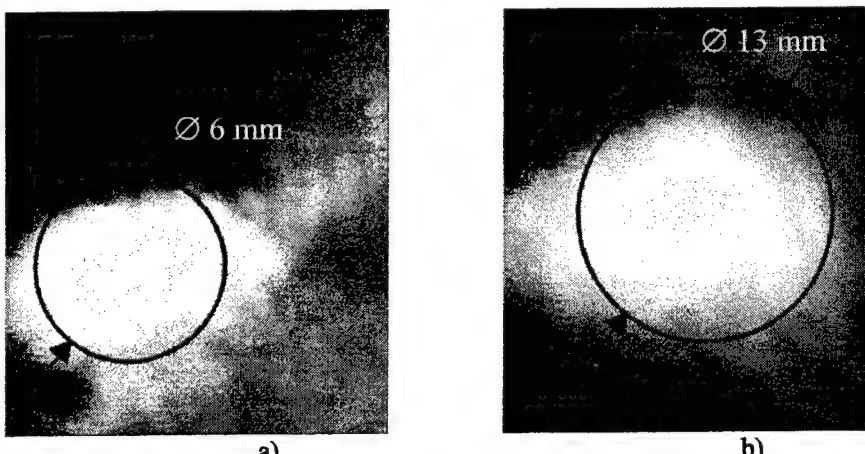


Fig. 5. Transverse profiles of the generation beam at distances 3 m (a) and 17 m (b) from the output of the laser.

The deviations in the generation direction were observed at maximum pump power (at pump pulse energy of 200 J for each amplifier and a repetition rate of 30 Hz). These deviations led to movement of the beam in the far field. The range of this movement coincided with the diameter of the generated beam's core. It was found that these deviations were caused by instability of the pulse energy of flash-lamp pumping (due to instability of power supply), which led to instability of the focal distance of thermal lenses and instability of thermal edges induced in amplifiers. The deviations were minimized at a lower repetition rate when power supply of the amplifiers worked in a mode that provided high stability of pump pulse energy. At a repetition rate of 22 Hz and the same pump pulse energy the beam's shift in the far field was less than 20% of the beam diameter; however, the average power of the generated beam decreased by 25% in this case.

3.3. Additional test of self-adaptation of the laser cavity

The self-adaptive properties of the scheme were tested by inserting a phase plate with large aberrations (it increased the beam divergence by 10 times) (Fig. 2). It was observed that the average power of the generated beam decreased to 160 W. The quality of the beam remained near diffraction ($M_x^2=1.5$, $M_y^2=3.6$). This result shows the self-adaptability of the nonlinear dynamic cavity to phase distortions. The mechanism for this adaptability is shown in Fig. 6. The nonlinear holographic cavity is formed so that the output beam E_4 and the initial noise E_1 are near Gaussian and are close to phase conjugated beams which play a role of pumping waves in the four-wave interaction. The beam E_2 , which is strongly aberrated, interacts with the pumping waves in the Nd:YAG amplifier. This four-wave interaction gives rise to a beam E_3 that is phase conjugated to E_2 . Thus all phase distortions that deteriorated the beam E_2 are compensated for the beam E_3 . The near-Gaussian beam E_3 has small aperture losses in the long-distance scheme and transforms to a near-Gaussian output beam E_4 . In order to decrease the generation threshold and hence increase the generated pulse energy, the beam E_2 is reflected backward by the mirror. This provides a high initial level for the conjugated beam E_3 . Indeed, the linear reflection of the beam E_2 has a component that is phase conjugated. At the same time, a non-conjugated component will be deteriorated once again by the phase plate and will have very large losses in the long-distance scheme with Fresnel parameter of 1-3. Therefore we provide conditions under which the self-starting scheme is forced to operate in the phase conjugation mode with a near-Gaussian output beam.

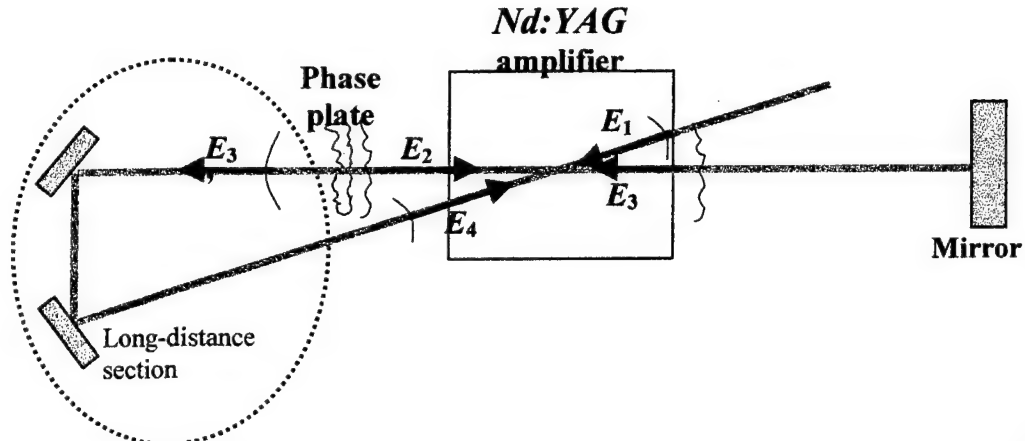


Fig. 6. Schematic view of four-wave mixing in self-starting laser-oscillator that provides self-adaptive compensation for phase distortions.

The profiles of the beam in the near and far fields generated in the optimal scheme with a phase plate are shown in Fig. 7. The average power of the generation beam in the near field was 160 W. The transformation of the output beam profile during its propagation was studied. The average power of the beam core within $\varnothing 17$ mm in the far field was 75W. It can be seen that the contributions to the large-angle components and to the central core are approximately the same as in the scheme without phase plate. This demonstrates once again the ability of the dynamic cavity to compensate internal phase distortions.

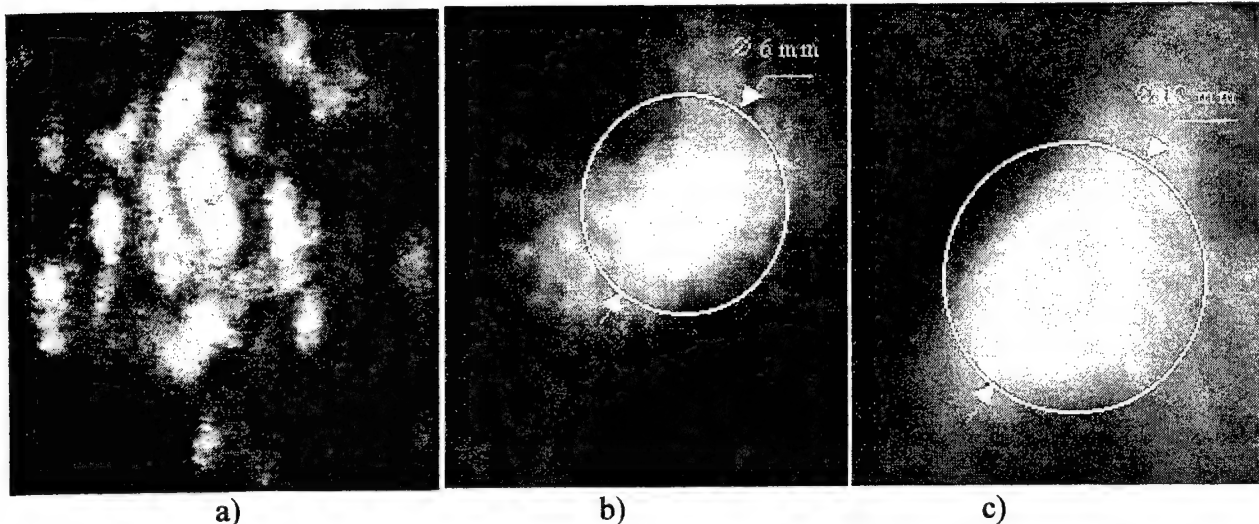


Fig. 7. Transverse profile of a Gaussian beam passed through the phase plate in the far field (a). Transverse profiles of the generation beam at distances 3 m (b) and 17 m (c) from the output of the laser with a phase plate.

Thus the self-adaptive properties of the nonlinear holographic mirror were demonstrated. Taking the scheme that incorporates a phase plate with high aberrations as an example, we show how aberrations thermally induced in laser crystals are compensated by the nonlinear holographic cavity. The conditions for generation of a beam with high quality and high average power were determined. It was demonstrated that beam distortions caused by birefringence thermally induced in a Nd:YAG rod can be significantly reduced by use of polarization rotation elements. A further increase in the efficiency of the high average-power laser with good quality of the generated beam can be achieved by use of diode pumping.

4. CONCLUSION

We have studied experimentally a self-starting laser oscillator with cavity completed by population gratings in Nd:YAG laser crystals. It is shown that this generation is caused by self-consistent formation of the refractive index and gain gratings accompanying the population gratings. It was found that the Nd:YAG laser with the cavity formed by dynamic gratings possesses self-adaptive properties and has the capability to generate radiation with high beam quality in the pulse-repetitive regime. The single transverse mode operation of the self-starting laser (comprising three amplifiers and having loop geometry) with an output average power up to 200 W was demonstrated. Similar laser architectures appear to be attractive for creation of more powerful generators with an output power at the sub-kilowatt level.

ACKNOWLEDGMENT

This work was supported in part by INTAS (through grant I 97-2112), EOARD/Air Force Research Laboratory through grant No. SPC99-4028 (under contract No. F61775-99-WE028) and the NATO "Science For Peace" foundation (through grant No. 974143).

REFERENCES

1. I.M. Bel'dyugin, V.A. Berenberg, A.E. Vasil'ev, I.V. Mochalov, V.M. Petnikova, G.T. Petrovskii, M.A. Kharchenko, and V.V. Shuvalov, "Solid-state lasers with self-pumped PC mirrors in the active medium", *Sov. J. Quantum Electr.* **16**, pp. 1142-1145 (1989).
2. M.J. Damzen, R.P.M. Green, K.S. Syed, "Self-adaptive solid-state oscillator formed by dynamic gain-gratings holograms", *Opt. Lett.* **20**, pp. 1704-1706 (1995).
3. O.L. Antipov, A.S. Kuzhelev, V.A. Vorob'yov, A.P. Zinov'ev, "Millisecond pulse repetitive Nd:YAG-laser with self-adaptive cavity formed by population gratings," *Optics Comm.* **152**, pp. 313-318 (1998).
4. A. Minassian, G.J. Crofts, M.J. Damzen, "Self-starting Ti:sapphire holographic laser oscillator," *Opt. Lett.* **22**, pp. 697-699 (1997).

5. P. Sillard, A. Brignon, and J.-P. Huignard, "Gain-grating analysis of a self-starting self-pumped phase-conjugate Nd:YAG loop resonator," *IEEE J. Quant. Electron.* **34**, pp. 465-472 (1998).
6. O.L. Antipov, S.I. Belyaev, A.S. Kuzhelev, A.P. Zinov'ev, "Nd:YAG laser with cavity formed by population inversion gratings", *SPIE Proceeding* (Edited by P. Galarneau and A.V. Kudryashov) **3267**, pp. 181-190 (1998).
7. O.L. Antipov, A.S. Kuzhelev, A.P. Zinov'ev, "High average-power solid-state lasers with cavity formed by self-induced refractive index gratings," in *Laser resonators II*, A.V. Kudryashov and P. Galarneau, eds., *Proc. SPIE* **3611**, 147-156 (1999).
8. O.L. Antipov, A.S. Kuzhelev, A.P. Zinov'ev, et all., "Single-mode Nd:YAG laser with cavity formed by population gratings," in *Nonlinear and Coherent Optics*, V.E. Sherstobitov, eds., *Proc. SPIE* **3684**, pp. 59-63 (1998).
9. O.L. Antipov, A.S. Kuzhelev, D.V. Chausov, "Formation of the cavity in a self-starting high-average power Nd:YAG laser oscillator," *Optics Express* **5**, No. 12, pp. 286-292 (1999).
10. O.L. Antipov, S.I. Belyaev, A.S. Kuzhelev, D.V. Chausov, "Resonant two-wave mixing of optical beams by refractive index and gain gratings in inverted Nd:YAG," *J. Opt. Soc. America B* **15**, pp. 2276-2281 (1998).
11. O.L. Antipov, A.S. Kuzhelev, D.V. Chausov, and A.P. Zinov'ev, "Dynamics of refractive index changes in a Nd:YAG laser crystal under Nd³⁺-ions excitation," *J. Opt. Soc. America B* **16**, pp. 1072-1079 (1999).
12. A.E. Siegman, P.A. Belanger, A. Hardy, *Optical Resonators Using Phase-Conjugate Mirrors*, in "Optical Phase Conjugation", R.A. Fisher, Ed., Academic Press, New York, (1983), p. 465.
13. B.Ya. Zel'dovich, N.F. Pilipetsky, V.V. Shkunov, *Principles of phase conjugation*, Springer, Berlin (1985).
14. "Optics and optical instruments – Test methods for laser beam parameters: beam width, divergence angle and beam propagation factor" (ISO/DIS 11146:1995).
15. W.A. Clarkson, N.S. Felgate and D.C. Hanna, "Simple method for compensation of thermally-induced birefringence in high-power solid-state lasers," Technical digest of CLEO/Europe'98, paper CWD1, 151, 1998.

Low-power and midpower diode-pumped lasers and their application

Georgiy M. Zverev ^A, Ivan I. Kuratev ^B

^A (Polyus RDI, Moscow, Russia), ^B (Laser-compact Co. Ltd., Moscow, Russia)

ABSTRACT

The state and development prospects of diode-pumped solid-state Nd:YAG lasers are discussed using the devices developed by Polyus RDI and Laser-compact company as examples. Low-power CW and Q-switched IR, green and blue lasers are successfully used for completing medical and industrial devices. The lasers operate in TEM00 mode with stability no worse than 2% per 8h of operation. Pulsed lasers providing a pulse energy of 50 mJ form the basis for a new generation of optoelectronic devices. The problem of stable operation of diode-pumped Nd:YAG laser within a wide operating temperature range is considered.

Keywords: diode-pumped solid-state lasers, wide operating temperature range, CW and Q-switched lasers, stability

In the last ten years the solid-state laser technology underwent considerable changes. Formerly, to pump solid-state lasers, gas-discharge lamps (arc lamps and flashlamps) were mainly used. Now, in connection with significant progress in development of high-power semiconductor lasers, the latter became widely used to pump solid-state lasers.

Polyus RDI turned to diode pumping of solid-state lasers in 1965, when at helium temperature lasing was produced in the $U^{3+}:CaF_2$ crystal* at $2.613 \mu m$ pumped by the stack of 35 GaAs laser diodes with a total pump energy of 3.5 mJ^1 .

Later this work was continued in the direction of the use of high-power LEDs to pump $Nd^{3+}:YAG$ lasers, which led to development in 1981 of the LTI-101 laser model providing an output up to 10 mW at $1.064 \mu m^{2,3}$. In 1986 the LTI-407 $Nd^{3+}:YAG$ laser model with frequency conversion into second harmonic in the $Ba_2NaNb_5O_{15}$ crystal and an output up to 10 mW was developed.

In 1987 the use of high-power laser diodes for pumping allowed us to obtain 0.36 W output of the cw Nd:YAG laser in one transverse mode⁴.

Since 1992 the line of low-power diode-pumped lasers has been successfully developing at Laser-compact scientific and production company founded by the group of specialists of Polyus RDI under the leadership of Ivan I. Kuratev.

The point in that in low-power lasers the distinctions between pumping by laser diodes and lamp pumping are best realized. The design of pump lamps and a spontaneous character of their radiation do not allow focusing a large part of radiation into a small volume of active medium. An emission of power laser diode may be easily focused into a spot about 0.1 mm . As a consequence diode pumping allows easily producing generation of solid-state laser with a volume of active medium about 10^{-5} cm^3 , whereas previously an active volume for lamp pumping was no less than 0.1 cm^3 . Decrease of a volume of active medium by a factor of 10^4 allowed reduction of threshold pump power from $<1 \text{ kW}$ to $<1 \text{ W}$ and providing milliwatt level of output powers by solid-state lasers. Just this problem has been accomplished by the specialists of Laser-Compact company. They have developed an original series of models of low-power solid-state lasers and organized their production.

* The fluorite crystals have been grown at State Optical Institute (Leningrad, USSR).

Further author information –

G.M.Z. (correspondence): E-mail: mail@polyus.msk.ru; Telephone: (095) 334-20-66; Fax: (095) 333-00-03

I.I.K.: E-mail: ik@lcompact.msk.ru; Telephone: (095) 333-02-89, (095) 720-54-50; Fax: (095) 333-94-44, (095) 720-54-51

For the last few years the model series of lasers has been updated more than once. Now the products of the company are widely sold to more than twenty countries and regularly presented at the major laser shows. A number of domestic and foreign OEM companies use the laser modules of Laser-compact in their systems.

The products of the company can be divided into two main groups (see the tables 1, 2). The first group includes the compact laser modules designed for use as completing articles in OEM equipment. The green (532 nm) output of serial CW laser modules is 1 mW and 10 mW, the infrared (1064 nm) output is 10 mW and 50 mW. The blue (473 nm) laser modules are also manufactured.

Table 1. Laser modules for OEM

Laser-compact Co. Ltd.

Wavelength, nm	MODEL NAME, OUTPUT POWER	
532	LCL-LL-01cc/250	0.25 – 0.3 mW, CW
532	LCM-T-01ccs	0.5 mW, CW 1 mW CW
532	LCM-T-11ccs	3 mW, CW 10 mW, CW
1064	LCM-T-02ccs	10 mW, CW
1064	LCM-T-12ccs	50 mW, CW
473	LCM-F-6c	1 mW, CW
473	LCM-F-6q	3 mW, Q-switch

The laser module is a tube 15 mm in diameter and 112 mm in length (Fig. 1). To supply the module, a DC voltage (3.3...3.5 V) source is required providing a current up to 1.4 A. The basic optical diagram of the module is shown in Fig. 2.

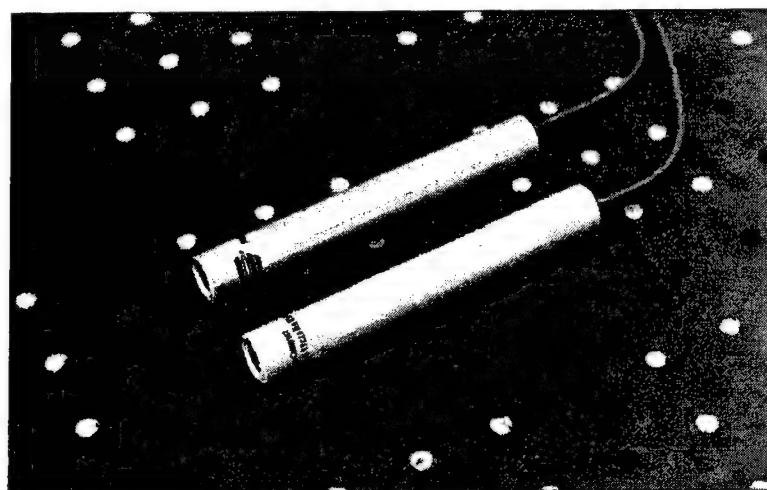


Fig. 1. Laser modules for OEM

An optical pump emission of the power laser diode is focused into the thin slab (typically Nd:YAG) placed inside the laser resonator. The nonlinear element is also placed inside the resonator. A required output emission is filtered by the optical filter. Nonlinear frequency conversion into second harmonic is produced in KTP crystals for "green" modules and LiIO₃ or KNbO₃ crystals for "blue" modules. The use of periodically poled nonlinear crystals for frequency doubling is also studied.

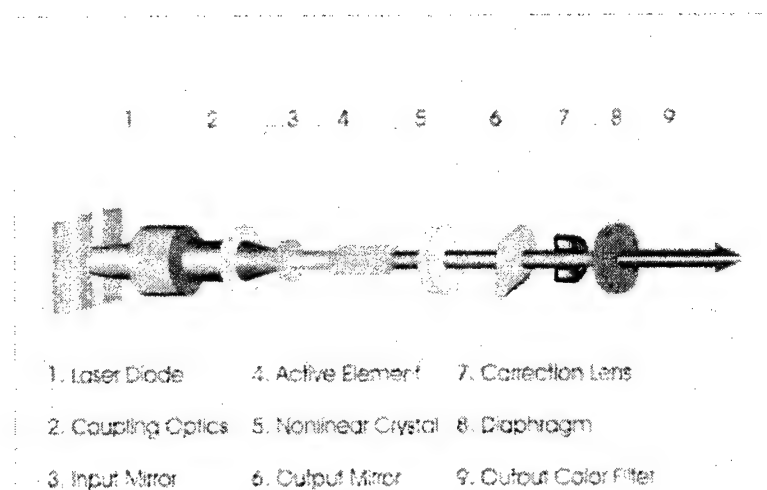


Fig. 2. Optical schematic diagram of blue/green laser module

Another group of products includes more powerful lasers with high performance that are designed both for laboratory use and for application in industrial and medical systems (Fig. 3). These lasers have a green output up to 200 mW, an infrared output up to 1 W and a blue output up to 20 mW. These devices operate from AC mains.

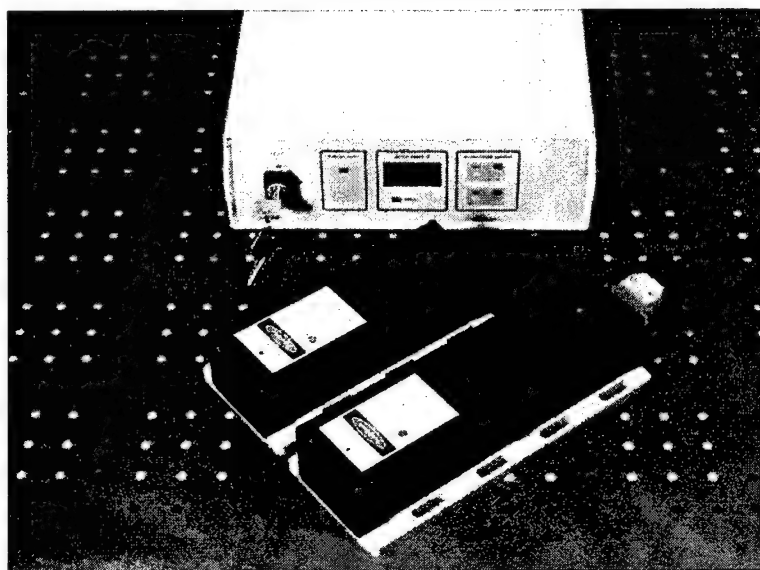


Fig. 3. Line 300 DTL-series laser systems

The laser modules are used where compact lasers with good beam divergence and low power consumption are needed. The green laser modules are the most needed for the users.

Most of their applications are connected with visualization of laser emission when using high-power infrared invisible lasers (wood and marble plate sawing, cloth and paper cutting, laser surgical systems, etc.). In the green region the human eye has the maximum sensitivity, so it is possible to provide sufficient visibility of an emission without exceeding permissible powers for different classes of laser hazard.

Table 2. Line 300 DTL-series laser systems

Laser-compact Co. Ltd.

CW MODELS		
Wavelength, nm	MODEL NAME	Output power, mW
1340	LCS-DTL-332	200
		100
1064	LCS-DTL-322	1000
		500
		300
		150
532	LCS-DTL-312	200
		150
		100
		50
473	LCS-DTL-362	20
		10
Q-SWITCH MODELS		
Wavelength, nm	MODELS WITH PASSIVE Q-SWITCH	Pulse energy, μ J
532 & 1064	LCS-DTL-112QT	> 1 (532nm) & > 2 (1064nm)
1064	LCS-DTL-122QT	> 10
Wavelength, nm	MODELS WITH AOM Q-SWITCH	Pulse energy, μ J
1064	LCS-DTL-324QT	100 μ J (1 kHz) & 40 μ J (10 kHz)
532 & 1064	LCS-DTL-314QT	20 μ J (1 kHz) & 3 μ J (10 kHz)

The visibility of emission at 532 nm more than 20 times exceeds that of semiconductor lasers at 670 nm. In particular, a 0.8-mW "green" module is equivalent in visibility of emission to a 20-mW red semiconductor laser that for its power is classified as a laser of group 3B. A green laser corresponds to group 2 and is practically safe for a user. In this

connection, the applications of visible laser modules include also laser pointers and laser games. In this case the problems of cost of the products are put in the forefront.

For a number of applications a green light source is needed due to the optical properties of exposed medium. For example, when a laser light exposes the tissues of human body or when illuminating a hot or melted metal. In addition to visibility and safety a high directivity of emission is often required. For example, in systems for remote reference of patients in some medical systems a green laser light is to be formed into a line of 1 mm thickness at a distance more than 7 m. Besides, a laser is to retain serviceability and stable parameters within wide temperature range at small sizes using a self-contained power supply. The conventional green laser sources (lamp-pumped solid-state lasers, argon and He-Ne lasers) do not meet these requirements. In this case the laser modules of Laser-Compact company are indispensable.

The compact blue lasers will be needed for microbiological investigations associated with excitation of luminescence of objects under investigation as well as in color display, complex imaging and target designation systems, etc.

The more powerful devices of the second group (table 2) are also offer the new possibilities to a user relative to conventional visible and infrared laser sources: they are compact, do not require large cooling systems, have moderate power consumption, are ready for operation within seconds after switching-on, and conform with all safety standards.

A serious problem facing the developer of diode-pumped lasers which affects their performance is due to the thermal drift of wavelengths of pump diodes. Conventionally, to provide matching of a rather narrow emission spectrum of a laser diode to the absorption lines for active ions, thermal stabilization of laser diodes by TE coolers based on the Peltier effect is used. This method is used in more powerful lasers of Laser-Compact. In this case the most laser power is achieved due to the maximum absorption of pump emission. The drawback of this method is inevitable increase in overall dimensions, power consumption and heat-evolution of the laser. For example, the head of the LCS-DTL-312 200-mW green CW laser measures 46x90x225 mm, the power supply measures 260x197x85 mm. Power consumption in steady operation is tens of watts, and in going into the mode it can achieve 100 W. However, these parameters are much less than those of an argon laser with such characteristics.

One may also try to provide a wide range of operating temperatures without thermal stabilization of laser diodes when the wavelength of a pump source varies with temperature. This is realized in the compact modules.

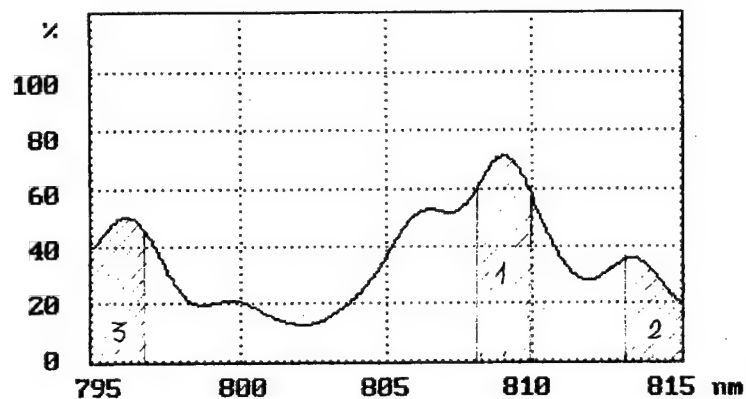


Fig. 4a. Absorption of YAG : Nd
Bands 1,2,3 are the pumping diodes
spectra at the 20 C, 37 C, -20 C/

Shown in Fig. 4 a, b, c are respectively the absorption spectrum of the Nd³⁺ ion in the YAG crystal, the temperature dependence of the LCM-T-11 ccs laser module output with the output power stabilization system switched off, and the same dependence with this system switched on. The vertical lines in Fig. 4 a show the wavelength of the pump diode at three temperatures: -20°C, +20°C, and +37°C.

the absorption spectrum as the wavelength of the pump source varies. The existence of a considerable dynamic range of the module allows smoothing the temperature changes by means of the power stabilization system (Fig. 4 c).

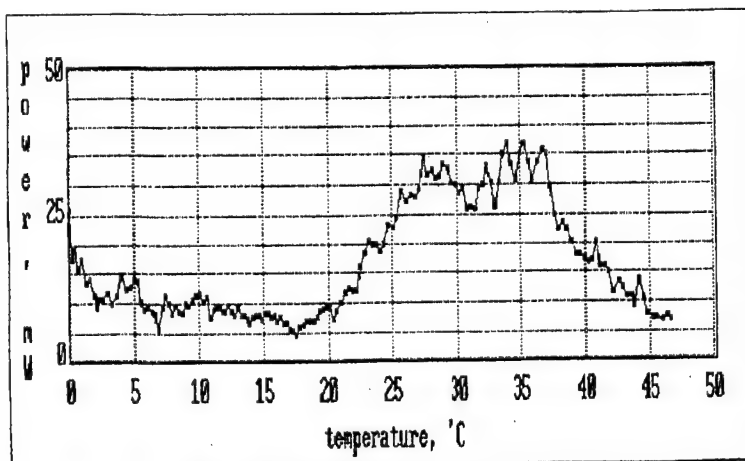


Fig. 4b. Output power of the LCM-T-11ccs laser
(control system - switch off)

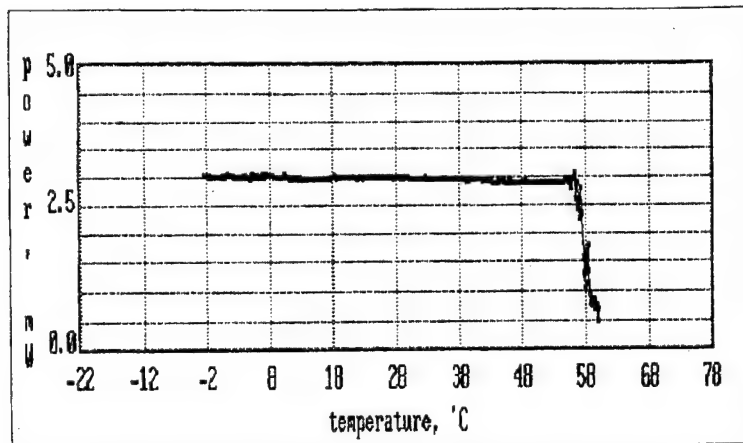


Fig. 4c. Output power of the LCM-T-11ccs laser

The output parameters of the modules are very stable in time. Fig. 5 shows the time stability of laser output. After a small warm-up an instability of laser output does not exceed 1%.

Due to the wide range of output parameters and modes of operation, the diode-pumped lasers developed by Laser-Compact arouse continued interest and growing consumer demand. Within the past few years about 10,000 modules and lasers of various models have been manufactured and sold. In our estimation, this amount is no less than third of the total number of diode-pumped lasers produced all over the world in this period.

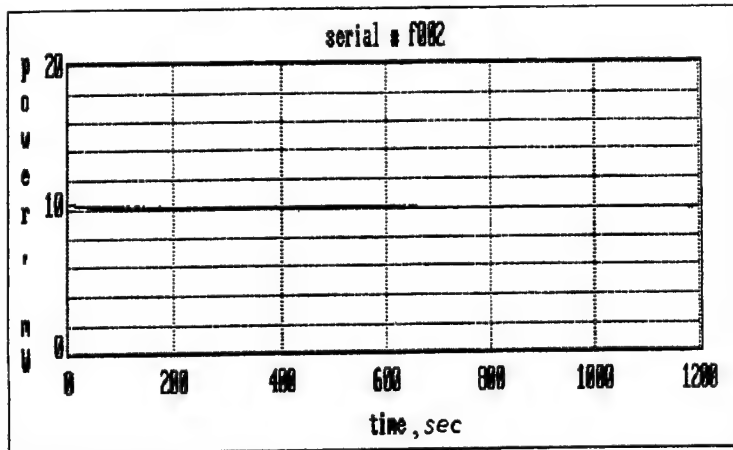


Fig. 5. Stability of the LCM-T-11ccs output power

At present Laser-compact is preparing for production the laser models with a built-in acoustooptic Q-switch (LCS-DTL-324QT and LCS-DTL-314QT) as well as a series of models of low-noise CW green and blue lasers.

Polyus RDI carries out intensive work on development of diode-pumped Q-switched lasers. If for pumping of the above-mentioned low-power lasers the high-power single diodes were sufficient, to pump a laser with output energy of 10...100 mJ and more, linear laser diode arrays and laser diode arrays are required. The reliable 10-mm linear arrays with output energy of 10...15 mJ at 808 nm manufactured at Polyus RDI allowed development of the first successful designs of such devices. Shown in Fig. 6 is the design of the electrooptically Q-switched Nd:YAG laser with an output energy up to 25 mJ and a pulse repetition rate up to 50 Hz using lithium niobate Q-switch being traditional for the institute. Pumping is carried out by 12 10-mm linear arrays according to the side pumping scheme (3 groups of 4 arrays in series). Fig. 7 shows the output energy of this laser as a function of pump energy. The temperature of the pump diodes is controlled by the TE cooler.



Fig. 6. Electrooptical Q-switch diode-pumped laser head

The first designs of the diode-pumped devices provided double increase in total efficiency of the laser, decrease in beam divergence, and increase in lifetime of the devices.

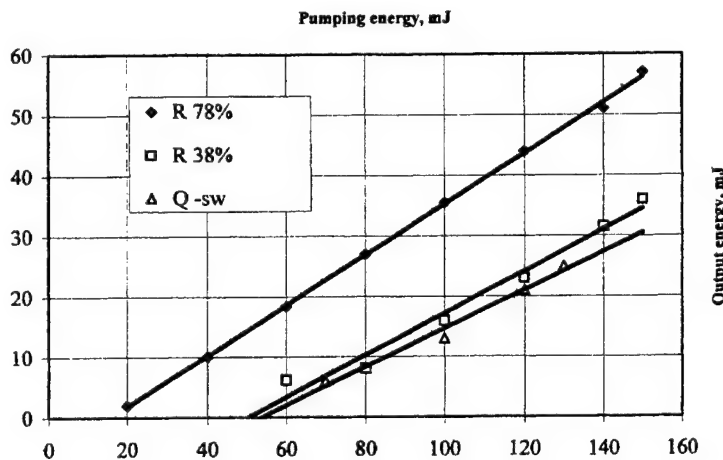


Fig. 7. Dependence of output energy vs pumping energy

The devices with an output energy up to 200 mJ for airborne and field applications (ranging, measurement of cloud boundary and wind velocity, lidars, etc.) are under development.

The further development and improvement of the developed devices are a key problem of Polyus RDI and Laser-compact company.

REFERENCES

1. V.I.Shveikin, Yu.I.Kruzhilin. Report on "Kremnii" (silicon) research work, Polyus RDI, Moscow, 1965.
2. V.I.Bilak, I.S.Goldobin, G.M.Zverev, I.I.Kuratev, V.A.Pashkov, N.M.Soloviova, M.F.Stelmakh, Yu.V.Tsvetkov. Nd: YAG lasers pumped by LEDs. "Kvantovaya elektronika", 1981, N 11, pp.2408-2417.
3. LTI-101 Nd: YAG laser pumped by LEDs (IAI 379.079 OO). "Elektronnaya promyshlennost", 1981, N 5-6, p.157.
4. I.I.Kuratev. High-efficiency solid-state lasers pumped by semiconductor emitters. "Elektronnaya promyshlennost", 1987, N 9, pp.97-102.

Investigations of pulsed Nd:YAG laser with diode-laser bars side-pumped rod geometry.

A.J. Abazadze^a, J.M. Kolbatskov^a, V.L. Pavlovitch^a, and G.M. Zverev^a

^a R&D "Polyus", Vvedensky st. 3, Moscow, Russia

ABSTRACT

An experimental studing of Nd:YAG rod side-pumping with quasy-cw laser-diode bars as a function of the laser rod and the pumping submount parameters was carried. We have found that the side-pumped-of-rod geometry without coupler optics between the laser diodes and the laser rod provides sufficiently high slope and optical efficiencies of Nd:YAG laser. Utilizing the concentric pumping arrangement with eight laser diode bars maximum optical efficiencies of 50% and 45% in long pulse mode was obtained when 5-mm and 4-mm-diameter Nd:YAG (1.2% at) rods respectively were used. In Q-switched operation Nd:YAG laser with this pumping sheme and 5-mm-diameter (1.2% at) rod had an output of 23 mJ in multimode 10 ns pulse when output coupler was of 60%.

Keywords: diode-pumped, Nd:YAG laser, quasy-cw laser-diode bar, Q-switched operation.

1. INTRODUCTION.

We report on results of investigations of quasy-cw diode-laser bars-pumped Nd:YAG laser with side-pumped rod geometry performance in free-running and Q-switched by LiNbO₃ -Pockels-cell modes. It is well-known that side-pumping permits to upscale output power or pulse energy with sufficiently high optical-optical efficiency and good beam quality^{1,2}. The aim of this work consisted in experimental studing of Nd:YAG rods side-pumping with laser-diode bars as a function of following parameters - a rod diameter and neodimium concentration, overall pump pulse energy, radii-of-curvature of HR-mirror and geometry of diode bars-in-submount arrangement around a rod.

2. THE EXPERIMENTAL SET-UP AND THE RESULTS.

1-cm-long quasi-cw laser diode bars with output of better than 60 W (in 60° divergence angle in the fast axis) were specially designed and fabricated to optimise parameters of studied pumping modules. Firstly we experimented with highly nonuniform pumping scheme of four-diode-laser bars in two submounts with 45° between the axes of pumping beams (see Fig. 1) that was a single unit of projected pumping module. This pumping scheme provided the optical slope efficiencies of 50% and 45% respectively when reflector coated 3-mm and 5-mm-diameter Nd:YAG (0.85% at and 1.2% at) rods were side-pumped (see Fig.4a,b). And that was an experimental evidence of the possibility to realize side-pumping-of-a rod geometry with sufficiently high slope and optical efficiencies. Then we have used more complex pumping modules provided pump pulse energy upscaling and a smooth spatial distribution of the population inversion in the active element. The first module contained sixteen laser-diode bars in two air-cooled submounts arranged symmetrically around the laser rod as is seen on Fig. 2. Each submount in this case included eight laser-diode bars which was done to uniform pump emission in the laser rod and to provide good quality of laser beam. Utilizing this concentric pumping arrangement maximum optical efficiencies of 50% and 45% in long pulse mode was obtained when 5-mm and 4-mm-diameter Nd:YAG (1.2% at) rods respectively were pumped (see Fig.5a,b). As it is seen from Fig.5,a when Nd:YAG (0.85% at) rods with diameters of 3-mm and 4-mm were used in the concentric scheme the laser performance was less effective because of decreasing of pump absorption in the laser rod volume. In Q-switched operation Nd:YAG (1.2% at) laser with eight-bars-around 5-mm-diameter laser rod pump module had an output of 23 mJ in multimode 10 ns pulse when output coupler was of 60% (Fig.5,c). It had to be mentioned that this case we did not use a polarizer in a quarter-wave Q-modulation scheme. Because of a low depolarization factor and population inversion density in the laser rod Brewster angle positioned LiNbO₃ - Pockels cell's windows were enough to obtain Q-switching process. The second module included twelve laser-diode bars in three air-cooled submounts arranged asymmetrically near one side of the laser rod which contained the Ag-coated reflector on its opposite side as seen on Fig. 3. Each submount in this case included four laser-diode bars. In compare to eight-bars-around-rod scheme this asymmetrical approach had less opportunity to increase pump pulse energy but allowed to transfer heat from an active element to external

Futher authors information -

G.M.S. (correspondence): E:mail: mail@polyus.msk.ru; WWW:<http://polyus.msk.ru>; Telephone 095-334-2066; Fax: 095-333-0003

radiator. In experiment with this twelve-bars-one side-around-rod approach maximum optical efficiency of 45% was obtained when reflector coated 3-mm-diameter Nd:YAG (0.85% at) rod was pumped with 160 mJ as seen on Fig.6,a. In Q-switched 10 ns-pulse output energy was of 25 mJ when pumping energy was of 130 mJ and output coupler of 40% (Fig.6,b). Repetition rate during this experiment was varied from 5 Hz to 20 Hz.

The resulstes of carried experiments were used to develope. the first sample (shown on Fig.7) of laser-diode bars side-pumped Nd:YAG laser head with 3-mm-diameter rod and with output of 20-mJ in Q-switched pulse. This is the first sample of our air cooled Q-switched all-solid-state laser with output in 1.064- μ m ten milijoules-range. It shows that the all-solid-state side-pumped laser approach has a number of advanteges characteristics as compared to the lamp-pumped and laser-diode-end-pumped laser designs which may be successfully realized in a lot of applications.

3. CONCLUSION.

Now we hope to continue our experiments to realize actively Q-switched diode-side-pumped Nd:YAG laser with multimode 1.064- μ m output of 50 mJ or more with repetition rate of 30 Hz using four eight-diode-bars submounts in a pump module around 5-mm-diameter Nd:YAG (1.2% at) rod. Then we plan to add SHG and OPO modules to Q-switched laser-diode side-pumped Nd:YAG laser to provide efficient 0.53- μ m and 1.5- μ m generation.

4. ACKNOWLEDGEMENTS.

The authors would like to thank our colleagues from Semiconductor Division of R&D "Polyus" for their support in constructing and fabricating of laser diode bars for our pumping modules. The pumping modules designes and graphical materials for this paper were prepared with the assistance of An.V. Gusev.

5. REFERENCES.

1. J.Kasinski, W.Hughes, J. DiBiase, P.Bournes, and R. Burnham, *Journal of Quantum Electronics*, vol.28, No4, April 1992.
2. T.Rutherford, W. Tulloch, and R. Byer, *Laser Focus World*, March 2000, pp. 63-69.

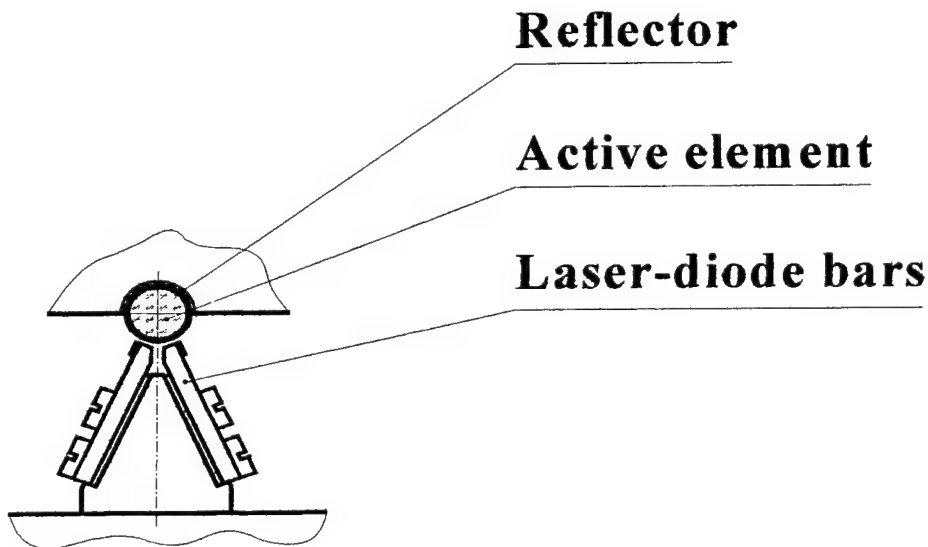


Figure 1. A single unite of projected pumping module of four-diode-laser bars in two submounts with 45° between the axes of pumping beams.

Laser-diode bars

Active element

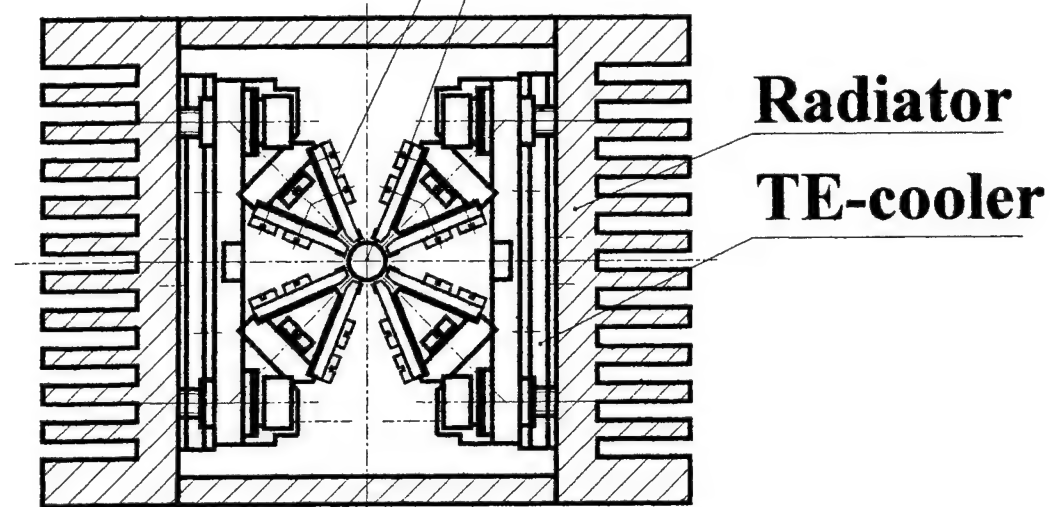


Figure 2. The pumping module of sixteen laser-diode bars in two air-cooled submounts contained of eight bars arranged symmetrically around the laser rod.

Reflector

Active element

Laser-diode bars

Radiator

TE-cooler

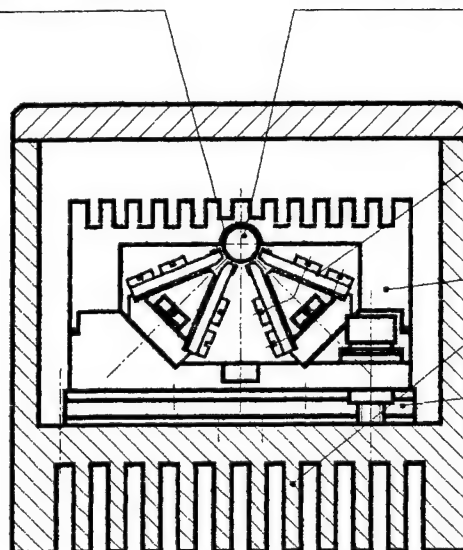
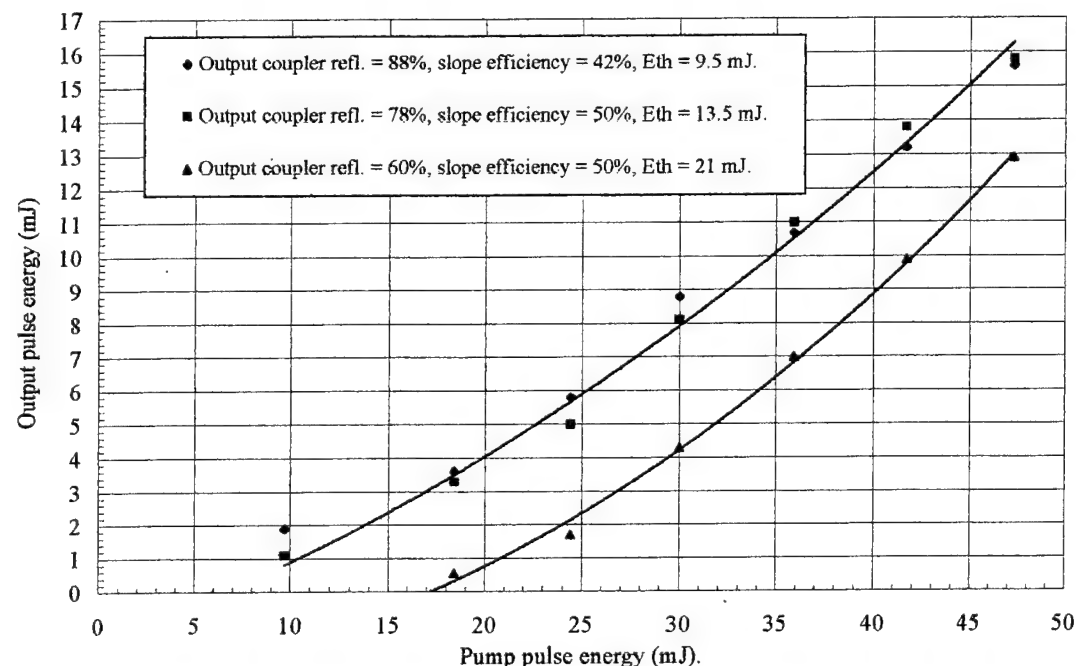
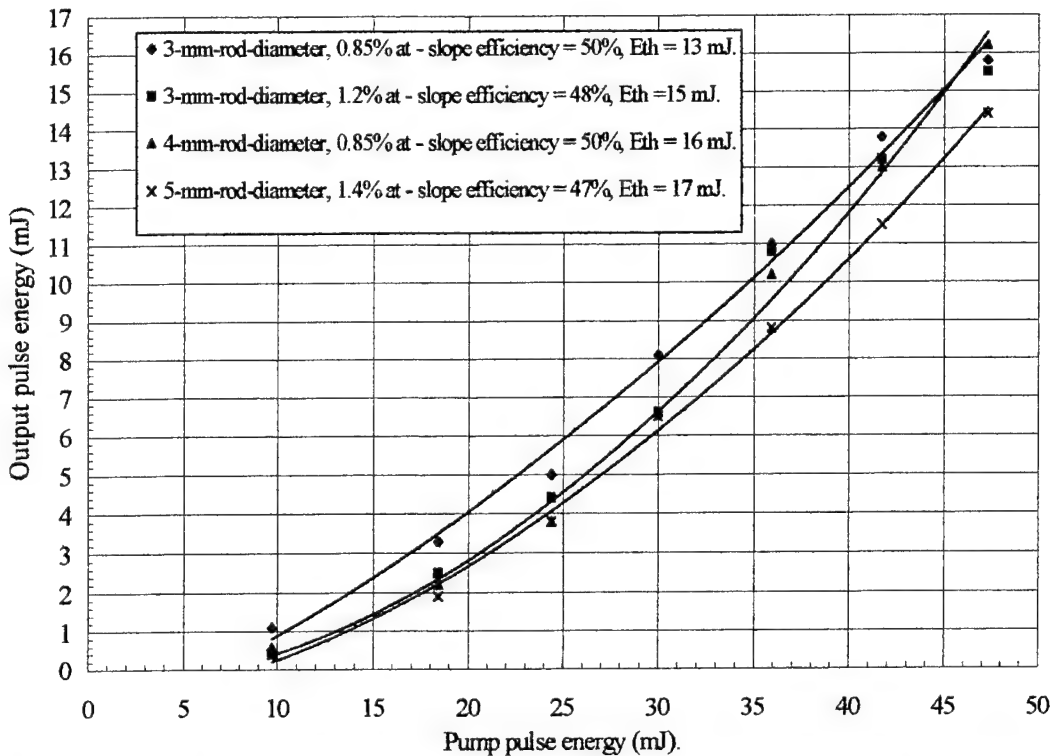


Figure 3. The pumping module of twelve laser-diode bars in three air-cooled submounts included four bars arranged asymmetrically near one side of the laser rod which contained the Ag-coated reflector on its opposite side.



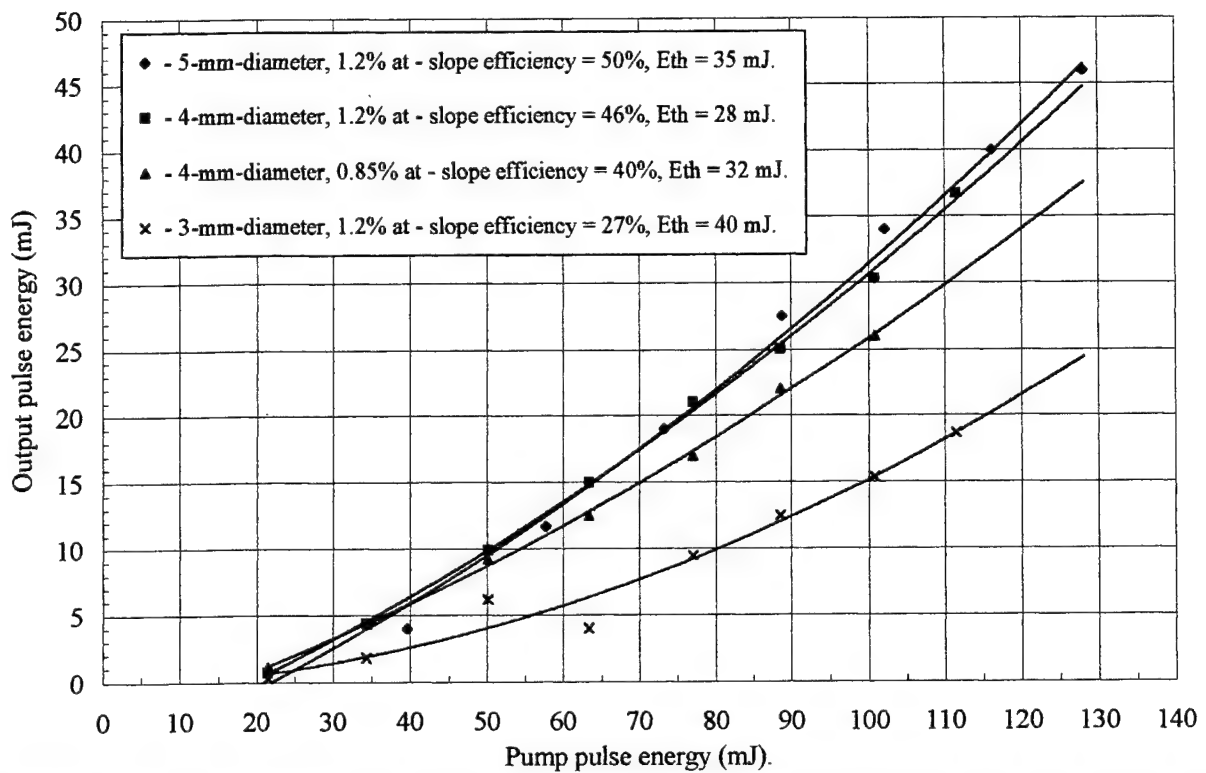


Figure 5.a. Measured output energy versus the pump pulse energy of Nd:YAG laser in the free-running mode with different rods and symmetrical-pumping module with sixteen laser-diode bars (see Fig.2), the output coupler reflectivity of 78%, the curvature-of-HR coupler of 100 cm.

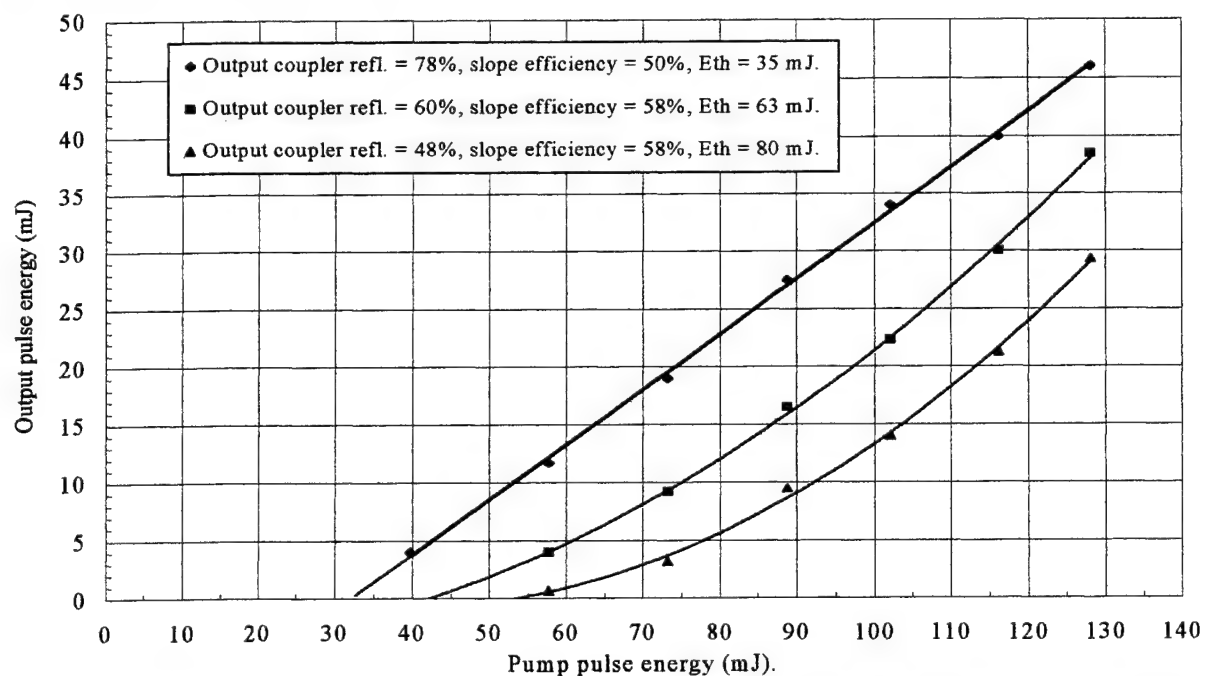


Figure 5.b. Measured output energy versus the pump pulse energy of Nd:YAG laser in the free-running mode with 5-mm diameter laser rod ($C_{Nd} = 1.2\%$ at -) and symmetrical-pumping module with sixteen laser-diode bars (see Fig.2), the curvature-of-HR coupler of 100 cm, the cavity length of 18 cm.

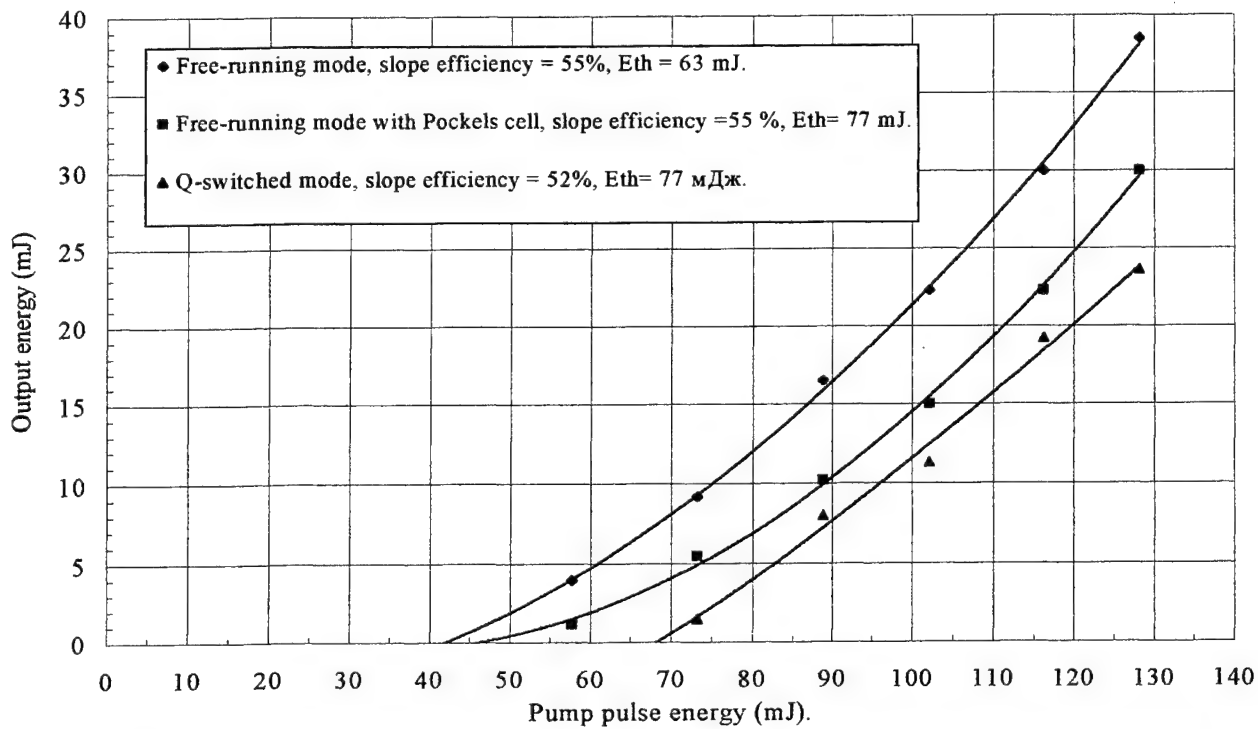


Figure 5.c. Measured output energy versus the pump pulse energy of Nd:YAG laser with 5-mm diameter laser rod ($C_{Nd} = 1.2\%$ at) and symmetrical-pumping module with sixteen laser-diode bars (see Fig.2), reflectivity of the output coupler of 60%, the HR-curvature of 100 cm, the cavity length of 18 cm.

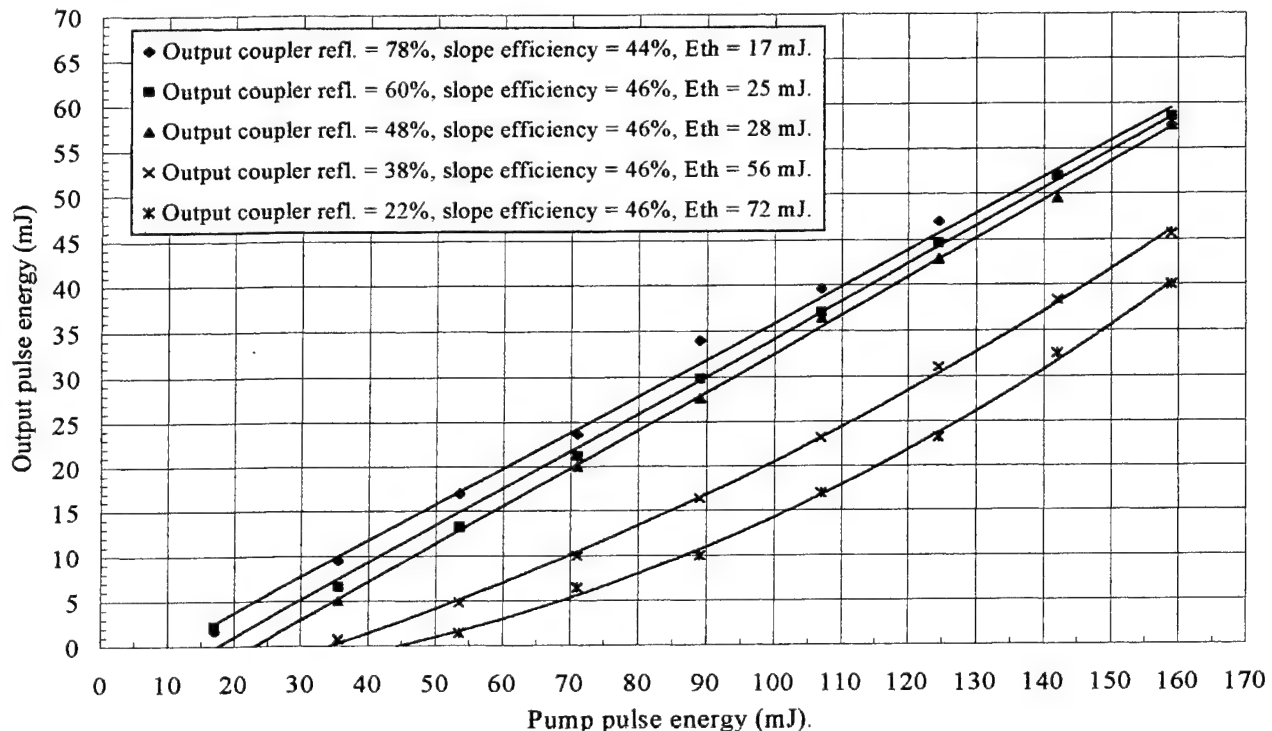


Figure 6.a. Measured output energy versus the pump pulse energy of Nd:YAG laser in the free-running mode with different rods and asymmetrical-pumping module with twelve laser-diode bars (see Fig.3), the curvature-of-HR coupler of 100 cm, the cavity length of 22 cm.

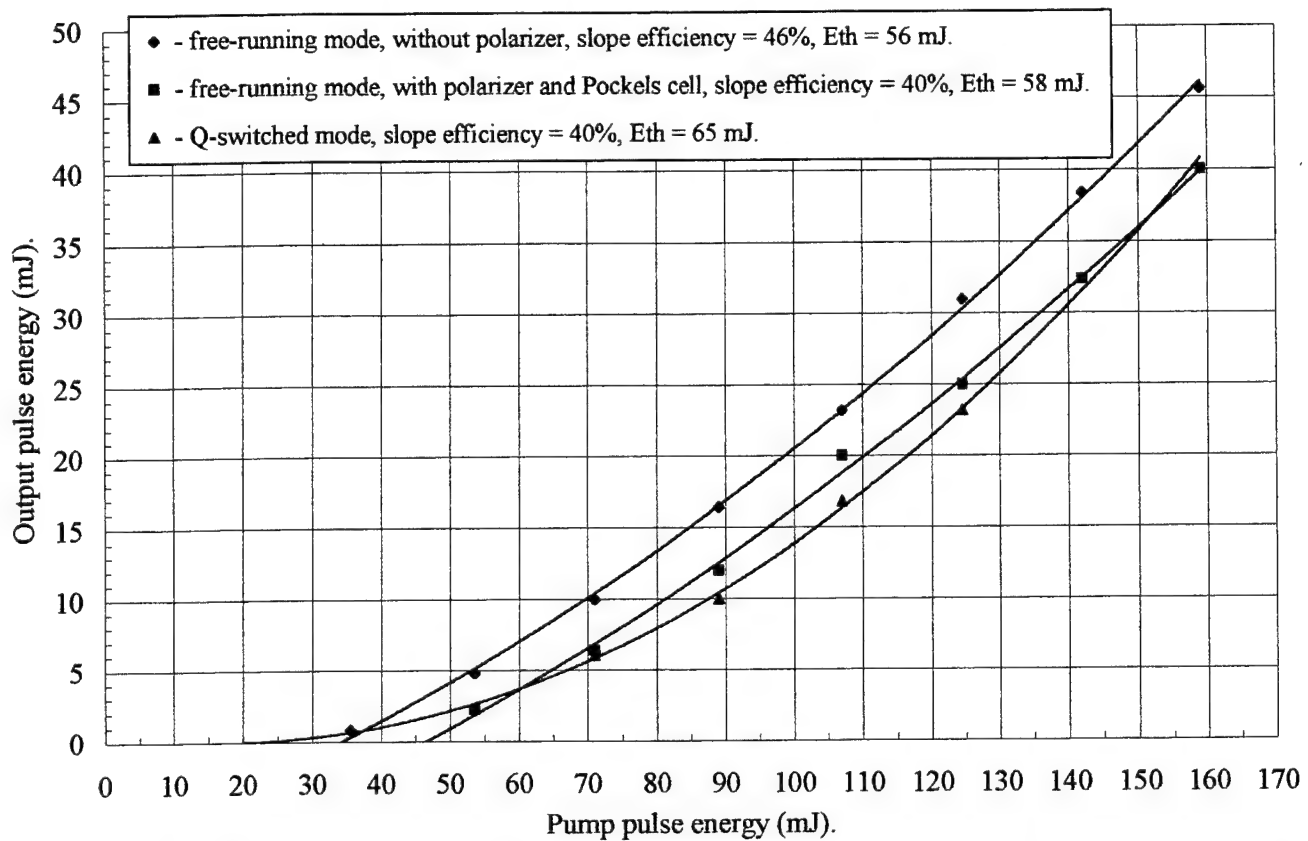


Figure 6,b. Measured output energy versus the pump pulse energy of Nd:YAG laser in the free-running and Q-switched modes with 3-mm diameter laser rod ($C_{Nd} = 0.85\%$ at) and asymmetrical-pumping module with twelve laser-diode bars (see Fig.3), the output coupler reflectivity of 38%, the cavity length of 22 cm.

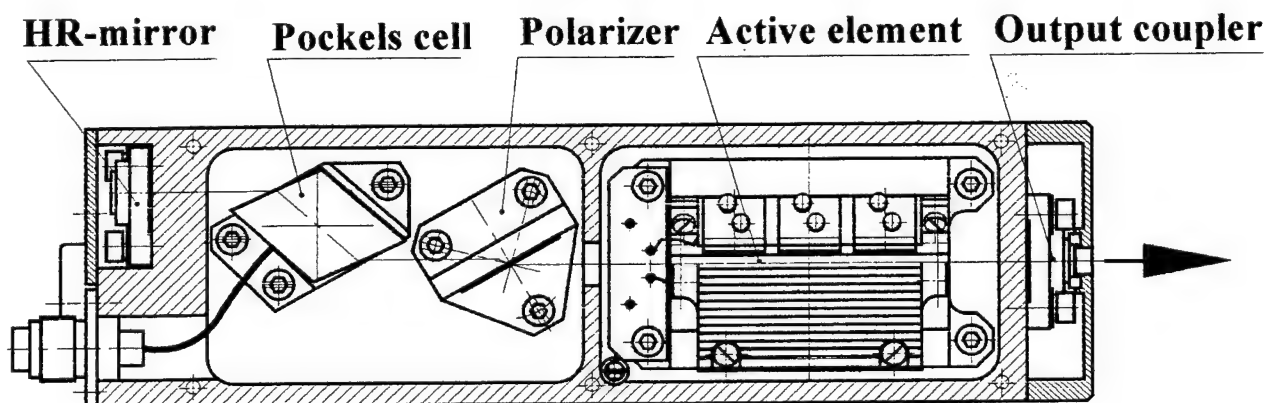


Figure 7. The first sample of our air cooled laser-diode bars side-pumped Nd:YAG laser head with the 3-mm-diameter rod and with the output of more than 25-mJ in Q-switched multimode pulse.

Passive Q-switch operation of PbSe-doped glass at 2.1 μm

A. M. Malyarevich¹, V. G. Savitski¹, P. V. Prokoshin¹, K. V. Yumashev¹, A. A. Lipovskii²

¹International Laser Center, bldg. 17, #65 F. Skaryna Ave., 220027 Minsk, Belarus,

E-mail: malyar@ilc.unibel.by

²St.-Petersburg State Technical University, 29 Polytechnicheskaja str., St.-Petersburg, 195251 Russia

ABSTRACT

Saturable absorber Q-switching of Ho³⁺:Y₃Al₅O₁₂ laser at 2.1 μm using PbSe-doped phosphate glass was demonstrated. Q-switched pulses of 22 mJ in energy and 85 ns in duration were obtained. Temperature dependence of luminescence spectra of phosphate glasses doped with PbSe QDs of different sizes was analyzed.

Keywords: Semiconductor Quantum Dots; Q-switch; Lead Selenide.

1. INTRODUCTION

Lasers emitting at $\lambda=2$ μm have important application in medical treatment procedure (see e.g. Ref. 1 and references therein). Q-switching of these lasers are of high importance to produce short and powerful pulses. Passive Q-switches are more attractive over active modulators of solid-state lasers because of their compactness, simplicity and low-cost. Several saturable absorber Q-switches for the 2-μm holmium and thulium lasers have been recently reported.²⁻⁴ Passive Q-switching of Ho³⁺:Y₃Al₅O₁₂ (Ho:YAG) laser has been demonstrated using Z₄ color centers in RbCl-Ba crystal² and more recently with Cr²⁺-doped CdMnTe crystal.³ Ho:YLiF₄ has been presented as a saturable absorber Q-switch for Tm:YAG laser at 2.017 μm.⁴ From the other hand, lack of passive Q-switches for 2 μm lasers can be explained in some extent due to insufficient knowledge of materials demonstrating saturable absorption in this spectral region.

In this paper passive Q-switching of a 2.1 μm Ho:YAG laser was accomplished with a PbSe-doped phosphate glass as a saturable absorber. Q-switched pulses with duration of 85 ns and energy up to 22 mJ were achieved. The small band gap of bulk PbSe (0.28 eV at room temperature⁵) allowed to obtain the lowest optical transition in PbSe nanocrystals in the vicinity of 2 μm due to quantum confinement effect. Saturable absorption of this transition was used for Q-switching of Ho:YAG laser operating at 2.1 μm. Temperature dependence of luminescence spectra of phosphate glasses doped with PbSe QDs of different sizes was analyzed.

2. GLASS FABRICATION

The PbSe-doped glasses were prepared using the P₂O₅-Na₂O-ZnO-AlF₃-Ga₂O₃ glass system by the technique described in details in Ref. 6. Glass modifiers were used to decrease the volatility of the chalcogenide compound in the process of glass synthesis and to get semiconducting PbSe in the batch melt as a result of a chemical reaction occurring in the melt. This last-minute formation of PbSe caused increase of the homogeneity and the concentration of the solid solution of the semiconductor in glass samples, obtained after conventional room temperature quenching the glass. The glass preforms after quenching were transparent and slightly yellow, that was typical for lead-containing glasses. Secondary thermal treatment of these preforms at 390-420°C led to their coloring from brownish to black depending on the temperature and the duration of the annealing.

3. ABSORPTION AND LUMINESCENCE SPECTRA MEASUREMENTS

Room temperature PbSe QD absorption spectra for different dot radius are presented in fig. 1. The quantum confinement of narrowly size-distributed dots manifests itself in structured and dot size dependent spectra. The PbSe-doped glasses were studied using TEM and secondary X-ray diffractometry. Both of them showed formation of PbSe nanocrystals with average 20% size distribution near the mean particle's radii. The values of mean particle's diameter (5.0, 4.0, 3.5 and 1.5 nm) are in a good agreement with the results of theoretical calculations of energy levels in PbSe nanocrystals presented in Ref. 7. The

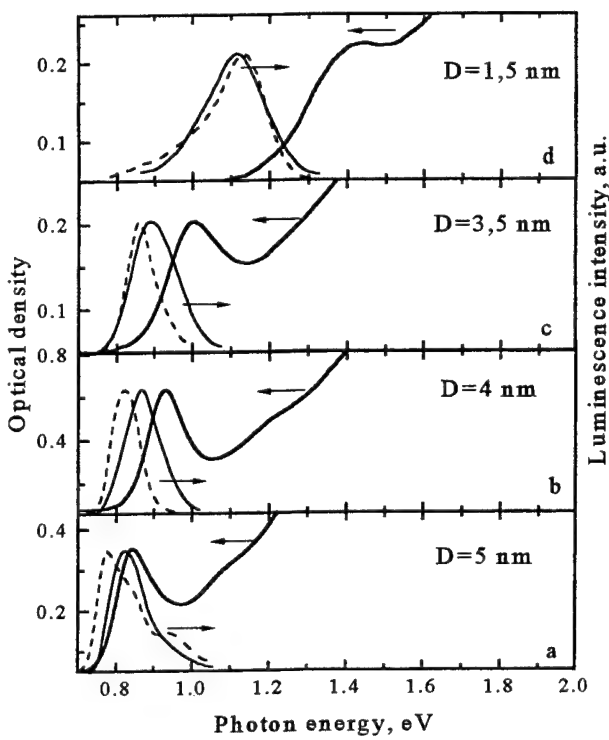


Figure 1. Absorption and luminescence (300K – solid line, 77K – dashed line) spectra of PbSe QDs of different diameters in phosphate glass

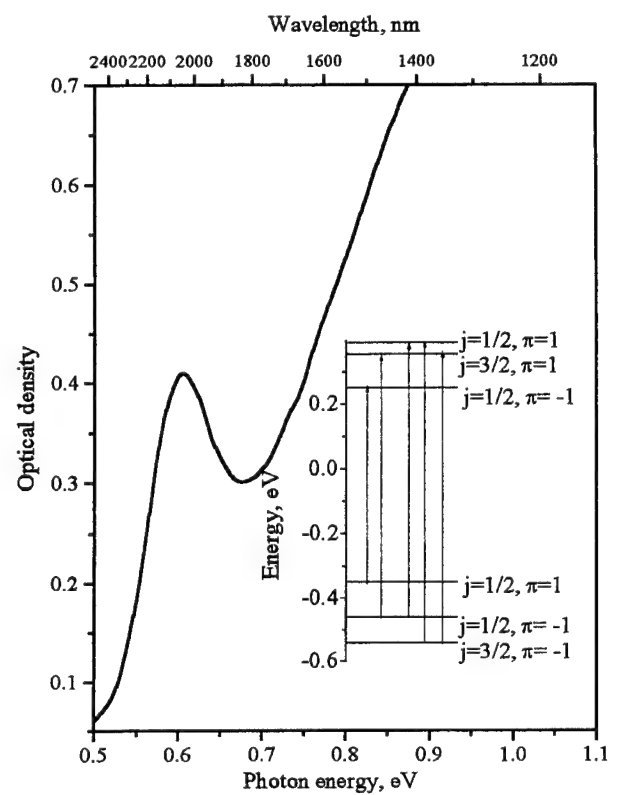


Figure 2. Absorption spectrum of PbSe QDs doped glass (D=8.5 nm) and the electron structure (inset) of the direct transitions (shown by arrows).

absorption spectrum of the sample with the mean dot diameter of 8.5 nm is shown in fig.2. The electron structure of the direct transitions for this sample calculated in Ref. 8 with four-band envelope formalism is presented in the inset in fig.2.

Angular momentum quantum numbers j and the parity π label each energy level. The selection rules for the direct transitions are as follows: $\Delta j=0, \pm 1, \pm 1; \pi_c^* \pi_v=-1$.

Luminescence spectra were obtained under stationary excitation from cw Ar⁺-laser with a wavelength of 488 nm (2.54 eV). The cooled Ge p-i-n diode was used as a detector. In order to cool the samples they were immersed into liquid N₂ (77K) or He (4.2K).

Luminescence spectra of PbSe QD in phosphate glass of 5, 4, 3.5 and 1.5 nm at 77 and 300K are presented in fig.1 (luminescence spectra at different temperatures are normalized). Size dependence of emission peaks position is in agreement with that of the absorption spectra. Stokes shift between the luminescence peak and the first absorption peak dependence on particle size is shown in fig.3. This shift increases from 16 up to 330 meV as the dot size decreases from 5 to 1.5 nm. It can be explained by increasing of exciton-phonon interaction in smaller QDs.⁹

As the temperature is lowered from 300 down to 4.2K the luminescence intensity increased and the luminescence peaks exhibit low energy (samples a-c for 64, 46 and 50 meV respectively) and high energy (sample d – 20 meV) shift. Absorption spectra dependence of PbS QDs in phosphate glass on temperature has been performed in Ref.10. It was found that for relatively large QDs the sign of the thermal shift of the first excitonic peak coincides with that of the energy gap of the bulk lead sulfide (generally, bulk lead salts exhibit negative value of temperature coefficient of the

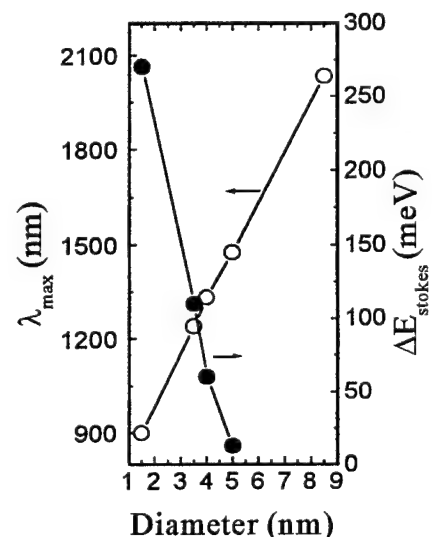


Figure 3. First exciton peak position (open circles) and Stokes shift (solid circles) dependencies on QD diameter.

minimum energy gap⁵). It has also been pointed out that decrease of QD size leads to decrease of the thermal shift of the first excitonic peak and, for smaller particles, to change the sign of thermal shift (it becomes positive). This effect can be the result of stronger spatial confinement effects for smaller particles.

4. Q-SWITCH EXPERIMENTS

The design of the passively Q-switched laser cavity is schematically shown in Fig. 4. The highly reflectivity curved mirror (M2, radius-of-curvature $r=1$ m) and the flat output coupler (M1, reflectivity at $2.1\text{ }\mu\text{m }R=70\%$) are used to form a cavity close to semispherical one. A flash-lamp pumped $\text{Ho}^{3+}\text{:Cr}^{3+}\text{:Tm}^{3+}\text{:YAG}$ rod with a size of $\mathcal{O}5\text{x}85$ mm was used as the laser active medium. A 0.8-mm-thick PbSe-doped glass saturable absorber had small-signal transmission of 50% at $2.1\text{ }\mu\text{m}$. It had no antireflection coating and was placed near the output coupler M1.

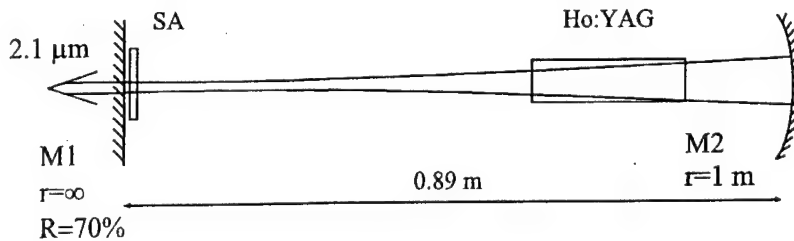


Figure 4. Scheme of passively Q-switched $2.1\text{ }\mu\text{m}$ Ho:YAG laser cavity with the PbSe-doped phosphate glass saturable absorber.

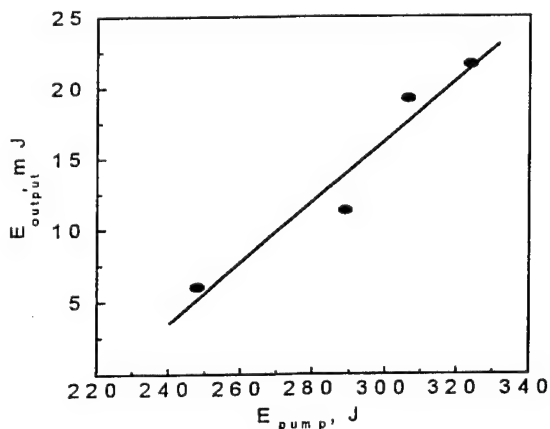


Figure 5. Input-output characteristic for Ho:YAG laser with PbSe-doped glass as saturable absorber.

Q-switched laser pulses up to 22 mJ in energy corresponding to $\sim 6\%$ of the free-running one at the same pumping level were obtained. The dependence of output energy of the laser with PbSe-doped glass Q-switch vs input electrical energy is presented in Fig. 5. This input-output characteristic was measured for the single transverse mode operation of the laser. Only single Q-switched laser pulse was generated. Time duration of second harmonics of Q-switched laser pulse was measured to be 60 ns using LiNbO_3 crystal and fast Si detector with oscilloscope as a detecting system. Assuming Gaussian form of the Q-switched pulse we obtained its duration to be ~ 85 ns ($60\text{ ns} \times \sqrt{2}$). For 6-mJ Q-switched output pulses, energy fluence at the saturable absorber was $\sim 1\text{ J/cm}^2$ (corresponding intensity is $\sim 12\text{ MW/cm}^2$). It is worth mentioned that, for glasses doped with relative compound PbS, saturation intensity was measured to be 180 kW/cm^2 ¹¹.

Earlier the following parameters for passively Q-switched laser pulses at $\sim 2\text{-}\mu\text{m}$

wavelength were achieved: (i) with $\text{RbCl}\text{-Ba:Zn}_4$ saturable absorber - 1 mJ in energy and 100 ns in duration,² (ii) with $\text{Cr}^{2+}\text{:CdMnTe}$ one - 8 mJ and 200 ns;³ (iii) with Ho:YLiF_4 saturable absorber - 11 mJ, 45 ns.⁴ So the PbSe-doped glass saturable absorber demonstrates higher pulse energy and approximately the same pulse duration in comparison with the best above result. In our opinion higher optical quality and antireflection coating of PbSe saturable absorber will lead to better Q-switching efficiency of Ho:YAG laser.

5. CONCLUSIONS

In conclusion, passive Q-switch operation of the Ho:YAG laser has been demonstrated using a PbSe-doped phosphate glass as a saturable absorber. Pulses of 60 ns in duration and 22 mJ in energy at $2.1\text{ }\mu\text{m}$ were obtained. Temperature dependence of luminescence spectra of phosphate glasses doped with PbSe QDs of different sizes was analyzed.

REFERENCES

1. R. Sroka, A. Perlmutter, T. Pongratz, R. Muschter, R. Baumgartner, "In-vivo investigations on interstitial Ho:YAG laser ablation in urology", *OSA Trends in Optics and Photonics Vol. 22, Biomedical Optical Spectroscopy and Diagnostics / Therapeutic Laser Applications*, Eva M. Sevick-Muraca, Joseph A. Izatt, and Marwood N. Ediger, eds. (Optical Society of America, Washington, DC 1998), pp. 317-319.

2. B. A. Ermakov, A. V. Lukin, and L. M. Sobolev, "Laser passive Q-switch operating in a 2 μm region", *Optika i Spektroskopiya*, **63**, 233-234 (1987).
3. A. V. Podlipensky, N. V. Kuleshov, V. I. Levchenko, V. N. Yakimovich, "Passive Q-switching of Cr, Tm, Ho: YAG 2.09 μm laser with Cr:CdMnTe solid-state saturable absorber", *CLEO/QELS 2000 Advanced Program*, p. 154.
4. Y-K. Kuo, M. Birnbaum, W. Chen, K. Yue, M-F. Huang, "Passive Q-switching of the Tm,Cr:YAG 2 μm laser with a Ho:YLF solid-state saturable absorber". *OSA Proceedings on Advanced Solid-State Lasers*, 1995, vol. 24 Bruce H. T. Chai, and Stephen A. Payne (eds.).
5. *Landolt-Bornstein, New Series*, ed. by O. Madelung (Springer, New-York, 1983), vol. 17, subvol. F, pp. 155-169.
6. A. A. Lipovskii, E. V. Kolobkova, V. D. Petrikov, "PbSe quantum dot doped phosphate glass", *Electronics Letters*, **33**, No 1, 101-102 (1997).
7. A. D. Andreev, A. A. Lipovskii, "Anisotropy induced forbidden transitions in PbSe and PbS spherical quantum dots" *Phys. Rev. B* **59**, 15402-15404 (1999).
8. I. Kang, F.W. Wise, "Electronic structure and optical properties of PbS and PbSe quantum dots", *JOSA B* **14**, 1632-1646 (1997).
9. P. Russignol, D. Ricard, C. Flytzanis, N. Neuroth, "Phonon broadening and spectral hole burning in very small semiconductor particles" *Phys. Rev. Lett.* **62**, 312-315 (1989).
10. A. A. Lipovskii, E. V. Kolobkova, A. Olkhovets, V. D. Petrikov, F. Wise, "Synthesis of monodisperse PbS quantum dots in phosphate glass", *Physica E* **5**, 157-160 (2000).
11. P. T. Guerreiro, S. Ten, N. F. Borrelli, J. Butty, G. E. Jabbour, N. Peyghambarian, "PbS quantum-dot doped glasses as saturable absorbers for mode-locking of a Cr:forsterite laser", *Appl. Phys. Lett.*, **71**, 1595-1597 (1997).

SRS Lasers with self-conversion of radiation frequency based on $\text{NaLa}(\text{MoO}_4)_2:\text{Nd}^{3+}$ and $\text{KGd}(\text{WO}_4)_2:\text{Nd}^{3+}$ crystals

Gulin A.V., Pashkov V.A., Ustimenko N.S.

R&DI "Polyus", Russia.

ABSTRACT

Efficient multiwave generation in nanosecond regime SRS self-converter based on $\text{NaLa}(\text{MoO}_4)_2:\text{Nd}^{3+}$ crystals by SRS-active mode $\omega=888 \text{ cm}^{-1}$ has been obtained. Also, parameters of new miniature eye-safe SRS laser ($\lambda=1538\text{nm}$) with self-conversion based on $\text{KGd}(\text{WO}_4)_2:\text{Nd}^{3+}$ crystal is demonstrated. This laser has differential efficiency 0.3% by pump energy threshold about 1J.

Keywords: eye-safe laser, SRS laser, self-conversion

1. MULTIWAVE GENERATION OF THE STOKES COMPONENTS IN SRS LASER BASED ON $\text{NaLa}(\text{MoO}_4)_2:\text{Nd}^{3+}$ CRYSTAL

Efficient multiwave generation of the Stokes components has been performed in solid state SRS lasers with self-conversion for nanosecond pulse duration¹ so far just on crystals $\text{KGd}(\text{WO}_4)_2:\text{Nd}^{3+}$. Since there is a rising interest to research of new materials for SRS lasers, we have studied generation characteristics of crystal $\text{NaLa}(\text{MoO}_4)_2:\text{Nd}^{3+}$, having high third – order nonlinear susceptibility χ^3 . Tests showed: generation efficiency of laser on crystal $\text{NaLa}(\text{MO}_4)_2:\text{Nd}^{3+}$ ($\lambda = 1065 \text{ nm}$) near to the same on crystals $\text{NaLa}(\text{MoO}_4)_2:\text{Nd}^{3+}$ ($\lambda = 1067 \text{ nm}$) and $\text{Y}_3\text{Al}_5\text{O}_{12}:\text{Nd}^{3+}$ ($\lambda = 1064 \text{ nm}$). Generation characteristics were compared in the modes of free running generation and passive Q-switch. Laser rods had a 50 mm length and 3 mm in diameter. The laser cavity was formed by two plane mirrors with reflectivity of $R=99.9\%$ and $R=40\%$. Passive Q-switch has been performed by doped crystals $\text{Cr}^{4+}:\text{YAG}$. Initial transmissions T_0 of passive Q-switch were optimized for each type of element. Results of comparison are presented in Table 1.

Table 1

Type of element	Pump energy threshold (J)	Initial transmission coefficient (%)	Output energy (mJ)
$\text{KGd}(\text{WO}_4)_2:\text{Nd}^{3+}$	4	45	24
$\text{Y}_3\text{Al}_5\text{O}_{12}:\text{Nd}^{3+}$	4	37	20
$\text{NaLa}(\text{MoO}_4)_2:\text{Nd}^{3+}$	5	55	23

Thus, properties of high efficiency laser material and low threshold SRS self-converter combine in crystal $\text{NaLa}(\text{MO}_4)_2:\text{Nd}^{3+}$. This allowed to realize scheme of multiwave laser on $\text{NaLa}(\text{MO}_4)_2:\text{Nd}^{3+}$ crystal in regime of SRS self-conversion for nanosecond pulse duration, generating simultaneously on wavelengths 1065 nm, 1176 nm, 1313 nm with help of SRS-active frequency $\omega=888 \text{ cm}^{-1}$. Pump energy of this laser equals about $\sim 5\text{J}$.

The rear mirror of laser cavity had the reflection coefficient $R=99.9\%$ on wavelength 1064 nm, 1180 nm and 1320 nm. Output coupler had the transmission of 2.4%, 8.6% and 64 % on these wavelengths.

Thus, we had strong first and second Stokes component from wavelength 1065 nm by relatively low pump energy. Simultaneously, the second harmonics of Stokes components were obtained. Also, we have realized scheme of multiwave laser (fig.1)

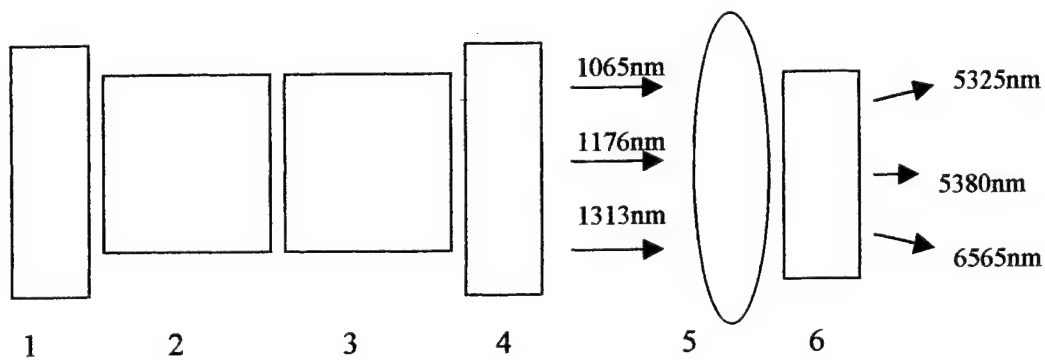


Fig.1 Schematic diagram of laser

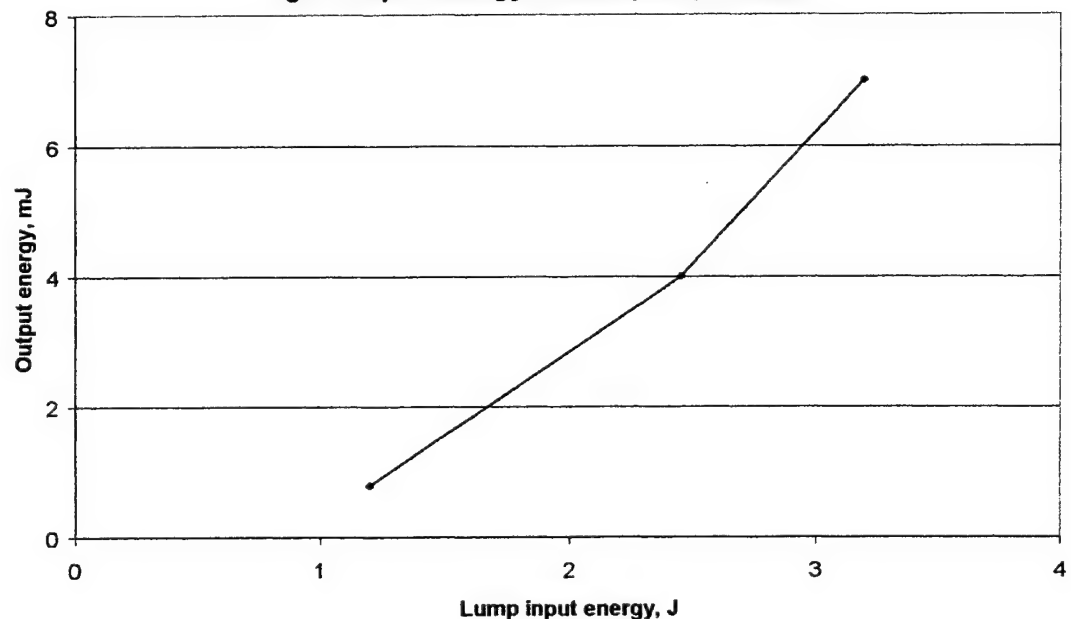
1-Rear mirror; 2-Q-switch; 3-Laser rod; 4-Output coupler; 5-Focusing lens; 6-LiNbO₃

However, it should be pointed that relatively low damage threshold of crystal NaLa(MO₄)₂:Nd³⁺ is limiting it's application.

2. NEW EYE-SAFE LASER CONSTRUCTIONS BASED ON KGd(WO₄)₂:Nd³⁺ CRYSTAL

We have optimized the laser scheme on crystal KGd(WO₄)₂:Nd³⁺, which generation on $\lambda = 1351$ nm (transition $^4F_{3/2} - ^4I_{11/2}$) converts to first Stokes component $\lambda = 1538$ nm by SRS-active frequency $\omega = 901$ cm⁻¹ [1]. This allowed us to create construction of high efficiency eye-safe laser. Laser operates on electrooptical Q-switch based on crystal LiNbO₃ with Brewster-angle ends. This allowed to minimize internal losses and to use Brewster-angle as polarizer. Laser rod was 50 mm length and 3 mm in diameter. Weight of laser head is about 50 g. Figure 2 illustrates output energy on wavelength 1538 nm versus pump energy.

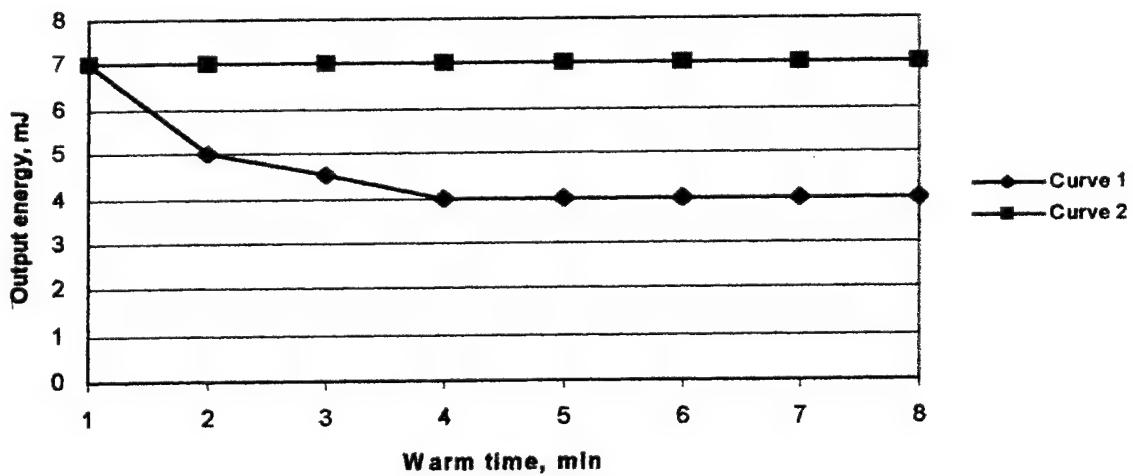
Fig.2 Output energy versus pump energy.



One can see, that differential efficiency of this laser is about 0,3% by pump energy threshold less than 1J. Repetition rate is about 0,3 Hz without decrease of output energy or 1Hz with decrease about 40% (Fig.3 curve1).

Some improvements allowed us to create construction of laser with repetition rates 1Hz without decrease of output energy (Fig. 3 curve 2).

Fig.3 Output energy versus warm time



3. CONCLUSION

SRS solid-state lasers demonstrate high efficiency. Such lasers allow to extend spectral region for various application.

4. REFERENCES

1. Gulin A. V., Narkhova G.I., Ustimenko N.S., *Kvantovaja elektronika*. Vol.25, № .9, p.p 825-826 (1998).

The 1.53- μ m Lasing by SRS in Barium Nitrate in Focused Beams and in Resonator

S.N. Karpukhin

Institute for Laser Physics, Research Center "Vavilov State Optical Institute", Russia

Abstract

Spatial-angular and spectral-energy characteristics of eye-safe lasing by SRS in barium nitrate, pumped by 1.32 μ m Nd:YAG laser radiation in focused beams and resonator are studied. The pump-to-first-Stokes-component energy conversion factor 55% was obtained for lasing in resonator with single-mode pumping. With the multimode pumping essential gain in the lased radiation brightness compared with pump (beam clean-up) was received. It was shown that in the focused beams SRS take place in the wavefront replication mode. Thermal lens focal length in crystal was measured.

Keywords: eye-safe radiation, SRS, Raman scattering, barium nitrate, Stokes wave, focused beams, beam divergence, beam clean-up, wave front replication (reproduction).

1. Introduction

Most of the preceding papers on SRS in crystalline media in nanosecond time range were carried out with the use of pumping by 1.064 μ m or its second harmonics¹⁻⁵. These activities revealed the novel crystalline media with the low generation threshold, demonstrated the possibility of the efficient energy conversion via SRS. It was shown that it is possible to obtain the diffraction limited radiation in the mode of phase conjugation, as well as to realize the amplification of weak wave without distortions. The use of stimulated Raman scattering (SRS) in barium nitrate crystal for Nd:YAG laser 1.32 μ m emission conversion is rather promising idea, providing the possibility of realization of the completely solid-state source of the eye-safe radiation. The eye-safe 1.53 μ m radiation is first Stokes component for 1.32 μ m emission conversion. Such a possibility was for the first time noted and experimentally tested in^{6,7}. The efficiency of generating eye safe radiation equalled 48 % with 1.32 μ m radiation pumping in barium nitrate crystal was received in paper⁸ for generating inside the resonator of the pump laser. Present work is aimed at a study of space-angular and spectral-energy characteristics of radiation lased in focused beams and in external resonator.

2. Generation in the focused beams

This section presents the results of the experimental study of the Stokes radiation generation in the focused single and multi mode beams. The crystal was pumped by an Nd:YAG Q-switched laser with a 30-ns pulse length, 0.4-cm⁻¹ spectrum width, up to 170-mJ multimode and 15-mJ single-mode pulse energies. Divergence of multy mode beam was $\theta_{0.8E} = 2.7\text{mrad}$. The laser radiation contained two spectral components. The main part of output energy had a wavelength 1.319 micron and approximately 5 % of output energy had a wavelength 1.338 micron. Laser beam diameters being, respectively, 6 and 2 mm (diameters of apertures in laser cavity) for multimode and single-mode regime, repetition rate up to 20 Hz. (During all experiments, described below, pump lamps in the laser worked on constant frequency 20 Hz, variation of the output pulse repetition rate was carried out by changing of the frequency of the Pockels cell opening. This provided an invariance of pump radiation parameters at changing of pulses repetition rate). In all of the experiments, radiation was focused at the centre of the crystal of 6 cm length. The crystal geometrical axis was parallel to [110] crystallography axis and pump polarization direction was parallel or perpendicular to [001] crystallography axis so as to provide low radiation depolarisation⁹.

At first we have experimentally measured the dependence of the efficiency of the conversion to Stokes components vs. the focal length of the lens in order to determine the optimal focal length. The optical scheme of the experiment is shown in the Fig.2.1.

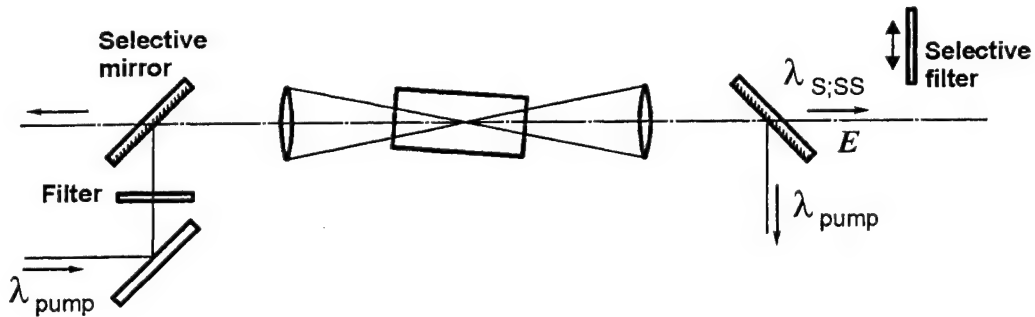


Fig.2.1. The optical scheme of the experiment for generation in the focused beams.

The crystals were tilted in order to prevent the generation in the direction, perpendicular to their butt-ends. In the Fig.2.2 are shown the results of these measurements for the single and the multi-mode beams at the constant energy. One can see that in the case of the single mode beam the curve is saturated for the shorter focal length. The reason is that for the focal length of 20 cm the length of the focal waist for single mode pumping practically coincides with the length of the crystal. Further shortening of the focal length results in just negligible growth of the increment, while the focal density of the intensity grows. Such a growth is not desirable in the case of pulse-repetitive mode of laser action. (For example, in the experiments with the copper vapor laser⁹ radiation, focused by lens with the focal length of 50 cm, after some period of the experiments there was observed the occasional breakdown of the crystal, while in course of the consequent experiments with the focal length of 60 cm no damage occurred). In the case of the multi-mode pumping the length of the focal waist exceeded the length of the crystal for all lens we have used. Hence the conversion efficiency was reducing with the focal length growth (Fig.2.2 b). However, in our further experiments we have not used the focal lengths, shorter than 20 cm, due to the higher energy in the pulse of the multi-mode pump and to the limitations, imposed by the possibility of the optical damage.

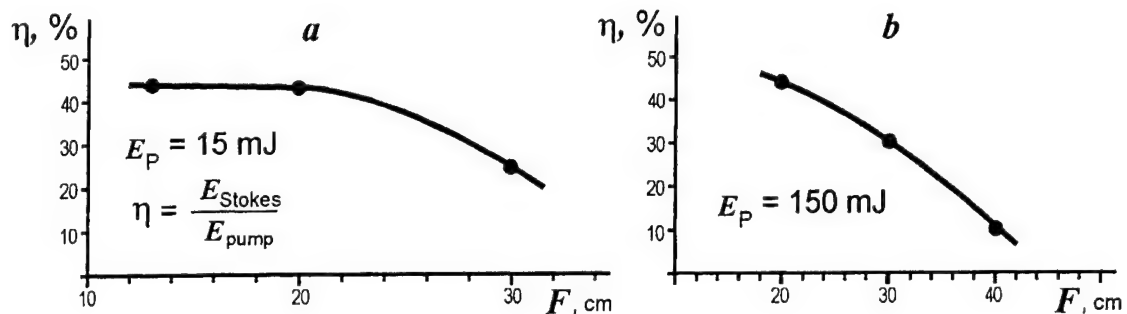


Fig.2.2 Dependence of the conversion efficiency to the both Stokes components vs. the focal length of the lens for single mode beam (a) and multi mode beam (b).

The two-component spectral distribution of pump radiation was revealed in a spectral distribution of Stokes radiance (Fig.2.3) (The spectrum was produced due to the dispersion of the Stokes radiation in the glass prism and was photographed from the screen with the photosensitive layer.). Note the splitting of the second Stokes component line owing to threshold-less parametric four-wave mixing conversion of the weak pumping component at the wavelength 1.338 μm . (The possibility of such conversion is caused by affinity of wavelengths of both pump component, because of length of nonlinear parametric conversion equalled for the first Stokes component $1/\Delta k$, where $\Delta k = (k_1 - k_{1S}) - (k_2 - k_{2S})$; k_1, k_2, k_{1S}, k_{2S} - correspondingly wave numbers of pump components and their Stokes components) One can see that its longer wavelength subcomponent reveals lower intensity. In the given below experimental results the total energy in the given Stokes component was measured only, because the thin spectral distribution depends on selection properties of the pump laser resonator and can be changed.

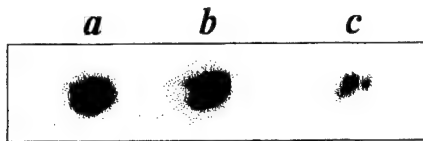


Fig.2.3. Spectrum of the radiation, generated via the single mode beam focusing:
a - pump; **b** - first Stokes; **c** – second Stokes.

In the Fig.2.4 are shown the results of measuring of the conversion efficiency to the Stokes components vs. pump energy. The energy of the second Stokes component was measured with the use of the selective glass filter, cutting off the first Stokes component.

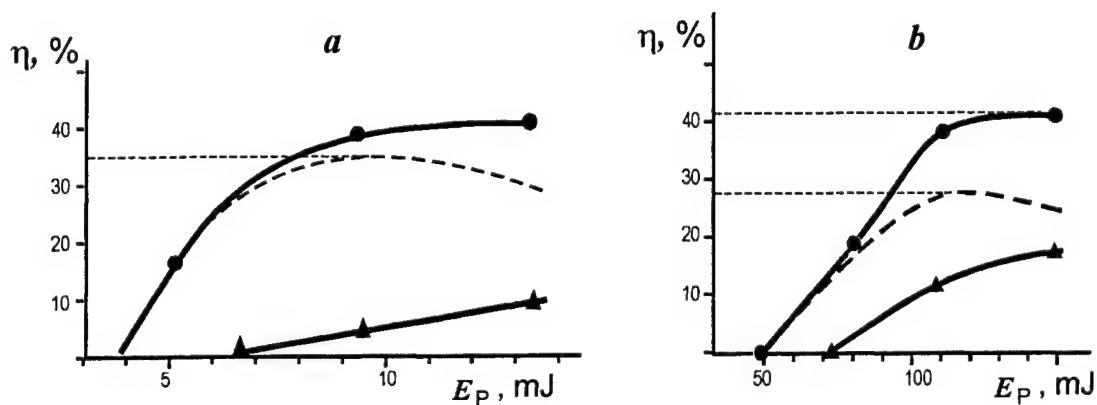


Fig.2.4 Conversion efficiency to the separate Stokes components vs. pump energy for single mode beam (a) and multi mode beam (b).

● - total output Raman radiation, - - - - first Stokes component, ▲ - second Stokes component;

As one would expect, the efficiency of the conversion to the most interesting first Stokes component was limited by the excitation of the second Stokes component. Both Stokes components were excited only in the forward direction; the reason is the slightly smaller gain of the backward SRS amplification in the field of the multi-frequency pump in our case. The maximal technical efficiencies reached 35% for the single-mode pump and 27% for the multi-mode pump. The corresponding values of the physical efficiency (accounting for the Fresnel reflection at the butt-ends and for the incomplete transmission through the selective mirror) were thus 41% for the single-mode and 32% for the multi-mode pump. One can see that in the case of the single-mode pumping the influence of the second Stokes generation onto the efficiency of the first Stokes component generation is smaller. The reason of this effect is as follows. For scattering with the Gaussian single-mode pumping there is a decrease of the beam waist diameter of the Stokes radiation as compared with the pump, as the intensity at the beam axis is higher¹⁰. As the consequence the beam waist diameter of the second Stokes component (for which the first component is pump) should be even less than for the first one. It means, that the diffraction losses for the second Stokes component are higher than for first one. For scattering with the multimode pumping the intensity in beam waste has distribution nearer to "flat top". Therefore in this case increasing of diffraction losses of the second Stokes component take place to a lesser degree, than with single-mode pumping.

In Fig.2.5 are shown oscillogram of pump and Stokes pulses for one mode radiation (pulse duration was measured with the use of the Tektronics oscilloscope TDS 744 and of the coaxial photosensitive element Fek-19). Let's note, that the Stokes pulse became closer to rectangular.

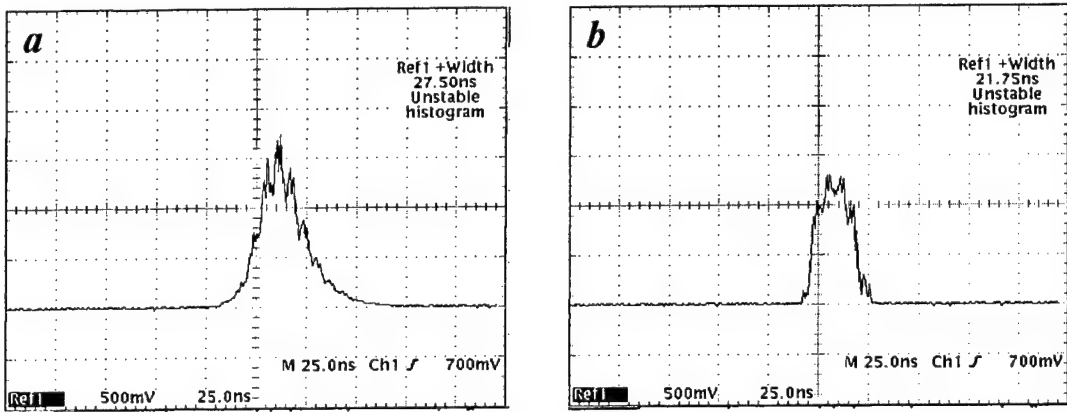
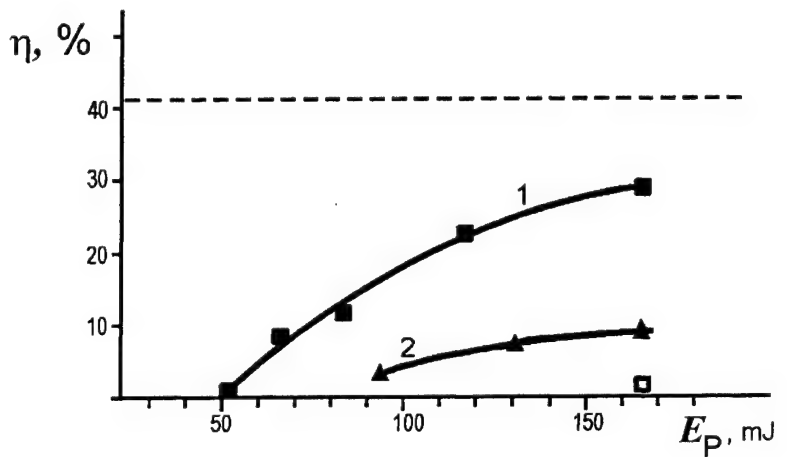


Fig. 2.5. Temporal profile of the one mode pump pulse(a) and Stokes pulse(b).

Another variant of the experiment geometry has revealed higher efficiency of the energy conversion to the first Stokes component of the multi-mode radiation, but for sum of forward and backward Stokes radiation. In this case the radiation was focused by lens with the longer focal length equalled 41cm in the direction, which was perpendicular to the butt-ends of the crystal, so the butt-end edges act as the cavity mirrors, and the SRS excitation threshold was approximately two times lower than in the case of the tilted edges. In such the geometry there is also observed the excitation of the backward SRS. Results of these measurements are shown in the Fig.2.6 Summing of forward and backward Stokes radiation can be done by polarization using simple scheme with 90° polarization rotator and polarizer, so efficiency about 40% for multi mode beam also can be received.

Fig.2.6. Conversion efficiency to Stokes components vs. pump energy.
1 - one crystal scheme (first Stokes component); 2 – backward.

- second Stokes component.



However, such an experiment can not be treated as the generation in the cavity, as far as in this case the structure of the angular distribution of the Stokes radiation energy almost replicate that of the pump. Radiation divergence was measured with the use of the pinholes, mounted in the beam waist after the special measuring lens (Fig.2.7). We have also measured the divergence of the pumping beam. In this case the beam energy was attenuated beyond the SRS threshold by the thin neutral filter, and the selective mirror was taken off the scheme. The results of the divergence measurements are shown in the Fig.2.8. One can see that - both for the single-mode and the multi-mode pumping - the Stokes beam divergence was slightly less than that of the pumping beam. In the case of the single mode beam such a situation is possible only due to the beam diameter increase at the measuring lens. This, in turn, means that the diameter of the beam of the Stokes radiation in the crystal is smaller than that of the pump beam, as always mentioned above, and the near-field diffraction results in the wider beam in the plane of the measurement lens. For multi-mode beam this is the result of partial nonlinear spatial filtration of radiation during scattering.

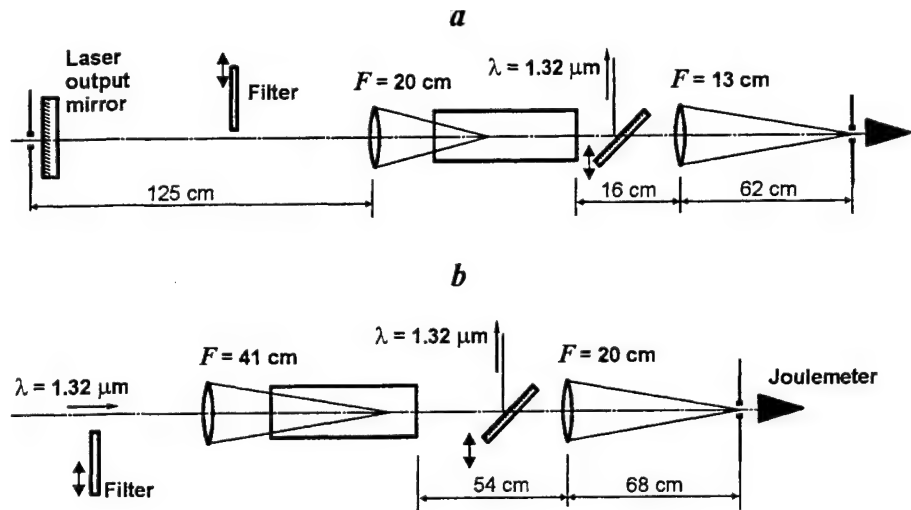


Fig. 2.7. The optical scheme for divergence measurement with one mode pump beam (a) and multi mode (b).

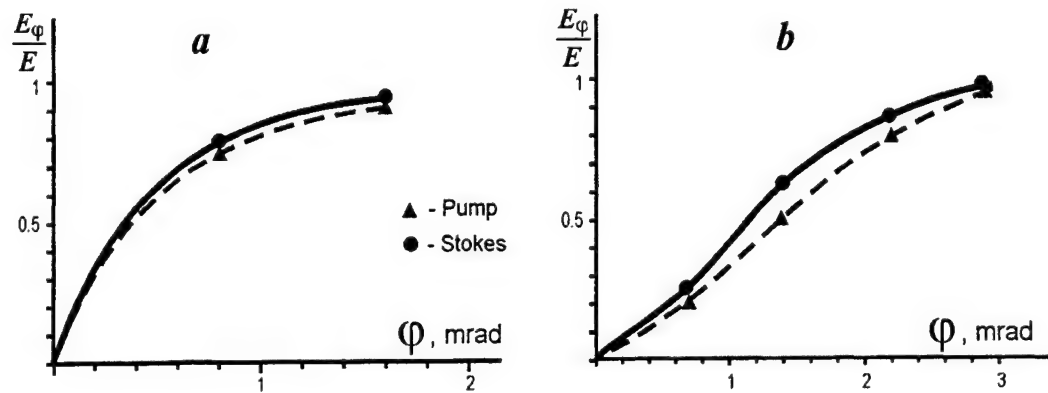


Fig. 2.8. The results of the divergence measurements.

We have tested in the experiment that the parameters of the converted beams did not vary up to the pulse repetition rates of 20 Hz.

Using the single-mode radiation, SRS gain in barium nitrate crystal was measured. For this purpose beam, whose energy exceeds the SRS threshold, is focused into the crystal. The threshold power was measured by means of registration of the pump pulse shape at the crystal input and output. We have evaluated the power, which corresponded to the moment of the character break of the temporal profile of the pumping pulse at the crystal output. SRS gain calculated using formula¹¹, which hold when single mode beam waist equalled crystal length.

$$g = \frac{\pi}{2} \frac{M_F}{k_0 P_{th} n}$$

where $M_F = 30 \dots 35$, $k_0 = \frac{2\pi}{\lambda}$. The Table summarizes the result of the present gain measurement as well as the values,

which were measured by author earlier for the wavelengths of 1.064 μm and of 0.532 μm in Ba(NO₃)₂ and in KGd(WO)₂. One can see that the gain reduce with the wavelength grow is described by the law, which faster than the just inversely proportional. The possible reason is the influence of the resonant terms in the expression for the Raman scattering, accounting for the structure of the crystalline electron levels¹².

Parameters of SRS crystals

Materials	Polarization	$g \cdot 10^3 \text{ cm/MW}$			$v, \text{ cm}^{-1}$
		$\lambda = 0.5 \mu\text{m}$	$\lambda = 1.06 \mu\text{m}$	$\lambda = 1.32 \mu\text{m}$	
$\text{Ba}(\text{NO}_3)_2$		47	11	7.1	1046 1047 ¹³
$\text{KGd}(\text{WO}_4)_2$	n_m - axis n_p - axis	—	6	—	901.5 767.3

3. Generation in the cavity

Better conversion efficiency of pump radiation was received by generation in the cavity. The parameters of the cavity, which are shown in the Fig.3.1, were chosen with the account for the mutual adjustment of the volume of the zero mode of this cavity and of the focused pumping beam. The Gauss diameter of the zero mode was determined according to the formula¹⁴, where L is cavity length, and l is crystal length:

$$d_0 = 2 \sqrt{\frac{\lambda_s}{\pi}} \sqrt{L'(R - L')} \quad (3.1)$$

$$L' = L - l \left(1 - \frac{1}{n}\right)$$

For single mode pumping it was equal 0.42 mm. The diameter of the single mode pump beam in the crystal were chosen to be 0.44 and 0.32 mm (80% of energy) correspondingly for lens focus equalled 40cm and 30 cm. The coupling mirror reflected the pump completely. According to the results of the paper³ this useful to make better the discrimination of the second Stokes component generation.

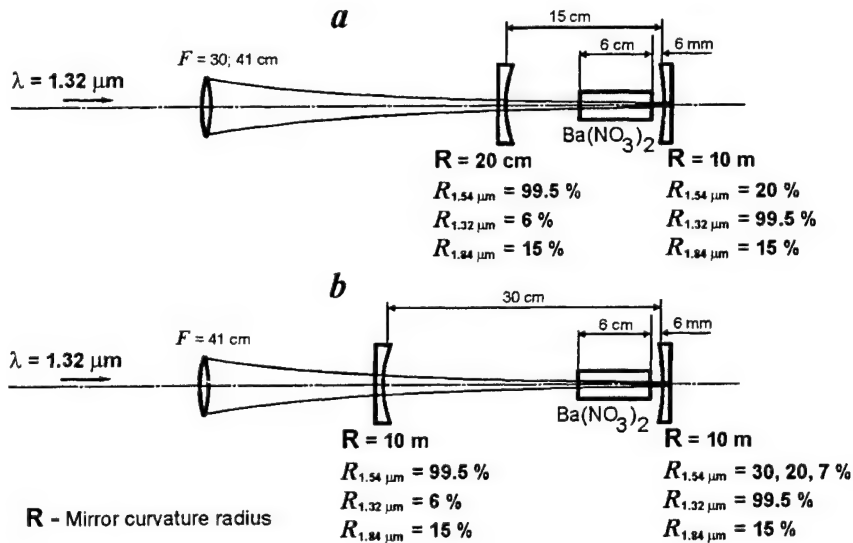


Fig. 3.1 The parameters of the cavity for generation with single-mode pumping (a) and multimode pumping (b).

When the butt-end edges of the crystal were orthogonal to the cavity axis we have observed the dual mode generation. Small tilt of the crystal has resulted in generation of the single mode. Fig.3.2 illustrates the results of measuring of the dependence of the conversion efficiency to first Stokes component vs. pump intensity. The maximal efficiency was as high

as 55% (accounting for the possibility of the AR coating of the input edge of the crystal). Account for the incomplete transmission of the output mirror indicates the physical level of 58%. Note that generation of the second Stokes component was negligibly small.

It is interesting to note that obtained result is a little bigger than received in paper ⁸ for SRS in pump laser resonator, despite existing in our case residual pump. The reason of this, from our point of view, is as follows. The carried out numerical simulation has shown, that at SRS inside the pump laser resonator, the inverse population in a laser active element, reserved until moment of Q- switch opening, is not completely (up to threshold level) used due to the starting of SRS sharply reduces density of photons in the resonator on pump frequency. The inverse population remains approximately at that level, which was at the moment of a beginning of steep decrease of the pump radiation intensity in the resonator. The increasing of initial inverse population does not improve her exhausting, but produces the second pump and Stokes pulses.

No modification of the generation parameters took place in considering one mode cavity for the pulse-repetitive modes of action up to 20 Hz.

With the use of the multi-mode pumping we also focused radiation into the volume of the zero mode of the cavity. The parameters of the cavity we have studied are indicated in the Fig.3.1b. We have used the symmetrical cavity with the concave mirrors. In this case one has to replace in the formula (3.1) L by L/2 so as to evaluate the mode volume. Neglecting in the long cavity by the cavity length modification due to the refraction in the crystal we get for the Gaussian diameter of the zero mode the value of 1.54 mm. For the focal length of the focusing lens 41 cm the diameter of the beam in the crystal (energy level 0.8) was equal 1.64 mm.

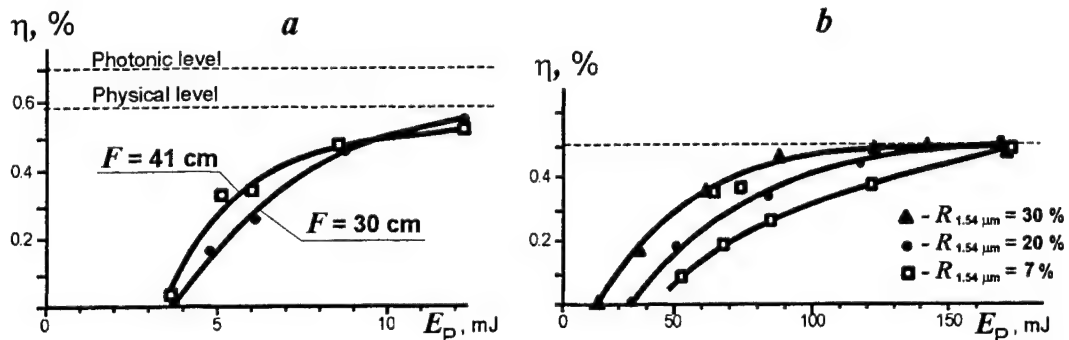


Fig. 3.2. Dependence of the conversion efficiency vs. pump pulse energy for generation in the cavity with single- mode pumping (a) and multi- mode pumping (b).

In the Fig.3.2 b are shown the results of measuring the conversion efficiency vs. the pumping energy for the different coefficients of the mirror reflectivity. Note, that for the mirror with the reflectivity 7% the threshold is just slightly lower than in the case of the single-pass SRS when the crystal edges are orthogonal to the optical axis (Fig.2.6). The reason is that in the mode of the wave front replication the increment of the Stokes wave amplification twice exceeds the corresponding value for the waves in the cavity, which are not spatially correlated with the pump¹⁰. The maximal efficiency (without the account for the reflection by the input edge of the crystal) was equal 50%. Hence both variants of the pump reveal approximately one and the same conversion efficiency, but not the radiation divergence. The Gaussian angle of the zero mode divergence in the described cavity can be calculated according to the formula¹⁴:

$$\Delta\theta = 2 \frac{\sqrt{\frac{\lambda}{\pi}}}{\sqrt[4]{\frac{L}{2} \left(R - \frac{L}{2} \right)}}$$

It is equal 1.2 mrad. In the Fig.3.3 are shown the results of measuring of the energy distributions in the near and far-field zones. One can see from these figures that the Stokes radiation contains the core and the wide wings. High quality of the core radiation can be seen also from the Fig.3.4.

The brightness improvement was measured with the higher accuracy in the following experiment. At some distance from the output mirror we have mounted the aperture, cutting off the main part of the radiation wings. The

efficiency of the conversion in the presence of such an aperture was only 25%. In such a geometry we have also measured the near and the far-field energy distributions. The coefficient of the brightness improvement k for beams reduced to the same diameters, according to the following formula, equalled 5.9:

$$k = \eta \left(\frac{D_p}{D_s} \right)^2 \left(\frac{\theta_p}{\theta_s} \right)^2$$

Here D_p is the pumping beam diameter, θ_p is the pumping beam divergence for the given diameter, and D_s and θ_s are the same parameters of the Stokes radiation in the plane of the measuring lens.

Hence the SRS generation in the cavity makes it possible to improve significantly the brightness of the remote object irradiation.

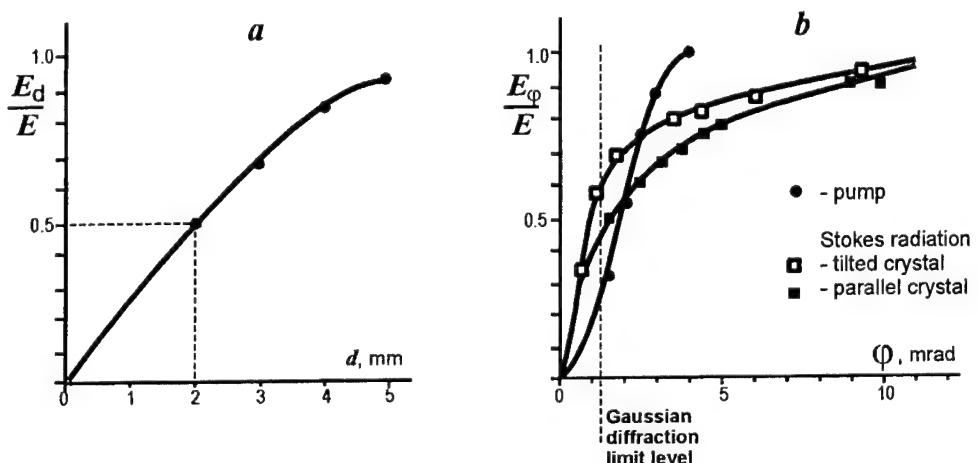


Fig.3.3. Near field distribution (a) and angular energy distribution (b) for generation in the cavity with multi-mode pumping.

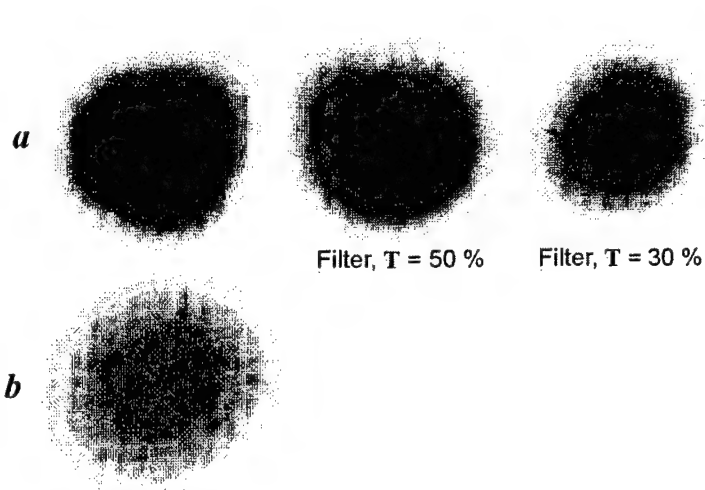


Fig. 3.4. Near (a) and far (b) field patterns for generation in the cavity with multi-mode pumping.

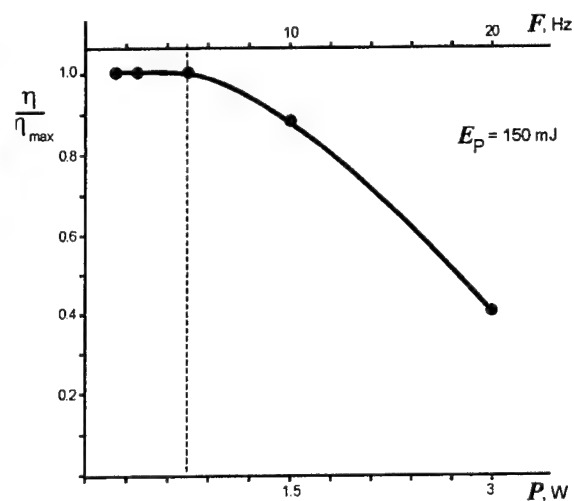


Fig. 3.5. Dependence of the conversion efficiency for generation in the cavity with multi-mode pumping vs. pump pulse frequency

Generation in the described cavity differs from the schemes we have described before: it reveals the significant reduce of the efficiency with the growth of the pulse repetition rate (Fig. 3.5). We have found out that the reason is the negative thermal lens, which modifies the cavity. It was interesting to evaluate optical force of the thermal lens. Was shown that the account of the relationships between the photoelastic coefficients in Barium Nitrate ($(p_{13} - p_{12})/p_{12} \ll 1$) makes it possible to use the theory, described thermal effects, elaborated for the crystals of higher symmetry, such as YAG (see appendix). The average value of the focal length of the thermal lens for two orthogonal eigen - polarizations is described by the formula¹⁴:

$$F = \frac{2\chi S}{P P_h} \quad (3.2)$$

where P_h is the heating power, S is the beam section area, χ is the thermal conductivity coefficient, $P = \beta - \frac{\alpha n_0^3}{4} \frac{1+v}{1-v} (p_{11} + p_{12})$, $\beta = \frac{dn}{dT}$, n is the refraction index, α is the coefficient of linear expansion, v is the Poisson coefficient and p_{11} , p_{12} are the photoelastic coefficients. Substituting values of constants in the given formula $n=1.555$, $\beta=2 \times 10^{-5} \text{ degree}^{-1}$, $\alpha=1.1 \times 10^{-5} \text{ degree}^{-1}$, $\chi=1.1 \text{ W/mK}^0$, $v=0.237$, $p_{11}=2.49$, $p_{12}=3.40$, $p_{13}=3.20$, $p_{44}=-0.021^{16,17}$ we received value $P=-7.9 \times 10^{-5} \text{ degree}^{-1}$, so it is negative. One can see from relationships (3.2) that the thermal lens reveals the negative focal length. This length was measured for $0.62 \mu\text{m}$ radiation in the optical scheme, which is shown in the Fig.3.6.

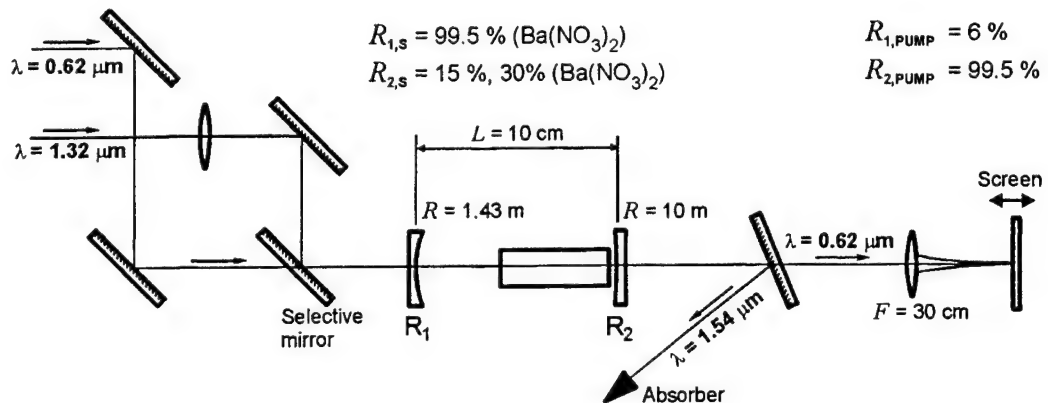


Fig. 3.6. Optical scheme for measuring thermal lens.

Diameter of the beam in the crystal was enlarged up to 2.2 mm (0.9E, nearly flat top distribution) by means of the spherical mirror, replacing one of the flat mirrors in the pumping laser cavity. We have measured in the experiment the distance from the plain of the auxiliary lens to the center of the focal waist of the He-Ne laser radiation beam. Such measurements were done in the presence of the SRS excitation in the cavity and in its absence. The calculation was performed with the use of the lens formula. (Preliminary – in the absence of SRS – we have measured the radius of the He-Ne laser beam wave front curvature in the plane of the crystal). For the pulse energy 115 mJ, pulse repetition rate 20 Hz, efficiency of generation to the first Stokes component 50% and to the second one 7% the measured value of the thermal lens focal length was equal minus 150 cm.

It was interesting to compare this value of the thermal lens focal length with the value, calculated for the deposited thermal power:

$$P_h = P_p \left(\eta_1 \frac{\Omega}{v_s} + \eta_2 \frac{2\Omega}{v_{ss}} \right) \quad (3.3)$$

Here η_s and η_{ss} are the efficiencies of the pump conversion to the first and to the second Stokes components and v_s and v_{ss} are the frequencies of these components. If one uses in the formula (3.2) the value of the thermal losses of 0.24 W and calculated value for P , he will evaluate the focal length of the lens as rather short – equal to minus 35 cm. This is a contradiction with the experimental result. Let us use the experimental value of the focal length for evaluation of the

thermo-optical constant P . It is thus equal to -2.3×10^{-5} degree $^{-1}$, while calculated value is -7.9×10^{-5} degree $^{-1}$. Note that this constant is calculated as the difference between two constants, and is thus rather sensitive to the accuracy of measuring them. (Let us, for example, assume, that the real value of β exceeds twice the value, available from the literature, and let us also assume, that the value of α is, vice versa, twice smaller. In this case the calculated value of the P would change in an order of magnitude and would be thus 2.5 times smaller (by modulus) than the experimentally measured.)

4. Conclusion

Let us in conclusion enumerate the main results of the work:

1. We have realized in the experiment the 55% efficiency of generation of the eye-safe single-mode first Stokes component in the cavity, the six-times growth of the Stokes beam brightness with respect to that of the pump (beam clean-up).
2. We have established that in the focused beam and at the low quality cavity the generation reveals the feature of the wavefront replication up to the achievement of the saturation. Hence the Stokes beam divergence is close to that of the pump.
3. For the focused single-mode beam the efficiency of the first Stokes component generation is higher than that for the multi-mode beam (35 and 27% correspondingly) due to the higher diffraction losses during the second Stokes component generation. With the low cavity scheme it is possible to receive the efficiency up to 40%.
4. We have measured the Raman gain for 1.32 μm radiation in the crystal of barium nitrate and the constant, responsible for the thermal lens in barium nitrate.

5. Appendix

The crystal of barium nitrate is the cubic crystal of the symmetry m3. The indicatrix of the refraction index is spherically symmetrical ($Bx_i x_i = 1$, $i=1,2,3$, where $B=1/n^2$, n - refraction index of the crystal). Thermal distortions of the crystal results in this sphere transformation into the ellipse, described by the equation:

$$B_{ij} x_i x_j = 1 \quad i,j = 1,2,3$$

Here B_{ij} is the tensor of the relative dielectric impermeability. In general case the modification of the indicatrix in comparison with its primary shape is described by the relationship¹⁶:

$$\Delta B_{ij} = p_{ij,k,l} \varepsilon_{k,l} \quad i,j,k,l = 1,2,3$$

Here $p_{ij,k,l}$ is the tensor, describing the photoelastic effect, and $\varepsilon_{k,l}$ is the tensor, which describes the thermally induced deformations. The crystal symmetry results in zero value of some components of the photoelastic tensor. So the modification of the tensor of the relative dielectric impermeability can be described in the simpler way¹⁶:

$$\Delta B_i = p_{ij} \varepsilon_j \quad i,j = 1,2,3$$

In the same paper there was given the description of the tensor p_{ij} for the crystals of various symmetry classes. Let us write out the expressions for the components of tensor ΔB_i for the symmetry m3 and reorder the terms:

$$\begin{aligned} \Delta B_1 &= p_{11} \varepsilon_1 + p_{12} \varepsilon_2 + p_{13} \varepsilon_3 = p_{11} \varepsilon_1 + p_{12} \varepsilon_2 + p_{12} [1 + (p_{13} - p_{12})/p_{12}] \varepsilon_3 \\ \Delta B_2 &= p_{13} \varepsilon_1 + p_{11} \varepsilon_2 + p_{12} \varepsilon_3 = p_{11} \varepsilon_2 + p_{12} \varepsilon_3 + p_{12} [1 + (p_{13} - p_{12})/p_{12}] \varepsilon_1 \\ \Delta B_3 &= p_{12} \varepsilon_1 + p_{13} \varepsilon_2 + p_{11} \varepsilon_3 = p_{11} \varepsilon_3 + p_{12} \varepsilon_1 + p_{12} [1 + (p_{13} - p_{12})/p_{12}] \varepsilon_2 \\ \Delta B_4 &= p_{44} \varepsilon_4. \quad \Delta B_5 = p_{44} \varepsilon_5. \quad \Delta B_6 = p_{44} \varepsilon_6. \end{aligned}$$

Let us now neglect the value of $(p_{13} - p_{12})/p_{12} = -0.06$ as very small in comparison with 1 in the expressions for ΔB_1 , ΔB_2 , ΔB_3 . So the expressions for ΔB_i would be quite the same as for the class m3m of higher symmetry. So one can apply the existing theory in YAG crystals for the analysis of the thermal effects in barium nitrate crystal.

6. References

1. A.S.Eryomenko, S.N. Karpukhin, A.I. Stepanov., Stimulated Raman Scattering of the Neodymium Laser Second Harmonic in Nitrate Crystals., *Kvant. Elektron.*, (Moscow) v.7, p. 196-197 (in Russian), 1980.
2. S.N. Karpukhin, V.E.Yashin., Stimulated Emission and Amplification of Radiation Under SRS in Crystals., *Kvant. Elektron.(Moscow)* v.11, 1984, p.19982, (1984),[Sov. j. Quantum Electron. v14, 1337(1984)].
3. S.N. Karpukhin, A.I. Stepanov., Stimulated Emission From the Cavity Under SRS in $\text{Ba}(\text{NO}_3)_2$, NaNO_3 and CaCO_3 Crystals., *Kvant. Elektron.(Moscow)* v.13, 1572(1986) [Sov. J. Quantum Electron. v. 16,1027(1986)].
4. V.A. Berenberg,, S.N. Karpukhin, I.V. Mochalov, Stimulated Raman Scattering of Nanosecond Pulses in $\text{KGd}(\text{WO}_4)_2$ Crystals., *Kvant. Elektron. (Moscow)*, v. 14, №9, 1987.
5. C. He, T. H. Chyba, Solid-state barium nitrate Raman laser in visible region. *Optics Communications*, v.135, p. 273-278, 1997.
6. S.N.Karpukhin, A.A.Nikitichev. Close IR range of spectrum radiation via SRS in barium nitrate. *Proceedings of All-Union Conference Laser Optics'90*, Leningrad, p. 311, 1990 (in Russian).
7. V.N.Voitsekhovskii, S.N. Karpukhin, V.E. Yacobson, Single-cristal barium nitrate and sodium nitrate as efficient materials for laser-radiation frequency based on stimulated Raman scattering, *J.Opt.Technol.*, v.62 (11), p.770-776, 1995.
8. J.T. Murray, R.C. Powell, N.Peyghambarian, D.Smith, W.Austin, R.A.Stolzenberger., Generation of 1,5- μm radiation through intracavity solid-state Raman shifting in $\text{Ba}(\text{NO}_3)_2$ nonlinear crystals., *Optics Letters*, , v.20, No.9, p.1017-1019, 1995.
9. S. A. Vitsinskii, V.K. Isakov, S.N. Karpukhin, I.L. Lovchii, Stimulated Raman scattering of copper-vapor laser radiation in a barium nitrate crystal., *Kvant. Elektron. (Moscow)* v.20, p.1155, 1993. [Sov. j. Quantum Electron.v.23, p.1001, 1993].
- 10.V.I.Bespalov, A.A.Betin, G. A. Pasmanik, Reproduction of a pump wave in stimulated scattering radiation. *Proseedings of higher educational institutions, Radiophysc*, v.21, No.7, p.961-980, 1978 (in Russian).
- 11.V.I.Bespalov, G. A. Pasmanik. *Nonlinear optics and adaptive laser systems*, Moscow, Nauka publishers, 1986 (in Russian).
12. N. Bloembergen., *Nonlinear optics.*,W.A. Benjamin, Inc., NewYork –Amsterdam, 1965.
13. T.T. Basiev, W. Jia, H. Liu, P.G. Zverev, Raman Spectroscopic and Nonlinear Optical Properties of Barium Nitrate Crystal., *OSA TOPS on Advanced Solid-State Lasers.*,1996, v.1, p.554-559.
14. Y. A. Anan'ev. *Optical Resonators and Laser Beams*, Nauka Publishers, 1990 (in Russian).
15. Mezenov A.V., Soms L.N., Stepanov A.I. Thermal optics of solid-state lasers, *J. of Soviet Laser Research*, v.8, No.5, p.427-549, 1987.
16. J.F. Nye, *Physical Properties of crystals.*, Oxford at the Clarendon Press 1964.
17. Belevceva L.I., Voitsekhovsky V.N., Nazarova N.A., Romanova G.I., Shvedova M.V., Yakobson V.E. Basic properties of optical crystals of barium nitrate. *Optiko-mekhanicheskaya promyshlennost*, No.4, 1989 (in Russian).

Study of the single-mode beam amplification in a multimode pump field during SRS in a barium nitrate crystal

S. N. Karpukhin and V. A. Berenberg

Institute for Laser Physics, Research Center, "Vavilov State Optical Institute",
199034, St. Petersburg, Russia

ABSTRACT

The theoretical and experimental study of eye-safe single-mode beam SRS amplification in the barium nitrate crystal at $1.32 \mu\text{m}$ Nd:YAG laser pump field with wide angular spectrum was performed. It was ascertained that most effective method for improving of Stokes beam divergence lies in inclining of the pump beam.

Keywords: eye-safe radiation, SRS, amplification, barium nitrate, Stokes wave, Gauss-Hermit mode, beam divergence

1. INTRODUCTION

Theoretically and experimentally we have studied the SRS amplification of a single-mode beam in barium nitrate in a multimode Nd:YAG laser pump field when the angular divergence of a pump beam is more than by an order of magnitude larger than the diffraction divergence, but the known distortion-free gain criterion, which specifies the condition of effective averaging of inhomogeneities in the pump field¹, is invalid. This situation is typical when multy-mode solid-state laser radiation is used for pumping SRS amplifiers.

The using of multy-mode radiation for pumping represents the special interest when cross-section of induced transition in laser active medium is relatively low, because this introduces limitation upon the energy of single-mode radiation generation or increases the laser resonator dimension. We used $1.32 \mu\text{m}$ Nd:YAG laser radiation as a pump for SRS amplification in nitrate barium crystal. Such approach gives the possibility for realization of the completely solid-state source of the eye-safe radiation^{2,3,4}.

2. THE MODEL OF SRS AMPLIFIER

2.1. EQUATIONS AND RELATIONSHIPS

The numerical simulation of amplification of the Stokes wave with the primarily diffraction limited quality in the field of the wide angular spectrum laser beam was carried out in the stationary two dimensional approximation. It was done on the base of the following set of equations, which is widely used in the theory of SRS:

$$\begin{aligned} \left[\frac{\partial}{\partial z} - \frac{i}{2k_s} \frac{\partial^2}{\partial x^2} \right] E_s &= \frac{1}{2} g |E_L|^2 E_s, \\ \left[\frac{\partial}{\partial z} - \frac{i}{2k_L} \frac{\partial^2}{\partial x^2} \right] E_L &= -\frac{1}{2} g \frac{k_L}{k_s} |E_s|^2 E_L, \\ E_s|_{z=0} &= E_{s0}, \quad E_L|_{z=0} = E_{L0}, \end{aligned} \quad (1)$$

here E_L , E_s are the electric tensions of the pumping and Stokes waves, g is the gain of SRS, x and z are the transverse and the longitudinal coordinates.

It is well known⁵ that the set of equations (1) provides the quite adequate description of the Stokes wave amplification for the wide range of the SRS-active media parameters when the duration of the relaxation process is negligibly short. For the condensed media this duration is in the picosecond range⁶. That is why the stationary approximation is applicable for pulse with the nanosecond duration.

One can generalize the calculations by the use of the dimension-less parameters:

$$\frac{z}{L} \Rightarrow z, \quad \frac{x}{x_0} \Rightarrow x, \quad \frac{E_s}{\sqrt{I_0}} \Rightarrow E_s, \quad \frac{E_L}{\sqrt{I_0}} \Rightarrow E_L,$$

here L and $2x_0$ are the length and the width of the SRS-active medium. I_0 is the so-called normal intensity fluency. Thus the set of equations (1) is transformed into:

$$\left[\frac{\partial}{\partial z} - \frac{i}{4C_L} \frac{k_L}{k_s} \frac{\partial^2}{\partial x^2} \right] E_s = \frac{1}{2} G |E_L|^2 E_s, \quad (2)$$

$$\left[\frac{\partial}{\partial z} - \frac{i}{4C_L} \frac{\partial^2}{\partial x^2} \right] E_L = -\frac{1}{2} G \frac{k_L}{k_s} |E_s|^2 E_L,$$

here $G = gLI_0$, $C_L = k_L x_0^2/2L$ is the parameter, which characterizes the geometry of the amplifier (it is some analog of the Fresnel number). One can use various methods for establishment of the relationship between the dimension values of the Stokes and pumping beam intensities at the amplifier input, on the one hand, and the value of the normal intensity I_0 , on the other hand. In the experiment it is most simple to measure the Stokes and pumping beam intensities, integrated across the beam section. Hence it is reasonable to use the following equations to establish the said relationship between the dimension and dimension-less values:

$$\int_{-1}^1 |E_{LO}|^2 dx = 1, \quad \int_{-1}^1 |E_{SO}|^2 dx = q, \quad (3)$$

here q is the coefficient, which determines the relationship between the Stokes beam power P_{SO} and the pumping beam power P_{LO} at the amplifier input ($q = P_{SO}/P_{LO}$).

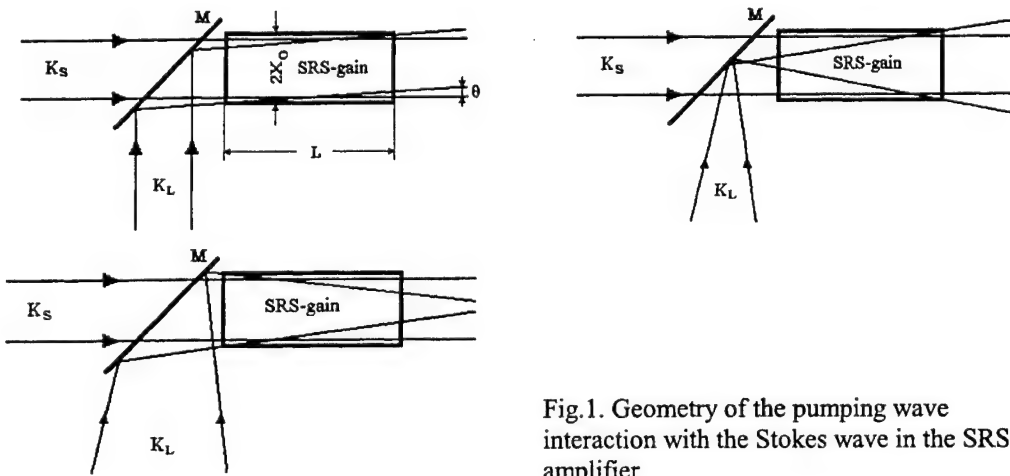


Fig.1. Geometry of the pumping wave interaction with the Stokes wave in the SRS-amplifier

On the Fig.1 shown the various configurations and positions of the pumping beam with respect to the Stokes beam we studied, in particular, with focusing of the pumping radiation and without and when the pumping wave is tilted with respect to the Stokes wave in some angle θ .

In the calculations the Stokes wave E_{SO} was described by the real hyper-Gauss function, and the pumping wave E_{LO} was described by the superposition of the finite number N_H of the Gauss-Hermit modes, whose random phases and amplitudes are distributed according to the definite law. Such a description of E_{SO} and E_{LO} is quite adequate to the experimental situation, because it describes the diffraction-limited beams and the beams with the wide angular spectrum, generated in the solid-state laser with the stable cavity⁷. Hence, E_{SO} and E_{LO} look like:

$$E_{SO} = \left[q \frac{x_0}{r_s} \frac{m 2^{1/2m}}{\Gamma(1/2m)} \right]^{\frac{1}{2}} \exp \left[- \left(\frac{x_0}{r_s} x \right)^{2m} \right], \quad (4)$$

$$E_{LO} = \exp \left[i \left\{ C_R (x - h)^2 - k_L x_0 \theta x \right\} \sum_{n=0}^{N_H} a_n \exp(i\phi_n) \Psi_n \left[\frac{x_0}{r_L} (x - h) \right] \right],$$

here $\Gamma(y)$ is the Gamma-function, m is the integer value, which describes the shape of the hyper-Gauss function, θ is the angle between the Stokes and the pumping beams, $h = L\theta/2x_0$, $C_R = k_L x_0^2/2R$, R is the curvature radius of the wavefront, a_n are the real amplitudes, which are proportional to the function $\exp[-\gamma(n-n_m)^2]$, n_m is the number of the mode with the largest amplitude, $\gamma > 0$ is the parameter, which determines the variation of the amplitudes a_n , ϕ_n are the random phases,

which are uniformly distributed across the range $[0, 2\pi]$, r_s and r_L are the characteristic sizes (see further), and Ψ_n are the normal Gauss-Hermit modes, described by the formula:

$$\Psi_n\left(\frac{x_0}{r_L}x\right) = \left[\frac{2x_0^2}{\pi r_L^2}\right]^{\frac{1}{2}} (2^n n!)^{-\frac{1}{2}} H_n\left(\sqrt{2}\frac{x_0}{r_L}x\right) \exp\left[-\left(\frac{x_0}{r_L}x\right)^2\right],$$

here H_n are Hermit polynomials: $H_n(x) = 2xH_{n-1}(x) - 2(n-1)H_{n-2}(x)$, $H_0 = 1$, $H_1 = 2x$.

One can see from the formula (4) that in the case, when the pumping beam is tilted with respect to the Stokes beam or when it is focused ($\theta, 1/R \neq 0$), the pumping field distribution contains the terms, which reveal strong oscillations. One can see that in the cases of practical interest the number of oscillations across the range $x \in [-1, 1]$ can be as high as several hundreds. These oscillations to a large extent tantalize the numerical solution of the set of equations (2). That is why it is reasonable to describe the field $E_L(x, z)$ as a product of the slowly oscillating function $U_L(x, z)$ and of the fast oscillating function:

$$E_L(x, z) = U_L(x, z) \exp[iF_L(x, z)]. \quad (5)$$

According to the estimations, one can replace the function $F_L(x, z)$ by some phase factor, which is one and the same for all the Gauss-Hermit modes. It is produced while the free-space propagation of the pumping beam E_{LO} . On the base of the Huygens-Fresnel principle and of the well-known relationships for the Hermit polynomials⁸ one can outline the following relationship for the function $F_L(x, z)$:

$$F_L(x, z) = C_L[\alpha(x + 2hz - h)^2 - 4h(x + hz)] \quad (6)$$

here $\alpha = \frac{z + C_R(zC_R + C_L)(r_L/x_0)^4}{z^2 + (zC_R + C_L)^2(r_L/x_0)^4}$.

With the help of the relationships (5) and (6) one can transform the set of equations (2) to:

$$\left[\frac{\partial}{\partial z} - \frac{i}{4C_L} \frac{k_L}{k_s} \frac{\partial^2}{\partial x^2} \right] E_s = \frac{1}{2} G |U_L|^2 E_s, \\ \left[\frac{\partial}{\partial z} - \{2h - \alpha(x + 2hz - h)\} \frac{\partial}{\partial x} - \frac{i}{4C_L} \frac{\partial^2}{\partial x^2} \right] U_L = - \left[\frac{1}{2} G \frac{k_L}{k_s} |E_s|^2 + \frac{\alpha}{2} - iC_L(\alpha^2 - \beta)(x + 2hz - h)^2 \right] U_L,$$

here $\beta = \frac{1 + C_R^2(r_L/x_0)^4}{z^2 + (zC_R + C_L)^2(r_L/x_0)^4}$.

The characteristic dimensions r_s and r_L were determined from a requirement of the small amplitude of the fields at $x = \pm 1$. According to evaluations, the field of a Stokes and pump waves can be neglected outside of an interval $|x| > 1$, if at $x = \pm 1$ the amplitudes of fields does not exceed 10^{-3} from the peak value. In accordance with this requirement for an evaluation of typical dimensions the relations submitted in the table 1 are received.

Table 1

x_0/r_s	$[3\ln 10]^{1/2m}, C_L \gg 1$		
$1/R$	0	>0	<0
x_0/r_L	$[d - \{d^2 - C_L\}^{1/2}]^{1/2}$	$\rho C_L [2d]^{-1/2}$	$C_L [2d]^{-1/2}$

were $\rho > 1$ – coefficient determining the degree of compression or of extension of the field at its focusing ($R > 0$) or defocusing ($R < 0$) in the medium, d – parameter, equaled $C_L^2(1-h)^2/6\ln 10$, when $N_H = 0$, and $\frac{1}{2} [C_L(1-h)/(0.863\sqrt{N_H} + 2.087)]^{\frac{1}{2}}$, when $N_H > 0$.

Setting values of parameter ρ , the focal length of a lens can be calculated from the following relations:

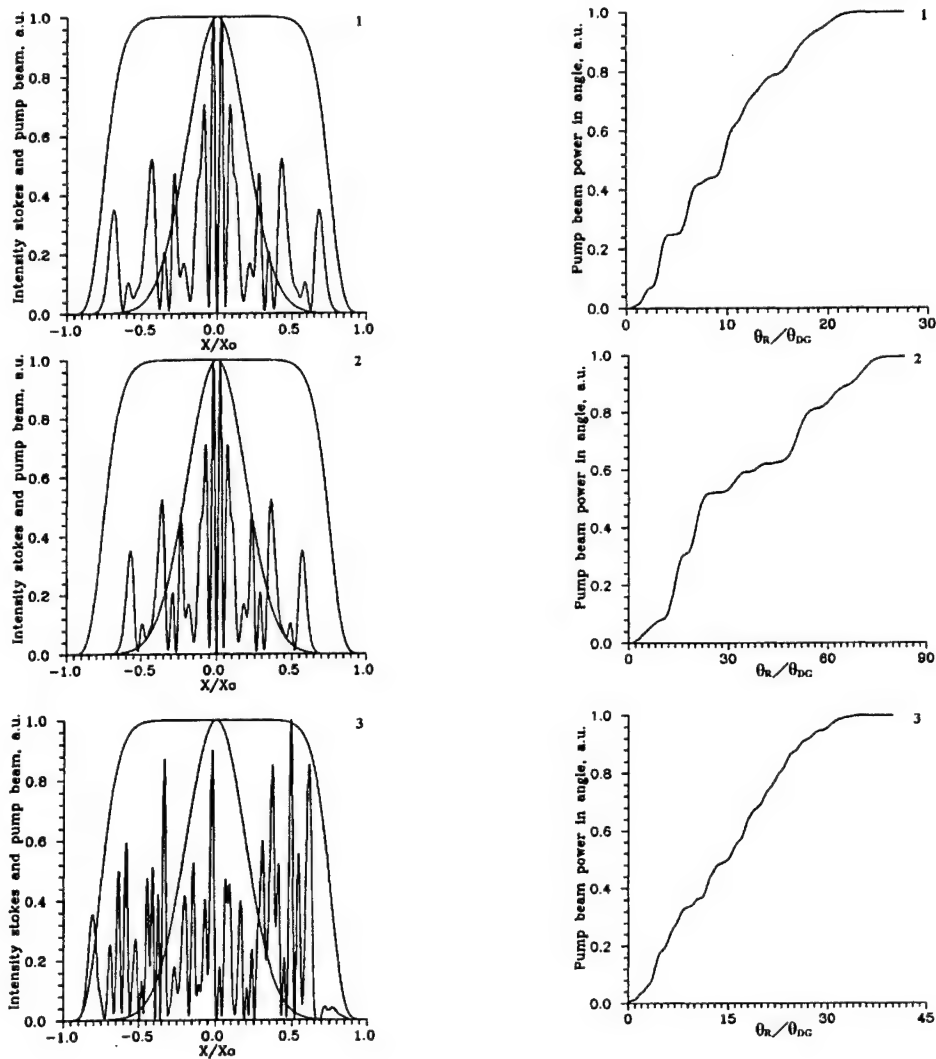
$$C_R = -C_L + \sqrt{\rho^2 C_L^2 - x_0^4/r_L^4}, \quad (R > 0), \\ C_R = -C_L + \sqrt{C_L^2/\rho^2 - x_0^4/r_L^4}, \quad (R < 0).$$

2.2. RESULTS OF CALCULATIONS AND DISCUSSION.

The goal of the calculations was to determine the influence of the pumping wave field structure onto the spatial structure of the Stokes wave, and, in particular, onto its angular divergence and direction. With this purpose we have varied

across the wide range the amplitude and the phase distribution of the pumping wave at the input of the amplifier, of the SRS gain, and of the relationship between the intensities of the Stokes and the pumping waves for various geometry of their interaction in the SRS-active medium. Our situations differs from that in the paper⁹. In the said paper there was numerically simulated the experiment with the severely aberrated XeCl eximer laser radiation and its SRS in hydrogen. Usually the angular divergence of the solid-state laser radiation, used for the pumping purposes, equals from about one to several dozens of the diffraction limits. That is why it was very interesting to investigate the dependence of the spatial distribution of the amplified Stokes beam upon the pumping beam quality without application of any special means of the forced control over the spatial coherence of this radiation (produced, for instance, by the aberrant) used in reference⁹.

Results of numerical simulation are illustrated by the following figures. In the Fig.2 is shown for an example four variants of the primary distributions of the pumping beam intensity in the transverse direction and of the corresponding angular divergences. In the first and in the second variants the pumping beam consisted of odd Gauss-Hermit modes ($N_H = 29$). In the second variant the beam was also focused (the value of the parameter $\rho = 1.2$). In the variants 3 and 4 the pumping beam consisted of both odd and even modes ($N_H = 50 \text{ u } 8$). The angular distributions are presented as the functions of the current angle θ_R ratio to the angle θ_{DG} , which contains 80% of the diffraction-limited Gauss beam. Its amplitude at $x = \pm 1$ equals 10^{-3} of the maximal value. One can see in the same figure the distributions of the Stokes beam intensity, described by the hyper-Gauss function at $m = 1$ and 5.



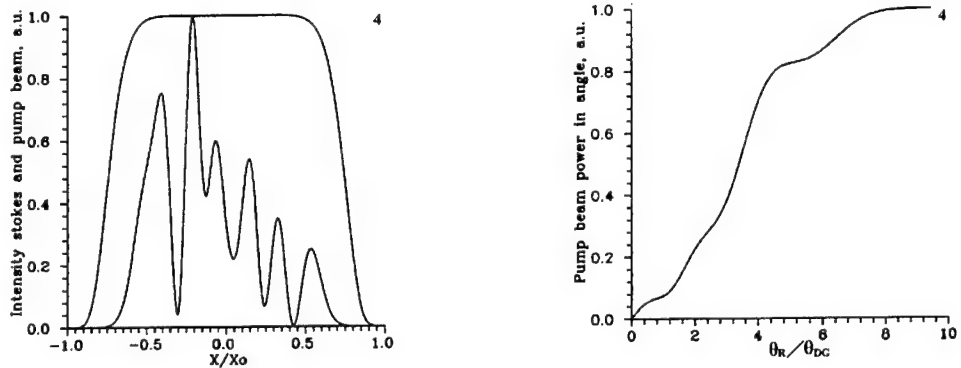


Fig.2. Primary intensities of the Stokes beam and of the pumping beam in the transverse section of the amplifier and the angular distribution of the pumping beam power: $\theta_{LO}/\theta_{DG} = 15.43$ (1), 54.35 (2), 22.64 (3) and 4.55 (4).

In the Fig.3 are shown the results of studying of the dependence of the amplified Stokes beam divergence θ_S (θ_S is the angle, containing 80% of the power of the amplified Stokes beam) vs. the angle θ . The curves 1, 2 and 4 correspond to the variant 1 ($\theta_{LO}/\theta_{DG} = 15.43$), the curve 3 corresponds to the variant 2 ($\theta_{LO}/\theta_{DG} = 54.35$, $R > 0$, the diverging pumping beam), the curve 5 - to the variant 3 ($\theta_{LO}/\theta_{DG} = 22.64$) of the primary distributions of the pumping beam field. Other conventions are described in the caption for the Fig.3. The calculations were carried out for $C_L = 1000$, $q = 0.01$, $k_L/k_S = 1.1$ and variation of h from 0 to 0.1.

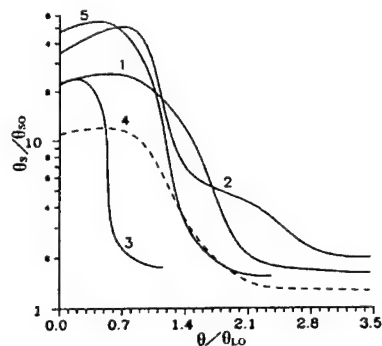
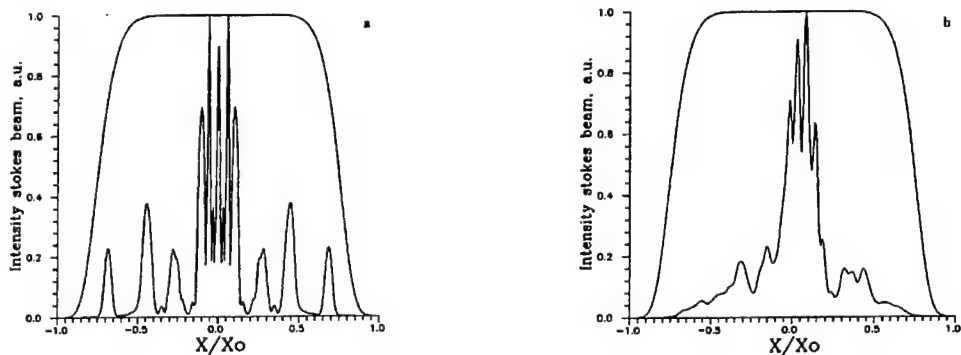


Fig.3. Variation of the angular divergence of the amplified Stokes beam with the pumping beam tilting: $G = 4$ (2) and 6 (1, 3, 4, 5), $m = 1$ (4) and 5 (1, 2, 3, 5).

In the Fig.4-6 are shown the distributions of the intensity, phase and angular distributions of the amplified Stokes beam for $h = 0$ and 0.1, corresponding to the curves 1-5 (Fig.3).



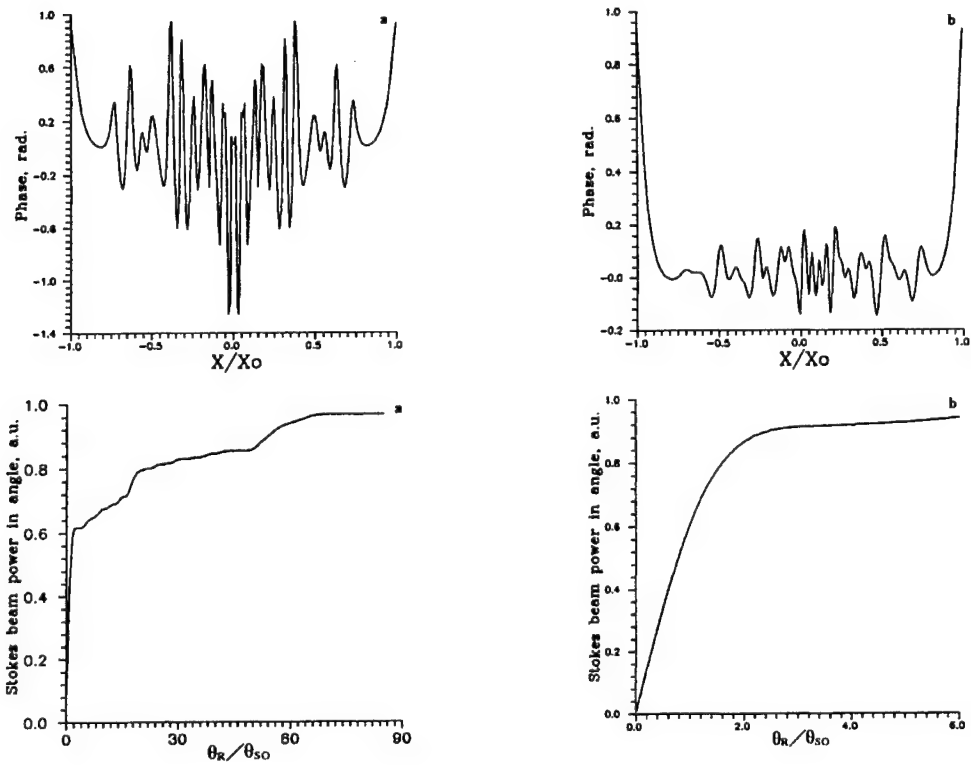
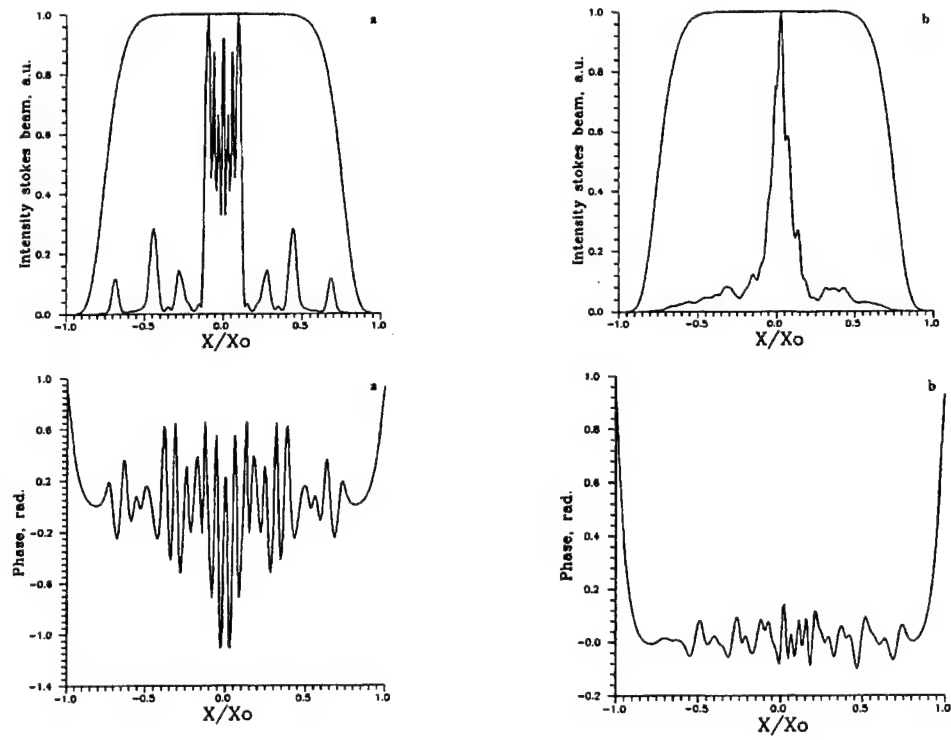


Fig.4. Distributions of the intensity, phase and angular distribution of the amplified Stokes beam, corresponding to the curve 1 of Fig.3 for $\theta/\theta_{LO} = 0$ (a) and 3.46 (b).



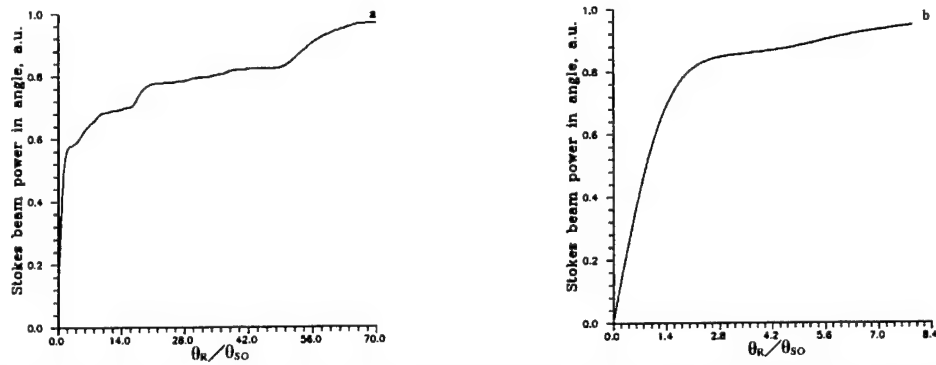


Fig.5. Distributions of the intensity, phase and angular distribution of the amplified Stokes beam, corresponding to the curve 2 of Fig.3 for $\theta/\theta_{LO} = 0$ (a) and 3.46 (b).

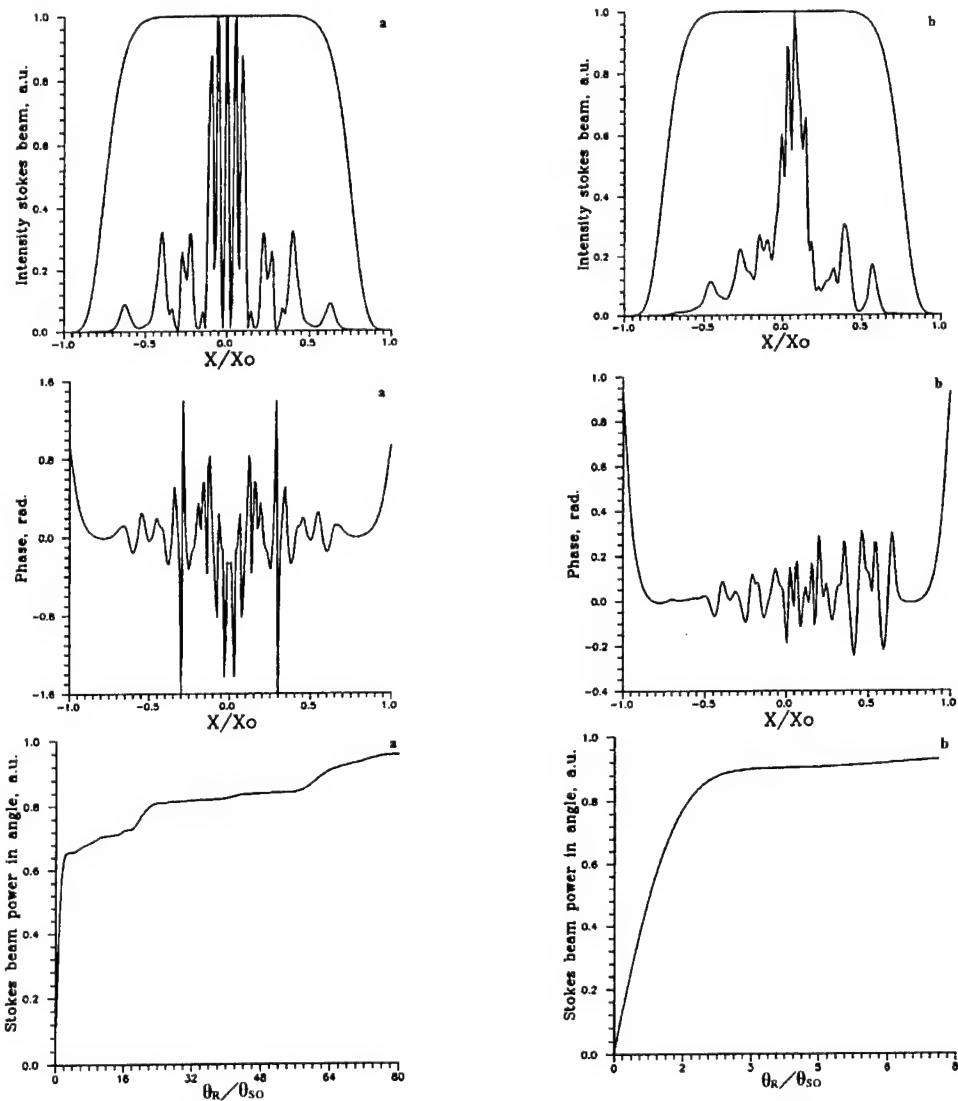


Fig.6. Distributions of the intensity, phase and angular distribution of the amplified Stokes beam, corresponding to the curve 3 of Fig.2.3 for $\theta/\theta_{LO} = 0$ (a) and 1.15 (b).

The presented data obviously evidence that the amplified Stokes beam spatial structure varies in a similar way for a wide range of the amplifier and pumping beam parameters. One can see from the given curves that when $\theta = 0$ even for the pumping beam divergence of several dozens of diffraction limits 50-60% of the Stokes radiation power at the amplifier output P_S contains in 1.5-3 diffraction limited angles. Pumping beam tilt results first of all in dumping of the wings in the angular distribution of the Stokes radiation. Such an evolution of the Stokes beam divergence quite corresponds to the theory of the parametric mechanism of generation of the Stokes radiation with the wide angular spectrum¹⁰. For the higher divergence of the pumping beam, equal to $(10-20)\theta_{DG}$, the divergence of the amplified Stokes beam is close to the diffraction limit already for $\theta \approx (1-3)\theta_{LO}$.

We have made two series of calculations so as to reveal the influence of the geometric size of the amplifier (parameter C_L) and by focusing the pumping radiation onto the Stokes beam spatial structure. In the first series the parameter C_L was varied at $h = 0$, $\rho = 1$ and $C_R = 0$. In the second series we have varied the parameter ρ for $h = 0$ and for $C_L = \text{const}$. Pumping radiation was focused both to the plane $z = 0$ and to the plane $z = 1$. The curves in the Fig.7 illustrate the character of the Stokes radiation divergence variation with the variation of the parameter C_L . The calculations were carried out for variation of C_L from 135 to 1000 and for the primary pumping beam, corresponding to the variant 3 in the Fig.3.

For the pumping beam focusing case the Stokes beam divergence reveals the same character of variation. Noteworthy, that the angular divergence of the converging beam is better than that of the diverging. Probably, this feature can be explained by the difference in the value of the local increment of SRS. Modification of the angular divergence of the Stokes beam with variation the pumping beam focusing is illustrated by the Fig.8. The calculations were carried out for $C_L = 1000$ and for the pumping beam, corresponding to the variant 3 in the Fig.3. The curve 1 was calculated for the diverging pumping beam ($R > 0$), while the curves 2-4 - for the converging beams ($R < 0$). The curves 1-3 were calculated for the Stokes beam, described by the hyper-Gauss function for $m=5$, while the curve 4 corresponds to the Gauss beam.

Worth mentioning that the angular divergence of the Stokes wave strongly depends not only upon the considered factors, but also upon the ratio of its starting power to that of the pump. In the Fig.9 is shown for example the dependence of the Stokes beam divergence vs. the ratio $q = P_{SO}/P_{LO}$. The calculations were carried out for $C_L = 1000$, $h = 0$ and $C_R = 0$. The curves 1 and 2 correspond to the variant 1 in the Fig.2-3, and the curve 3 - to the variant 3 of the pump. The curves 1 and 3 were calculated for the case of the Stokes beam, described by the hyper-Gauss function for $m=5$, and the curve 2 corresponds to the Gauss beam. In the same Figure are shown the dependencies of the power gain K ($K = P_S/P_{SO}$) of the Stokes beam and of the efficiency of the pumping radiation use determined according to the formula $\eta = q(P_S/P_{SO} - 1)$ vs. the parameter q for its variation from 0.001 to 1.

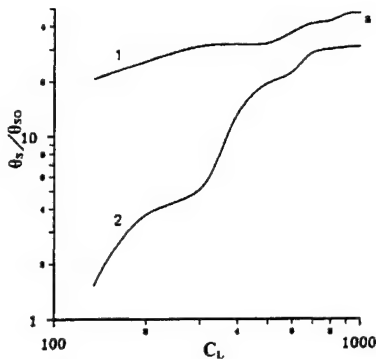


Fig.7. Variation of the Stokes beam divergence with the variation of the amplifier's geometry size for $G = 6$ (1) and 3 (2).

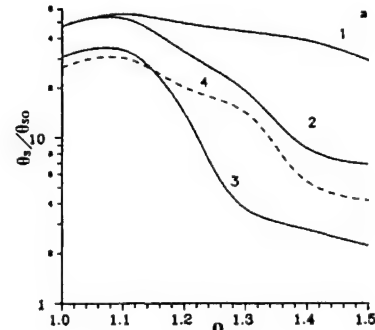


Fig.8 Variation of the amplified Stokes beam divergence with the pumping beam focusing for $G = 6$ (1, 2, 4) and 3 (3).

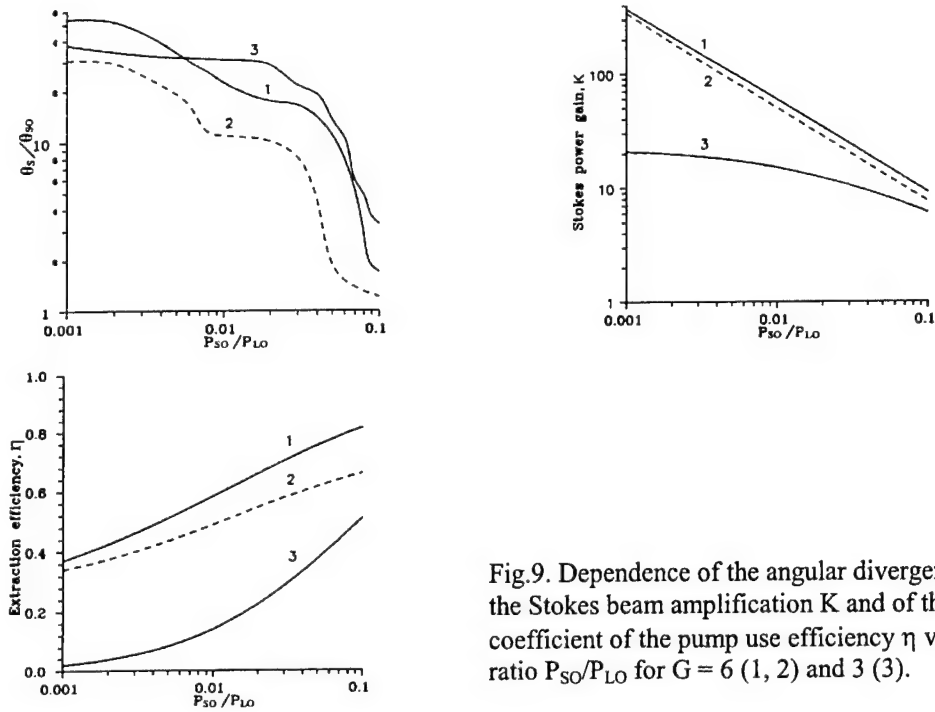


Fig.9. Dependence of the angular divergence, of the Stokes beam amplification K and of the coefficient of the pump use efficiency η vs. the ratio P_{SO}/P_{LO} for $G = 6$ (1, 2) and 3 (3).

We can summarize as follows the main results of the numerical studies of the diffraction limited Stokes beams in the field of pumping by the beams with the wide angular spectrum:

- In the case of the collinear propagation of the Stokes and pumping beam through the amplifier and of the angular divergence of the pumping beam of several dozen diffraction limits, only some 50...60% of the amplified Stokes radiation fills into the angle of $(1-2)\theta_{SO}$ (here θ_{SO} is the angle, containing 80% of the Stokes beam power at the amplifier input). All other power is emitted to the wide wings.
- In the case, when the divergence of the pumping beam equals several dozen of the diffraction limited angles, the Stokes beam divergence can be efficiently improved by means of tilting the pumping beam. If this tilt is equal to some 1-3 angles of the pumping beam divergence, the amplified Stokes beam reveals nearly diffraction limited divergence, and its intensity distribution is efficiently smoothed.

3. EXPERIMENTAL STUDY OF AMPLIFICATION

The experiment was carried out using a Nd:YAG laser emitting at a $1.319 \mu\text{m}$ wavelength. The laser pulse length was 30 ns. The half of the laser energy was sent by a beam splitter for the SRS-generator pumping, and the residual part was amplified in the laser amplifier and then used for the SRS amplifier pumping. SRS generation was realized with the use of the scheme of the pumping radiation into the volume of the cavity zero mode with the consequent selection by the remote diaphragm. We have studied the amplification in 6 cm length barium nitrate crystal in collinear and the quasi-collinear schemes. In the Fig.10 is shown the optical scheme, which was used for the amplifier studies.

The maximum energy of the amplifier pumping was equal to either 108 mJ (divergence of 12 diffraction limits, produced by the laser cavity with the plain mirrors) or 80 mJ (divergence 22 diffraction limits, produced by the cavity, where one of the mirrors was concave). For both divergences the diameter of the pumping beam in the crystal equaled 1.6 mm (the reason was approximately double difference of the beam diameters in the plane of the focusing lens). At the input of the SRS-amplifier crystal the energy of the Stokes beam with the near diffraction limited divergence was equal 9 mJ for lower pump divergence and 7 mJ for higher one. For the said parameters the maximal efficiency of the amplifier equaled 40% for lower pumping divergence. Similar to the calculations, the amplifier efficiency was determined as the ratio of the difference of the output and input Stokes signals to the energy of the wave, pumping the amplifier. Note that measured value was less than that obtained in Section 2.

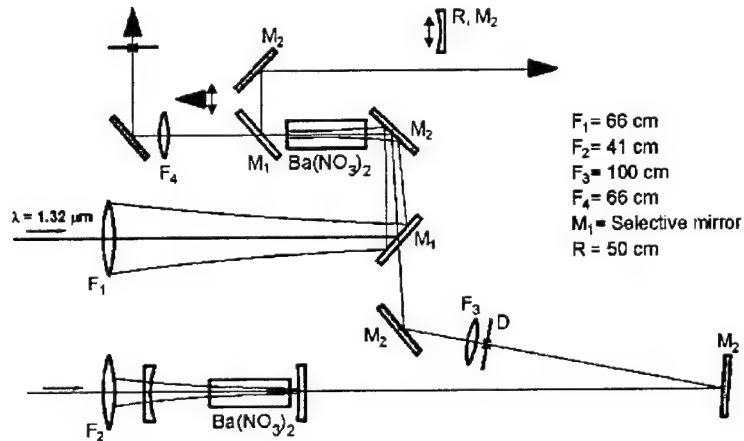


Fig. 10. Optical scheme used for the amplifier studies.

The reason is that there was simulated the stationary process without account for the temporal overlap of the pulses. The pulse shapes of a output signal and passed without conversion pump are shown in the Fig.11. The higher efficiency equaled 46% was observed in the two-pass pumping scheme, which was realized by means of relay of the pumping beam back to the crystal with the use of the spherical mirror (see the Fig.10). In the Fig.12 is shown the dependence of the amplifier efficiency in the collinear amplification geometry vs. the pumping energy and on Fig.14 the Stokes beam amplification K and of the coefficient of the pump use efficiency η . As seen from this figure the reveals the same character as in numerical calculations (see Fig.9).

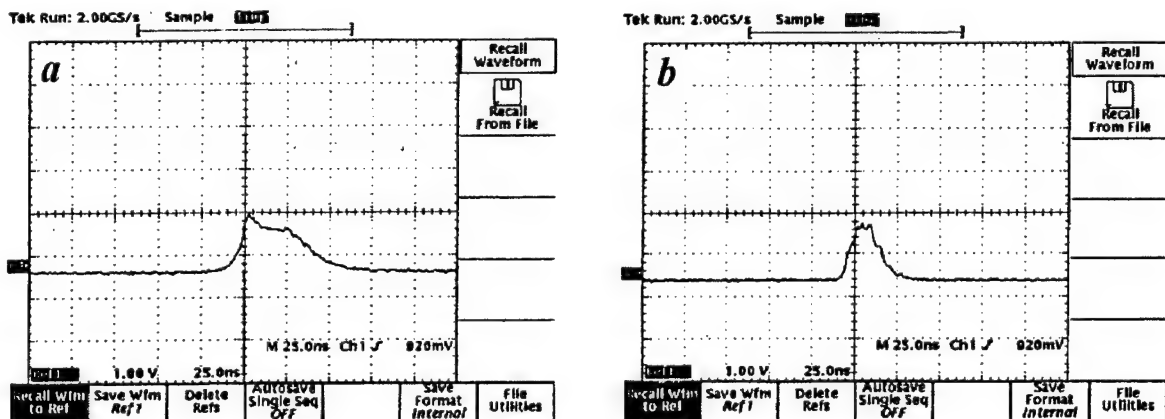


Fig.11. The pulse shapes of passed without conversion pump (a) and the output signal (b).

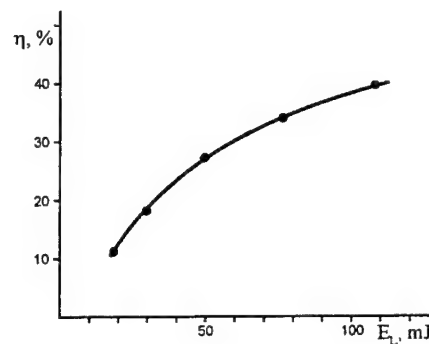


Fig.12. The dependence of the amplifier efficiency in the collinear amplification geometry vs. the pumping energy.

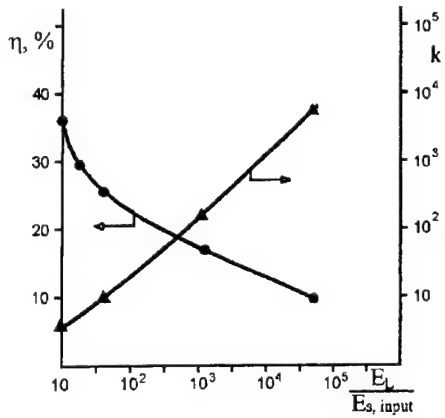


Fig.13. The dependencies for the collinear geometry of the gain and of the amplifier efficiency vs. ratio of the signal energy to the pump energy equaled 86 mJ.

In the Fig. 14 and 15 are shown the results of measuring of the divergence in the collinear and quasi-collinear schemes for the various values of the gain and of the pump divergence as well as for the different values of input signal values. In the quasi-collinear mode of interaction beams crossed in the center of the crystal at the angle equaled $2\theta_L$ (here θ_L - pump divergence in the crystal). One can see from the Fig.14 that in the case of the collinear geometry of interaction the spatial structure of radiation contains the nearly diffraction limited core and the wide wings. Just in agreement with the calculations the increase of the pump divergence from 12 to 22 diffraction limits is not accompanied by variation of the amplified signal divergence. The reduce of the input signal energy under the constant pumping results in the reduce of the relative energy of the core, accompanied by the minor reduce of the energy, going to the maximal angle (due to the crossing of the curves 2 and 3 in the Fig.14); its shape becomes closer to the shape of the pump divergence contour.

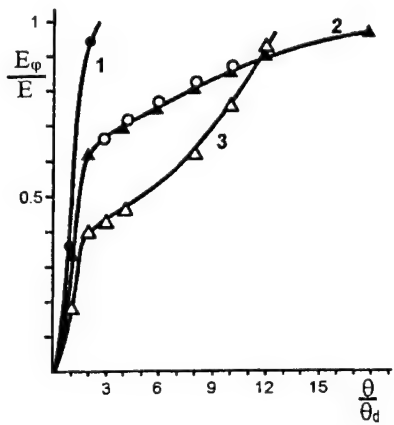


Fig.14. The divergence of Stokes beams for the collinear amplification scheme.

1-input Stokes beam;
2- $\theta_L/\theta_D = 12$, $E_{S,\text{input}} = 9$ mJ, $E_L = 86$ mJ (\blacktriangle);
3- $\theta_L/\theta_D = 22$, $E_{S,\text{input}} = 7$ mJ, $E_L = 80$ mJ (\circ)

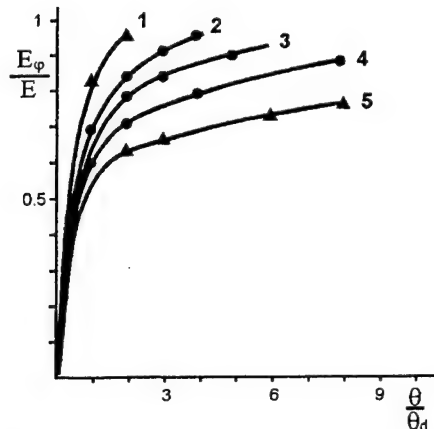


Fig.15. The divergence of Stokes beams for the quasi-collinear amplification scheme with the angle in the crystal between Stokes beam and pumping beam $\theta = 2\theta_L$ ($\theta_L/\theta_D = 12$) and for the collinear amplification scheme ($\theta = 0$) with the same θ_L ,
1- input Stokes beam; 2,3 - $\theta = 2\theta_L$, 4,5 - $\theta = 0$; signal amplification $K=2$ (2,4) and 2,7-(3,5).

This is an evidence of the absence of the core while amplification of the weak signal, while the signal divergence becomes equal to that of the pump. Hence for weak signal the amplification is carried out in the mode of the wavefront reproduction. For the equal gain (increment), the quasi-collinear amplification scheme reveals much smaller part of the energy, going to the wings, than it takes place in the collinear scheme (see curves 2 and 4, 3 and 5 in the Fig.14 which represent equaled amplification).

The important practical conclusion is that it is reasonable to use the quasi-collinear amplification geometry so as to improve the output divergence. The use of this method results, of course, in the reduction of the amplifier efficiency for the same pumping energy. The practical scheme, shown in the Fig.16¹⁰, probably will improve the amplifier performance, because it provides for the averaging during the amplification and for the spatial overlapping of the interacting beams (one has to prevent, of course, the self-excitation of the amplifier).

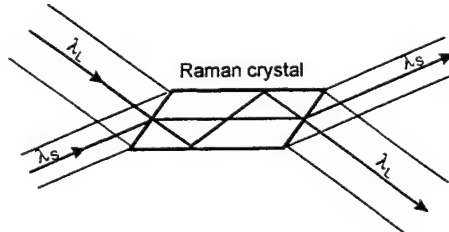


Fig. 16. Scheme for amplification

All the described results qualitatively confirm the conclusions, drawn out from the numerical simulation. Let us once again enumerate the conclusions, which are confirmed by both theory and experiment:

1. Presence of the diffraction-limited core and of the wide wings in the single mode beam, amplified in the multi-mode pumping field.
2. Increase of the relative energy in the core with the growth of the input signal energy under the constant pumping level.
3. Significant reduce of the relative energy of the wings in the case of the quasi-collinear pumping when the angle exceeds in 1.3 times the divergence of the pump.

4. MAIN RESULT

We have theoretically and experimentally established the following. For the collinear amplification of the single-mode beam in the field of the multi-mode pump with the divergence of 10-20 diffraction limits and for the energy of the input signal of ~ 0.1 of the saturated pump energy, the structure of the amplified radiation contains the nearly diffraction-limited core, which contains approximately one half of the total energy, and the wide wings. Tilt of the pumping beam in the angle, exceeding its divergence, results in significant improvement of the amplified signal divergence. So, presented results will be useful for the development of Raman crystal amplifiers in the eye-safe spectral range.

REFERENCES

1. V.I.Bespalov, A.A.Betin, G.A. Pasmanik , Reproduction of a pump wave in stimulated scattering radiation. Proceedings of higher educational institutions, Radiophysc, Vol. 21, No. 7, pp. 961-980, 1978 (in Russian).
2. S.N.Karpukhin, A.A.Nikitichev. Close IR range of spectrum radiation via SRS in barium nitrate. Proceedings of All-Union Conference Laser Optics'90, Leningrad, p. 311, 1990 (in Russian).
3. V.N.Voitsekhovskii, S.N. Karpukhin, V.E. Yacobson. Single-cristal barium nitrate and sodium nitrate as efficient materials for laser-radiation frequency based on stimulated Raman scattering, J. Opt. Technol., Vol. 62, pp. 770-776, 1995.
4. J.T. Murray, R.C. Powell, N.Peyghambarian, D.Smith, W.Austin, R.A.Stolzenberger., Generation of 1,5- μ m radiation through intracavity solid-state Raman shifting in Ba(NO₃)₂ nonlinear crystals., Optics Letters, Vol.20, No. 9, pp. 1017-1019, 1995.
5. Yu. E. D'yakov, S.Yu. Nikitin., SRS of the Laser Radiation with a Wide Angular Spectrum, Kvant. Elektron.(Moscow),Vol. 14, No. 10, p. 1925-1957, 1987 [Sov. J. Quantum Electron. Vol. 17, pp. 1227-1247, (1987)].
6. Y. R. Shen, The principles of nonlinear optics, John Wiley & Sons., 1984.
7. A.V. Mezenov, L.N. Soms, A.I. Stepanov Thermal optics of solid-state lasers, J. of Soviet Laser Research, Vol. 8, No. 5, pp. 427-549., 1987.
8. N.Ya.Vilenkin. Special functions and the theory of group presentation. Moscow, Nauka, 1965 (in Russian).
9. Robert S.F. Chang, Robert H. Lenmberg, Michael T. Duignan, N. Djeu., Raman Beam Cleanup of a Severely Aberrated Pump Laser., IEEE J. Quantum Electron., Vol. QE-21, No. 5, pp. 477-487, 1985.
10. J. Goldhar, J. R. Murray. Intensity Averaging and Four-Wave Mixing in Raman Amplifiers. IEEE J. Quantum Electron., Vol. QE-18, No. 3, pp. 399-409, 1982.

Family of highly efficient erbium-doped phosphate glasses

A.A.Izyneev, P.I.Sadovski

Branch of the Institute of Radio Engineering and Electronics, Russian Academy of Sciences,
pl. ak.Vvedenskogo 1, Fryazino, Moscow province, 141120, Russia

ABSTRACT

An investigation was made of several relationships governing excitation transfer in Cr-Yb-Er phosphate glasses. The activator concentrations were optimized. A family of the new erbium-doped laser glasses was developed.

Keywords: erbium glass, erbium laser, "eye -safe" wavelength, pulse rangefinders, medical devices, erbium laser rod.

1. INTRODUCTION

The first report on progress in phosphate erbium glass, coactivated by Cr³⁺ ions, which proved to have comparable output characteristics (threshold and efficiency) with neodymium glasses, appeared in 1982¹. But only recently designers have begun to apply erbium glass in laser devices. This active material became favourite at development of new medical devices and pulse rangefinders, due to its capability for emission of radiation at the "eye -safe" wavelength (1,54 microns).

All following years intensive investigations were proceeding along the following directions: improvements in the glass matrix and optimization of the activator concentrations^{2,3}, search for efficient materials to be used as passive switches at the 1.54 μm wavelength⁴, and replacement of traditional pump sources (xenon flash lamps) with selective sources (semiconductor lasers)^{4,5}.

In spite of considerable recent progress in the development of pulsed semiconductor pump sources, emitting in the spectral range of the absorption bands of ytterbium ions (900-1000 nm), preference in commercial erbium-glass devices is given to miniature flash lamps with a discharge gap 25 - 35 mm because of their high reliability and low cost, and also because of the simplicity of design of such systems.

2. OPTIMIZATIONS

2.1. Spectral properties of the chromium ions

One of the most important parameters, which has a decisive influence on the efficiency of Cr - Yb - Er laser glasses, is the rate of back transfer of energy in the Cr - Yb ion pair. As demonstrated by us earlier, this rate depends strongly on the composition of the glass and on the conditions during its fabrication. It was established for the first time in Ref.⁶ that a phosphate glass contains not only Cr³⁺ but also Cr²⁺ ions. The latter ones are the main agents quenching the luminescence of ytterbium ions and they give rise to additional inactive losses in the wavelength range 0.9-1.5 μm . Depending on the composition of a glass and on the conditions during its fabrication, the Cr²⁺ content ranged from 0.1 to 20% of the total amount of chromium. The Cr²⁺ concentration in the LGS-Kh -series glass could be minimized in order to reduce significantly the rate of the back-transfer process and positive role of the chromium ions to the sensitization of the erbium luminescence was observed up to extremely high chromium ion concentrations, amounting to $(7\text{-}8) \times 10^{19} \text{ cm}^{-3}$ in contrast to KGSS-0135/153 glass² and QX/ER⁷ where the positive effect of sensitization is reduced starting from Cr³⁺ concentration equal to $1 \times 10^{19} \text{ cm}^{-3}$. The results of detailed investigations of chromium behaviour in phosphate glass will be published in our paper¹⁰.

E-mail: aai219@ire216.msk.su; WWW: http://193.232.21.26/fire_pages/lab219/default.htm; Tel.: +7 (095) 526 9277;
Fax: +7 (095) 203 8414.

2.2 Optimization of the Yb³⁺ concentration

An increase in the Yb³⁺ concentration is desirable for two reasons. When the ytterbium ion concentration is raised up to $N_{Yb} = 2,5 \times 10^{21} \text{ cm}^{-3}$ the rate of transfer of the excitation energy in the Yb-Er pair increases⁸ and so the absorbed pump energy does. In our case, there was no danger that an increase in the ytterbium concentration would give rise to nonuniform pumping of the active element across its diameter, because this diameter was small (2-4 mm).

We investigated⁸ the dependence of the rate of the back transfer of energy on the Cr-Yb pair on ytterbium ion concentration and found that the rate of the back-transfer process in the Cr-Yb pair increased with the ytterbium ion concentration, but the increase declined from linear dependence throughout the investigated range of the ytterbium ion concentration, $(0.4-2.3) \times 10^{21} \text{ cm}^{-3}$. So, increase of ytterbium ion concentration up to $3 \times 10^{21} \text{ cm}^{-3}$ is possible.

2.3. Dependence of the back-transfer rate in the Cr - Yb pair on the temperature

The rate of the back transfer of energy in the Cr-Yb pair depends on the temperature of the ambient medium and this reduces the energy parameters of the Cr-Yb-Er glass lasers operating in the pulse-periodic regime. The temperature dependence of W_{Yb-Cr} was determined for samples with the ytterbium ion concentration $2,3 \times 10^{21} \text{ cm}^{-3}$ and with various chromium ion concentrations (fig.1).

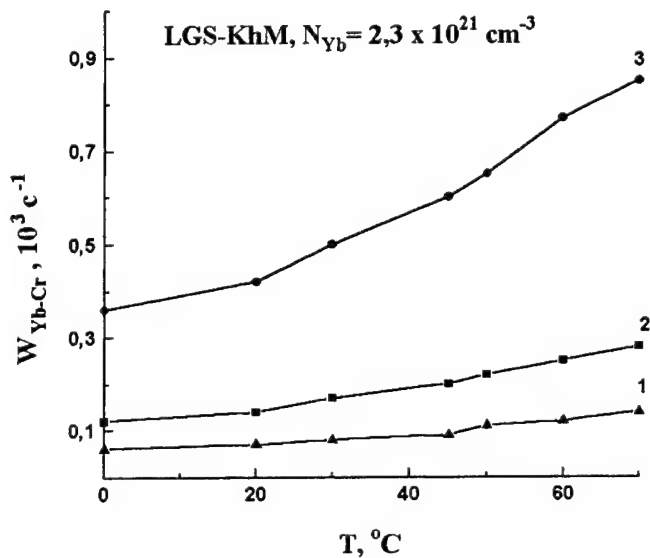


Fig.1. Back-transfer rate in the Cr-Yb pair vs temperature. $N_{Cr} = 1 \times 10^{19}$ (1), 2×10^{19} (2) and $6 \times 10^{19} \text{ cm}^{-3}$ (3).

So, an increase in the back-transfer rate in the Cr-Yb pair with increase in temperature was the only factor which restricted the chromium ion concentration in glass LGS-KhM to be used in repetition-rate lasers.

2.4. Selection of the erbium ion concentration

Selection of the erbium ion concentration is a very important task. The results of calculation of working volume of rod, necessary for storage of 20 mJ output energy in Q-sw mode (FTIR) and maximum efficiency are shown in fig.2. One can see from fig. 2, that the efficiency grows with increase of concentration of erbium ions, and working volume of needed rod decreases from $0,29 \text{ cm}^{-3}$ for $N_{Er} = 1 \times 10^{19} \text{ cm}^{-3}$ up to $0,105 \text{ cm}^{-3}$ for $N_{Er} = 1,65 \times 10^{19} \text{ cm}^{-3}$. If to take into account the experimental result, that maintenance of necessary pumping energy needs a lamp with a discharge interval of 35 mm, it is

necessary to choose a rod diameter 3,2 mm for $N_{Er} = 1 \times 10^{19} \text{ cm}^{-3}$, 2,5 mm for $N_{Er} = 1,2 \times 10^{19} \text{ cm}^{-3}$ and 1,9 for $N_{Er} = 1,65 \times 10^{19} \text{ cm}^{-3}$.

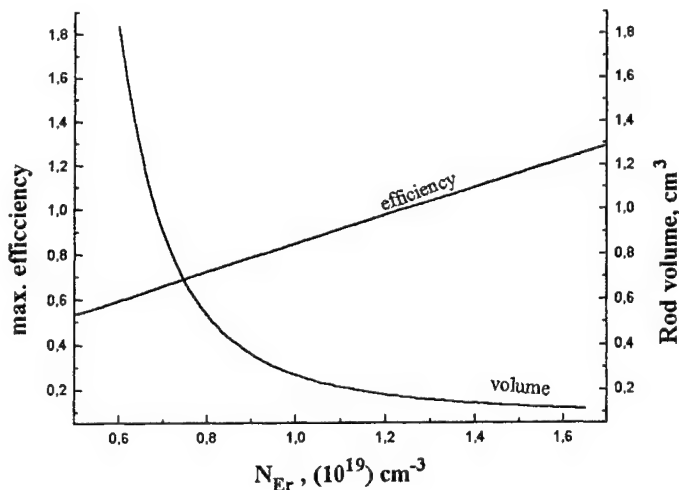


Fig.2. The dependence of max. efficiency of storage energy, normalized on $N_{Er} = 1,2 \times 10^{19} \text{ cm}^{-3}$, and volume of rod needed for 20 mJ output (Q-sw mode) vs N_{Er} .

3. RESULTS AND DISCUSSION

As a result of the investigations carried out we developed three commercial brands of glass.

3.1. LGS-KhM -glass for uncooled lasers, operating in a mode with a single pulse and low repetition rate.

It has a low value of thermal expansion coefficient, high chemical resistance and excellent output parameters. The base chromium ions concentration in the new glass is $2.2 \times 10^{19} \text{ cm}^{-3}$. We also produced two modifications of this glass, differing from the base composition by the concentration of the Cr^{3+} ions: KhM/Cr0.9 ($N_{Cr} = 0.9 \times 10^{19} \text{ cm}^{-3}$) and KhM/Cr5.6 ($N_{Cr} = 5.6 \times 10^{19} \text{ cm}^{-3}$). Fig. 3 gives the energy characteristics of the active elements operating in free-running mode and also in the Q-switched single-pulse mode.

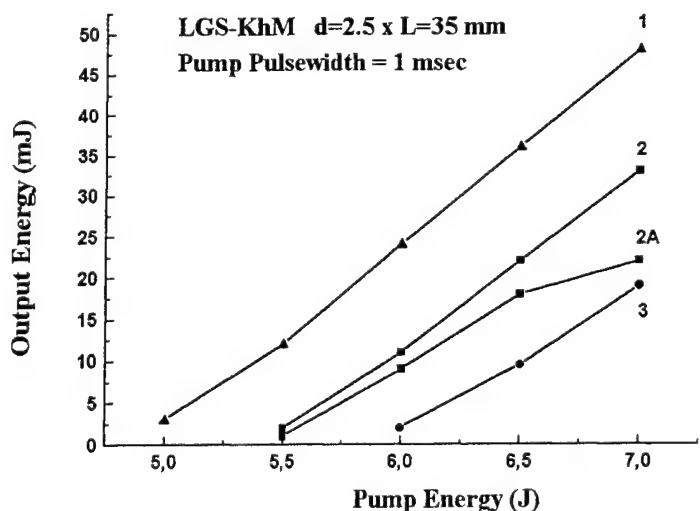


Fig.3. Laser output energy vs lamp pump energy.
1 - KhM/Cr5.6, 2,2A - KhM, 3 - KhM/Cr0.9,
1-3 - FR-mode, 2A - Q-sw mode.

Depending on projected pulse repetition rate and range of working temperatures there is an opportunity of optimization of chromium ions concentration (fig.3). For example, if one has the purpose, that the output energy of a pulse in Q-switch mode was within the range of 15 mJ in the 1-st a pulse and 12 mJ in the last one in a pack from 10 pulses then the limiting repetition rate is 0,125 Hz ($E_{th}=4.8\text{J}$, $\eta =2.5\%$) - for KhM/Cr5.6 (1), 0,5 Hz ($E_{th}=5.4\text{J}$, $\eta =2.2\%$) - for a base chromium concentration (2) and 1 Hz ($E_{th}=5.8\text{J}$, $\eta =2.0\%$) - for KhM/Cr0.9 (3). Initial rod temperature was 20 °C.

3.2. LGS-KhCh - glass for high average output power applications.

Along with properties inherent to glass LGS-KhM this glass has value of thermooptical constant W , optimum for high average output power applications. The active elements from this glass work at very severe conditions, and the losses of absorbed energy in them should be decreased to a minimum. Taking into account, that the main source of a heating in system Cr-Yb-Er is induced by chromium ions absorption and that the working temperature is high, the compromise value of chromium ions concentration is in the range of $(0,25 - 1) \times 10^{19} \text{ cm}^{-3}$. Fig. 4 demonstrates the dependence of output power vs pump power at various repetition rates for the laser with laser rod of 4 mm in diameter and 80 mm in length working in free-running mode. Length of the resonator was chosen minimally possible. Quartz cylindrical monoblock silvered pumping cavity with a lamp INP-3/75 was used. Lamp and laser rod were cooled by distilled water.

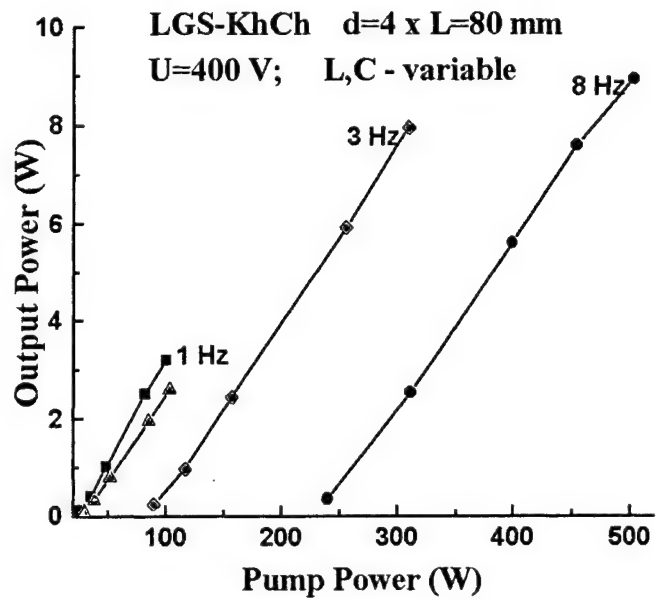


Fig.4. Laser output power vs lamp pump power.

Nine Watts of average power has been achieved. The pump power is far below the maximum thermal-loading capability of this glass. Further optimization of the laser design opens new possibilities to higher efficiencies. Left curve on fig.4 for 1 Hz repetition rate demonstrates such increase as result of using D_2O water (instead of the distilled) one and quartz silvered tube pumping cavity of small diameter. Calculations demonstrate, that output power more than 20 Watts it is quite achievable at increase of length of a laser rod from 80 mm up to 160 mm,

3.3. LGS-DE - glass for diode-pumped lasers.

The Yb-Er glass LGS-DE characterized by low thermal expansion coefficient ($90 \times 10^{-7} \text{ }^{\circ}\text{C}^{-1}$) and high thermal conductivity (0,75 W / mxK) is suitable for diode-pumped devices.

Erbium diode-pumped lasers have not found now such wide application as lamp-pumped lasers. There is no a common design of such laser. Depending on the considered pump circuits it is not always possible to obtain the necessary parameters at the expense of selection of a configuration of a laser element and there is a necessity for a choice of optimum concentration of activators for each design. As an example, the fig.5 demonstrates the calculated data for a glass LGS-DE with various concentration of ytterbium ions. The model of Yb-Er system developed earlier [9] was used, which takes into account such mechanisms as effect of leaving of Er ions most closely connected with neighbor Yb ions, cumulative transfer through the scheme $Yb^{3+}(^2F_{5/2} - ^2F_{7/2}) - Er^{3+}(^4I_{13/2} - ^4F_{9/2})$ and back transfer process from erbium to ytterbium. One can see, that the efficiency of storage energy is the same in very wide range of ytterbium ions concentrations $(1,5 - 4) \times 10^{21} \text{ cm}^{-3}$.

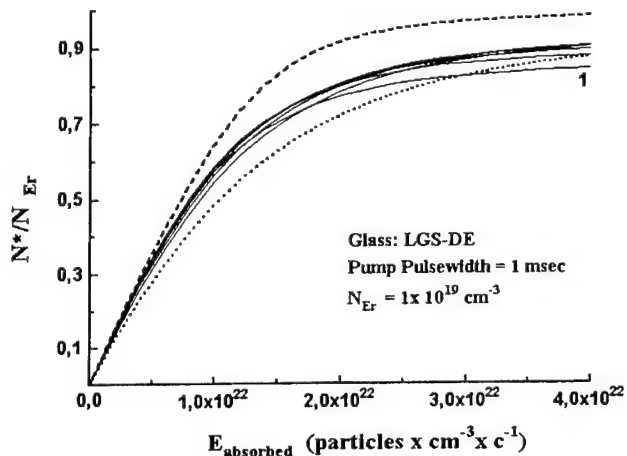


Fig.5. Dependence of top population of Er-exited state ${}^4I_{13}$ vs absorbed pump energy. $N_{Yb} = (1,4 - 3) \times 10^{21} \text{ cm}^{-3}$ (unnumbered lines), 4×10^{21} (1) and 1×10^{21} (dot line). Dash line - for $N_{Yb} = 2,3 \times 10^{21} \text{ cm}^{-3}$ without effect of leaving of Er ions most closely connected with neighbor Yb ions and cumulative transfer.

So, we can choose optimal concentration from this range being guided by requirements of uniformity of energy absorbed and taking in to account the limited efficiency of pumping cavity.

4. CONCLUSION

A new glass base for different applications has been developed.

The Cr-Yb-Er glass LGS-KhM having low thermal expansion coefficient ($87 \times 10^{-7} \text{ }^{\circ}\text{C}^{-1}$), enhanced thermomechanical strength, and high chemical stability (solubility in water is less then 0,024% weight loss after 1 h at $100 \text{ }^{\circ}\text{C}$) in combination with its excellent laser characteristics is ideal for uncooled miniature lasers. Under free-running conditions the differential efficiency was 2.5% at the threshold pump energy of less than 5 J reached in active elements 2.5 mm in diameter and 35 mm long. Under Q-switching conditions a pulse of 30 ns duration and of 10 mJ energy was emitted when the pump energy was 5-6 J.

The Yb-Er glass LGS-DE characterized by a low thermal expansion coefficient ($90 \times 10^{-7} \text{ }^{\circ}\text{C}^{-1}$) and high thermal conductivity ($0,75 \text{ W / mK}$) is suitable for diode-pumped devices.

The athermal behavior makes the Cr-Yb-Er glass LGS-KhCh ideal for devices with forced cooling operating at high repetition rates (tens of Hz) and output powers (tens of Watts).

5. REFERENCES

1. V.P. Gapontsev, A.K. Gromov, A.A. Isineev, V.B. Kravchenko, S.M. Matitsin, M.R. Sirtlanov, N.S. Platonov. "Progress in laser glasses activated by chromium". *Proc. of the International Conference on Lasers'82*, pp. 310 - 314. 1982.
2. S.G. Lunter, A.G. Murzin, M.N. Tolstoi et al. "Energy parameters of lasers utilizing erbium glasses sensitized by ytterbium and chromium". *Kvant. Elektronika*, 11, pp. 103 - 108. 1984.
3. V.P. Gapontsev, P.I. Sadovski, I.E. Samartsev. "1.5- μ m Erbium Glass Lasers". *Proc. of the International Conference CLEO*, pp. 682 - 683. 1990.
4. R. Stultz, D. Sumida, H. Bruesselbach. *Proceedings of the Eleventh Topical Meeting on Advanced Solid-State Lasers*, San Francisco, CA, (Washington, DC: Optical Society of America) 1996.
5. E. Tanguy, J. P. Pocholle, G. Feugnet, C. Larat, M. Schwartz, A. Brun, P. Georges. *Electron. Lett.* 31 pp. 458-463. 1995.
6. V.P. Gapontsev, A.K. Gromov, A. Izyneev, P.I. Sadovski. "Optical properties of Cr²⁺ in phosphate glass". *Proc. of the Fifteenth All-Union Symp. on Optical and Spectral Properties of Glasses*. p. 108. 1989.
7. Sh. Jiang, J. Myers, D. Rhonehouse, M. Myers, R. Belford, S. Hamlin. "Laser and thermal performance of a new erbium doped phosphate laser glass". *Proc. of the International Conference SPIE*, 1994.
8. A.A. Izyneev, P.I. Sadovski. "New highly efficient LGS-KhM erbium-doped glass for uncooled miniature lasers with a high pulse repetition rate". *Quantum Electronics*, 27, pp. 771 - 775. 1997.
9. V.P. Gapontsev, S.M. Matitsin, A.A. Isineev, V.B. Kravchenko. "Erbium glass lasers and their applications" *Proc. of the International Conference on Lasers'81*. pp. 1135 - 1141. 1981.
10. L.O. Byshevskaja-Konopko, A.A. Izyneev, Ju.S. Pavlov, P.I. Sadovski. "About a cerium role in chromium-itterbium-erbium phosphate glass". *Kvant. Elektronika*, 9 2000.

Spectroscopic and laser properties of BeLaAl₁₁O₁₉ single crystals doped with Cr³⁺, Ti³⁺ and Nd³⁺ ions

E.V.Pestryakov, V.V.Petrov, V.I.Trunov, A.V.Kirpichnikov, A.I.Alimpiev^a

Institute of Laser Physics of Siberian Branch of RAS, Novosibirsk, 630090, Russia

^aTechnological Institute of Monocrystals SB RAS, Novosibirsk, 630058, Russia

ABSTRACT

The new laser crystals BeLaAl₁₁O₁₉ doped with Cr³⁺, Ti³⁺ and Nd³⁺ ions were grown by the Czochralski technique. The absorption and fluorescence spectra of impurity ions are reported and the temperature dependence of the fluorescence lifetime are described. The laser properties these ions were investigated. The laser action has been achieved on $^4F_{3/2} - ^4I_{11/2}$ (1052 nm) transition of Nd³⁺-ions under selective laser pumping. The physical properties of BeLaAl₁₁O₁₉ crystal were studied: the values of all independent component of elastic constant tensor were determined. On they base a number dynamic parameters of crystals, such as Young's modulus, the shear modulus, the volume elasticity modulus and Poisson's factor, Debye temperature and specific heat capacity were calculated. The investigation show that the BeLaAl₁₁O₁₉ is a promising host for a creature the new solid state laser media.

1. INTRODUCTION

The new laser crystal - hexagonal aluminate of beryllium-lanthanum (HALB) - BeLaAl₁₁O₁₉ in system BeO-La₂O₃-Al₂O₃ was grown. This crystal have a structural type closing to the magnetoplumbite structure (PbFe₁₂O₁₉) with space group P6₃/mmc as a well-known laser crystal - hexagonal aluminate of magnesium- lanthanum (HALM) - LaMgAl₁₁O₁₉.^{1,2} BeLaAl₁₁O₁₉ has a high physical properties and a crystal structure that is possible to selectively substitute Al³⁺ and La³⁺ ions with metal ions of first transitions group with d- and f-configuration of electronic shells, accordingly. The experimental investigations of physical properties of HALB crystal and spectroscopic and laser properties of Ti³⁺ and Cr³⁺ (d-ions) and Nd³⁺ (f-ion) in this crystal are presented and with those in HALM single crystals compared.

2. CRYSTAL GROWTH AND CRYSTAL STRUCTURE

Pure crystals of HALB were grown from melt in rf-heated iridium crucibles under neutral atmosphere by using Czochralski technique. HALB melts incongruently at 1850 °C. The quality of HALB crystals strongly depends on axial and radial gradients of temperature and on crystallization and rotation rates. A heating system with good thermal insulation was applied in order to achieve appropriate radial and axial temperature gradients in the crystallization chamber of "Kristall" unit. The low-loss high optical quality single crystals were obtained in [001] directions, 15-17 mm in diameter, 50-70 mm long. It must be noticed that the weak cleavage plane [001] keeps difficult the pulling of crystal to the [001] directions. In that direction growing crystals had a shape of hexagonal prisms. The HALB crystals doped with the transition metals such as chromium, titanium, neodymium, ytterbium and erbium were grown also.

Earlier some characteristics of crystal structure of HALB have been reported.¹ X-ray analysis of those crystals showed that HALB is hexagonal system crystal with space group P6₃/mmc: $a = 5.542 \text{ \AA}$, $c = 21.959 \text{ \AA}$. Later, crystal space group was revised as P3m1 with $a = 5.5433 \text{ \AA}$, $c = 21.9535 \text{ \AA}$.³ Our optical measurements and EPR data⁴ show that the P6₃/mmc space group of HALB is more real.

For further author information:

E-mail: pefvic@laser.nsc.ru

fax: 7 (3832) 332067

3. OPTICAL PROPERTIES

3.1. Index of Refraction

According to its space group symmetry HALB is an centrosymmetric optically uniaxial crystal.⁵ The dispersion of refractive indices was measured using the prism method.⁶ The refractive indices were determined by measuring the angle of minimum deviation between incident and refracted rays. The indices of refraction were measured for the different wavelengths of CW mercury lamp and He-Ne laser. The wavelength dependence of the principal indices of refraction – n_o and n_e is shown on Fig. 1. Both of them exhibit a normal dispersion and steeple increase in the ultraviolet side of spectra. The accuracy of the refractive index determination was $5 \cdot 10^{-4}$.

The dots indicate direct measured values and the full lines represent a Sellmeier fit to the experimental values. The spectral dependence of refractive indices were fitted by least-squares method to a two-pole Sellmeier equation

$$n_i^2 = A_i + \frac{B_i}{\lambda^2} - C_i \cdot \lambda^2, \quad (1)$$

where n_i are the principal refractive indices of ordinary ($i = o$), and extraordinary ($i = e$) rays, λ is wavelength in nm, A , B , C are constant parameters chosen to give the best agreement with experimental data.

Table 1. Sellmeier coefficients A, B, C for the principal indices of refraction of HALB crystal.

Index of refraction	Sellmeier coefficients		
	A	B	C
n_o	3.144370	23027.65	$0.1186 \cdot 10^{-7}$
n_e	3.171734	23349.27	$0.1393 \cdot 10^{-7}$

The values of the parameters of Eq. (1) for both refractive indices of HALB crystal are given in Table 1. It has to be mentioned that BeLaAl₁₁O₁₉ and MgLaAl₁₁O₁₉ crystals are similar by their dispersion properties of refractive indices, though absolute values of the indices in case of HALB are slightly smaller than those of HALM.

3.2. Optical Absorption Spectra

The optical absorption spectra of the HALB were studied in UV and VIS regions on the 0.3 mm thick polished crystal plates, oriented along main crystallographic axes. Direct optical transmission measurements were made at room temperature using "SF-26" (UV) and "SF-8" (VIS- IR) spectrophotometers. The optical transmission spectrum of HALB for unpolarized light is presented on Fig. 2. Analysis of absorption edge of HALB shows that the exponential dependence of absorption coefficient – α on photon energy – $\hbar\omega$ can be fitted to the Urbach rule⁷

$$\alpha(\hbar\omega) = \alpha_0 \cdot \exp\left[G \frac{\hbar\omega - E_0}{kT}\right], \quad (2)$$

where $G = G_0 \left(\frac{2kT}{\hbar\omega_p}\right) \tanh\left(\frac{\hbar\omega_p}{2kT}\right)$, with G_0 is a constant, $\hbar\omega_p$ is a phonon energy, E_0 is an estimate of the optical gap,

α_0 is a constant, k is the Boltzmann's constant, T is the absolute temperature.

The optical gap of the HALB was obtained from the linear extrapolation of α versus photon energy – $\hbar\omega$. There was estimated to 48190 cm^{-1} (207.5 nm). Our experimental results can be accounted for it in terms of the theory,⁷ which ascribes the Urbach tail to the electron-phonon interaction. Characteristic frequency of the effective optical phonon – ω_p was deduced from the experimental spectra according to Eq.(2). The magnitude of ω_p equal to 250 cm^{-1} is in good agreement with the frequency of phonon in the fluorescence spectra.

4. DYNAMIC PROPERTIES

By the use of Cristoffel equations ^{7,8} the elastic constant C_{ijkl} of HALB crystal were calculated from experimental data of the acoustic plane wave velocities and the density of crystal host. The density of HALB crystal was measured by flotation method. The value density of HALB obtained at room temperature using distilled water is $4.17 \pm 0.02 \text{ g/cm}^3$. This result is in good agreement with that obtained by X-ray analysis³. The value of HALM density defined by us is $4.26 \pm 0.02 \text{ g/cm}^3$. The velocities of propagation a sound waves in along main crystallographic directions of crystals were measured by new interferometric acoustooptical techniques ⁹. The magnitudes of all independent components of elastic constant tensor C_{ijkl} of HALB are presented in Table 2. On they base a number dynamic parameters of crystals^{7,10}, such as Young's modulus, the shear modulus, the volume elasticity modulus and Poisson' ratio, also Debye temperature were calculated. The magnitude of them is listed in Table 3. It should be noted that the Debye temperature – T_D is the important parameter for vibronic solid state lasers since one define the maximal frequency of phonon – $\hbar\omega_{ph}^{max}$ of vibronic spectra of crystal lattice: $kT_D = \hbar\omega_{ph}^{max}$. This expression corresponded to $\hbar\omega_{ph}^{max}=665 \text{ cm}^{-1}$ for HALB. This value is same what higher than in HALM ($\hbar\omega_{ph}^{max}=600 \text{ cm}^{-1}$). We have made comparison dynamic parameters with same parameters of $\text{MgLaAl}_{11}\text{O}_{19}$. It may be readily shown from Table 3 that the dynamic characteristics of $\text{BeLaAl}_{11}\text{O}_{19}$ crystal close to $\text{MgLaAl}_{11}\text{O}_{19}$.

5. SPECTROSCOPIC AND LASER PROPERTIES

5.1. Crystal Doped with Chromium and Titanium Ions

Chromium and titanium doped $\text{BeLaAl}_{11}\text{O}_{19}$ exhibits the typical absorption and emission spectra of octahedral coordinated three valence ions. Both ions enter the lattice substitutionally for the Al^{3+} ions. The samples used in this work contained 0.2 at.% chromium or titanium.

Chromium

The room temperature absorption spectra of chromium in HALB are presented in Fig. 3. It consists of two broad bands occurring at 420 nm and 588 nm and weak peak at 675 and 694 nm, those are due to $^4\text{A}_2$ - $^4\text{T}_1$, $^4\text{A}_2$ - $^4\text{T}_2$, $^4\text{A}_2$ - $^2\text{T}_1$ and $^4\text{A}_2$ - ^2E transitions of three valence ions, respectively. EPR measurements ⁴ of chromium in HALB have shown the existence of three kinds of octahedral sites in structure of crystal: regular sites – 2a; distorted octahedral sites –12k; antiprism sites - 4f with C_{3v} symmetry. According to the EPR data occupation rates of sites is 2:1:30, respectively. In agreement with EPR data the absorption spectra of Cr^{3+} ions in HALB are due to the transitions of ions occupying the 4f sites with C_{3v} symmetry. From the positions of absorption bands the crystal field parameters are estimated: $Dq=1770 \text{ cm}^{-1}$, $B=700 \text{ cm}^{-1}$, $C=2770 \text{ cm}^{-1}$, $Dq/B=2.53$. This value of Dq is high than one in alexandrite, BeAl_2O_4 ; Cr^{3+} , and other well-known Cr^{3+} doped crystals.¹¹

The fluorescence spectra of Cr^{3+} at room temperature obtained under excitation into $^4\text{T}_2$ -absorbtion band with the 532 nm SHG of Nd:YAG laser are presented in Fig.4. The general features consist of narrow R line at 694 nm, its phonon side band with the peak wavelength at 702.5, 714, 727 nm and the broadening band in the range from 700 to 1000 nm. The intensity of broad band relative to that of R-line is 0.5:1. These characteristics are typical for a d^3 ion in a relatively strong crystal field environment ¹¹⁻¹³. The broad band fluorescence cross-section - σ has been calculated with the expression ¹⁴:

$$\sigma(\lambda) = \frac{\eta\lambda^5 I_5(\lambda)}{8\pi c \tau_f} \left[\frac{n_\pi^2}{3} \int \lambda I_\pi(\lambda) d\lambda + \frac{2n_\sigma^2}{3} \int \lambda I_\sigma(\lambda) d\lambda \right]^{-1}, \quad (3)$$

where η is a quantum yield of the fluorescence, τ_f is fluorescence lifetime, n_π и n_σ is the indices of refraction, I_π и I_σ - the fluorescence intensity for π and σ polarizations, accordingly.

The emission cross section is estimated to be $\sigma \sim 2 \cdot 10^{-20} \text{ cm}^2$ at 755 nm.

The fluorescence lifetimes were measured as a function of temperature between 77 and 800 K. There are plotted in Fig. 5. The effective lifetime exhibits two distinct temperature regions: from 300 K to 600 K and for temperature higher than 600 K. This situation can be explained that the effective fluorescence lifetime of Cr^{3+} in HALB is totally determinate by the thermal equilibrium between the ^2E state and $^4\text{T}_2$ and the thermal quenching of fluorescence because at level crossing the excited $^4\text{T}_2$ and the ground $^4\text{A}_2$ states.¹⁵ The fluorescence lifetime is given by

$$\tau_{\text{eff}} = \tau_R \left[\frac{1 + 3 \exp \left(\frac{-\Delta E}{kT} \right)}{1 + \frac{\tau_R}{\tau_T} \exp \left(\frac{-\Delta E}{kT} \right) + \frac{\tau_R}{\tau_Q} \exp \left(\frac{-\Delta E - \Delta Q}{kT} \right)} \right]^{-1} \quad (4)$$

where T is the temperature, k is Boltzman's constant, τ_R and τ_T are the lifetime of the 2E and 4T_2 state, accordingly, τ_Q^{-1} is the thermal quenching rate at level crossing the excited state 4T_2 and the ground state 4A_2 , ΔE is the energy difference between the 2E and 4T_2 levels, ΔQ is the energy of thermal quenching of fluorescence.

The magnitudes of ΔE and ΔQ were determined by using this expression. The best agreement between calculated and experimental data was obtained where $\Delta E = 850 \text{ cm}^{-1}$ and $\Delta Q = 5860 \text{ cm}^{-1}$. The energy gap ΔE of HALB is similar to that one in HALM ($\Delta E = 860 \text{ cm}^{-1}$).¹³

Titanium

According to the EPR⁴ and optical measurements the Ti^{3+} ions are located mainly in octahedral positions with C_{3v} symmetry of HALB crystal.

The absorption spectrum of $\text{BeLaAl}_{11}\text{O}_{19}$ doped with Ti^{3+} ions is shown in Fig. 6. $\text{BeLaAl}_{11}\text{O}_{19}:\text{Ti}^{3+}$ exhibits the spectrum in form a broad double structured band with peaks at 515 and 580 nm with common bandwidth about 5500 cm^{-1} . Double structure are due to transitions from the ground state 2T_2 to the two components of the excited state 2E that splitting caused by Jahn-Teller effect.¹⁶ The weak peaks of absorption at 626, 583 and 463 nm are correlated to the impurity three and two valence iron ions.

Typical fluorescence spectrum of Ti^{3+} under doubled Nd:YAG laser (532 nm) excitation is presented in Fig. 7. That at room temperature consist of broad band of emission centered at 770 nm. The emission vibronic bands Ti cover the spectral region from 700 nm to 1000 nm. The magnitude of emission cross section at room temperature is estimated to be $\sim 1.6 \cdot 10^{-19} \text{ cm}^2$ at 780 nm. At polarization parallel to c axis and to a axis the fluorescence spectra have double structure. We conclude that the nature of such spectra is caused by Jahn-Teller effect of ground state of Ti^{3+} . If the Jahn-Teller interaction in the ground state more than energy of spin-orbital interaction that Jahn-Teller effect remove the degeneracy of ground state 2T_2 and split the emission band.¹⁷ The splitting of emission band in form of two overlapping Gaussian bands is shown in Fig. 7.

The temperature dependence of fluorescence lifetime at the peak of the vibronic emission band is shown in Fig. 8. It is almost constant from 77 to about 500 K and then decreases as an exponential with increasing temperature. Fluorescence lifetime at liquid nitrogen temperature is about 7.0 μsec and one decreased to 4.8 μsec at room temperature.

5.2. Crystal Doped with Neodymium Ion

The absorption spectrum of HALB doped with Nd ion exhibits the typical transitions associated with tetrahedral coordinated three valence ions, since Nd^{3+} enter the lattice substitutionally for the La^{3+} ions.² The absorption spectra of this crystal compared to Nd:HALM are presented in Fig. 9.

The fluorescence spectra of Nd^{3+} have been observed from the $^4F_{3/2}$ level towards the $^4I_{13/2}$ and $^4I_{11/2}$ levels. The second transition is made of five lines, strongest one at 1054 nm and 1079 nm. Typical fluorescence spectra of $^4F_{3/2} - ^4I_{11/2}$ transition are presented in Fig. 10. The emission cross section is estimated to be $\sim 1.54 \cdot 10^{-19} \text{ cm}^2$ at 1054 nm. The fluorescence lifetime of the Nd^{3+} is about 280 μsec at room temperature. We have tested $\text{Nd}:\text{BeLaAl}_{11}\text{O}_{19}$ crystal under laser pumping (532 nm and 514.5 nm) with Nd concentration about 3 and 5 wt. %. The laser oscillation at 1054 nm has been achieved at room temperature.

The broadest emission lines at 1054 and 1079 nm (width about $5-7 \text{ cm}^{-1}$) are perspective for generation of ultrashort laser pulses. It must be noticed that laser properties of Nd:HALB is very similar to them of Nd:HALM,¹⁸ but laser on Nd:HALB has potential possibilities of tuning emission in the total region from 1045 to 1085 nm.

6. CONCLUSION

The lanthanum beryllium hexagonal aluminate crystals - $\text{BeLaAl}_{11}\text{O}_{19}$ of high optical quality were grown and their physical properties were investigated. The experimental study of spectroscopic and laser parameters of Ti^{3+} , Cr^{3+} and Nd^{3+} ions in this crystals were carried out. We have made comparison these parameters with same parameters of well-known laser medium - a crystal of lanthanum magnesium hexaaluminate - $\text{MgLaAl}_{11}\text{O}_{19}$. Our investigations are showed that on optical and dynamic characteristics $\text{BeLaAl}_{11}\text{O}_{19}$ single crystal close to $\text{MgLaAl}_{11}\text{O}_{19}$ and one is a promising host for creating the new active material for solid state lasers on d and f ions.

7. ACKNOWLEDGMENTS

The authors thank S.V.Bogdanov, I.I.Zubrinov, I.N.Nyushkov for their help during the experimental part of this investigation. This work was performed in part under the support of the Russian National Foundation for Basic Research grant No.98-02-17787 and Siberian Branch of Russian Academy of Sciences grant No.IG2000-49.

REFERENCES

1. A.Alimpiev, V.Gulev and P.Mokruchnikov, "Crystal growth of $\text{LaBeAl}_{11}\text{O}_{19}$ and field of crystallization in the system $\text{La}_2\text{O}_3\text{-BeO-Al}_2\text{O}_3$ ", Cryst. Res. Technol., **30**, pp. 295-297, 1995.
2. A.Kahn, A.Lejus, M.Madsac, J.Thery and D.Vivien, "Preparation, structure, optical and magnetic properties of lanthanide aluminate single crystal (LAMAL₁₁O₁₉)", J. Appl. Phys., **52**, pp. 6864-6869, 1981.
3. *International Centre for Diffraction Data, PDF, set.49, card 458.*
4. V.Solntzev, A.Alimpiev and A.Jurkin, "EPR and absorption spectra of Cr in $\text{BeLaAl}_{11}\text{O}_{19}$ single crystal", J. Appl. Spectroscopy (Russia), in press.
5. J.Nye, *Physical properties of crystals*, Oxford, Carendon press, 1957.
6. S. Louisnathan, F.Bloss and E.Korda, "Measurement of refractive indices and their dispersion", J. Am. Mineral., **63**, pp.394-400, 1978.
7. J. Reissland, *The physics of phonons*. London-New York-Sydney-Toronto: John Wiley & Sons, 1973.
8. M.Born, Huang Kun, *Dynamical theory of crystal lattices*, Oxford, Clarendon Press, 1954.
9. I.I.Zubrinov, V.I.Semenov, E.V.Pestryakov, V.V.Petrov and A.I.Alimpiev, "Elastic and elasto-optical properties of $\text{BeAl}_6\text{O}_{10}$ crystal", Crystallography Reports, **43**, pp.675-660, 1998.
10. S. V.Bogdanov, I.I.Zubrinov, E.V.Pestryakov and V.K.Sapozhnikov, "Interference acoustooptic technique for sound velocity measurements", Acoustical Phys., **46**, pp.27-32, 2000.
11. A.A.Kaminski, *Crystalline lasers: Physical properties and operating schemes*. B.Raton-Ann Arbor-Boston, 1995.
12. V.A.Antonov, P.A.Arsenev, D.T.Sviridov, R.K.Sviridova and I.T.Makhmudov, "Optical spectra of Cr ions in $\text{LaMgAl}_{11}\text{O}_{19}$ single crystal", Crystallography Reports, **33**, pp.908-911, 1988.
13. C.Borel, C.Wyon, J.Aubert, H.Manaa and R.Moncorgé, "Luminescence properties, crystal growth and laser capability of Cr doped LMA", J. Luminescence, **55**, pp.95-103, 1993.
14. P.Moulton, "Spectroscopic and laser characteristics of $\text{Ti:Al}_2\text{O}_3$ ", J. Opt. Soc. Am., **3B**, pp.125-133, 1986.
15. Z.Y.Zhang, K.T.V.Grattan and A.W.Palmer, "Temperature dependence of the YAG:Cr fluorescence lifetime over the range 77 to 900 K", Phys. Rev., **B51**, pp.26562660, 1995.
16. B.Martinat, D.Gourier, A.Lejus and D.Vivien, "Optical properties of $\text{LaMgAl}_{11}\text{O}_{19} : \text{Ti}$ - a potential tunable laser material", J. Sol. State Chemistry, **89**, pp.147-154, 1990.
17. E.V.Pestryakov, V.V.Petrov, V.I.Trunov, A.V.Kirpichnikov, K.P.Komarov and A.I.Alimpiev, "Ultrabroadband active media for generation of ultrashort optical pulses", Proceedings of Second International Symposium on Modern Problem of Laser Physics, Novosibirsk, vol.1, pp.202-217, 1997.
18. V.M.Garmash, A.A.Kaminski, M.I.Polyakov, S.E.Sarkisov and A.A.Filimonov, "Luminescence and stimulated emission of Nd ions in $\text{MgLaAl}_{11}\text{O}_{19}$ crystal", Phys. Stat. Sol., **75A**, K111-K116, 1983.

Table 2. Magnitudes of elastic constants of HALB and HALM crystals.

Crystal	Components of the elastic tensor $C_{mn} (\times 10^{11} \text{ N/m}^2)$					
	C_{11}	C_{33}	C_{44}	C_{66}	C_{12}	C_{13}
BeLaAl ₁₁ O ₁₉	4.235	3.27	1.130	1.345	1.540	1.088
MgLaAl ₁₁ O ₁₉	4.196	3.26	1.135	1.275	1.647	1.025

Table 3. Dynamic parameters of HALB and HALM crystals.

Crystal	Volume elasticity, $K, 10^{11} \text{ N/m}^2$	Shear modulus, $G, 10^{11} \text{ N/m}^2$	Young's modulus, $E, 10^{11} \text{ N/m}^2$	Poisson's factor, μ
BeLaAl ₁₁ O ₁₉	2.08	1.25	3.05	0.22
MgLaAl ₁₁ O ₁₉	2.08	1.24	3.03	0.22

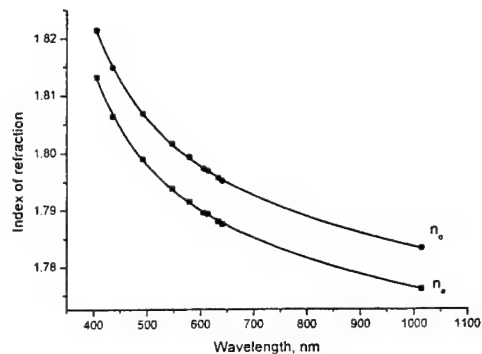


Fig.1. The indices of refraction of HALB crystals.

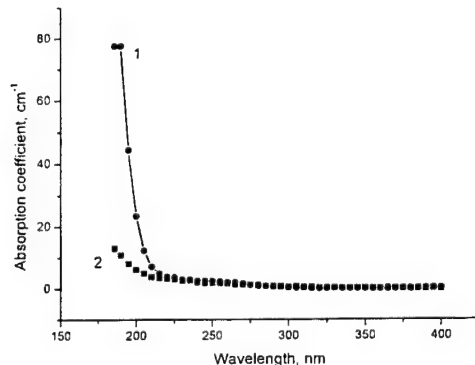


Fig.2. The absorption coefficients of HALB (1) and HALM (2) in UV range.

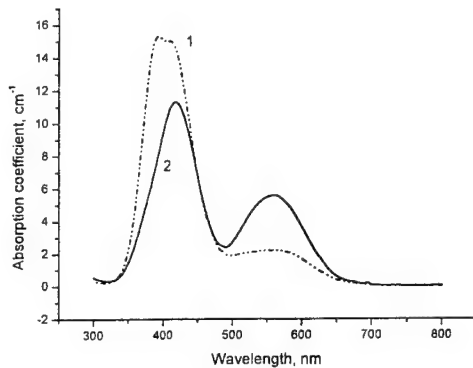


Fig.3. Absorption spectra of Cr:HALB for EIIc (1) and EIIa (2).

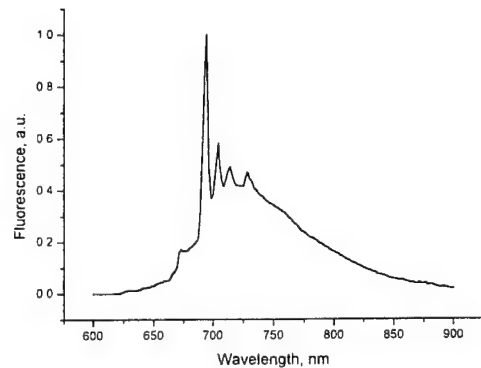


Fig.4. Fluorescence spectrum of Cr:HALB for EIIc at 300 K.

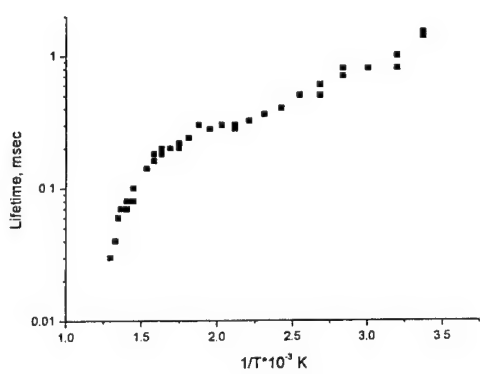


Fig.5. Fluorescence lifetime of Cr:HALB.

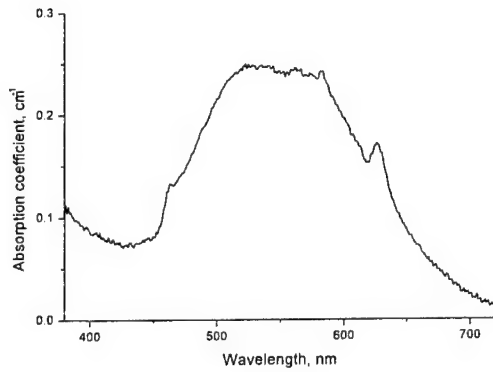


Fig.6. Absorption spectrum of Ti:HALB for EIIa.

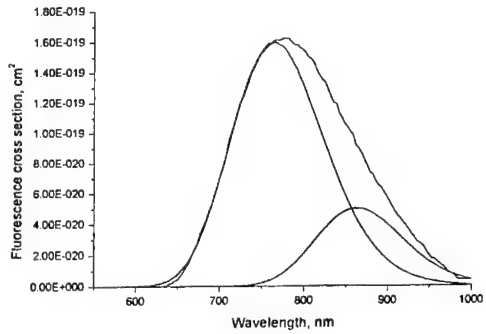


Fig.7. Fluorescence cross section of Ti:HALB for EIIc polarization.

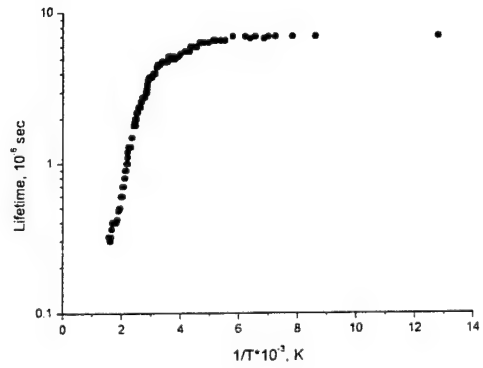


Fig.8. Fluorescence lifetime of Ti:HALB.

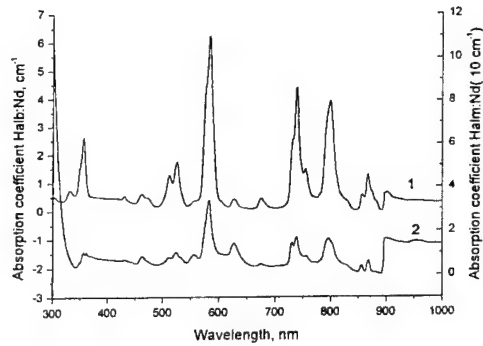


Fig.9. Absorption coefficients of Nd:HALB (1) and Nd:HALM (2).

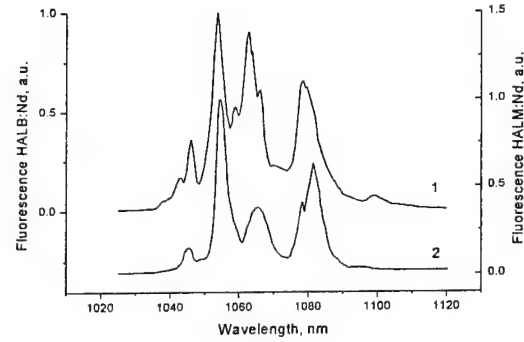


Fig.10. Fluorescence spectra of Nd:HALB (1) and Nd:HALM (2) at 300 K.

Concentration and power dependences of level population of 2.8 - μ m laser transition in YLF : Er crystals under CW laser diode pumping

A. M. Tkachuk¹, I. K. Razumova¹, A. A. Mirzaeva², G. E. Novikov², O. A. Orlov², A. V. Malyshev³, and V. P. Gapontsev⁴

¹ Federal Research Center “Vavilov State Optical Institute”,
St. Petersburg, 199034 Russia, E-mail: tkachuk@mail.rcom.ru,

² Institute for Laser Physics, St. Petersburg, 199034 Russia,

³ A. I. Ioffe Physical-Technical Institute, St. Petersburg, 194121 Russia,

⁴IPG-Laser, GmbH, Siemensstrasse, 7, D-57299 Burbach, E-mail:
valentingapontsev@compuserve.com

ABSTRACT

An influence of interionic cross relaxation processes (upconversion, selfquenching) on concentration and power dependences of the inverse population of $^4I_{11/2}$ and $^4I_{13/2}$ laser levels in YLF:Er crystals under CW laser-diode pumping were studied both theoretically and experimentally. Computer simulations were carried out taking into account not only pair interaction but also the multi-ion interaction in the whole system. Optimal Er concentration for 3 - μ m CW lasing was estimated as 10 – 15%.

Keywords: crystal, doped ion, rare earth, energy transfer, population.

1. INTRODUCTION

YLF: Er^{3+} crystals are well-known laser media generating in the VIS and IR under selective laser-diode pumping. Possibility for obtaining the inverse population of working levels of laser transitions strongly depends on macrorates of the interionic coupling processes, since just these processes define the working levels' population. Role of interionic coupling sharply increases with dopant concentration.

We report results of theoretical and experimental studies of formation of the inverse population of the working $^4I_{11/2}$ and $^4I_{13/2}$ levels of a 3- μ m laser transition in $LiY_{1-x}Er_xF_4$ ($x=0.003 \div 1$) under CW laser-diode pumping. Mechanisms of the interionic interaction processes and the concentration and pump power density dependences of their macrorates are obtained.

2. EXPERIMENTAL METHODS

Series of 11 samples of $LiY_{1-x}Er_xF_4$ crystals with dopant concentration 0.3 – 100 at.% were studied. Crystals were grown by modified Bridgman – Stockbarger technique.

Experimental dependences of population of the studied levels on erbium concentration were obtained from the intensity of the steady-state luminescence in spectral ranges of transitions from $^4I_{11/2}$ (0.9 – 1 μ m and 2.7 – 2.9 μ m) and $^4I_{13/2}$ (1.4 – 1.6 μ m) levels under selective laser-diode pumping in $^4I_{11/2}$ state. Spectra were recorded with a MDR-23 monochromator with computer control. Selective excitation of the $^4I_{11/2}$ level was performed by emission of a DL – 5M module of five InGaAs laser diodes (LD) summed in a fiber with a 230 μ m core diameter. The laser diodes emitted radiation in the $\lambda = 966$ -982 nm range which matched the YLF:Er $^{3+}$ absorption was focused on the face of the YLF:Er $^{3+}$ crystals by lens. Output power of the DL-5M module varied within 0-5 W

Computer simulations were carried out for the spectroscopic model involving 5 lower excited states of erbium ions taking into account the multi-ion interaction in the whole system. A system of rate equations for populations of the excited levels of erbium ions was solved and the population dependences on the dopant concentration and pump power density were derived. For all principal energy-transfer processes, such parameters as radiative and non-radiative

probabilities, life-time of excited levels, luminescence selfquenching and upconversion rates were determined from the independent experimental results and theoretical estimations within the framework of known energy transfer theory.

3. RESULTS AND DISCUSSION

Theoretical concentration dependences of steady-state populations of $^4I_{11/2}$ and $^4I_{13/2}$ erbium levels under different pumping power densities were obtained from the system of rate balance equations for the six lowest levels of erbium ion with allowance for intracenter relaxation and inter-ionic coupling processes, such as luminescence self-quenching and up-conversion. All processes involved into calculations under IR LD excitation of YLF: Er³⁺ crystals are indicated by arrows in the energy level scheme in Fig. 1.

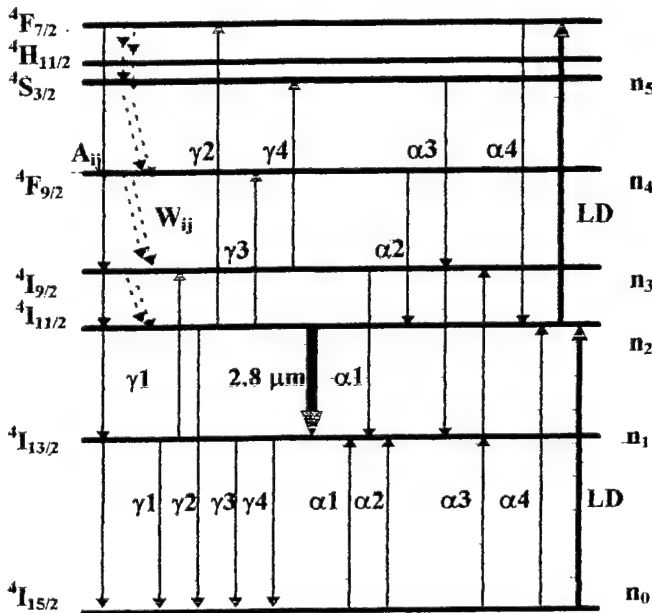


Fig. 1. Energy levels and schemes of radiationless Er-Er coupling in YLF: Er³⁺. A_{ij} - radiative $i \rightarrow j$ transition probabilities, W_{ij} - radiationless relaxation, α_i - self-quenching and γ_i - upconversion processes. Bold arrow - laser transition.

The system of rate balance equations for normalized populations of erbium levels $n_i = n_i(\text{Er})/n(\text{Er})$, where $n(\text{Er})$ is the relative concentration of Er³⁺ ion $n(\text{Er}) = N_{\text{Er}}/N_Y$ was written as follows:

$$\begin{aligned}
 dn_1/dt &= -A_{10}n_1 + \sum_{i=2}^5 A_{ii}n_i + 2\alpha_1n_0n_3 + \alpha_2n_0n_4 + \alpha_3n_0n_5 - 2\gamma_1(n_1)^2 - \gamma_3n_1n_2 - \gamma_4n_1n_3 = 0 \\
 dn_2/dt &= -\sum_{j=0}^1 A_{2j}n_2 + \sum_{i=3}^5 A_{i2}n_i + W_{32}n_3 + \alpha_2n_0n_4 + 2\alpha_4n_0n_5 - 2\gamma_2(n_2)^2 - \gamma_3n_1n_2 + R_{02}n_0 - R_{25}n_2 = 0 \\
 dn_3/dt &= -\sum_{j=0}^2 A_{3j}n_3 - W_{32}n_3 + \sum_{i=4}^5 A_{i3}n_i + W_{43}n_4 - \alpha_1n_0n_3 + \alpha_3n_0n_5 + \gamma_1(n_1)^2 - \gamma_4n_1n_3 = 0 \\
 dn_4/dt &= -\sum_{j=0}^3 A_{4j}n_4 + (A_{54} + W_{54})n_5 - \alpha_2n_0n_4 + \gamma_3n_1n_2 = 0 \\
 dn_5/dt &= -\sum_{j=0}^4 A_{5j}n_5 - W_{54}n_5 - (\alpha_3 + \alpha_4)n_0n_5 + \gamma_2(n_2)^2 + \gamma_4n_1n_3 + R_{25}n_2 = 0 \\
 dn_0/dt &= \sum_{i=1}^5 A_{i0}n_i - \alpha_1n_0n_3 - \alpha_2n_0n_4 - (\alpha_3 + \alpha_4)n_0n_5 + \gamma_1(n_1)^2 + \gamma_2(n_2)^2 + \gamma_3n_1n_2 + \gamma_4n_1n_3 - R_{02}n_0 = 0,
 \end{aligned}$$

Table 1. Probabilities of intacenter transitions A_{ij} , W_{ij} and τ_{exp}^{-1} in YLF: Er³⁺ [5].

$n_i \rightarrow n_j$	A_{ij}, c^{-1}	$\tau_{\text{exp}}^{-1}, \text{c}^{-1}$	W_{ij}, c^{-1}
$1 \rightarrow 0$	129	90	0
$2 \rightarrow 0$	143	250	
$2 \rightarrow 1$	17	0	
$3 \rightarrow 0$	19		
$3 \rightarrow 1$	50	$1.5 \cdot 10^5^*$	
$3 \rightarrow 2$	10		$6.9 \cdot 10^4$
$4 \rightarrow 0$	745		
$4 \rightarrow 1$	31	$3.3 \cdot 10^4$	
$4 \rightarrow 2$	66		
$4 \rightarrow 3$	1.0		$3.2 \cdot 10^4$
$5 \rightarrow 0$	1375		
$5 \rightarrow 1$	567		
$5 \rightarrow 2$	43	$2.5 \cdot 10^3$	
$5 \rightarrow 3$	56		
$5 \rightarrow 4$	10		$2.2 \cdot 10^3$

* the value of τ_{exp} is from ⁶.

where A_{ij} [c^{-1}] are the probabilities of radiative transitions from "i" to "j" levels; W_{ij} [c^{-1}] are the probabilities of non-radiative multiphonon transitions; parameters α_i ($i = 1 - 4$) are the macrorates for self-quenching processes (Er - Er self-quenching), parameters γ_j ($j = 1 - 4$) are the macrorates of up-conversion processes (up-conversion Er - Er) for the cross-relaxation schemes indicated by arrows in Fig. 1.

Parameters of radiative and non-radiative relaxations for $\text{LiY}_{1-x}\text{Er}_x\text{F}_4$ ($x=0.003-1$) reported in [5-6] and the values of A_{ij} , W_{ij} and lifetimes of excited levels measured for low-concentrated samples ($x = 0.5\%$) are given in the Table 1.

Energy transfer microparameters of migration C_{DD} (Table 2) and selfquenching C_{DA} (Table 3) were obtained by the model quantum-mechanical calculation in [1-4]. The energy level diagram in Fig. 1 shows schemes of cross-relaxation transitions, for which migration and energy-transfer microparameters were calculated within the framework of electro-static (multipole-multipole) interaction of erbium ions. From the ratio of C_{DD} and C_{DA} microparameters, the transfer mechanisms were determined and macrorates were estimated for the self-quenching and up-conversion processes in framework of jump (J) or static (S) decay models. Good agreement between theoretical and experimental estimates of the energy-transfer macrorates and their concentration dependences calculated in different energy-transfer models [1, 4] enabled us to estimate the effective values of the energy transfer constants α_i and to obtain the analytical form of their concentration dependences, which were substituted into the rate balance equations. Up-conversion constants γ_i were estimated using calculated microparameters and formulas from [1-4].

Table 2. Calculated microparameters of migration (C_{DD}) in YLF-Er^{3+}

Level $n_{i, a}$	Cross-relaxation process, transition $(i \rightarrow j)_a : (j \rightarrow i)_b$	$C_{DD}^{dd} \cdot 10^{40}$ $\text{cm}^6 \text{s}^{-1}$	$C_{DD}^{dq} \cdot 10^{55}$ $\text{cm}^8 \text{s}^{-1}$	$C_{DD}^{qq} \cdot 10^{69}$ $\text{cm}^{10} \text{s}^{-1}$
$^4\text{I}_{13/2}$	1. $(^4\text{I}_{13/2} \rightarrow ^4\text{I}_{15/2}) : (^4\text{I}_{15/2} \rightarrow ^4\text{I}_{13/2})$	24.43	21.04	3.377
$^4\text{I}_{11/2}$	2. $(^4\text{I}_{11/2} \rightarrow ^4\text{I}_{15/2}) : (^4\text{I}_{15/2} \rightarrow ^4\text{I}_{11/2})$	1.557	8.54	8.725
$^4\text{I}_{9/2}$	3. $(^4\text{I}_{9/2} \rightarrow ^4\text{I}_{15/2}) : (^4\text{I}_{15/2} \rightarrow ^4\text{I}_{9/2})$	0.167	0	0
$^4\text{F}_{9/2}$	4. $(^4\text{F}_{9/2} \rightarrow ^4\text{I}_{15/2}) : (^4\text{I}_{15/2} \rightarrow ^4\text{F}_{9/2})$	4.67	0	0
$^4\text{S}_{3/2}$	5. $(^4\text{S}_{3/2} \rightarrow ^4\text{I}_{15/2}) : (^4\text{I}_{15/2} \rightarrow ^4\text{S}_{3/2})$	1.013	0	0
$^4\text{H}_{11/2}$	6. $(^2\text{H}_{11/2} \rightarrow ^4\text{I}_{15/2}) : (^4\text{I}_{15/2} \rightarrow ^2\text{H}_{11/2})$	7.31	504	6475
$^4\text{F}_{7/2}$	7. $(^4\text{F}_{7/2} \rightarrow ^4\text{I}_{15/2}) : (^4\text{I}_{15/2} \rightarrow ^4\text{F}_{7/2})$	11.04	0	0

Table 3. Calculated microparameters of self-quenching and up-conversion (C_{DA}) in YLF-Er^{3+} .

Levels, $n_{i, a}; n_{k, b}$	Cross-relaxation process, transition $(i \rightarrow j)_a : (k \rightarrow l)_b$	$C_{DA}^{dd} \cdot 10^{40}$ $\text{cm}^6 \text{s}^{-1}$	$C_{DA}^{dq} \cdot 10^{55}$ $\text{cm}^8 \text{s}^{-1}$	$C_{DA}^{qq} \cdot 10^{70}$ $\text{cm}^{10} \text{s}^{-1}$
$^4\text{I}_{9/2}, ^4\text{I}_{15/2}$	Er - Er self-quenching			
$^4\text{F}_{9/2}, ^4\text{I}_{15/2}$	1. $(^4\text{I}_{9/2} \rightarrow ^4\text{I}_{15/2}) : (^4\text{I}_{15/2} \rightarrow ^4\text{I}_{13/2}) - \hbar\omega$	0.60	5.44	7.9
$^4\text{F}_{9/2}, ^4\text{I}_{11/2}$	2. $(^4\text{F}_{9/2} \rightarrow ^4\text{I}_{11/2}) : (^4\text{I}_{15/2} \rightarrow ^4\text{I}_{13/2}) - 2\hbar\omega$	0.019	0.094	0.124
$^4\text{S}_{3/2}, ^4\text{I}_{15/2}$	3. $(^4\text{S}_{3/2} \rightarrow ^4\text{I}_{9/2}) : (^4\text{I}_{15/2} \rightarrow ^4\text{I}_{13/2}) - \hbar\omega$	10.83	9.32	0
$^4\text{S}_{3/2}, ^4\text{I}_{15/2}$	4. $(^4\text{S}_{3/2} \rightarrow ^4\text{I}_{13/2}) : (^4\text{I}_{15/2} \rightarrow ^4\text{I}_{9/2}) - \hbar\omega$	0.84	0	0
$^2\text{H}_{11/2}, ^4\text{I}_{15/2}$	5. $(^2\text{H}_{11/2} \rightarrow ^4\text{I}_{9/2}) : (^4\text{I}_{15/2} \rightarrow ^4\text{I}_{13/2})$	38.31	1217	1902
$^4\text{I}_{13/2}, ^4\text{I}_{13/2}$	Er→Er up-conversion			
$^4\text{I}_{11/2}, ^4\text{I}_{11/2}$	1. $(^4\text{I}_{13/2} \rightarrow ^4\text{I}_{9/2}) : (^4\text{I}_{13/2} \rightarrow ^4\text{I}_{15/2}) + \hbar\omega$	47	42.2	1.47
$^4\text{I}_{11/2}, ^4\text{I}_{13/2}$	2. $(^4\text{I}_{11/2} \rightarrow ^4\text{F}_{7/2}) : (^4\text{I}_{11/2} \rightarrow ^4\text{I}_{15/2})$	4.15	30.36	32.11
$^4\text{I}_{13/2}, ^4\text{I}_{11/2}$	3. $(^4\text{I}_{11/2} \rightarrow ^4\text{F}_{9/2}) : (^4\text{I}_{13/2} \rightarrow ^4\text{I}_{15/2}) + 2\hbar\omega$	1.39	1.803	0.515
$^4\text{I}_{13/2}, ^4\text{I}_{11/2}$	4. $(^4\text{I}_{13/2} \rightarrow ^4\text{F}_{9/2}) : (^4\text{I}_{11/2} \rightarrow ^4\text{I}_{15/2}) + 2\hbar\omega$	0.027	0.24	0.515
$^4\text{I}_{9/2}, ^4\text{I}_{13/2}$	5. $(^4\text{I}_{9/2} \rightarrow ^4\text{S}_{3/2}) : (^4\text{I}_{13/2} \rightarrow ^4\text{I}_{15/2}) + \hbar\omega$	27.6	23.77	0
$^4\text{I}_{13/2}, ^4\text{I}_{9/2}$	6. $(^4\text{I}_{13/2} \rightarrow ^4\text{S}_{3/2}) : (^4\text{I}_{9/2} \rightarrow ^4\text{I}_{15/2}) + \hbar\omega$	0.61	0	0

The analytical form of concentration dependence of the constants of the luminescence self quenching and up-conversion are listed in Tables 4.

To compare calculated results with the experimental values of luminescence intensity, which represent the integrated signals of excited volume, we had to spatially integrate the calculated $N_i = n_i x N_Y$ magnitude over the excited volume ($N_Y = 1.39 \cdot 10^{22} \text{ cm}^{-3}$ is the number of substituted yttrium positions per unit volume). Since n_i itself strongly depends on a distance from irradiated crystal surface, numerical integration was carried out for fixed $x = 0.01 \div 1$ values.

Table 4. Analytical form of concentration dependence of the macrorates of the cross-relaxation processes of the luminescence self-quenching (α_i) and up-conversion (γ_i) in YLF: Er³⁺ crystals. Parameters were obtained for the jumping (J) and static (S) models using the calculated values of the transfer microparameters C_{DD} and C_{DA} from [1].

Model	Transition ($i \rightarrow j$) _a : ($k \rightarrow l$) _b	Parameters (α_i, γ_i), s^{-1}
S	($^4\text{I}_{9/2} \rightarrow ^4\text{I}_{15/2}$):($^4\text{I}_{15/2} \rightarrow ^4\text{I}_{13/2}$) - $\hbar\omega$	$\alpha_1 = 1.29 \cdot 10^2 x^2 + 3.35 \cdot 10^2 (x^2)^{4/3} + 2.85 \cdot 10^2 (x^2)^{5/3}$
J	($^4\text{F}_{9/2} \rightarrow ^4\text{I}_{11/2}$):($^4\text{I}_{15/2} \rightarrow ^4\text{I}_{13/2}$) - $2\hbar\omega$	$\alpha_2 = 1.91 \cdot 10^2 x^2$
S	($^4\text{S}_{3/2} \rightarrow ^4\text{I}_{9/2, 13/2}$):($^4\text{I}_{15/2} \rightarrow ^4\text{I}_{13/2, 9/2}$) - $\hbar\omega$	$\alpha_3 = 2.5 \cdot 10^3 x^2 + 5.75 \cdot 10^2 (x^2)^{4/3}$
J	($^2\text{H}_{11/2} \rightarrow ^4\text{I}_{9/2}$):($^4\text{I}_{15/2} \rightarrow ^4\text{I}_{13/2}$)	$\alpha_4 = 5.4 \cdot 10^3 x^2$
J	($^4\text{I}_{13/2} \rightarrow ^4\text{I}_{9/2}$):($^4\text{I}_{13/2} \rightarrow ^4\text{I}_{15/2}$) + $\hbar\omega$	$\gamma_1 = 2.26 \cdot 10^4 (n_i \cdot x)^2$
S	($^4\text{I}_{11/2} \rightarrow ^4\text{F}_{7/2}$):($^4\text{I}_{11/2} \rightarrow ^4\text{I}_{15/2}$)	$\gamma_2 = 8.9 \cdot 10^2 (n_i \cdot x)^2 + 3.35 \cdot 10^2 (n_i \cdot x)^{8/3} + 2.85 \cdot 10^2 (n_i \cdot x)^{10/3}$
J	($^4\text{I}_{11/2} \rightarrow ^4\text{F}_{9/2}$):($^4\text{I}_{13/2} \rightarrow ^4\text{I}_{15/2}$) + $2\hbar\omega$	$\gamma_3 = 1.0 \cdot 10^3 (n_i \cdot x) (n_i \cdot x)$
J	($^4\text{I}_{9/2} \rightarrow ^4\text{S}_{3/2}$):($^4\text{I}_{13/2} \rightarrow ^4\text{I}_{15/2}$) + $\hbar\omega$	$\gamma_4 = 1.0 \cdot 10^3 (n_i \cdot x) (n_i \cdot x)$

Excited volume was divided into layers, where n_i was assumed to be constant. For a fixed layer within excited volume located at the distance r from the sample surface, the pump power density P is determined by the Bouguer law: $P(r) = P_0 \exp(-\sum \sigma_{ij} n_i x N_Y r)$, where P_0 is the incident power density, $x = N_{Er}/N_Y$ is the relative concentration of dopant ions. $R_{ij} = \sigma_{ij} P/p_0$ are the rates of absorption transitions under the pumping radiation with the photon energy $p_0 = hc/\lambda_p$. According to the spectral composition of the emission of the LD-module, absorption can only occur from the ground $^4\text{I}_{15/2}$ and the second excited $^4\text{I}_{11/2}$ states. Absorption cross-section σ_{02} for the ground $^4\text{I}_{15/2}$ state was obtained from the experimental absorption spectra [5] and σ_{25} – absorption from $^4\text{I}_{11/2}$ state was taken from the excited state absorption spectrum [7].

Theoretical dependences of the steady-state populations of $^4\text{I}_{11/2}$ and $^4\text{I}_{13/2}$ levels on relative erbium concentration $x = 0 \div 1$ were calculated for the pump power densities used in experiments $P = 127, 223, 318$, and 395 kW/cm^2 (LD emission with the incident power, respectively, 1, 1.75, 2, and 3 W focused in a spot with 1 mm diameter).

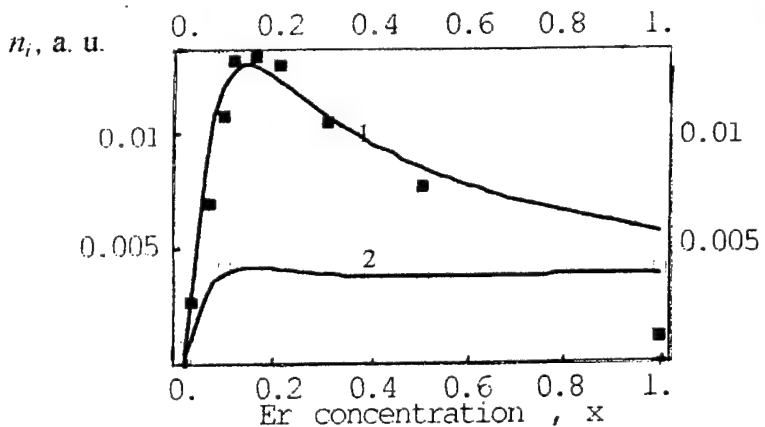


Fig. 2. Calculated (solid curves) and experimental (squares) concentration dependences of relative populations $N_i/N_Y = n_i x$ of the $^4\text{I}_{11/2}$ (curve 1) and $^4\text{I}_{13/2}$ (curve 2) working levels of $3\mu\text{m}$ laser transition on the Er concentration x under CW LD pumping in $\text{LiY}_{1-x}\text{Er}_x\text{F}_4$:Er crystals. Pump power density $R_{02} = 100 \text{ W} \cdot \text{cm}^{-2}$, $T = 300^\circ\text{K}$.

Experimental concentration dependences of populations of $^4I_{11/2}$ and $^4I_{13/2}$ erbium levels in YLF:Er³⁺ crystals with $x=0.003 \div 1$ were obtained from the luminescence spectra recorded at the same pump power densities. Under CW pumping, relative population of $^4I_{11/2}$ increases with erbium concentration up to the maximum in the region $N_{Er} \approx 10 \div 15$ at% and decreases for $N_{Er} > 20$ at%. Relative population of $^4I_{13/2}$ level increases with erbium concentration to ≈ 10 at% and remains constant within the range of high erbium concentration up to $N_{Er} > 50$ at%. Comparison of the calculated and experimental results are given in Fig. 2.

Experimental dependences of relative population of the $^4I_{11/2}$ and $^4I_{13/2}$ working levels of 3 μm transition on the pump power density were measured for all 11 samples with different erbium concentrations for pump power densities 57, 100, 141, and 175 W/cm^2 (LD emission with, respectively, 1, 1.75, 2, and 3 W – incident power focused in a spot with 1.5 mm diameter).

Fig. 3 shows experimental and theoretical data for the erbium concentration $x = 0.15$ ($N_0 = 15$ at. %).

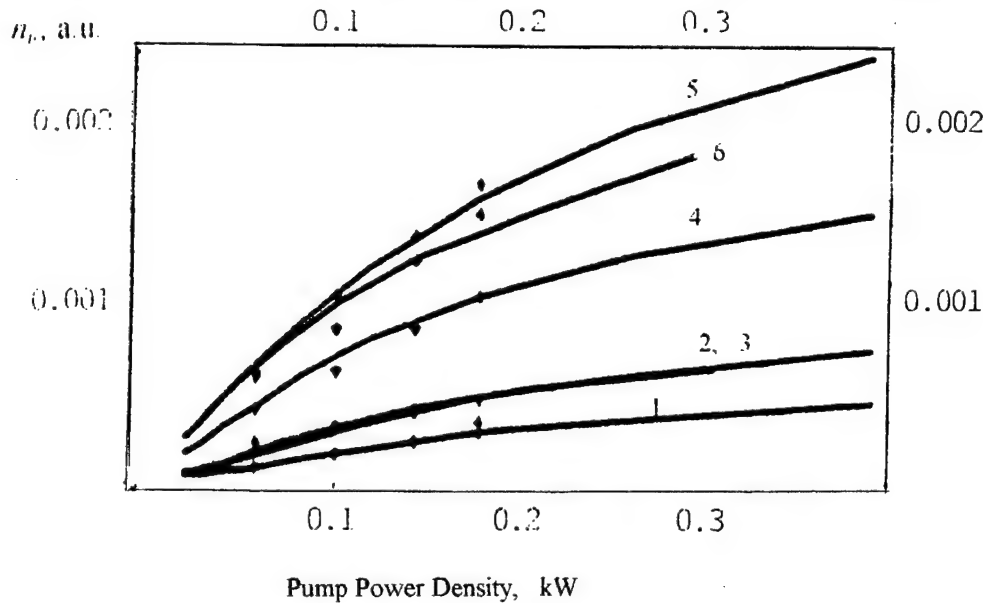


Fig. 3. Calculated (solid curves) and experimental (points) dependences of relative populations $N_r/N_0 = n_r x$ of the $^4I_{13/2}$ ($1 - 3$) and $^4I_{11/2}$ ($4 - 6$) erbium levels on pump power density R_{02} in $\text{kW}\cdot\text{cm}^{-2}$ under CW LD pumping in $\text{LiY}_{1-x}\text{Er}_x\text{F}_4$:Er crystals. The Er concentration $x = 0.05$ (curves 1, 4), 0.15 (curves 2, 5) and 0.3 (curves 3, 6), $T = 300^\circ\text{K}$.

Obtained theoretical results are in a good agreement with presented experimental data and also with results reported on experimental studies of the concentration dependence of the efficiency of 3 μm lasing in YLF:Er³⁺ on the $^4I_{11/2} \rightarrow ^4I_{13/2}$ transition under CW pumping of $^4I_{11/2}$ level [8-10]. The maximal slope efficiency of YLF:Er laser $\eta_{sl} = 50\%$ was obtained in crystals with erbium concentration $N_{Er} = 15$ at.% [8]. Noteworthy is that, in contrast with the data reported e. g. in [8], the theoretical model used in our work does not involve any fitting parameters. Therefore, one can conclude that the set of parameters used in our calculations for the intracenter radiative and non-radiative probabilities and the estimated macrorates of the inter-center energy transfer processes (selfquenching and upconversion) obtained by the model quantum-mechanical calculation could be further employed for estimation of the output characteristics of 2.8 μm YLF:Er³⁺ CW lasers and optimization of the composition of their active elements.

4. CONCLUSION

Theoretical calculations with the energy transfer constants of self-quenching and up-conversion obtained by the method of model quantum-mechanical calculation show good agreement with experimental results. One can conclude that population of the working levels of 3- μm laser transition in $\text{LiY}_{1-x}\text{Er}_x\text{F}_4$ ($x=0.003 \div 1$) can be reliably described with the rate balance equations allowing for the non-linear energy transfer processes with theoretically estimated transition probabilities and energy transfer rates.

Thus, proposed spectroscopic model of YLF:Er³⁺ crystals without any fitting parameters reliably describes experimental concentration and power dependences of the steady-state population of the erbium levels, and can be used for prediction of the laser properties of studied crystals.

5. ACKNOWLEDGMENTS

The work was partly supported by INTAS, Grant No INTAS-97-787, and Russian Foundation for Basic Researches, Grants No 98-02-18102 and 00-02-16637

6. REFERENCES

- 1 Tkachuk A M , Klokishner S I , and Petrov M V *Opt. Spectrosc. (USSR)* **59**, (4), pp 485-491, 1986
[*Opt. Spektrosk.* Vol 59, No 4, pp 802-811, 1985]
- 2 Klokishner S I , and Tkachuk A M *Opt. Spektrosk.* **68**, (4), pp 745-752, 1990
- 3 Tkachuk A M , Klokishner S I *Opt. Spectrosc. (USSR)*, **61**, (1), pp 55-61, 1986 [*Opt. Spektrosk.* **61**, (1), pp 84-90, 1986]
- 4 Tkachuk A M *Opt. Spectrosc. (USSR)*, **68**, (6), pp 775-783, 1990
[1990 *Opt. Spektrosk.* **68**, (6), pp 1324-1336, 1990]
- 5 Tkachuk A M , Poletimova A V , and Petrov M V *Opt. Spektrosk.* **59**, (5), pp 1136-1139, 1985
- 6 Li C , Guyot Y , Linares C , Moncorge R , and Joubert M -F *OSA Pros. of Advansed Solid State Lasers.* **15**, pp 91-95 1993
- 7 Labbe Ch *Theses, University of Caen, France* 1999
- 8 Tikerpae M , Jackson S D , and King T A *J. of Modern Optics* **45**, (6), pp 1269-1284 1998
- 9 Pollnau M , Luthy W , Weber H P , Jensen T , Huber G , Cassanho A , Janssen H P , McFarline R A
Opt. Lett. **21**, (1), pp 48-50 1996
- 10 Wyss Chr , Luthy W , Weber H P , Rogin P , Hulliger J *Opt. Commun.* **139**, pp 215-218, 1997

Upconversion processes, luminescence kinetics, and CW diode pumped 2.8 - μ m laser action in Er doped double fluoride crystals.

A.M.Tkachuk¹, I.A.Mironov¹, V. M.Reiterov¹, G.E.Novikov², O.A.Orlov²
H.-J.Pohl³, R.Steiner⁴, M. Edelmann⁴, and V.P.Gapontsev⁵

¹Federal-Russia Scientific Center "S.I.Vavilov State Optical Institute"

St. Petersburg, 199034, Russia. <tkachuk@mail.rcom.ru>

²Scientific Research Institute for laser Physics, 199034, St. Petersburg,

³Vitcon, 0-6900 Jena/Thuringen, Otto-Schott-Str.13, Germany, <pohl.vitcon@t-online.de>

⁴ University Ulm, Germany, <rudolf.steiner@ilm.uni-ulm.de>, <martin.edelmann@ilm.uni-ulm.de>.

⁵IPG Laser GmbH, Siemensstrasse, 7, D-57299 Burbach,
E-mail: valentingapontsev@compuserve.com

ABSTRACT

We studied theoretically and experimentally the luminescence decay from excited erbium levels and laser action at 2.8 μ m of lithium-yttrium double-fluoride $\text{LiYF}_4:\text{Er}^{3+}$ (YLF:Er³⁺) crystals. Experimental studies of the luminescence decay curves were carried out using selective laser excitation at $^4\text{I}_{13/2}$ level by Q-switch pulsed Yb-Er glass laser ($\lambda_{\text{pump}}=1.53\mu\text{m}$). The spectroscopic model was developed to simulate the population kinetics of excited Er levels, emitting in VIS and IR spectral regions including the 3 μm laser transition levels in YLF:Er³⁺ crystals. The rate equations for the six lowest energy levels of YLF:Er³⁺ were numerically solved for short pulse excitation. It is shown the theoretical and experimental results are in good agreement.

Single mode CW laser action at 2.8- μ m was demonstrated in YLF:Er³⁺ and $\text{BaY}_2\text{F}_8:\text{Er}^{3+}$ crystals under LD pumping for the first time. Output power as high as 0.32 W and slope efficiencies about 20% were obtained with YLF:Er³⁺ (10%) laser rod in longitudinal pump scheme. No spike structure was observed in output beam. The dependences of output power versus absorbed pump power were studied in laser rods with erbium concentrations 10 at.% using LD pumping module (Model DL-5M) with fiber output.

Keywords: crystal, doped ion, energy transfer, population kinetics, laser action.

1. INTRODUCTION

The double fluoride YLF:TR³⁺ crystals are well known as active laser media for laser operation in a wide spectral range from 0.325 to 2.8 μ m pumped with pulse lamps, solid-state lasers, and laser diodes. In the past several years, laser action of Er-doped crystals has been achieved in a wide spectral interval from 0.55 to 2.9 μ m under upconversion selective and laser diode pumpings. 3- μm solid-state CW lasers are of a great interest for numerous practical applications. The slope efficiency up to 50% was demonstrated at 2.8 μm in YLF:Er³⁺¹ under pumping at 973 nm, and output power 1.1 W was achieved in² under LD pumping. Optimal erbium concentrations in YLF:Er³⁺ and $\text{BaY}_2\text{F}_8:\text{Er}^{3+}$ crystals, 15 and 20 at. %, respectively, were found out^{1,3}.

It is known that in TR³⁺-doped crystals the possibility for obtaining the inversion population on the excited levels strongly depends on the ratio of the rates of the non-radiative energy transfer processes such as selfquenching, and nonlinear interaction of the excited states of rare-earth ions. These processes are mostly important for the selective pumping by LD, since they determine the rate of populating of laser transition levels and limit the output laser characteristics. The upconversion excitation or quenching processes strongly depend on pump power density can be induced by:

1. ground state absorption (GSA)
2. excited state absorption (ESA) or multistep absorption,
3. "avalanche" absorption.
4. non-radiative energy transfer (ET) via selfquenching and nonlinear quenching at cross-relaxation schemes,
5. co-operative (CC) ion-ion coupling.

Taking care about the possible applications of YLF: Er³⁺ lasers, we studied concentration dependences of

energy transfer rates (upconversion and selfquenching) in these crystals theoretically and experimentally. We elaborated YLF:Er³⁺ crystals among fluoride based single crystals as model system for which the main spectroscopic properties were studied previously. The spectroscopic model was considered to simulate the population kinetics of excited Er levels, emitted in VIS and IR. This model was used to determine the most important energy transfer processes, which should be taken into account for predicting of laser action and composition of active elements of VIS and IR YLF:Er³⁺ lasers. The rate equations for the six lowest energy levels of YLF:Er³⁺ were numerically solved for short pulse (Q-switched) excitation. It was shown the theoretical and experimental results were in good agreement.

Single mode CW laser action at 2.8- μ m in Er³⁺ doped YLF:Er³⁺ and BaY₂F₈:Er³⁺ crystals has been demonstrated under InGaAs laser diode (LD) pumping for the first time. Output power as high as 0.32 W and slope efficiencies about 20% were obtained with YLF:Er(10%) laser rod (diameter 5x3 mm³) in longitudinal pump scheme. No spike structure was observed in output beam. The dependences of output power versus absorbed pump power were studied in active elements with erbium concentrations 10 at.% using LD pumping module (Model DL-5M) with fibre output (core diameter 230 μ m) emitted at 966-982 nm up to 5W.

2. METHODS

2.1. Crystal growth.

The Er³⁺ doped double fluoride crystals YLF:Er³⁺ and BaY₂F₈:Er³⁺ were grown from carbon crucibles by the modified high vacuum Stockbarger technique from the stoichiometric fusion mixture. YLF-crystals are uniaxial, positive, having scheelite structure with lattice parameters $a = 5.175$ and $c = 10.74$ \AA . Space symmetry group of YLF crystals is C_{4h} , point symmetry group at the Y³⁺ site is S_4 . BaY₂F₈ - crystals are biaxial, having monoclinic structure with lattice parameters $a = 6.972$, $b = 10.505$, and $c = 4.260$ \AA , space symmetry group $-C_{2p}^3$, point symmetry group at the Y³⁺ site is C_2 . Er³⁺ substitution occurs at the Y³⁺ site, and charge compensation is not required.

The YLF:Er³⁺ samples for luminescent measurements were polished cubes with crystallographic "c"-axis oriented along one of the ribs. Low concentrated (0.3 at. %) crystals were used for measurements of life times of excited erbium levels; the luminescence kinetics was studied with samples YLF: Er³⁺ 15 at. %; high optical quality YLF:Er³⁺ and BaY₂F₈:Er³⁺ crystals doped with erbium (10 at. %) were used for preparing of laser active elements.

2.2. Luminescence kinetics.

The luminescence decay curves of YLF:Er³⁺ (15 at. %) crystal were studied under selective laser excitation in the $^4I_{13/2}$ (1.53 μ m) Er³⁺ level. To realize such selective excitation, an Yb-Er-glass laser operating at 1.5 μ m in Q-switch mode (output energy 7 mJ, pulse duration about 20 ns, and variable repetition rate) was used. Pump pulse energy was changed with neutral glass filters. To avoid the influence of pump pulse mode structure on the distribution of excited energy on the sample face, the laser emission was focused on the YLF:Er³⁺ sample with the focusing lens followed by a glass fibre with a core diameter 600 μ m. The luminescence kinetics was detected at the emission wavelength of $^4I_{11/2}$, $^4I_{9/2}$, $^4F_{9/2}$, $^4S_{3/2}$ and $^2H_{9/2}$ erbium levels at different pumping power densities. The sample luminescence was analyzed with a monochromator and detected with an photomultiplier tube. This experimental set-up was computer-controlled. The decay time were measured using a digital C9-8 oscilloscope. The dynamic range of detection exceeded three orders of magnitude.

2.3. Computer simulations.

The theoretical estimation of the ion-ion coupling microparameters was provided with the method of model quantum - mechanical calculation ^{4,7}. The energy transfer macrorates were determined using formulas of the known energy transfer theory. The calculated population kinetics of excited Er³⁺ levels were found as numerical solutions of the system of balance rate equations for the six lowest energy levels of YLF:Er³⁺ (15 at. %) after short pulse excitation.

2.4. Laser experiments.

Laser test was provided for YLF:Er³⁺ (10 at. %) and BaY₂F₈:Er³⁺ (10 at. %) crystals at CW LD pumping

and room temperature. Laser active elements were 3 mm in diameter and 5 mm length, oriented with optical axis "c" \parallel to rod axes. For CW pumping we used laser diode system (Model DL-5M, pig tale) with varied output power (5 W). System consists of six laser diodes emitting in spectral region $\lambda = 967\text{-}981$ nm, output emission from each of the laser diodes focused into the fibre with a core diameter of 250 μm (Model DL-5M). We used longitudinal pumping scheme, a nearly concentric cavity formed by one input flat mirror (HT at λ_{pump} , HR at λ_{las}) and one of 34 mm radius output mirror with high reflectivity ($\sim 98.5\%$) at 2.8 μm . The propagation of pump light was coincide with laser beam, cavity waist diameter was ~ 340 μm , laser rod with π - orientation was used.

3. RESULTS

We considered the correlation between the luminescent and laser properties of Er^{3+} -doped crystals with different Er concentration to check the spectroscopic model developed to simulate the population kinetics of the excited levels of laser transitions in YLF:Er^{3+} crystals. Energy level diagram of considered crystals and schemes of nonradiative coupling between doped ions are shown in Fig. 1. All processes involved into consideration which take place under IR excitation of YLF:Er^{3+} crystals are indicated by arrows and labelled as: A_{ij} - probability of radiative transition from level " i " to level " j ", W_{ij} - non-radiative transition probability, α_i - constant of energy transfer (selfquenching) via cross-relaxation processes between ions "a" and "b" ($n_i \rightarrow n_j$)_{a*}: ($n_i \rightarrow n_j$)_{b*}, and γ_i - constant of Er^{3+} - Er^{3+} nonlinear coupling (upconversion) via schemes ($n_i \rightarrow n_j$)_{a*}: ($n_k \rightarrow n_l$)_{b*}. Numeration of Er^{3+} levels and coupling processes are shown in Fig. 1.

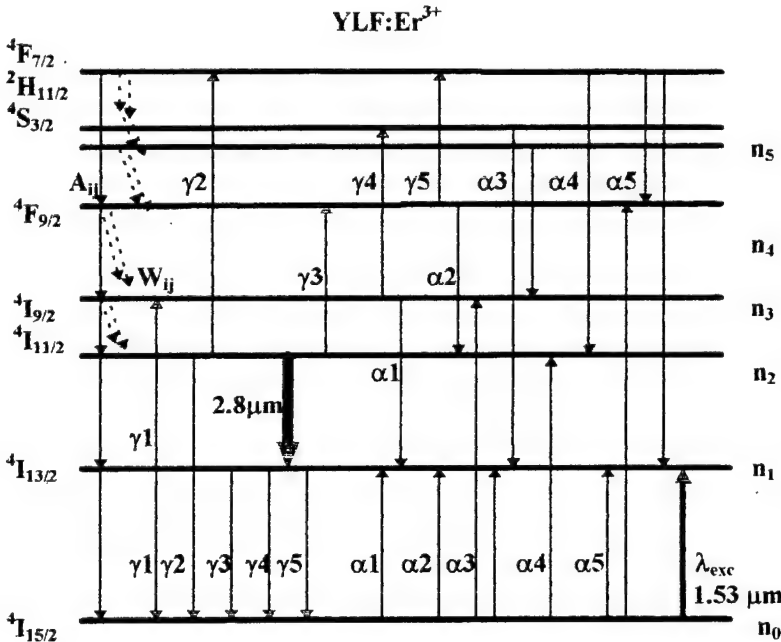


Fig. 1. Energy levels and schemes of radiationless Er-Er coupling: A_{ij} - radiative $i \rightarrow j$ transition probabilities, W_{ij} - radiationless relaxation rates, α_i - self-quenching and γ_i - upconversion processes. Bold arrow - 2.8 μm laser transition.

3.1. Balance rate equations.

The rate equations for the six lowest energy levels of YLF:Er^{3+} have been solved numerically for nanosecond pulse (δ -function) excitation. The system of balance rate equations for YLF:Er^{3+} crystal and normalized populations $n_i = n_i(\text{Er})/N(\text{Er})$, where $N(\text{Er})$ is the concentration of Er^{3+} ions in crystal, was:

$$dn_i/dt = -A_{10}n_1 + \sum_{i=2}^5 A_{ii}n_i + 2\alpha_1n_0n_3 + \alpha_2n_0n_4 + \alpha_3n_0n_5 + \alpha_5n_0n_5 - 2\gamma_1(n_1)^2 - \gamma_3n_1n_2 - \gamma_4n_1n_3 - \gamma_5n_1n_4$$

Table 1. Notation of the energy transfer parameters and corresponding cross-relaxation processes.

	Parameter, Transition $(i \rightarrow j)_a$: $(k \rightarrow l)_b$
n_5	$\alpha_1 ({}^4\text{I}_{9/2} \rightarrow {}^4\text{I}_{15/2})$: $({}^4\text{I}_{15/2} \rightarrow {}^4\text{I}_{13/2}) - h\omega$
n_4	$\alpha_2 ({}^4\text{F}_{9/2} \rightarrow {}^4\text{I}_{11/2})$: $({}^4\text{I}_{15/2} \rightarrow {}^4\text{I}_{13/2}) - 2h\omega$
n_3	$\alpha_3 ({}^4\text{S}_{3/2} \rightarrow {}^4\text{I}_{9/2}, {}^4\text{I}_{13/2})$: $({}^4\text{I}_{15/2} \rightarrow {}^4\text{I}_{13/2}, {}^4\text{I}_{9/2}) - h\omega$
n_2	$\alpha_4 ({}^4\text{F}_{7/2} \rightarrow {}^4\text{I}_{11/2})$: $({}^4\text{I}_{15/2} \rightarrow {}^4\text{I}_{11/2})$
n_1	$\alpha_5 ({}^4\text{F}_{7/2} \rightarrow {}^4\text{F}_{9/2}, {}^4\text{I}_{13/2})$: $({}^4\text{I}_{15/2} \rightarrow {}^4\text{I}_{13/2}, {}^4\text{F}_{9/2})$
n_0	$\gamma_1 ({}^4\text{I}_{13/2} \rightarrow {}^4\text{I}_{9/2})$: $({}^4\text{I}_{13/2} \rightarrow {}^4\text{I}_{15/2}) + h\omega$ $\gamma_2 ({}^4\text{I}_{11/2} \rightarrow {}^4\text{F}_{7/2})$: $({}^4\text{I}_{11/2} \rightarrow {}^4\text{I}_{15/2})$ $\gamma_3 ({}^4\text{I}_{11/2} \rightarrow {}^4\text{F}_{9/2})$: $({}^4\text{I}_{13/2} \rightarrow {}^4\text{I}_{15/2}) + 2h\omega$ $\gamma_4 ({}^4\text{I}_{9/2} \rightarrow {}^4\text{S}_{3/2})$: $({}^4\text{I}_{13/2} \rightarrow {}^4\text{I}_{15/2}) + h\omega$ $\gamma_5 ({}^4\text{F}_{9/2} \rightarrow {}^4\text{F}_{7/2})$: $({}^4\text{I}_{13/2} \rightarrow {}^4\text{I}_{15/2}) + 2h\omega$

$$\begin{aligned}
dn_2/dt = & - \sum_{j=0}^1 A_{2,j} n_2 + \sum_{i=3}^5 A_{i,2} n_i + W_{32} n_3 + \alpha_2 n_0 n_4 + 2\alpha_4 n_0 n_5 - 2\gamma_2(n_2)^2 - \gamma_3 n_1 n_2 \\
dn_3/dt = & - \sum_{j=0}^2 A_{3,j} n_3 - W_{32} n_3 + \sum_{i=4}^5 A_{i,3} n_i + W_{43} n_4 - \alpha_1 n_0 n_3 + \alpha_3 n_0 n_5 + \gamma_1(n_1)^2 - \gamma_4 n_1 n_3 \\
dn_4/dt = & - \sum_{j=0}^3 A_{4,j} n_4 - W_{43} n_4 + (A_{54} + W_{54}) n_5 - \alpha_2 n_0 n_4 - \alpha_5 n_0 n_5 + \gamma_3 n_1 n_2 - \gamma_5 n_1 n_4 \\
dn_5/dt = & - \sum_{j=0}^4 A_{5,j} n_5 - W_{54} n_5 = (\alpha_3 + \alpha_4 + \alpha_5) n_0 n_5 + \gamma_2(n_2)^2 + \gamma_4 n_1 n_3 + \gamma_5 n_1 n_4 \\
n_0 + n_1 + n_2 + n_3 + n_4 + n_5 = & I
\end{aligned} \tag{1}$$

Initial conditions for YLF:Er³⁺ direct pumping into ⁴I_{13/2} Er level ($\lambda = 1.53 \mu\text{m}$) by short pulse ($t_{\text{pulse}} = 20 \text{ ns}$) were:

$n_0 = 0.6$; $n_1 = 0.4$; $n_2 = 0$; $n_3 = 0$; $n_4 = 0$; $n_5 = 0$. Pulse duration was considered as δ - function.

Here A_{ij} [c^{-1}] are the probabilities of radiative transitions from "i" to "j" levels; W_{ij} [c^{-1}] are the probabilities of non-radiative multiphonon transitions; parameters α_i ($i = 1 - 5$) are the macrorates for self-quenching processes, and parameters γ_j ($j = 1 - 5$) are the macrorates of up-conversion processes for the cross-relaxation schemes indicated by arrows in Fig. 1. Notation of the energy transfer parameters and corresponded cross-relaxation processes are indicated in Table 1.

Parameters of radiative (A_{ij}) and non-radiative (W_{ij}) relaxation for YLF:Er³⁺ and life times of excited levels are studied in ⁸⁻¹⁰, energy transfer parameters α_i and γ_i were estimated using microparameters of migration C_{DD} and selfquenching C_{DA} which were obtained by the model quantum-mechanical calculation in ⁴⁻⁷ within the framework of electro-static (multipole-multipole) interaction of erbium ions. From the ratio of C_{DD} and C_{DA} microparameters, the transfer mechanisms were determined and macrorates were estimated for the self-quenching and upconversion processes using jump (J) or static (S) decay models ¹¹⁻¹⁷. Energy transfer rates for jump model were calculated using formula :

$$W_{DA}^J = \frac{4\pi^3 \sqrt{2\pi}}{9} N_A^2 (C_{DA}^{dd} \cdot C_{DD}^{dd})^{1/2}, \tag{2}$$

where N_A is the concentration of Er ions, and C_{DD}^{dd} and C_{DA}^{dd} are taken from ⁴.

The selfquenching parameters α_i were estimated on the basis of experimental and theoretical studies of the luminescence selfquenching in YLF:Er³⁺ crystals with different erbium concentrations: from 0.5 to 100 at. %. It was shown ⁷ that selfquenching of ⁴S_{3/2} erbium levels can be described in static model. In this case the value of selfquenching rate $W_{DA}^{SQ}(N_A)$ we determined as "effective" decay rate ¹⁶ $W^{\text{eff}} = (\tau_m)^{-1}$, where

$$\tau_m = \int_0^\infty t \cdot I_{\text{exp}}(t) dt / \int_0^\infty I_{\text{exp}}(t) dt. \tag{3}$$

Here $I_{\text{exp}}(t)$ is the experimental luminescence decay of ⁴S_{3/2} erbium levels in YLF:Er³⁺ recorded under their resonant selective pumping by second harmonic pulses of Q-switch YAG:Nd³⁺ laser. For description of selfquenching of ⁴F_{9/2} erbium levels J model was used.

As a result we have obtained the effective values of the energy transfer rates and the analytical form of their concentration dependences for all schemes of cross-relaxation transitions, shown in Fig. 1.

Upconversion constants γ_i were estimated using calculated microparameters and formulas from ^{5,6}. Macrorates of upconversion processes γ_{ij} were calculated in accordance with coupling model, using energy transfer formulas from ^{5,10}, in which the concentration of erbium ions participating in upconversion process was equal to the concentration of excited erbium ions: $N_A \equiv N_i^*$. For example in jumping model ($C_{DD}^{dd} / C_{DA}^{dd,NC} \gg 1$) we used formula (2), in the case of static model ($C_{DD}^{dd} / C_{DA}^{dd,NC} \ll 1$) we used formulas from ⁵. The number of excited at ⁴I_{13/2} level ions $N_i(t=0)$ was estimated in accordance with experimental conditions and the values of absorption cross section from ground (GSA) and excited (ESA) states at $\lambda = 1.53 \mu\text{m}$: $\sigma_{\text{GSA}} = 6 \cdot 10^{-21} \text{ cm}^2 (\pi + \sigma)$, $\sigma_{\text{ESA}} < 10^{-22} \text{ cm}^2$. Normalized energy transfer parameters α_i and γ_k which were substituted into the rate balance equations are listed in Table 2.

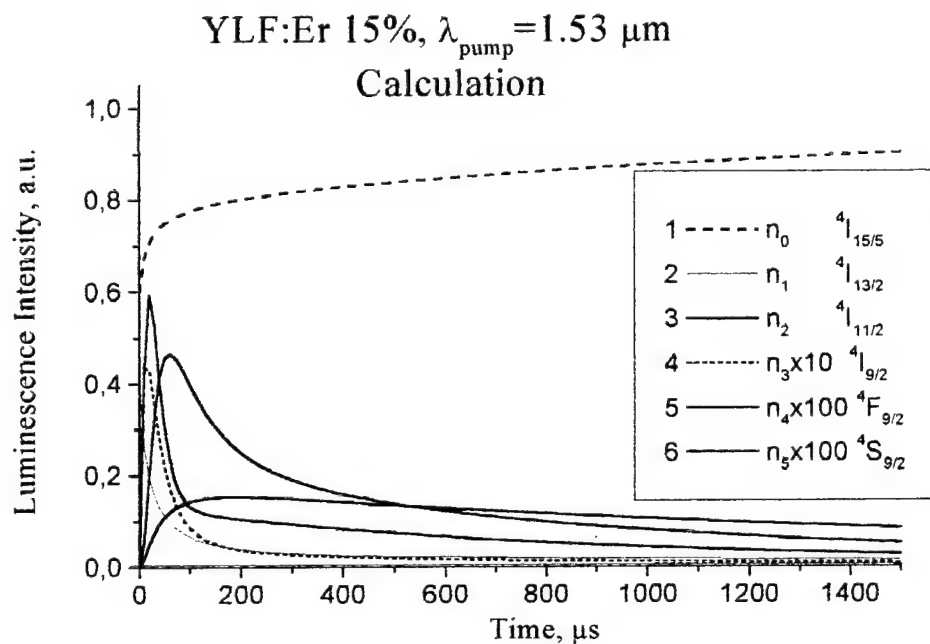
Table 2. The values of normalized parameters of energy transfer. α_i - the rate of selfquenching and γ_i - the rate of upconversion for YLF:Er³⁺ (15 at. %) crystal. Notation of the processes is given in Fig. 1.

Parameter of selfquenching	Selfquenching rate, α_i, ms^{-1}	Model	Parameter of upconversion	Upconversion rate, γ_i, ms^{-1}	Model
α_1	$4.3 \cdot 10^3$	Jump	γ_1	$6.5 \cdot 10^4$	Jump
α_2	$4.9 \cdot 10^3$	Jump	γ_2	$4.2 \cdot 10^3$	Jump
α_3	$7.5 \cdot 10^4$	Jump \approx Static	γ_3	$9.6 \cdot 10^3$	Jump
α_4	$2.0 \cdot 10^4$	Jump	γ_4	$6.5 \cdot 10^4$	Jump
α_5	$2.7 \cdot 10^4$	Jump	γ_5	$0.1 \cdot 10^2$	Jump

3.2. Results of computer simulations.

The calculated luminescence kinetics for different Er³⁺ levels at "high" pump power density (P_0) are shown in Figs 2a and 2b.

a)



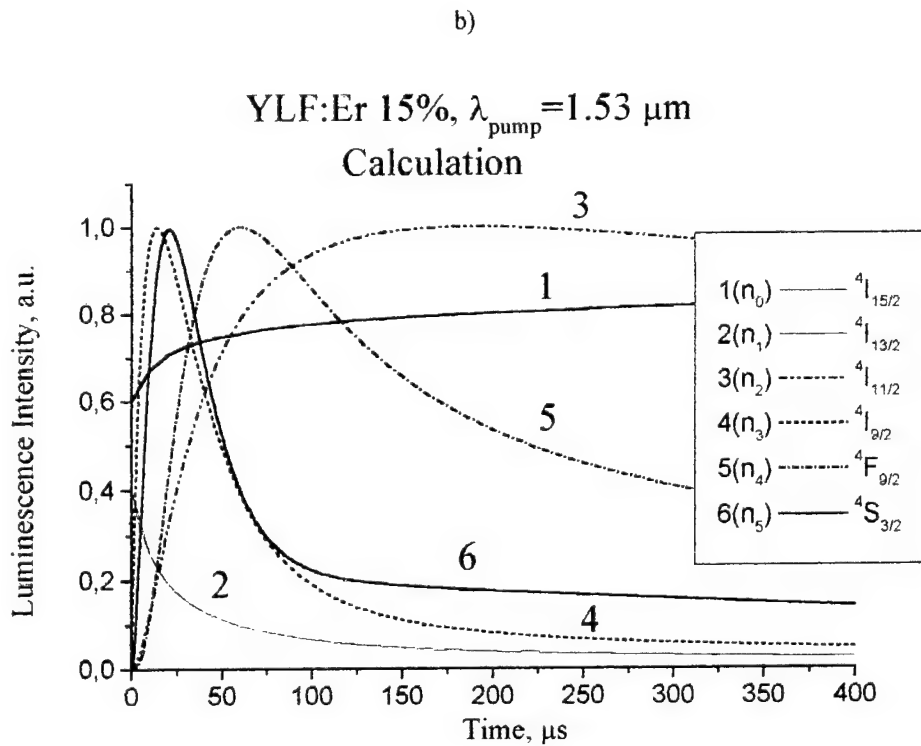


Fig. 2. The calculated luminescence kinetics for different Er^{3+} levels in YLF:Er $^{3+}$ (15 at. %) at "high" pump power density (P_0) in different time scales. a) Time dependences of relative populations n_i of six Er^{3+} levels. b) Time dependences of normalized relative populations ($n_i/n_{i,\text{max}}$) of erbium levels: 1 - $^4\text{I}_{15/2}$, 2 - $^4\text{I}_{13/2}$, 3 - $^4\text{I}_{11/2}$, 4 - $^4\text{I}_{9/2}$, 5 - $^4\text{F}_{9/2}$, 6 - $^4\text{S}_{3/2}$.

In Fig. 2 the calculated luminescence kinetics are shown for different excited Er^{3+} levels in YLF:Er $^{3+}$ (15 at. %) at "high" pump power density ($P_0 \approx 1 \text{ kW/cm}^2$). Pumping by short pulse (δ - function) with $\lambda_{\text{pump}} = 1.53 \mu\text{m}$ corresponded to transition $^4\text{I}_{15/2} \rightarrow ^4\text{I}_{13/2}$. The calculation demonstrated different rates of non-radiative cross-relaxation processes responsible for luminescence in visible and IR spectral ranges of YLF:Er $^{3+}$ crystals. As follows from the results in Fig. 2 the population inversion can be achieved between $^4\text{I}_{11/2}$ and $^4\text{I}_{13/2}$ levels in YLF:Er $^{3+}$ (15 at. %) crystal under pulse excitation with $\lambda = 1.53 \mu\text{m}$ in time interval $t > 50 \mu\text{s}$ after pumping and lasts several ms. The highest rates of upconversion processes can be achieved for the $^4\text{I}_{9/2}$ and $^4\text{S}_{3/2}$ levels (curves 4 and 6 in Fig. 2).

3.3. Experimental luminescence decay in YLF:Er $^{3+}$ crystals.

To verify the spectroscopic model of studied crystals we recorded the luminescence kinetics from erbium excited levels after excitation by a short pulse at $\lambda = 1.53 \mu\text{m}$ of Q-switch Er-glass laser. Experimental (a) and calculated (b) decay curves (normalised to 1) for YLF:Er $^{3+}$ (15 at. %) are shown in Fig 3.

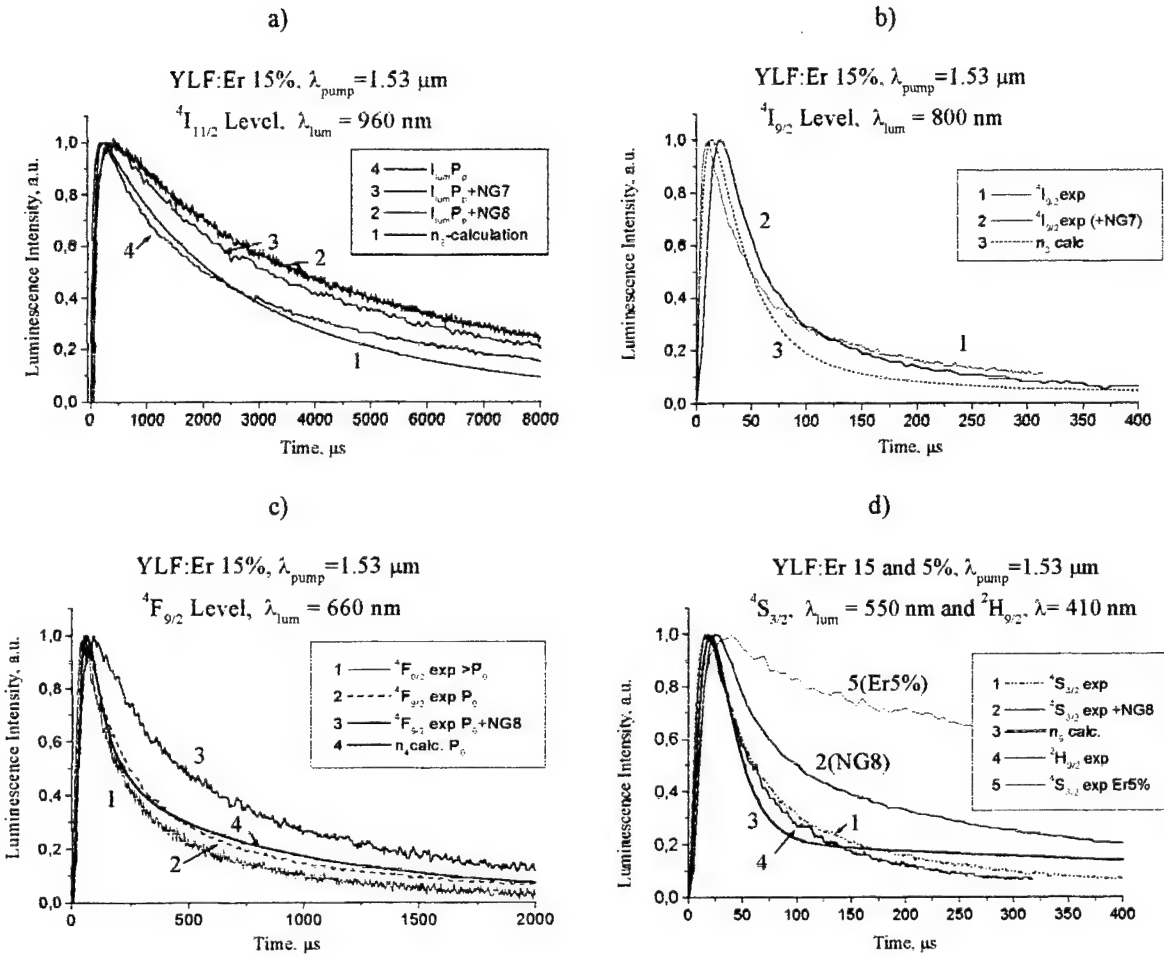


Fig. 3. Normalized experimental $I_{\text{lum}}(t)$ and calculated $n_i(t)$ luminescence kinetics for YLF:Er (15 at. %) crystal under upconversion excitation by Q-switch Yb-Er glass laser ($\lambda=1.53 \mu\text{m}$) under conditions of “high” and “lower” pump density ($P_0 \approx 1 \text{ kW/cm}^2$ or P_0 attenuated with neutral glasses NG7 or NG8). Luminescence decay curves recorded for transitions from different excited Er^{3+} levels: $^4\text{I}_{11/2}$ (a), $^4\text{I}_{9/2}$ (b), $^4\text{F}_{9/2}$ (c), $^4\text{S}_{3/2}$ (d, curves 1-3), $^2\text{H}_{9/2}$ (d, curves 4) in YLF:Er $^{3+}$ (15 at. %) (a-d), and $^4\text{S}_{3/2}$ in YLF:Er $^{3+}$ (5 at. %) – (d, curve 5). Decay curves recorded under lower pump power density are indicated as “+NG7” or “NG8”, accordingly.

3.4. Discussion

Comparison of experimental $I_{\text{lum}}(t)$ and calculated $n_i(t)$ luminescence kinetics for YLF:Er $^{3+}$ (15 at. %) crystal in Fig. 3 showed a good agreement for experimental and calculated population kinetics of the $^4\text{I}_{11/2}$ (a), $^4\text{I}_{9/2}$ (b), $^4\text{F}_{9/2}$ (c) erbium levels as well as close correlation between experimental and calculated curves for $^4\text{S}_{3/2}$ (d, curves 1-3) level in YLF:Er $^{3+}$ (15 at. %). The main results are as follows: population kinetics of all excited Er^{3+} levels strongly depend on the pump power density. Intensities of the VIS luminescence from $^4\text{F}_{9/2}$ and $^4\text{S}_{3/2}$ levels nonlinearly increase with pump power density and its decay rates change in accordance with the rate of upconversion coupling (see decay curves under high and lower pump power densities). For example, the $^4\text{S}_{3/2}$ and $^4\text{F}_{9/2}$ Er^{3+} level populations increase by ~ 100 times while pump power density increases by 10 times.

The influence of the erbium concentration on the rate of upconversion process is illustrated on the example of luminescence decay from $^4\text{S}_{3/2}$ level in crystals doped with 15 % (d, curves 1, 2) and 5 % (d, curve 5) of erbium ions (curves 1 and 5 in Fig. 3d) recorded under the same pumping conditions. The maximal population of $^4\text{S}_{3/2}$ level rapidly increased with erbium concentration, and its decay became faster. Moreover, in high concentrated samples the luminescence from highest $^2\text{H}_{9/2}$ was recorded. Curve 5 in Fig. 3d represents the luminescence kinetics at $\lambda \approx 410 \text{ nm}$ corresponding to $^2\text{H}_{9/2} \rightarrow ^4\text{I}_{15/2}$ transition. Upconversion processes ($^4\text{S}_{3/2}, ^4\text{I}_{13/2} \rightarrow ^4\text{I}_{15/2}$):($^4\text{I}_{13/2}, ^4\text{S}_{3/2} \rightarrow ^2\text{H}_{9/2}$) is

responsible for excitation of $^2\text{H}_{9/2}$ level and this conclusion is confirmed by the fact that luminescence decay curve for $^2\text{H}_{9/2}$ level is close to that for luminescence from $^4\text{S}_{3/2}$.

Obtained results permit us to explain the efficiency of upconversion processes responsible for laser action of YLF:Er crystals in VIS and IR spectral regions achieved under IR pumping by LD ($\lambda=1.53\text{ }\mu\text{m}$) [18], and by Ti-sapphire laser ($\lambda=969.3\text{ nm}$ or 769.9 nm) [19], and we can make the conclusion that obtained results are useful for optimization of laser rods' composition for upconversion LD pumped lasers, especially for laser action in visible spectral range.

3.5. Laser experiments

Single mode CW laser action of YLF:Er³⁺ and BaY₂F₈:Er³⁺ crystals at wavelength corresponding to 4I11/2 \rightarrow 4I13/2 transition was achieved with slope efficiency $\sim 20\%$ and $\sim 13\%$ and output power 320 and 210 mW respectively. Experiments were provided with π - oriented YLF:Er³⁺ and non-oriented BaY₂F₈:Er³⁺ laser rods (diameter 3 mm and length 5 mm). Lasing of YLF:Er³⁺ at $2.8\text{ }\mu\text{m}$ was obtained in the CW single transverse mode. No spike structure was observed in output beam. Output power about 320 mW was achieved in longitudinal pump scheme with YLF:Er³⁺ and about 220 mW with BaY₂F₈:Er³⁺. The dependences of output power versus absorbed pump power are shown in Fig. 4. The laser action of YLF:Er³⁺ and BaY₂F₈:Er³⁺ crystals was studied in laser rods with erbium concentrations 10 at.-% using LD pumping module (Model DL-5M) with fibre output (core diameter 230 μm) emitted at 966-982 nm up to 5W.

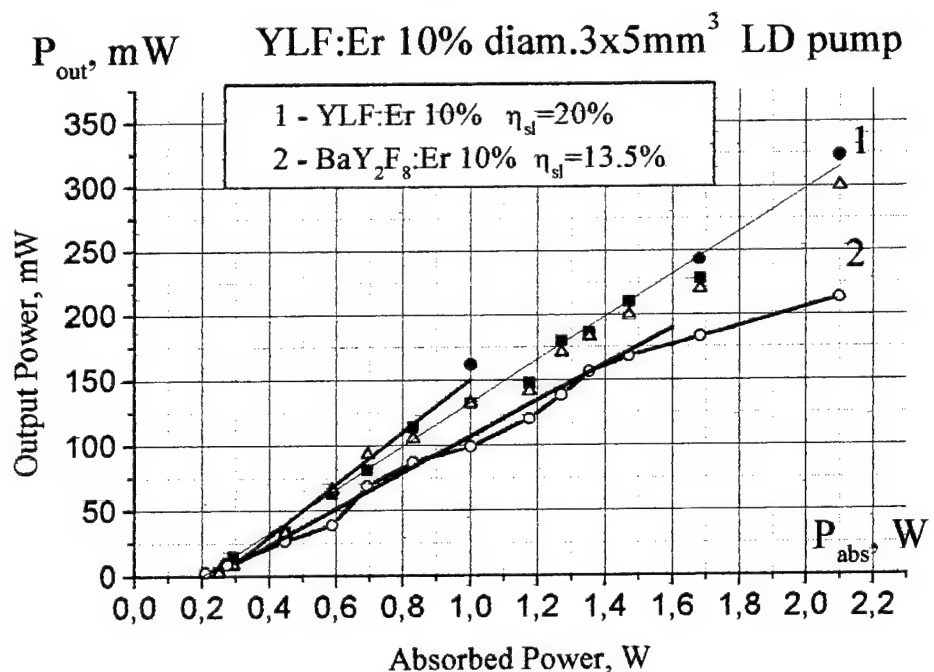


Fig. 4. The dependences of output power versus absorbed pump power for 1. YLF:Er³⁺ (squares, triangles and solid circles) and 2. BaY₂F₈:Er³⁺ (open circles) crystals. Points are experimental data, straight lines are linear fittings.

4. CONCLUSION

Our results demonstrate feasibility of spectroscopic model of YLF:Er³⁺ crystals and the possibility for using this model to estimate conditions of formation of population inversion on different Er³⁺ laser transitions and optimization of laser rod composition for laser action in different spectral ranges. It was shown that upconversion processes induced by non-radiative Er³⁺ - Er³⁺ coupling are responsible for luminescence of YLF:Er³⁺ in visible spectral range under IR ($\lambda=1.53 \mu\text{m}$) excitation. The upconversion-pumped blue luminescence from $^2\text{H}_{9/2}$ level was demonstrated. It was shown that fluoride crystals are promising laser media for LD pumped solid-state VIS lasers and for development of new solid-state UV lasers with upconversion pump schemes.

Single mode CW laser action at 2.8- μm in Er doped YLF:Er³⁺ and BaY₂F₈:Er³⁺ crystals has been demonstrated under InGaAs laser diode (LD) pumping for the first time. Output power as high as 0.32 W and slope efficiencies about 20% were obtained with YLF:Er³⁺ (10%) laser rod (diameter 5x3 mm³) in longitudinal pump scheme. No spike structure was observed in output beam.

5. ACKNOWLEDGMENTS

The work was partly supported by German Ministry of Science, Projects No. 13N7039 and 13N7508, INTAS, Grant No. 97-0787, and Russian Foundation for Basic Researches, Grant No. 00-02-16637.

6. REFERENCES

1. Wyss Chr., Luthy W., Weber H.P., Rogin P., Hulliger J. *"Optics Comm."* **139**, pp. 215-218, 1997
2. Jensen T., Diening A., Huber G., and Chai B.H.T. *Optics Lett.* **21**, pp. 585, 1996
3. Pollnau M., Luthy W., Weber H.P., Jensen T., Huber G., Cassanho A., Jenssen H.P., MacFarline R.A. *Opt. Lett.* **21**, (1), pp. 48-50.
4. Tkachuk A.M., Klokishner S.I., and Petrov M.V. *Opt. Spectrosc. (USSR)*. **59**, (4), pp. 485-491, 1986 [*Opt. Spektrosk.* Vol. 59, No. 4, pp. 802-811, 1985]
5. Klokishner S.I., and Tkachuk A.M. *Opt. Spektrosk.* **68**, (4), pp. 745-752, 1990.
6. Tkachuk A.M., Klokishner S.I. *Opt. Spectrosc. (USSR)*, **61**, (1), pp. 55-61, 1986 [*Opt. Spektrosk.* **61**, (1), pp. 84-90, 1986]
7. Tkachuk A.M. *Opt. Spectrosc. (USSR)*, **68**, (6), pp. 775-783, 1990. [*1990 Opt. Spektrosk.* **68**, (6), pp. 1324-1336, 1990]
8. Tkachuk A.M., Poletimova A.V., and Petrov M.V. *Opt. Spectrosc.* **59**, (5), pp. 1136-1139, 1985
9. Li C., Guyot Y., Linares C., Moncorge R., and Joubert M.-F. *OSA Pros. of Advansed Solid State Lasers*. **15**, pp. 91-95, 1993.
10. Labbe Ch. *Theses, University of Caen, France*. 1999.
11. Burshtein, A.I. *JETP*, **84**, (6), pp. 2001-2012, 1983
12. Burshtein, A.I., Sackun V.P. *Chem. Phys. Lett.* **103**, pp. 205-208, 1983.
13. Vugmeister B.E. *FTT*. **25**, pp. 2796-2798.
14. Kushida T. *Izv. Akad. Nauk SSSR, Ser. Fis.* **37**, (2), pp. 273-283.
15. Grant J.C.W. *Phys. Rev.* **B4**, p. 548, 1971.
16. Inokuti M., Hirayama F. *J. Chem. Phys.* **43**, p.1978-, 1965.
17. Voronko Ju.K., Mamedov T.G., Osiko V.V. *JETP*. **71**, (2), pp. 478-49.
18. Pollak S.A., Chang D.B., and Birnbaum M. *Appl. Phys. Lett.* **54**, (10), 1989.
19. Hebert T., Wannemacher R., Macfarline R.M., Lenth W. *Appl. Phys. Lett.* **57**, (17), 1990.

First-principle calculation for absorption spectrum of Cr⁴⁺:Ca₂MgSi₂O₇ (åkermanite)

T. Ishii^a, K. Fujimura^a, K. Ogasawara^a, I. Tanaka^b, and H. Adachi^a

^aDepartment of Materials Science and Engineering, Kyoto University, Kyoto 606-8501 Japan

^bDepartment of Energy Science and Technology, Kyoto University, Kyoto 606-8501 Japan

ABSTRACT

Peak energy and intensity in absorption spectrum of Cr⁴⁺:Ca₂MgSi₂O₇ (åkermanite) were calculated by first-principles method, which we have developed. We investigated the dependence on size of cluster models with [CrO₄]⁴⁻ (without point charges added), [CrO₄]⁴⁻ (with additional point charges), and [CrCa₆Mg₂SiO₃₈]⁵²⁻ models. All the models have low C_s symmetry at Cr⁴⁺ site. The best agreement with experimental spectrum was obtained in the larger [CrCa₆Mg₂SiO₃₈]⁵²⁻ model on the relative peak splittings which originate from the low symmetry, on the spectral anisotropy, and on the relative intensity. We conclude that the covalency between ligands and the outside cations have to be considered for the better description of spectrum in system with low symmetry.

Keywords: *Ab-initio* calculation, molecular orbital method, multiplet structure, impurity color center

1. INTRODUCTION

In the last decade, Cr⁴⁺-doped materials have been intensively studied, one of whose purpose is the application as solid-state lasers whose radiation is in near-infrared region. The first report on the laser action was in chromium-doped forsterite.¹ Interests on the spectral assignment had lead to studies from theoretical approaches. The most popular and simplest method for the analysis of optical absorption spectra produced by impurity color center has been the Tanabe-Sugano method² which is based on the ligand field theory. For the crystal system with low symmetry, M. F. Hazenkamp *et al.* applied the angular overlap model to Cr⁴⁺: Mg₂SiO₄ (forsterite) and Cr⁴⁺: Ca₂GeO₄ systems.³ The method successfully explained the large peak splittings and the spectral anisotropy due to the low symmetry. These methods handled the electronic states relevant to absorption spectra by use of some simplified empirical parameters. It would be indeed true that the larger the number of the parameters is introduced, the better the agreement between the calculated and experimental spectra becomes. However, when we introduce so many parameters, the ambiguity to determine them should become an inevitable problem, especially in the system with low symmetry. To avoid the ambiguity, *ab-initio* calculation is desired. For Cr⁴⁺: YAG system, A. B. Sobolev *et al.*⁴ investigated the electronic states by cluster method, and discussed the valence state of chromium ion. More recently, W. Y. Ching *et al.*⁵ conducted a band calculation, and proposed a model for the excited state absorption. Those methods under one-electron description, however, could not directly give the multiplet states which corresponded to the peaks in the absorption spectrum. For the direct discussion of energies of the multiplet states, Wissing *et al.*⁶ conducted a cluster calculation for Cr⁴⁺: Ca₂GeO₄ system. Since the method also lied under one-electron approximation, and the multiplet energy depended on an analytical result, their result, however, could only give the average energies of the multiplet states in hypothetical T_d symmetry, and could not discuss the large peak splittings and the spectral anisotropy derived from the low symmetry of the crystal.

In these three years, we have developed a general *ab-initio* method, the DV-ME method, for direct calculation of electronic structure that involve many-electron effect.⁷ The method had been applied especially to the systems concerning d-d transition, and had been confirmed to reproduce the peak energies in some optical absorption spectra of ruby, emerald, and other Cr³⁺-doped crystals.⁸ What is different in the DV-ME method compared to the traditional methods can be briefly summarized in the following three characteristics. The first characteristic of

Correspondence: Takugo Ishii. Phone: +81-75-753-5435; Fax: +81-75-753-5447; E-mail address: tack@dvxa4.MTL.kyoto-u.ac.jp. Research Fellow of the Japan Society for the Promotion of Science (JSPS Research Fellow.) Supported by a Grant-in-Aid for Scientific Research from the Ministry of Education, Sports, and Culture.

the DV-ME method is that the method can be applied to any symmetry (independent of analytical results), so that we can discuss spectral anisotropy. Secondly, the method has fundamentally no limitation on the size of cluster model (the maximum size just depends on the ability of computers used), so we can directly consider the effects of ions and defects outside ligands upon multiplet states (not in one-electron description). The last characteristic is that the DV-ME method gives us the transition probability of electric dipole transition, as the many-electron wave functions are explicitly obtained.

Our purpose in this study is to apply our DV-ME method to the calculation of optical absorption spectrum of Cr⁴⁺-doped Ca₂MgSi₂O₇ (åkermanite), and to confirm the applicability of the method to the crystal system with low symmetry. Additionally, we confirm the importance to consider ions outside ligands.

2. METHOD

2.1. DV-ME method

The DV-ME method⁷ is based on the *ab-initio* molecular orbital method within the framework of density functional theory. The based computational code is SCAT code.⁹ The applied exchange-correlation potential is X α potential. The *i*-th molecular orbital (MO) is expressed as a linear combination of atomic orbitals χ_k , such as,

$$\varphi_i(\mathbf{r}_1) = \sum_{k=1}^m c_{ik} \chi_k(\mathbf{r}_1), \quad (1)$$

where c_{ik} are the coefficients of the linear combination. The calculation is conducted with use of cluster model in which the information of crystal structure is included with the corresponding symmetry.

After finished the cluster calculation within one-electron approximation, *l*-th wave function of *N*-electron system Ψ_l is constructed as a linear combination of Slater determinants Φ_j , and is expressed as,

$$\begin{aligned} \Psi_l(\mathbf{r}_1, \mathbf{r}_2, \dots, \mathbf{r}_N) &= \sum_{j=1}^s C_{lj} \Phi_j(\mathbf{r}_1, \mathbf{r}_2, \dots, \mathbf{r}_N), \\ \Phi_j(\mathbf{r}_1, \mathbf{r}_2, \dots, \mathbf{r}_N) &= \frac{1}{JN!} \begin{vmatrix} \varphi_{1j}(\mathbf{r}_1) & \varphi_{2j}(\mathbf{r}_1) & \cdots & \varphi_{Nj}(\mathbf{r}_1) \\ \varphi_{1j}(\mathbf{r}_2) & \varphi_{2j}(\mathbf{r}_2) & \cdots & \varphi_{Nj}(\mathbf{r}_2) \\ \vdots & \vdots & \ddots & \vdots \\ \varphi_{1j}(\mathbf{r}_N) & \varphi_{2j}(\mathbf{r}_N) & \cdots & \varphi_{Nj}(\mathbf{r}_N) \end{vmatrix}, \end{aligned} \quad (2)$$

where C_{lj} are the coefficients of the linear combination. As we focus on the problems of impurity color center, we take only the Slater determinants whose elements are impurity-level MOs. For example, in the system of *d*² electron configuration (a problem of d-d transition), the number of the Slater determinants *s* in Eq. (2) is reduced to 45 (2 electrons in 10 spin orbitals).

Then the effective Hamiltonian of the *N*-electron system H_{eff} can be expressed as,

$$H_{\text{eff}}(\mathbf{r}_1, \mathbf{r}_2, \dots, \mathbf{r}_N) = \sum_{i=1}^N \left\{ -\frac{1}{2} \nabla_i^2 - \sum_v \frac{Z_v}{|\mathbf{r}_i - \mathbf{R}_v|} + V_{\text{rep}}(\mathbf{r}_i) \Big|_{\text{core \& valence}} \right\} + \sum_{i=1}^N \sum_{j=i+1}^N \frac{1}{|\mathbf{r}_i - \mathbf{r}_j|}. \quad (3)$$

The first bracket in the Hamiltonian is one-electron operator and is regarded as an averaged potential for the electrons in impurity levels. The terms involved in the bracket are kinetic energy of the electrons, Coulomb attractive potential between the electrons and nuclei with the charges of Z_v , and Coulomb repulsive potential between the electrons in impurity levels and in core & valence levels. The last term of the Hamiltonian is two-electron operator and expresses the Coulomb repulsive interaction between the electrons in impurity levels.

For the calculation of the matrix elements concerning the term of one-electron operator, we applied an analytical expression under X α formalism derived by Watanabe and Kamimura.¹⁰ The Coulomb repulsion term in that expression is

$$V_{\text{rep}}(\mathbf{r}_i) \Big|_{\text{core \& valence}} = \int \frac{\rho_0(\mathbf{r})}{|\mathbf{r}_i - \mathbf{r}|} d\mathbf{r} + \frac{3}{4} \left\{ \frac{\rho_{\text{total}}(\mathbf{r}_i) V_{X\alpha}[\rho_{\text{total}}(\mathbf{r}_i)] - \rho_0(\mathbf{r}_i) V_{X\alpha}[\rho_0(\mathbf{r}_i)]}{\rho_i(\mathbf{r}_i)} - V_{X\alpha}[\rho_i(\mathbf{r}_i)] \right\}, \quad (4)$$

where ρ_{total} , ρ_0 , and ρ_i are electron density of all electrons, of core and valence electrons, and of impurity levels, respectively. $V_{X\alpha}$ is exchange-correlation potential. This repulsive potential divides the interelectron interaction from that within impurity levels, which is described by the term of two-electron operator.

The matrix elements of the term of two-electron operator involve the following two-electron integrals,

$$\iint \varphi_i^*(\mathbf{r}_1) \varphi_j^*(\mathbf{r}_2) \frac{1}{|\mathbf{r}_1 - \mathbf{r}_2|} \varphi_k(\mathbf{r}_1) \varphi_l(\mathbf{r}_2) d\mathbf{r}_1 d\mathbf{r}_2. \quad (5)$$

In the DV-ME method, these two-electron integrals are calculated not analytically but numerically with use of pseudorandom sampling points, such as,

$$C \sum_{p=1}^{\Gamma} \sum_{q>p}^{\Gamma} \varphi_i(\mathbf{r}_p) \varphi_j(\mathbf{r}_q) \frac{1}{|\mathbf{r}_p - \mathbf{r}_q|} \varphi_k(\mathbf{r}_p) \varphi_l(\mathbf{r}_q) \omega(\mathbf{r}_p) \omega(\mathbf{r}_q), \quad (6)$$

where Γ is the number of the sampling points, ω are the weighted volume at each sampling point \mathbf{r} . C is explained soon after. This numerical integration makes us possible to freely apply the DV-ME method to various systems with low symmetry.

In the case of tetrahedrally coordinated Cr^{4+} ion, we can define an effective ligand field splitting Δ_{eff} from the energy difference between the impurity-level MOs with representative e and t_2 symmetries (in expression of T_d symmetry), such as,

$$\Delta_{eff} = \overline{\epsilon(t_2)} - \overline{\epsilon(e)}. \quad (7)$$

The attached lines in Eq. (7) mean to take the average energy when the symmetry is low. Then the electron configurations to be considered are $(e)^x(t_2)^y$, $(x,y) = (2,0), (1,1), (0,2)$, and the mean energies of them are

$$y \Delta_{eff}. \quad (8)$$

The diagonal elements of each electron configuration are shifted to satisfy the condition that the calculated average energy corresponds to the mean energy in Eq. (8). Finally, energies and wave functions of the N -electron system are obtained by the diagonalization of the matrix of the effective Hamiltonian.

In general, when the number of the Slater determinants is a finite one, the Coulomb repulsive energy between two electrons should be overestimated due to the insufficient consideration of correlation effect. In the DV-ME method, the two-electron integrals are multiplied by an correlation-correction factor C , to simply consider the sufficient correlation effect, as shown in Eq. (6). The correlation-correction factor C is determined to satisfy the condition that a spin-flip transition energy calculated from one-electron cluster calculation $\Delta\epsilon$ and the corresponding transition energy estimated from N -electron calculation ΔE are consistent. In the system of d^2 ion in tetrahedrally coordinated ligands, the condition for the determination of the correlation-correction factor C can be written as,

$$\overline{E(1E, 1A_1, 3A_2(e\uparrow e\downarrow))} - E(3A_2(e\uparrow^2)) = \Delta\epsilon(e\uparrow^1 e\downarrow^0.5), \quad (9)$$

where all the electron configurations belong to e^2 configuration (see the assignments in Fig. 3(c)). The right hand of Eq. (9) is the expression of the total energy difference calculated by the transition-state method proposed by Slater.¹¹

To obtain theoretical spectrum, oscillator strength of electric-dipole transition I_{0f} is calculated by

$$I_{0f} = 2(E_f - E_0) \iint \cdots \int \Psi_f \sum_{i=1}^N \mathbf{r}_i \cdot \frac{\mathbf{E}}{|\mathbf{E}|} \Psi_0 d\mathbf{r}_1 d\mathbf{r}_2 \cdots d\mathbf{r}_N^2, \quad (10)$$

where \mathbf{E} is electric field of incident light. The subscripts 0 and f mean initial and final states, respectively, and E are their energies. In this study, the initial state was 3A_2 ground state, and the final states were all of the other excited triplet states, that is, 3T_2 and 3T_1 states in $e\uparrow t_2\downarrow$ electron configuration, and 3T_1 states in t_2^2 electron configuration. Since the present version of the DV-ME method is non-relativistic one and spin-orbit

coupling is not considered, the transition probability is obtained only for spin-allowed transition. Finally, the theoretical spectrum is obtained by applying the oscillator strength I_{0f} to the Lorentz resonance curve with the full width at half maximum of 325 cm^{-1} . We note that we can discuss the peak energy and relative intensity, but could not yet discuss the peak width.

2.2. Cluster models

Åkermanite ($\text{Ca}_2\text{MgSi}_2\text{O}_7$) crystal belongs to melilite type structure in tetragonal system.¹² It has been said that Cr^{4+} ions substitute for the tetrahedrally oxo-coordinated Si^{4+} ions,^{13,14} as in the other Cr^{4+} systems. Although Cr-doped forsterite and YAG systems (which are in commercial use for laser materials) have both fourfold- and sixfold-oxo-coordinated sites, åkermanite has only fourfold-coordinated site. So the absorption spectrum is assumed to be produced only from the electronic states of tetrahedrally oxo-coordinated Cr^{4+} ions.

We used three types of cluster models; (a) $[\text{CrO}_4]^{4-}$ (without point charges) model, (b) $[\text{CrO}_4]^{4-}$ model, and (c) $[\text{CrCa}_6\text{Mg}_2\text{SiO}_{38}]^{52-}$ model, shown in Figs. 1 (a) & (b), and (c). The geometry of the model (a) was determined from the crystal structure centered at Si^{4+} site. The structural characteristic is the distortion from exact tetrahedron, expressed by the different Cr-O distances in Fig. 1 (a) & (b). The Cr^{4+} site has C_s symmetry. In the model (b), additional point charges with formal valences were placed at the atomic sites outside the cluster to express the effective Madelung potential of the crystal. The larger model (c) $[\text{CrCa}_6\text{Mg}_2\text{SiO}_{38}]^{52-}$ was expanded from the model (b) by adding ions outside the CrO_4 unit. Since all the ligands were completely packed by CaO_8 , MgO_4 , and SiO_4 polyhedra, we consider that the covalency of impurity-level MOs is well described by the model (c).

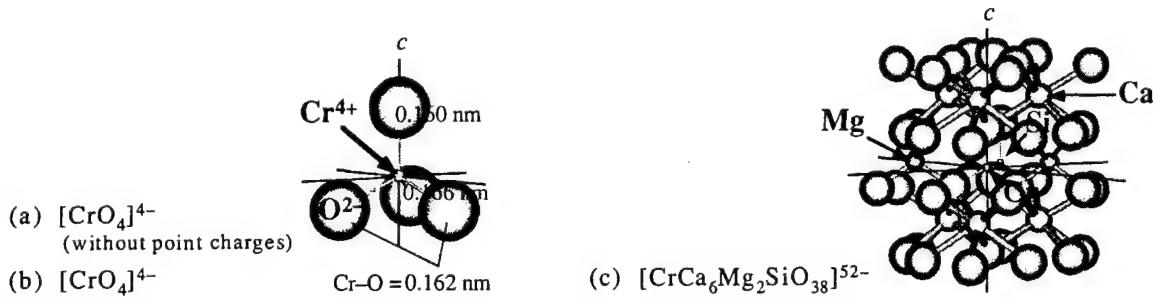


Figure 1. Cluster models. (a) $[\text{CrO}_4]^{4-}$ (without point charges) model, (b) $[\text{CrO}_4]^{4-}$ model, and (c) $[\text{CrCa}_6\text{Mg}_2\text{SiO}_{38}]^{52-}$ model. In the model (b) and (c), additional point charges are placed outside the clusters to reproduce the effective Madelung potential.

3. RESULTS AND DISCUSSION

3.1. One-electron MO energy

One-electron MO energies obtained from cluster calculations are shown in Figs. 2 (a), (b), and (c) for the three models. The energies of the highest-occupied MOs were taken at 0 eV. In all the results, impurity-level MOs which were mainly composed of Cr-3d orbitals appeared between the valence band ($\text{O}-2p$) and the non-occupied band. The five impurity-level MOs were taken to construct the Slater determinants.

Although the symmetries of the impurity-level MOs are low with a' or a'' symmetries, we can still approximately define the effective crystal field splitting Δ_{eff} in Eq. (7) as an average energy difference between the lower two levels (e symmetry) and the higher three levels (t_2 symmetry). The calculated values of Δ_{eff} were 1.59 eV, 1.68 eV, 1.62 eV from the models (a), (b), and (c), respectively. We have to note that the results are overestimated because we neglected in this study the local lattice relaxation which should exist when Cr^{4+} ion substitutes for smaller Si^{4+} ion. Hazenkamp *et al.* reported the value of $10Dq$ (approximately corresponds to Δ_{eff}) in Cr^{4+} -doped forsterite to be at 10095 cm^{-1} (1.25 eV).³ Since the site for the substitution of chromium ion in the forsterite and

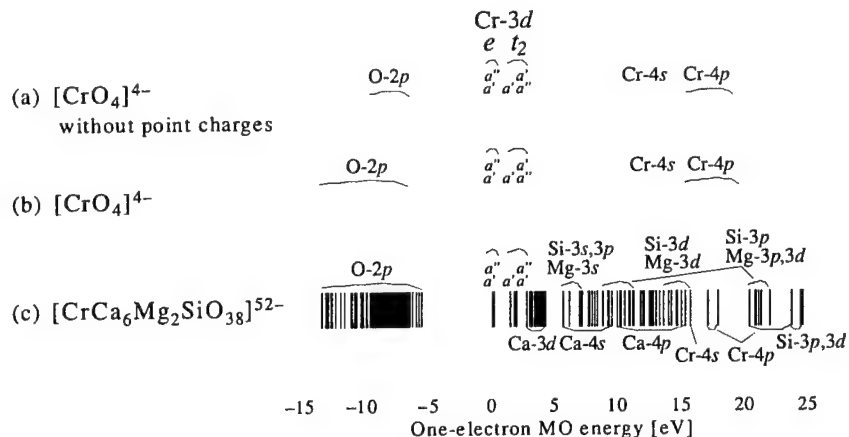


Figure 2. One-electron MO energies from (a) $[\text{CrO}_4]^{4-}$ (without point charges), (b) $[\text{CrO}_4]^{4-}$, and (c) $[\text{CrCa}_6\text{Mg}_2\text{SiO}_{38}]^{52-}$ models.

the åkermanite is the same Si^{4+} site, the degree of the relaxation in the two crystals will resemble each other. So the overestimation of the calculated Δ_{eff} would be about 3000 cm^{-1} (0.37 eV) in the larger model (c). The calculated singly excited triplet states (discussed in the next section) will shift about 3000 cm^{-1} to higher energy as a whole.

The significant difference between the results from the model (a) and (b) is their width of the valence O-2p bands. Comparing the results (b) and (c), we see that the widths of the valence bands did not significantly differ, independent of the size of the cluster models. From these results, we conclude that the width of the valence band is almost determined by the effective Madelung potential. That means the difference of the potentials on each ligand oxygen ion is involved in the model (b), but not in (a).

3.2. Theoretical absorption spectra

Calculated peak energies and intensities are shown in Figs. 3 (a), (b), and (c) for the three models. The calculated peak energies are drawn in the upper fields up to 40000 cm^{-1} , classified into singlet states (upper) and triplet states (lower). The ground state was set at zero. Multiplet-term indications are attached to the levels. In this study, we discuss only the triplet states. In the lower fields, theoretical absorption spectra are depicted to the same scale among (a), (b), and (c). For comparison, an experimental absorption spectrum taken from M. H. Garrett *et al.*¹⁵ is shown in Fig. 3 (d). The spectrum has anisotropy with respect to whether the polarization of electric field of incident light \mathbf{E} is parallel or perpendicular to the lattice axis c ($\mathbf{E}/\parallel c$ and $\mathbf{E}\perp c$).

In the result from (a) $[\text{CrO}_4]^{4-}$ model without additional point charges, we see that the relative peak positions qualitatively reproduced that in experimental spectrum, taking account of the overestimation about 3000 cm^{-1} denoted in section 3.1. The calculated result had peak splittings, which derived only from the low C_s symmetry involved in the cluster model. In the theoretical spectrum, the spectral anisotropy on intensity was produced. In this small cluster model, however, the spectral anisotropy on the peak intensity was not reproduced in 3T_2 states and the lowest state in $^3T_1(e^1t_2^1)$, as indicated by arrows in Fig. 3 (a). Furthermore, the relative peak intensity of the highest peak for $\mathbf{E}/\parallel c$ to the lower peaks was about a half compared to the experimental spectrum. These results indicate that mean energy of multiplet terms is rather easy to reproduce, on the other hand, intensity ratio is more difficult to be obtained in good agreement with experimental one.

In the result from (b) $[\text{CrO}_4]^{4-}$ model, where point charges with formal valences were added outside the cluster, the spectral anisotropy on the peak intensity, which was not reproduced in the model (a), became to agree with the experimental spectrum. The large difference of the effective Madelung potential on each oxygen ion affected the intensity. This result indicates that it is insufficient to consider only a circumstance within CrO_4 unit to discuss the spectral anisotropy on peak intensity. The calculated relative peak position between the lower two states in 3T_2 and the higher states in $^3T_1(e^1t_2^1)$, however, went too apart from each other. This is because the peak splitting in 3T_2 state was overestimated, and the tendency is seen also in the other multiplet terms. This indicates

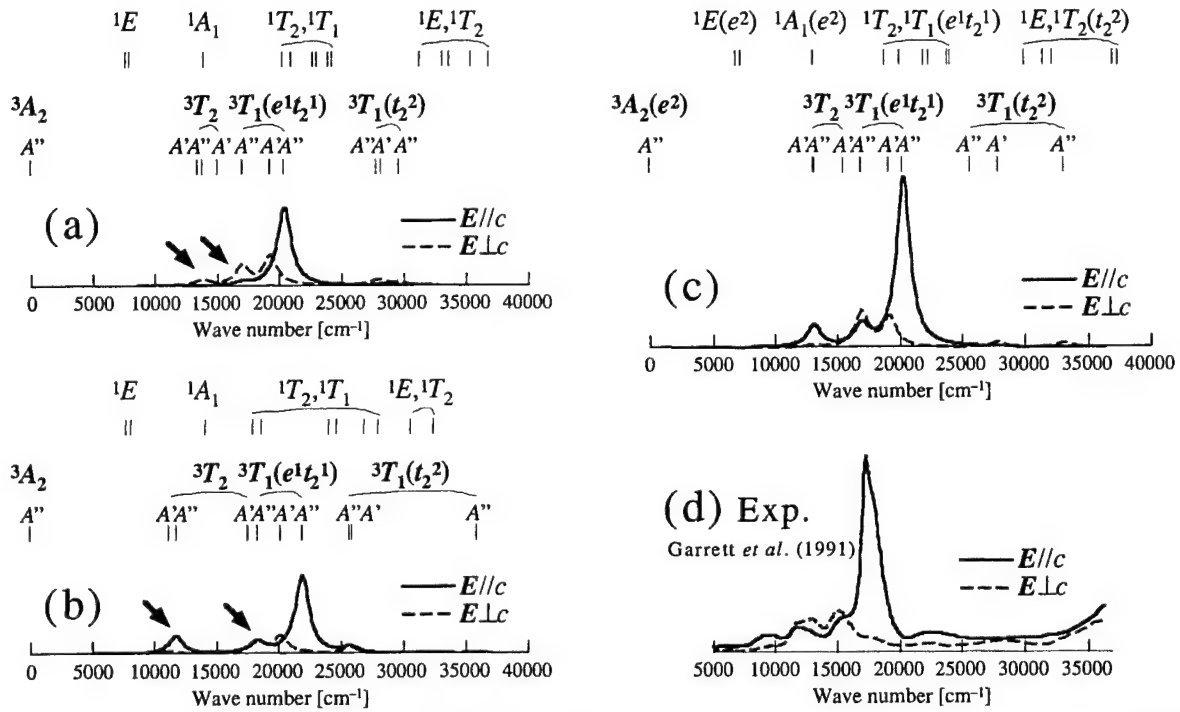


Figure 3. (a)-(c); Calculated peak energies (upper) and theoretical absorption spectra (lower) from $[CrO_4]^{4-}$ (without point charges), $[CrO_4]^{4-}$, and $[CrCa_6Mg_2SiO_{38}]^{52-}$ models. (d); Experimental absorption spectrum taken from Garrett *et al.*¹⁵

that the difference of the charge distribution on ligand oxygens was overestimated because there was no space other than the CrO_4 unit to relax the distribution.

In the result from the larger (c) $[CrCa_6Mg_2SiO_{38}]^{52-}$ model, the calculated spectrum had a good agreement with the experimental spectrum both on the relative peak splitting and on the relative intensity. This agreement indicates that the complete packing around the ligands with additional ions is really required for the good description of the many-electron wave function. The left disagreement with the experimental spectrum would be ascribed to the neglect of local lattice relaxation around the Cr^{4+} ion.

We have also confirmed that the calculated spectral anisotropy on peak intensity corresponded to the selection rule for the transition in C_s symmetry.³ Since the calculated result revealed that $^3A'$ state in 3T_2 had no significant intensity, the system can be considered to approximately follow the selection rule in higher C_{3v} symmetry.

3.3. Reduction of Coulomb repulsive energy

In general, Coulomb repulsive energy between electrons in d orbitals of transition-metal ion is greatly reduced when the ions are doped into crystals. We considered the reduction by two factors: one is the effect of the covalency which was expressed by the proportions of contribution of Cr-3d orbital to impurity-level MOs, and the other is the correlation-correction effect which was expressed by the correlation-correction factor C in Eq. (6).

We evaluated the covalency in the impurity-level MOs by the Mulliken's population analysis method,¹⁶ which quantifies the proportions of contribution of atomic orbitals to MOs through the evaluation of the coefficients c_{ik} in Eq. (1). The results of the analysis are summarized for the three models (a), (b), and (c) in Table 1, in representative description of the MOs with e and t_2 symmetries. The result says that the proportions of contribution of Cr-3d orbital to the impurity-level MOs were reduced differently in the MOs with e symmetry (82-85%) and in the MOs with t_2 symmetry (64-71%), by mixing with oxygen 2s,2p orbitals. In the models (a) and (b), the average degrees of the mixture of the atomic orbitals, that is, the covalency between chromium and oxygens were almost

Table 1. Proportions of contribution of atomic orbitals to impurity-level MOs for (a) $[\text{CrO}_4]^{4-}$ (without point charges), (b) $[\text{CrO}_4]^{4-}$, and (c) $[\text{CrCa}_6\text{Mg}_2\text{SiO}_{38}]^{52-}$ models.

(a)	Cr-3d	Cr-4sp	O-2sp	(b)	Cr-3d	Cr-4sp	O-2sp
e	0.85	0.00	0.15	e	0.85	0.00	0.15
t_2	0.70	0.08	0.22	t_2	0.71	0.08	0.22
(c)	Cr-3d	Cr-4sp	O-2sp	Ca-3d,4sp	Mg-3spd	Si-3spd	
e	0.82	0.00	0.14	0.04	0.01	0.01	
t_2	0.64	0.08	0.20	0.06	0.01	0.01	

the same. It is not surprising that the calculated peak energies and intensities have varied by the consideration of the effective Madelung potential, although the averaged covalency looks unchanged.

In the larger model (c), the MO construction varied by the incorporation of the additional orbitals of Ca^{2+} , Mg^{2+} , and Si^{4+} ions. From this result, we insist again that the wave functions of the cations outside ligands should not be neglected. Comparing the theoretical spectra from the models (c) and (a) in Figs. 3 (c) and (a), we find that the energies of the peaks with significant intensities do not differ largely between the two. This might indicate that in the traditional methods which lie under the consideration of the circumstance within CrO_4 unit, the effect of the ions outside ligands could be obscured by the analytical parameters, if the results are only for the peak energies but not also for the intensities. One reason for why the calcium orbitals had the main additional contribution to the MOs can be explained from the one-electron MO energy in Fig. 2 (c). From the diagram, we see that Ca-3d orbitals locate at the nearer energy to Cr-3d levels than the other cations' orbitals. This energy position, along with the larger number of the ion around the chromium ion, made the larger contribution of the calcium orbitals than the other cations' orbitals. Suppose a secondary dopant is introduced to the crystal under the situation of isovalent substitution, we can expect that the absorption spectrum will have a larger change when the ions substitute for the calcium sites than the magnesium and silicon sites.

Calculated values of the correlation-correction factor C were 0.55, 0.56, and 0.63 for the models (a), (b), and (c), respectively. A compensatory tendency on the reduction of Coulomb repulsive energy is found as that the factor C increases as the covalency decreases. We suppose, however, that the difference of the factor C among the three models have less influence upon the theoretical spectra than the difference of the covalency.

3.4. Interaction between the states in different triplet terms

In this last section, we mention the interaction between the different triplet terms, and the relationship between the interaction and peak intensity. Analogous to the analysis of covalency we have done in the previous section, we analyzed the coefficients of wave functions of N -electron system, C_{ij} in Eq. (2). The result from the larger model (c) $[\text{CrCa}_6\text{Mg}_2\text{SiO}_{38}]^{52-}$ is summarized in Table 2 for excited states in triplet terms, 3T_2 , ${}^3T_1(e^1t_2^1)$, and ${}^3T_1(t_2^2)$. The values are the proportions of the Slater determinants which each state is composed of, omitted if they are less than 0.005. The order of the states in Table 2 corresponds to the order of the calculated peak energy in Fig. 3 (c). From the Table 2, we first see that the orthogonality of the wave functions was preserved within the computational accuracy: ${}^3A'$ states were composed of the Slater determinants Φ_1 , Φ_3 , Φ_5 , and Φ_8 , on the other hand, ${}^3A''$ states were composed of Φ_2 , Φ_4 , Φ_6 , Φ_7 , and Φ_9 , so that ${}^3A'$ states and ${}^3A''$ states had no interaction with each other.

Focusing on the states in ${}^3T_2(e^1t_2^1)$, we see that their main components (diagonal elements) were reduced to 0.66-0.81. The higher two states had significant interaction between the states in ${}^3T_1(e^1t_2^1)$, through Φ_4 and Φ_6 , or Φ_5 . It is known that transition to 3T_2 state in T_d symmetry is forbidden for electric dipole transition, on the other hand, the transition to ${}^3T_1(e^1t_2^1)$ state is allowed. In C_s symmetry, however, those states split into the states with A' and A'' symmetry to mix with each other. As a consequence, the states in 3T_2 borrow the intensities from the states in ${}^3T_1(e^1t_2^1)$ to have peak intensities in the absorption spectrum.

The same explanation concerning the relationship between the coupling of parent multiplet terms and peak

Table 2. Proportions of contribution of Slater determinants to 3T_2 , $^3T_1(e^1t_2^1)$, and $^3T_1(t_2^2)$ states in the model (c) $[\text{CrCa}_6\text{Mg}_2\text{SiO}_{38}]^{52-}$. The Slater determinants of the triplet states are,

$$\begin{aligned}\Phi_1 &= |e(a'), t_2(a'_{(1)})|, & \Phi_2 &= |e(a''), t_2(a'_{(1)})|, & \Phi_3 &= |e(a''), t_2(a'_{(2)})|, \\ \Phi_4 &= |e(a''), t_2(a'')|, & \Phi_5 &= |e(a'), t_2(a'')|, & \Phi_6 &= |e(a'), t_2(a'_{(2)})|, \\ \Phi_7 &= |t_2(a'_{(1)}), t_2(a'_{(2)})|, & \Phi_8 &= |t_2(a'_{(1)}), t_2(a'')|, & \Phi_9 &= |t_2(a''), t_2(a'_{(2)})|,\end{aligned}$$

where $|\phi_1, \phi_2| = 1/\sqrt{2} \{ \phi_1(\mathbf{r}_1) \phi_2(\mathbf{r}_2) - \phi_2(\mathbf{r}_1) \phi_1(\mathbf{r}_2) \}$.

Slater determinants States Ψ	Φ	$(e^1t_2^1)$						(t_2^2)		
		Φ_1	Φ_2	Φ_3	Φ_4	Φ_5	Φ_6	Φ_7	Φ_8	Φ_9
$^3T_2(e^1t_2^1)$	$^3A'$	0.81		0.16		0.02				
	$^3A''$		0.66		0.23		0.10			
	$^3A'$	0.08		0.66		0.26				
$^3T_1(e^1t_2^1)$	$^3A''$		0.17		0.73		0.06			0.04
	$^3A'$	0.09		0.15		0.67				0.09
	$^3A''$	0.16		0.01		0.82				
Energy	$^3A''$							0.99		
	$^3A'$	0.02		0.02		0.05			0.91	
	$^3A''$					0.03	0.01			0.95

intensity is valid also for the states in $^3T_1(t_2^2)$. In general, electric dipole transition is allowed not for two-electron excitation but only for one-electron excitation, because the operator of the transition is one-electron operator. Nevertheless, the states in 3T_1 in two-electron excited t_2^2 electron configuration have intensities in the theoretical spectrum. This is ascribed to the existence of configuration interaction between the two 3T_1 states in $e^1t_2^1$ and t_2^2 electron configurations. From the Table 2, we see that the lowest $^3A''$ state in $^3T_1(t_2^2)$ was composed almost of its own component Φ_7 alone. This fact corresponds to the absence of the peak intensity in the theoretical spectrum. On the other hand, the higher two states in $^3T_1(t_2^2)$ both had interactions with the states in $^3T_1(e^1t_2^1)$, having little peaks in the theoretical spectrum.

4. SUMMARY

We have calculated absorption spectrum of $\text{Cr}^{4+}:\text{Ca}_2\text{MgSi}_2\text{O}_7$ (åkermanite) from first principles. The best agreement with experimental spectrum was obtained in larger $[\text{CrCa}_6\text{Mg}_2\text{SiO}_{38}]^{52-}$ model, not in $[\text{CrO}_4]^{4-}$ model. Also the covalency of impurity-level MOs was numerically analyzed. The results indicated that we should include wave functions of cations outside ligands when we discuss the many-electron states with significant spectral anisotropy.

ACKNOWLEDGEMENTS

We really thank Dr. Takafumi Yamazaki and his collaborators at Corporate R&D Center of Mitsui Mining & Smelting Co., Ltd. for their kindness to have given us much time for discussion, and useful advices.

REFERENCES

1. V. Petricevic, S. K. Gayen, R. R. Alfano, K. Yamagishi, H. Anzai, and Y. Yamaguchi, "Laser action in chromium-doped forsterite," *Appl. Phys. Lett.* **52**, pp. 1040-1042, 1988; V. Petricevic, S. K. Gayen, and R. R. Alfano, "Laser action in chromium-activated forsterite for near-infrared excitation: Is Cr^{4+} the lasing ion?" *ibid* **53**, pp. 2590-2592, 1988; H. R. Verdun, L. M. Thomas, D. M. Andrauskas, T. McCollum, and A. Pinto, "Chromium-doped forsterite laser pumped with $1.06 \mu\text{m}$ radiation," *ibid* **53**, pp. 2593-2595, 1988.
2. S. Sugano, Y. Tanabe, and H. Kamimura, *Multiplets of Transition-Metal Ions in Crystals*, Academic, New York, 1970.
3. M. F. Hazenkamp, H. U. Güdel, M. Atanasov, U. Kesper, and D. Reinen, "Optical spectroscopy of Cr^{4+} -doped

Ca_2GeO_4 and Mg_2SiO_4 ," *Phys. Rev. B* **53**, pp. 2367-2377, 1996.

- 4. A. B. Sobolev, I. F. Bikmetov, V. A. Lobach, A. I. Mit'kovets, A. A. Stavrov, and A. P. Shkadarevich, "Electronic structure of the Cr^{4+} centers in yttrium aluminum garnet," *Sov. Phys. Solid State* **33**, pp. 185-186, 1991.
- 5. W. Y. Ching, Yong-Nian Xu, B. K. Brickeen, "Ab-initio calculation of excited state absorption of Cr^{4+} in $\text{Y}_3\text{Al}_5\text{O}_{12}$," *Appl. Phys. Lett.* **74**, pp. 3755-3757, 1999.
- 6. K. Wissing, J. A. Aramburu, M. T. Barriuso, and M. Moreno, "Optical properties due to Cr^{4+} in oxides: Density functional study," *Solid State Commun.* **108**, pp. 1001-1005, 1998.
- 7. K. Ogasawara, T. Ishii, I. Tanaka, and H. Adachi, "Calculation of multiplet structures of Cr^{3+} and V^{3+} in a- Al_2O_3 based on a hybrid method of density-functional theory and the configuration interaction," *Phys. Rev. B* **61**, pp. 143-161, 2000.
- 8. T. Ishii, K. Ogasawara, Y. Ito, I. Tanaka, and H. Adachi, "First-principles calculation for multiplet structure in chromium ions doped laser materials," *Bull. Soc. Discrete Variational $X\alpha$* **11**, pp. 181-183, 1998.
- 9. C. Satoko, M. Tsukada, and H. Adachi, "Discrete variational $X\alpha$ cluster calculations. II. Application to the surface electronic structure of MgO ," *J. Phys. Soc. Jpn.* **45**, pp. 1333-1340, 1978.
- 10. S. Watanabe and H. Kamimura, "First-principles calculations of multiplet structures of transition metal deep impurities in II-VI and III-V semiconductors," *Mater. Sci. Eng.* **B3**, pp. 313-324, 1989.
- 11. J. C. Slater, *The Self-Consistent Field for Molecules and Solids, Quantum Theory of Molecules and Solids Vol. 4*, McGraw-Hill, New York, 1974.
- 12. Yu. A. Malinovskii and Z. V. Panina, "X-ray study of chromium doped akermanite ($\text{Ca}_2\text{Ge}[\text{Si}_2\text{O}_7]$) crystals," *Crystallogr. Rep.* **42**, pp. 946-950, 1997.
- 13. M. H. Whitmore, A. Sacra, and D. J. Singel, "Electron paramagnetic resonance spectroscopy of tetrahedral Cr^{4+} in chromium-doped forsterite and akermanite," *J. Chem. Phys.* **98**, pp. 3656-3664, 1993.
- 14. A. Sugimoto, Y. Nobe, T. Yamazaki, Y. Anzai, K. Yamagishi, Y. Segawa, and H. Takei, "Spectroscopic properties of Cr-doped melilite crystals," *Phys. Chem. Minerals* **24**, pp. 326-332, 1997.
- 15. M. H. Garrett, V. H. Chan, H. P. Janssen, M. H. Whitmore, A. Sacra, and D. J. Singel, "Comparison of chromium-doped forsterite and akermanite laser host crystals," *OSA Proc. Advanced Solid-State Lasers* **10**, pp. 76-81, 1991.
- 16. R. S. Mulliken, "Electronic population analysis on LCAO-MO molecular wave functions. I," *J. Chem. Phys.* **23**, pp. 1833-1840, 1955.

The mechanisms of slow bleaching in YAG:Cr⁴⁺ under CW pumping.

I. T. Sorokina^a, S. Naumov^a, E. Sorokin^a, and A. G. Okhrimchuk^b

^aInstitut für Photonik, TU Wien, Gusschausstr. 27/387, A-1040 Wien, Austria

^bFORC at GPI, 38 Vavilov Street, Moscow, 117756, Russia

ABSTRACT

We report on the results of lasing and spectroscopic investigations of the anomalously slow recoverable bleaching of Cr,Ca:YAG and Cr,Mg:YAG crystals. We propose two models for this effect: (i) Cr⁴⁺ reduction to Cr³⁺ due to oxygen valence band electron capture by Cr⁴⁺, and (ii) induced disorder in Cr⁴⁺ tetrahedral center due to effect of oxygen vacancies.

1. INTRODUCTION

During the last decade there has been a great interest in Cr⁴⁺:YAG crystal as an active medium for continuous-wave lasers tunable around 1.5 μ m. The Cr⁴⁺ ion in a tetrahedral position has been established as the main lasing ion [1]. However, there were reports [2] on the other optical centers, showing different polarization dependence. There is also a significant spread in the literature of the reported values for absorption cross-section, varying by nearly an order of magnitude. The authors of Ref.[3] have paid attention to the concentration effects. For example, in the low temperature absorption spectra (T=5K) of Cr⁴⁺:YAG with high Cr dopant concentration there are additional lines, which are normally absent in the spectra of crystals with the low concentration. However, in order to achieve efficient diode-pumped operation in Cr:YAG it is essential to use high concentration of Cr⁴⁺, with ≥ 1.5 cm⁻¹ initial absorption [4]. Growing crystals with high concentration of Cr⁴⁺ in tetrahedral sites is a challenging task because of simultaneous development during the growth and annealing process of a large concentration of parasitic Cr⁴⁺ and Cr³⁺ ions in octahedral sites as well as the presence of Cr⁶⁺ in tetrahedral sites [5]. Besides, because of the generally larger concentration of Mg²⁺ (or Ca²⁺) ions than that of Cr⁴⁺ ions there is a high probability of Mg²⁺ - Cr⁴⁺ pair center formation, which may add to the multicenter nature of the lasing ion.

In our first report on direct diode-pumping of Cr:YAG up to 200 mW of tunable output power has been reported [4]. However, at concentrations, corresponding to initial absorption of 1.5-3.5 cm⁻¹ slow (tens of minutes) degradation of the output power, accompanied by the equally slow bleaching, was observed. The effect has a local character. In the pump probe experiment with a Nd:YLF pump beam and a red He-Ne probe beam an induced lens could be seen, which had the same long characteristic lifetime. We explained this assuming that partial reduction of Cr⁴⁺ ions could take place under pump radiation. The ionic radii of the generated Cr³⁺ ions are larger than those of the Cr⁴⁺ ion, leading to the local lattice distortion and refractive index change.

Such a photoinduced local change in the refractive index, i.e. a photorefractive-like effect, is known to take place in some transition-metal-doped oxide crystals [6], including Cr-doped garnets [7]. In the latter case, reduction of Cr³⁺ to Cr²⁺ is responsible for photorefraction. This photoinduced anomalous absorption saturation and consequent photorefraction is the main factor, limiting the pump absorption and energy extraction in the active element.

The purpose of this paper is to perform a comparative study of spectroscopic and laser characteristics of concentrated Cr⁴⁺:YAG crystals, co-doped with Mg and Ca, with an aim to establish the mechanism of the observed slow bleaching. At this stage we suggest two physical models, both of which adequately describe experimental facts and both of which are based on multicenter nature within Cr⁴⁺ ions in tetrahedral positions. The first model assumes that as a result of local charge compensation of Cr⁴⁺ by Ca²⁺/Mg²⁺ and inhomogeneous distribution of Ca²⁺/Mg²⁺ relatively to Cr⁴⁺ ions there are different Cr⁴⁺ centers, varying by their oscillator strength as well as by proximity of their energy levels to the oxygen valence bands. Part of these centers, the energy levels of which are closest to the valence band, reduce to Cr³⁺ under pump radiation due to oxygen valence band electron capture by Cr⁴⁺. The second model assumes multicenter character of Cr⁴⁺ ions, which is a result of effect on crystal field of positively charged oxygen vacancies.

Correspondence: I. T. Sorokina, Email: sorokina@tuwien.ac.at ; Telephone: (43-1)-58801 38721; Fax: (43-1)-58801 38799; Supported by the Austrian National Science Foundation Projects no. T-64 and the Austrian National Bank Project no. 7913.

2. EXPERIMENTAL RESULTS

We performed a comparative study of the two Cr:YAG crystals (Cr concentration is 0.1 at % Al), the one being co-doped with Mg (0.3 at.% Al) and the other with Ca (0.5 at.% Al). We used a 20 W continuous-wave Nd:YLF laser as a pump source, and Carry-5 spectrophotometer for spectroscopic measurements. The temperature of the crystalline sample was kept constant with 0.5 °C accuracy. Acousto-optic modulator was used for saturation intensity measurements. The pump beam was polarized parallel to the 001 axis of Cr:YAG, and was modulated with the triangular shaped pulse with the characteristic time constant of ~50 µs in order to prevent heating of the crystal. At the same time 50 µs is more than 10 times larger than the Cr life-time (3.4 µs) so that population of the Cr energy levels can be considered in equilibrium.

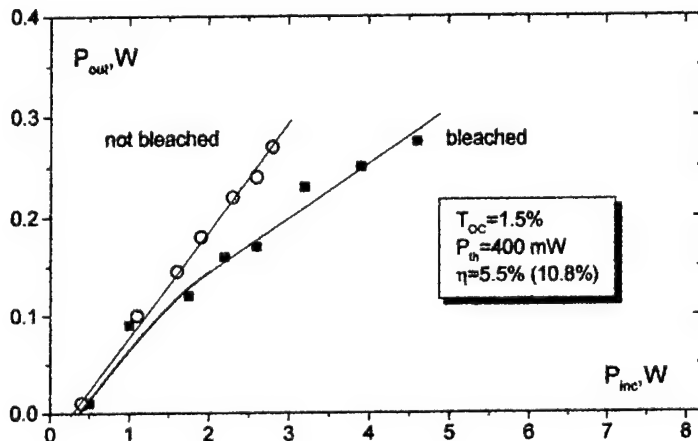


Figure 1. Typical output characteristics of the diode-pumped Cr:YAG laser. Each point was measured : a) in the steady-state regime (filled squares), b) immediately after shifting the crystal (open circles).

The described above slow laser output degradation, which was accompanied by the slow bleaching, was observed in both studied samples. In Fig.1 the typical output characteristics of Cr:YAG laser are plotted. The one curve exhibits the discussed slow bleaching. For comparison, the straight output characteristics line is given, where each point is taken right after shifting the crystal, i.e. when the bleaching did not take place yet. Comparison of these two curves shows that approximately a factor of two increase in the efficiency, as well as higher output power can be expected from the improved in respect to slow bleaching crystal.

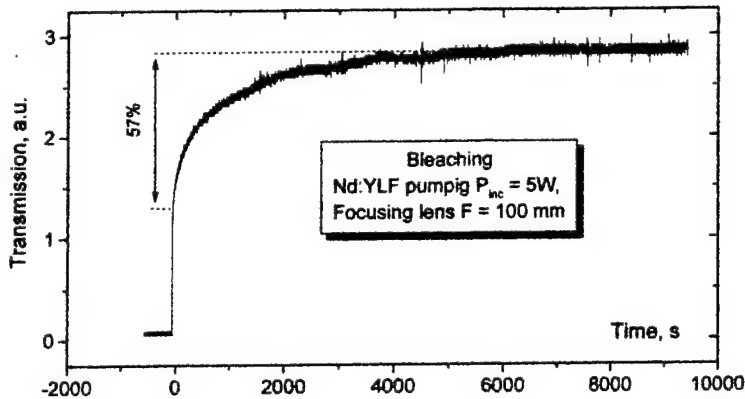


Figure 2. Bleaching curve of the Cr, Mg:YAG sample (Cr 0.1 at.% Al, Mg 0.3 at.% Al). taken at 5 W of the incident pump power.

The typical form of the time-dependence of bleaching is plotted in Fig. 2, where the crystal is bleached by as much as 57% of the initial transmission. The first natural explanation to the observed bleaching would be that it is due to the thermal effects. We could establish, however, that heating leads not to the bleaching, but to reduction of transmission at pump wavelength of 1054 nm.

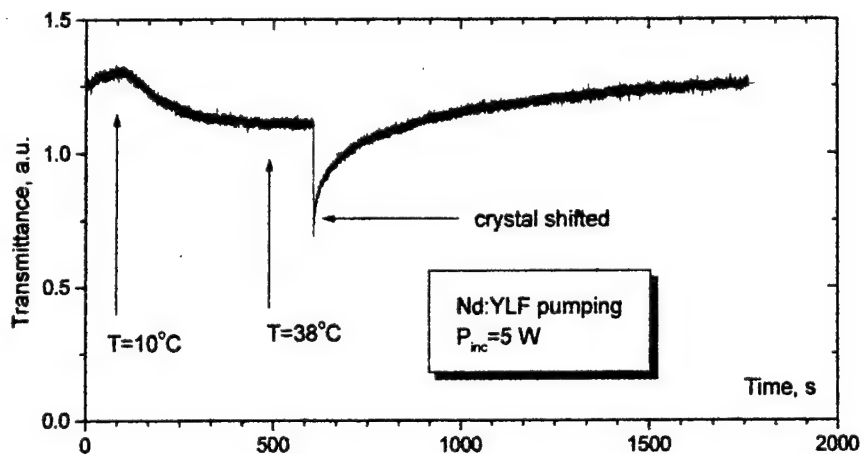


Figure 3. The Cr, Mg:YAG transmission (no lasing) under Nd:YLF pumping (5 W). The left part of the graph shows transmission behaviour with increasing temperature. The right part corresponds to the transmission of the shifted crystal at constant temperature.

In Fig. 3 one can see simultaneously the effect of heating and pump laser irradiation on the transmission behaviour. As it can be seen, gradual increase of the temperature of the crystal from ~ 20 °C to 38 °C is accompanied by the decrease of transmission. Then the crystal was shifted to the new place, followed by the discussed slow increase of the transmission. The same inverse effect of heating on transmission at the pump wavelength (1.054 μ m) can be also observed in the differential temperature dependent absorption spectra of Cr,Mg:YAG (Fig.4). The spectra in Fig.4 are the result of subtraction of the spectrum of the heated sample from the spectrum of the cold sample. All this evidences the fact that not the thermal effect causes the observed slow bleaching, but rather interionic processes under continuous-wave pump irradiation are responsible for the phenomenon.

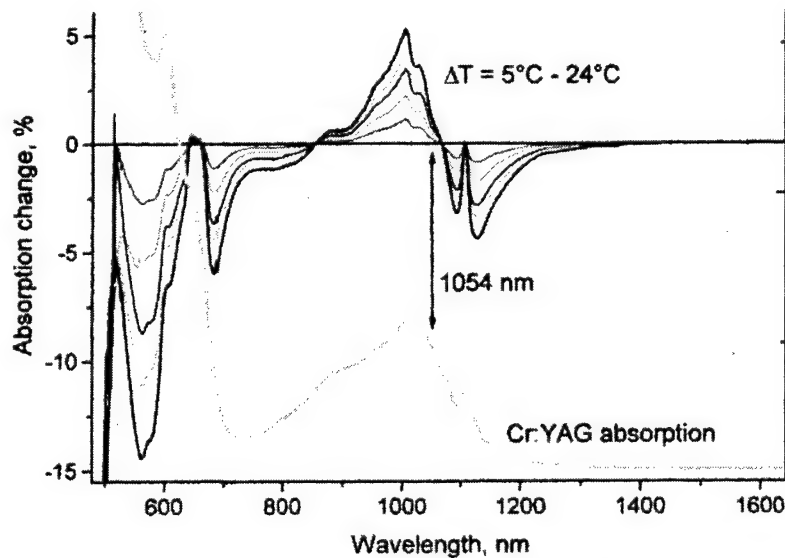


Figure 4. Differential absorption spectra of Cr,Mg :YAG crystal taken at $\Delta T=5$ °C, 10 °C, 15 °C, 19 °C, 24 °C.

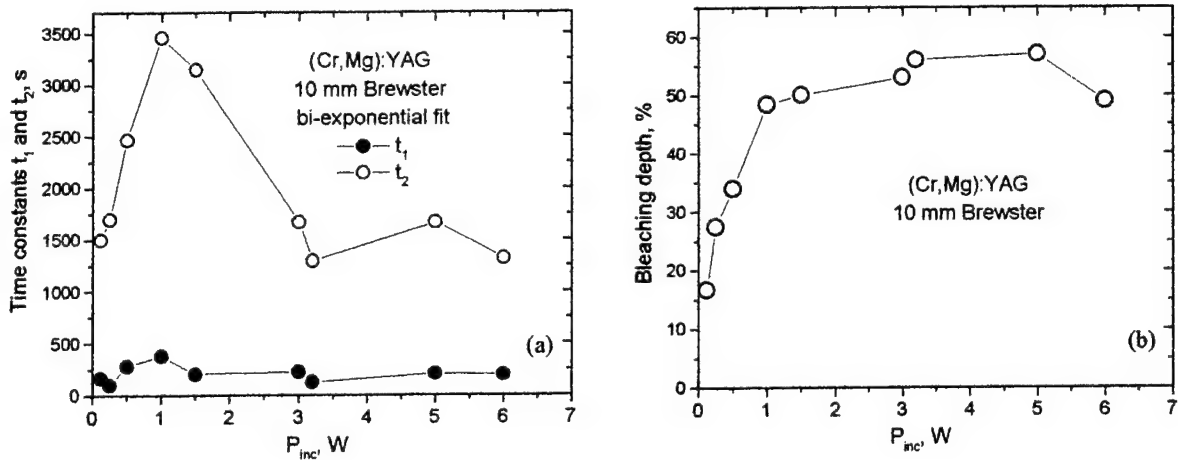


Figure 5. Dependence of characteristic time-constants of the bleaching on the incident power in Cr,Mg:YAG crystal (a). Dependence of the bleaching depth upon the incident power in the same sample (b). The F=100 mm focusing lens is used.

The temporal behaviour of the bleaching was found to be nonexponential, consisting of at least two exponential functions, having time constants of the order of 200 and 2000 sec in case of the Mg-codoped sample, and 600 and 3000 sec in case of the Ca-codoped sample. Unexpectedly, the time constant was found first to increase with pump intensity, reaching its maximum in the Mg-codoped sample at about 1 W of incident power, corresponding to the power intensity of ~ 1.6 kW/cm² (compare with saturation intensity of ~ 10 kW/cm²), and then gradually decrease with the increase of the incident pump power (see Fig. 5a). The bleaching depth is also characterized by the maximum (Fig. 5b). The decrease of the bleaching depth at higher intensities (barely seen in Fig. 5b) is much stronger in thin samples. The maximal bleaching depth seems to be achieved in Ca-codoped sample at lower pump intensities than in Mg-codoped sample.

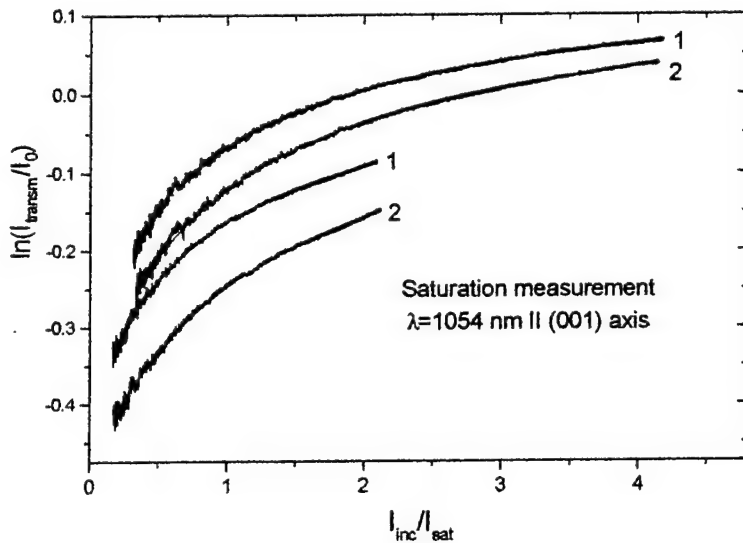


Figure 6. Transmittance of the bleached (curve 1) and not bleached (curve 2) Cr,Mg:YAG sample. Fitting these curves with the saturation model (1) allows to determine the changes in N and σ . The origin of the vertical axis is undefined.

The bleaching was found to be recoverable with the same time constants. We performed a comparative study of the two Cr:YAG crystals, codoped with Mg (0.3 at.%) and Ca (0.5 at.%). Unexpectedly, the usually better performing in CW regime Cr,Mg:YAG crystals were found to have higher bleaching depth than Cr,Ca:YAG. Bleaching amounts up to $\sim 10\%$ of initial concentration of Cr⁴⁺ ions in Mg-doped YAG and $\sim 3\%$ of Cr⁴⁺ ions in Ca-doped YAG (note that $\sim 57\%$ depth on Fig. 2 and Fig. 5b correspond to the change in overall transmission of the 10-mm crystal with 3.5 cm⁻¹ absorption

coefficient). The decrease of absorption is due to the changes in absorption cross-section σ as well as in number of absorbing ions N . We established these two values, having conducted absorption saturation measurements in the bleached and the not bleached samples (see Fig. 6) by modulating the amplitude of the incident beam in the range between $0.4 I_{sat}$ (saturation intensity) and $4 I_{sat}$ as well as between $0.2 I_{sat}$ and $2 I_{sat}$ in order to expand the dynamic range of the measurement. The curves have been fitted to the following formula, describing saturation:

$$I_{trans} = I_0 \exp\left(-\frac{\sigma N l}{1 + I_0 / I_{sat}}\right), \quad (1)$$

where l is the sample thickness, I_0 is the intensity of the incident light and I_{trans} is the intensity of the transmitted light. Fitting experimental results for Cr,Mg:YAG sample to this formula and comparing the curves taken for the bleached and the not bleached samples, we obtain that the effective cross-section increases in the bleached sample by $\sim 30\%$, σN decreases by as much as $\sim 10\%$, which results in the reduction of the active ions number N by $\sim 37\%$.

We have also measured the lifetime of Cr^{4+} in the bleached and not bleached cases, and found that it does not change and is exponential with the time constant equal to $3.4 \mu\text{s}$.

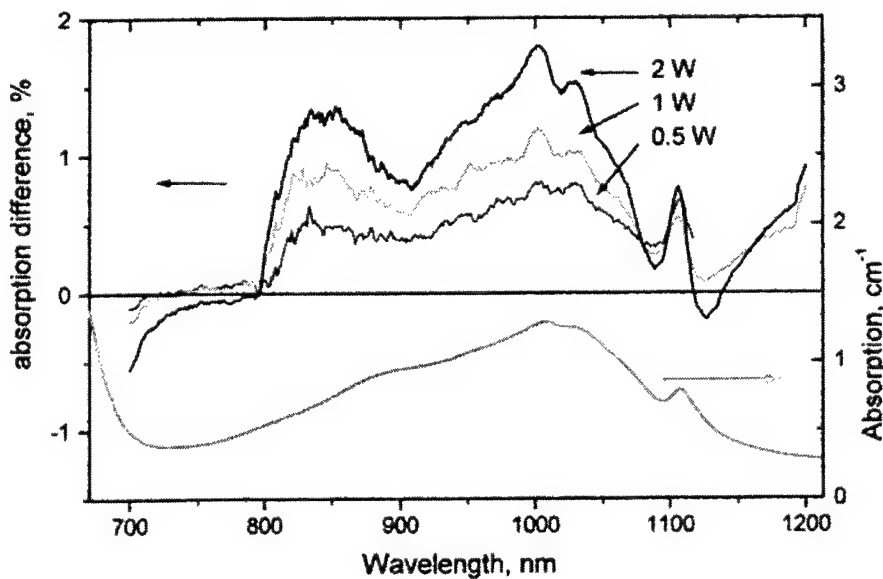


Figure 7. Differential absorption spectra of Cr,Mg:YAG crystal at room temperature at pump levels of 0.5, 1, and 2 W around $1 \mu\text{m}$. Lower part of the figure shows the absorption spectrum of the Cr:YAG. Due to the much smaller diameter of the bleached area compared to the spectrophotometer aperture, the measured bleaching depth is relatively small ($\sim 2\%$).

In Fig. 7 the typical differential absorption spectrum of Cr,Mg:YAG crystal around $1 \mu\text{m}$ is given. The spectra are taken about 10 minutes after irradiation with Nd:YLF laser. A double peak structure of the spectrum may suggest the development under the broad absorption band of Cr^{4+} of the peak in the vicinity of 900 nm.

In Fig.8 the differential absorption spectrum of Cr,Ca:YAG crystal is plotted in the whole region between 0.3 and $1.2 \mu\text{m}$. The spectrum is taken 2 hours after irradiation with 2 W of incident power. In the ultraviolet part of the spectrum the double peak structure can be seen. It is worth noting that according to experimental observation of Sugimoto et al. [5] in Cr,Ca:YAG crystals along with the absorption peak around 480 nm, which is usually referred to the charge-transfer band of octahedral Cr^{4+} , in crystals with high ratio of Ca to Cr there develops a new peak around 400 nm. This peak was attributed by the authors of [5] to Cr^{6+} ions. However, from Fig. 8 it is seen that the whole absorption band between 400 and 500 nm decreases under pump irradiation. Therefore, we are inclined to attribute this inhomogeneous (due to disordered nature of Cr^{4+} at relatively high concentration of Ca/Mg) band to the charge-transfer band of tetrahedral Cr^{4+} .

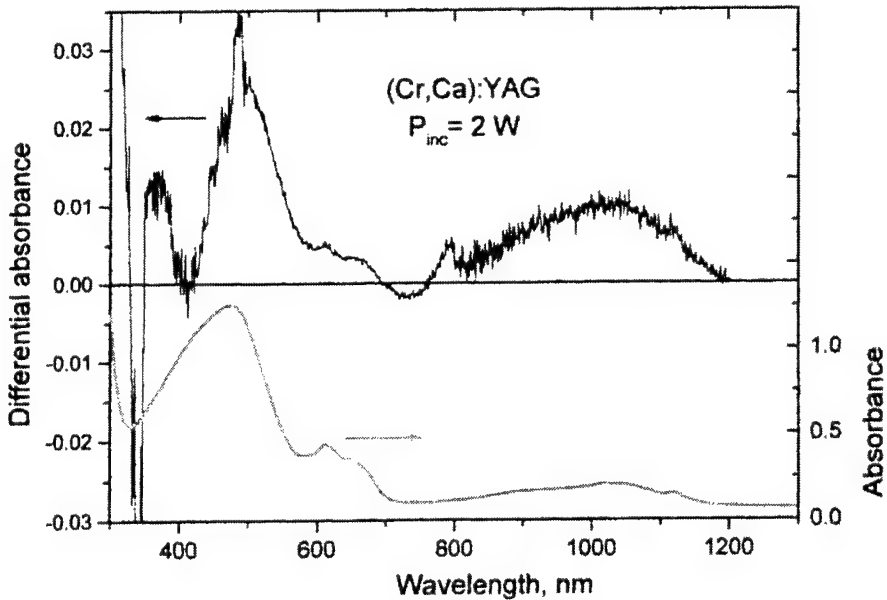


Figure 8. Differential absorption spectra of Cr,Ca:YAG crystal taken at room temperature 2 hours after irradiation with 2 W pump power.

3. DISCUSSION

One of the main conclusions following from the analysis of experimental results is that the slow bleaching is due to the multicenter nature of tetrahedral Cr^{4+} at large concentration of Ca/Mg.

In order to explain the observed effect we propose and consider two models, both adequately describing experimental facts and disordered character of tetrahedral Cr^{4+} . One model suggests photoinduced reduction of one type of the Cr^{4+} centers as a result of the charge-transfer process $\text{Cr}^{4+} + \text{e}^- (\text{VB}) \rightarrow \text{Cr}^{3+}$, which might be similar to the well studied process in $\text{Ti,Mg:Al}_2\text{O}_3$ [8].

According to this model a part of Cr^{4+} centers, which have smaller cross-section and energy levels lying within band gap less than 1.2 eV above the oxygen valence band [4] reduce under 1 μm pump radiation. The preference energy of isolated Cr^{3+} ion to occupy octahedral positions relatively to tetrahedral positions is 1.4 eV [11]. The local compensation of Cr^{4+} by Ca/Mg lowers this preference energy, thus, making the appearance of Cr^{3+} at tetrahedral positions probable.

Another model is dealing with oxygen vacancies effect on magnitude of Cr^{4+} center tetragonal distortion. Previous investigations [9,10] pointed out that the absorption cross section at 1.064 μm is not absolute constant for all YAG: Cr^{4+} crystals, but deviates about 25% from Ca to Mg doped crystals and in dependence of its heat treatment temperature. We assume that it could be because of the strength of tetragonal distortion of the center is subjected to influence of environment of other charged defect centers, in particular oxygen vacancies. It is known that the distortion of the Cr^{4+} center is stretching of its tetrahedron along the tetrahedrons-dodecahedrons chain [3]. Even a distant positively charged oxygen vacancy could partially pull back oxygen ions from nearest coordination sphere of the tetrahedron Cr^{4+} center. If this vacancy is from the same tetrahedron-dodecahedron chain, where the Cr^{4+} center is placed, then the tetragonal distortion of the center should be increased, and if the direction from the center to the oxygen vacancy is perpendicular to this chain, reduction of the distortion should be expected. Because of stochastic oxygen vacancy distribution in the lattice, we expect performance of multi-center behavior in Cr^{4+} ions system.

Volume of d^2 electronic shell of the Cr^{4+} ion in excited state is larger than in the ground state. When the excited state is maintained during several minutes, a caused lattice distortion tends to be reduced through retraction of oxygen vacancies to the tension region, that is they locate in the vicinity of excited Cr^{4+} centers. As a result dispersion of the cross section increases. Summarized small signal absorption at 1.064 μm reduced, because $^3\text{B}_1(^3\text{A}_2)-^3\text{A}_2(^3\text{T}_1)$ absorption band for a part of centers with reduced distortion shifts to shorter wavelengths, and we see an increase of absorption in 700 nm region (fig.8). Distortion of other part of centers increases and its absorption cross section becomes higher. In the saturation experiment

centers with higher cross sections play a larger role, because they are excited in the first order, and thus effective cross section deduced from this experiment increases. When pump is removed, oxygen vacancies diffuse and distribute stochastically in the lattice, the absorption returns to the initial value.

In conclusion, we have analysed the results of lasing and spectroscopic investigations of the anomalously slow recoverable bleaching of Cr,Ca:YAG and Cr,Mg:YAG crystals with relatively high concentration of Ca/Mg. We proposed two models for this effect: (i) Cr⁴⁺ reduction to Cr³⁺ due to oxygen valence band electron capture by Cr⁴⁺, and (ii) induced disorder in Cr⁴⁺ tetrahedral center due to influence of oxygen vacancies were migrating to excited centers. Both models adequately describe the observed photorefractive-like effect and slow bleaching. However, further investigations are necessary to confirm one or the other model.

ACKNOWLEDGEMENTS

The authors would like to thank A. V. Shestakov for providing the samples.

REFERENCES

1. N.I. Borodin, V.A. Zhitnyuk, A.G. Okhrimchuk, A.V. Shestakov, "Bull. of the Academy of Sciences of the USSR, Phys. Series **54**, 1500-1506(1990).
2. H. Eilers, U. Hömmerich, S. M. Jacobsen, and W. M. Yen, "On the optical center in Cr, M (M=Ca or Mg) doped YAG", OSA Proceedings on Advanced Solid-State Lasers, **15**, 437-440 (1993).
3. A.G. Okhrimchuk, A.V. Shestakov, "Performance of YAG: Cr⁴⁺: laser crystal", *Optical Materials* **3**, 1-13 (1994).
4. I.T. Sorokina, S. Naumov, E. Sorokin, E. Wintner, A. V. Shestakov, "Directly diode-pumped tunable continuous-wave Cr⁴⁺:YAG laser", *Opt.Lett.*, **24**, 1578 (1999).
5. A. Sugimoto, Y. Nobe, K. Yamagishi, "Crystal growth and optical characterization of Cr,Ca:Y₃Al₅O₁₂", *Journal of Crystal Growth*, **140**, 349-354 (1994).
6. G. B. Louts, M. Warren, L. Taylor, R. R. Rachimov, H. R. Ries, G. Miller III, M. A. Noginov, M. Curley, N. Noginova, N. Kukhtarev, H. J. Caulfield, and P. Venkateswarlu, "Manganese-doped yttrium orthoaluminate: A potential material for holographic recording and data storage", *Phys. Rev. B*, **57**, 3706-3709 (1998).
7. A. Suchocki and R. C. Powel, "Laser-induced grating spectroscopy of Cr³⁺-doped Gd₃Ga₅O₁₂ and Gd₃Sc₂Ga₃O₁₂ crystals", *Chem. Phys.* **128**, 59-71 (1988).
8. W.C. Wong, D.S. McClure, S.A. Basun, M.R. Kokta, "Charge-exchange processes in titanium-doped sapphire crystals. II. Charge-transfer transition states, carrier trapping, and detrapping", *Phys. Rev. B*, **51**, 5693 (1995).
9. A.G. Okhrimchuk and A.V. Shestakov, "Absorption saturation mechanism for YAG: Cr⁴⁺ crystals", *Phys. Rev. B* **61**, 988-995 (2000).
10. A.G. Okhrimchuk and A.V. Shestakov, "The nature of the residual absorption in the Y₃Al₅O₁₂:Cr4+ crystal Q-switch.", OSA Trends in Optics and Photonics, **34**, H. Injeyan, U.Keller, and C. Marschall eds. (OSA, Washington, DC, 2000), pp.529-535 .
11. L.A. Reznitskii, "Preference energies of cations and formation of solid solutions of spinels", *Izvestiya Akademii Nauk SSSR, ser. Neorganicheskie Materialy*, vol.20, pp.1867-1869 (1984).

New Co-containing glass ceramics saturable absorbers for 1.5 μm solid state lasers

Alexander M. Malyarevich^a, Igor A. Denisov^a, Konstantin V. Yumashev^a, Tamara I. Chuvaeva^b, Olga S. Dymshits^b, Alexei A. Onushchenko^b, Alexander A. Zhilin^b

^aInternational Laser Center, bldg. 17, #65 F. Skaryna Ave., 220027 Minsk, Belarus

^bS.I.Vavilov State Optical Institute, 197131, St-Petersburg, Russia

ABSTRACT

New saturable absorber Q-switch for 1.54 μm Er:glass laser is presented. The saturable absorber is transparent glass ceramic containing magnesium-aluminum spinel nanocrystallites doped with tetrahedrally coordinated Co^{2+} ions. Q-switched pulses of up to 5.5 mJ in energy and 80 ns in duration at 1.54 μm were achieved. Relaxation time of the $^4\text{A}_2 \rightarrow ^4\text{T}_1(^4\text{F})$ transition bleaching was measured to be (450 ± 150) ns. Ground-state and excited-state absorption cross-sections at 1.54 μm wavelength were estimated to be $(3.2 \pm 0.4) \times 10^{-19}$ cm^2 and $(5.0 \pm 0.6) \times 10^{-20}$ cm^2 , respectively. Results of study of absorption and luminescence spectra of different glass ceramics on the base of magnesium-aluminum, zink-aluminum, lithium-aluminum spinel nanocrystallites doped with tetrahedrally coordinated Co^{2+} ions are also analyzed.

Keywords: Saturable absorber, Q-switched lasers, transition metal ions

1. INTRODUCTION

Lasers emitting at 1.54 μm wavelength are under extensive study now. Their applications first of all for communication and eye-safe LIDARs and range finders cause need for short and powerful laser pulses. Passive Q-switching and mode-locking looks preferable over active ones because of simplicity, low cost and compactness.

During last few years several materials were suggested as saturable absorbers for 1.54 μm Er:glass lasers.¹⁻¹² Among them the media doped with divalent cobalt ions have attracted the great attention.⁴⁻¹² Spectroscopic properties and laser passive Q-switch operation of Co^{2+} ions were studied in different matrices: garnets,⁴ MgAl_2O_4 ⁵⁻⁷ and LiGa_5O_8 ⁷ spinel single crystals, $\text{LaMgAl}_{11}\text{O}_{19}$,⁸ ZnSe and ZnS.⁹⁻¹¹ All these materials containing tetrahedrally coordinated Co^{2+} ions have absorption cross-section at 1.54 μm significantly higher than Er:glass active medium emission one and allow to Q-switch Er:glass laser without focusing radiation into the saturable absorber. Another important parameter for passive Q-switch operation - the relaxation time of the 1.5 μm $^4\text{A}_2 \rightarrow ^4\text{T}_1(^4\text{F})$ absorption bleaching of the Co^{2+} ion - is strongly dependent on crystal matrix. It varies from ~ 15 ps in $\text{Gd}_3\text{Sc}_2\text{Ga}_3\text{O}_{12}$ ¹³ to ~ 290 μs in ZnSe.⁹

Recently there was suggested to use as the saturable absorber a transparent glass ceramic containing ZnAl_2O_4 spinel nanocrystals doped with Co^{2+} ions.¹² Q-switched pulses of 7 mJ in energy and 100 ns in duration were obtained. Glass ceramics is a material containing small crystal particles (several tens of nm in size) which are fabricated in it during preparation. Many commercial glass ceramics are valued primarily for their near-zero thermal expansion, besides, Co-doped glass ceramics may be used as solar concentrators with emission in the red-to-infrared region. Glass ceramics technology is based on the controlled nucleation and crystallization of the glass and posses several advantages over conventional powder-processed ceramics and glass preparation technique. They are: (i) ease of flexibility of forming in the glassy state, (ii) uniformity of microstructure, and (iii) reproducibility of properties that result from the homogeneity of the starting glass. In comparison with crystals glass ceramics are cheaper and small crystalline microstructures obtainable in it are of nanometer sizes, uniformly dispersed in the matrix and offer promise for many potential new applications, especially in laser technique.

This paper presents study of optical properties of transparent glass ceramics containing nanocrystallites of different spinels doped with Co^{2+} ions. Q-switch operation of 1.54 μm Er:glass laser with the studied Co-doped magnesium-aluminum glass ceramic as a saturable absorber is demonstrated.

2. PREPARATION AND CHARACTERIZATION OF THE SAMPLES

For this study we have chosen the glass of the composition 20-30 MgO (or ZnO , or Li_2O), 20-30 Al_2O_3 , 50-60 SiO_2 (mol%) yielding transparent nanocrystalline glass-ceramics. The glass was nucleated with 10 mol% TiO_2 (or ZrO_2) and coloured with

0.1 or 0.3 wt. % CoO, TiO_2 (ZrO_2) and CoO were introduced above total 100%. The raw materials were reagent grade. Batch for producing 400 g of glass was melted in crucibles made of quartz ceramics in a laboratory electric furnace at 1560°C for 8 hours with stirring. The glass was poured onto a metal plate, annealed at 640°C. One-stage and two-stage heat treatments in isothermal conditions in the temperature interval from 750 to 1000°C were carried out. As a result transparent glass ceramic with Co^{2+} -doped magnesium-aluminum or zink-aluminum, or lithium-aluminum spinel nanocrystallites (referred to as Co:MAS, Co:ZAS, Co:LAS below, respectively) was synthesized. X-ray diffraction (XRD) patterns of powdered samples were measured using Cu K_α radiation with a Ni filter. Relative fractions of crystallinity were estimated by measuring the square of the most intense peak of a crystalline phase on an X-ray pattern. Sizes of the inhomogeneous regions were calculated from SAXS data as described in Ref. [14] and were obtained to be 4-5 nm for all samples.

3. LINEAR OPTICAL PROPERTIES OF Co^{2+} -DOPED GLASS CERAMICS

Figure 1(a) shows the ground-state absorption (GSA) spectra of the Co:MAS glass ceramics samples before and after heat treatment. Initial glass has absorption band in the visible with three peaks at 510, 590 and 650 nm and very wide and weak band in the near IR. Previously, we made an assignment of absorption bands by comparison with spectra of single crystals having defined Co^{2+} coordination.¹⁵ We attributed the absorption band at 505-510 nm to an electron transition ${}^4\text{T}_{1g} \rightarrow {}^4\text{T}_{1g}({}^4\text{P})$ of octahedrally co-ordinated Co^{2+} . The strong absorption band centered at 600 nm can be assigned to the spin and electric-dipole allowed ${}^4\text{A}_2 \rightarrow {}^4\text{T}_1({}^4\text{P})$ transition and the broad absorption band at 1.1-1.7 μm - to the spin and electric-dipole allowed ${}^4\text{A}_2 \rightarrow {}^4\text{T}_1({}^4\text{F})$ transition of tetrahedrally co-ordinated Co^{2+} .⁶ By analogy with assignment of similar absorption features observed in the $\text{Co}^{2+}:\text{MgAl}_2\text{O}_4$ ^{5,7} complicated structure of the both visible and near-IR bands can be explained by the ${}^4\text{T}_1({}^4\text{P})$ and ${}^4\text{T}_1({}^4\text{F})$ states splitting due to slight distortion of oxygen tetrahedrons of Co^{2+} environment. A schematic energy-level diagram for Co^{2+} (electronic configuration d^7) in a tetrahedral crystal field is shown in the inset of Fig. 1(b). Figure 1(b) presents the GSA spectra of the Co:ZAS and Co:LAS glass ceramics samples after two stage heat treatment. They are analogous to the Co:MAS absorption spectra with tetrahedrally coordinated Co^{2+} ions.

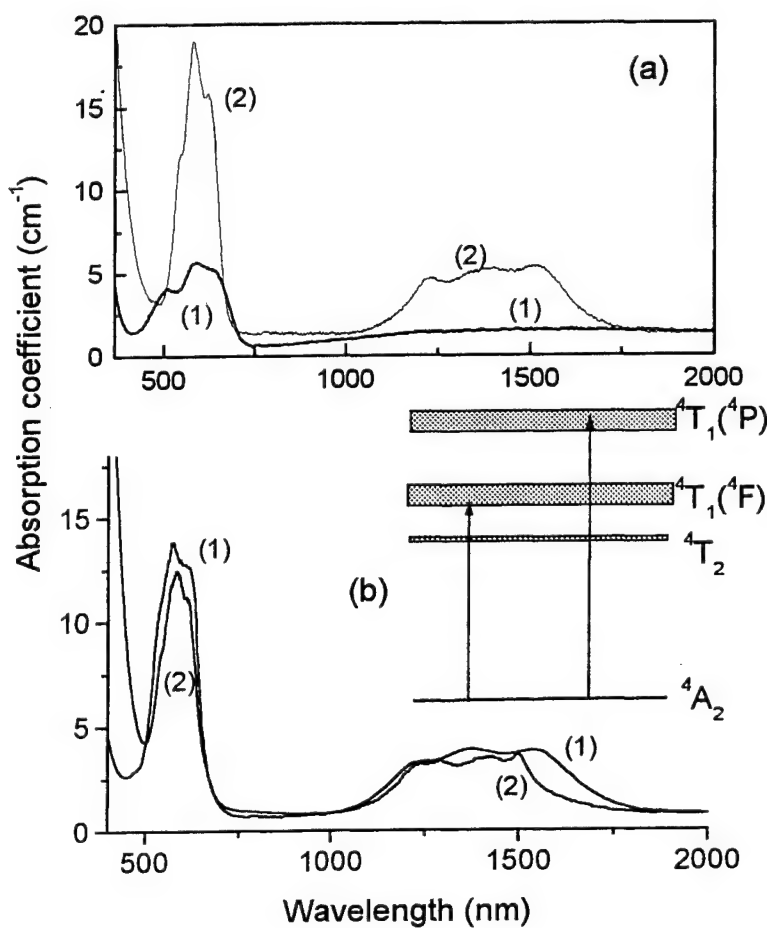


Figure 1. (a) Absorption spectra of the 0.1 Co:MAS sample before (1) and after (2) the second step of heat treatment. (b) Absorption spectra of the 0.1 Co:LAS (1) and 0.1 Co:ZAS (2) samples. Inset shows energy-level diagram of the Co^{2+} ion in a tetrahedral field of T_d symmetry.

Two stage heat treatments with a first hold at 750°C allowed us to obtain spinel nanometer sized crystals as the main crystalline phase and to suppress crystallisation of undesirable silicate phases.¹⁶ The absorption spectrum with narrow intensive bands is formed in the material heat treated at 800-1000°C after the first hold at 750°C. The intensity of absorption bands becomes maximal after heat treatment at 1000°C, the highest temperature after which the material still remains transparent (Fig. 2). The spectrum is characteristic of pure tetrahedrally co-ordinated Co^{2+} . The absence of bands at 500-510 nm manifests the almost full disappearance of octahedrally co-ordinated Co^{2+} . However, we cannot rule out the possibility for a small portion of Co^{2+} ions to remain in the residual silicate glass or to enter into magnesium alumino-titanate phase.

Figure 3 presents luminescence spectra of 0.1 and 0.3 Co:MAS samples. Excitation of the luminescence was made by the filtered Xe lamp

luminescence was made by the filtered Xe lamp irradiation (wavelengths 580 nm) into the $^4A_2 \rightarrow ^4T_1(^4P)$ transition of Co^{2+} ions. The both samples demonstrate very similar spectra with three range of emission: intense band at 680 nm (or 690 nm); less intense band centered at 935 nm, and wide weak band in the range of 1100 – 1600 nm. Rising the temperature from 78 to 300 K causes insufficient change of the spectra's shapes and ~5 times decrease of integral intensity. The $Co^{2+}:MgAl_2O_4$ crystal possesses three broad luminescence bands at 660 nm, 880 nm, and 1.3 μm corresponding to the transitions $^4T_1(^4P) \rightarrow ^2A_2$, 4T_2 , $^4T_1(^4F)$, respectively (Fig. 1). As soon as luminescence spectra of our samples and $Co:MgAl_2O_4$ crystal are very close, we attribute the luminescence bands to the same transitions as for $Co:MgAl_2O_4$ spinel crystal.

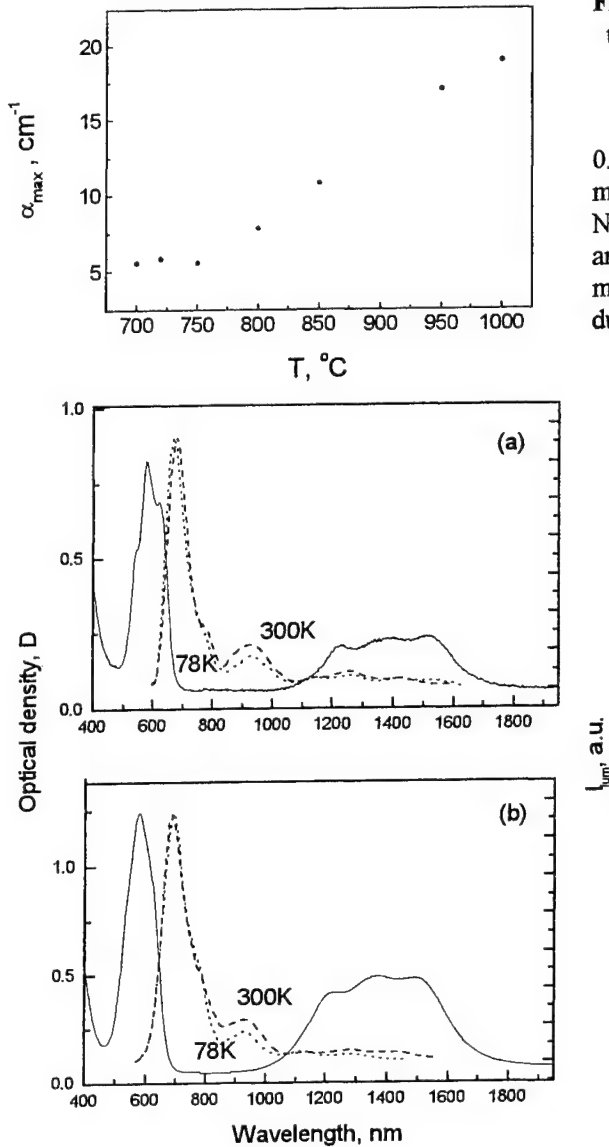


Figure 3. Absorption (solid line) and normalized luminescence (dashed lines) spectra of the 0.1 (a) and 0.3 (b) $Co:MAS$ samples.

different conditions of preparation are indicated in the Fig. 4 with different signs (circles, crosses, etc). This independence is a strong argument for that the spinel nanocrystallites which are formed during the annealing of glass does not change their primary structure during this process and Co ions conserve their tetrahedral co-ordination in them both under rising the temperature and lengthening the procedure. We estimated the characteristics times of the luminescence decay as the time of

Figure 2. Absorption coefficient in the maximum of the $^4A_2 \rightarrow ^4T_1(^4P)$ transition (~590 nm) for the 0.1 $Co:MAS$ sample in dependence on the temperature of the second stage of heat treatment.

Figure 4 demonstrates decay of integral luminescence signal for 0.1 and 0.3 $Co:MAS$ samples. Excitation of the luminescence was made using 20 ns pulses of second harmonics at 532 nm from Nd:YAG laser. The collected light was registered with fast Si diode and digital oscilloscope. For the both samples decay is not monoexponential, and does not depend on the temperature and duration of sample annealing. Results for the samples with the

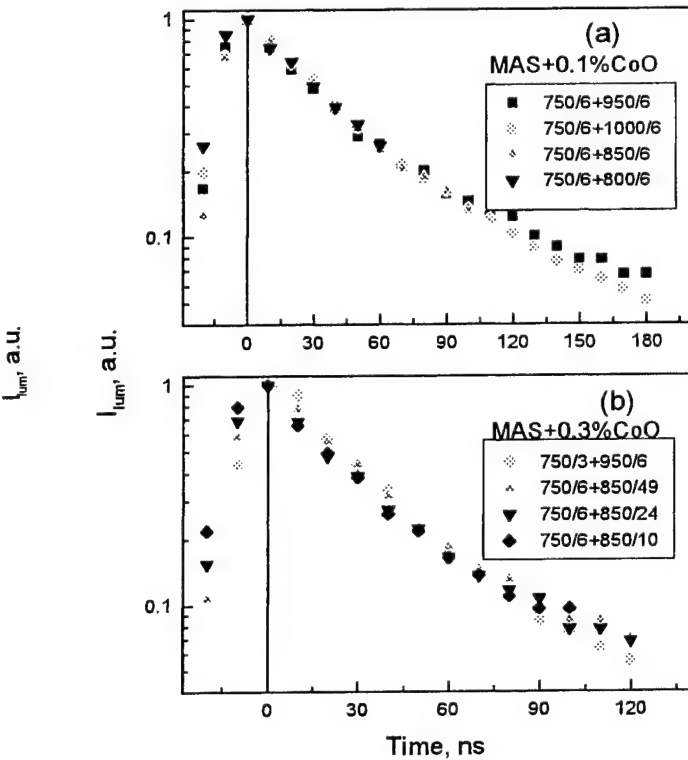


Figure 4. Decay of luminescence of the $^4T_1(^4P) \rightarrow ^4A_2$ transition for the 0.1 (a) and 0.3 (b) $Co:MAS$ samples with different temperatures of the second stage of heat treatment.

decrease to 1/e level and obtained values of 40 and 32 ns for 0.1 and 0.3 Co:MAS samples, respectively. These times are shorter than for Co:MgAl₂O₄ crystals (~150 ns)¹³ but Co ions concentration dependence of $\tau_{1/e}$ is the same: the higher concentration of Co ions the shorter the decay time. Shortening the decay time in glass ceramics in comparison with single crystals can be explained by the quick non-radiative relaxation through the defect states, concentration of which is essentially higher for nanocrystallites than for volume crystal due to higher surface-to-volume ratio for nanocrystallites in the glass ceramics. The same measurements for 0.1 Co:ZAS and 0.1 Co:LAS samples gave the values of $\tau_{1/e}$ as 200 ns and 28 ns, respectively.

Summarizing results from linear optical properties of our samples study we can conclude that increasing the temperature and/or duration of annealing of glass ceramics causes the increase of the amount of spinel nanocrystallites in the volume of sample (mainly due their increase in size). This leads to the increase of absorption. Luminescence decay is independent on the both these parameters indicating that the nanocrystallites structure and Co ions co-ordination in them do not change during these processes. So one could obtain the necessary transmission of the material either by short duration (or low temperature) of annealing with a thick sample or by longer duration (or higher temperature) of the process with a thinner one. It can be essential for design of devices where sizes of components are important.

4. NONLINEAR OPTICAL PROPERTIES OF CO²⁺-DOPED MAGNESIUM-ALUMINUM GLASS CERAMICS

The bleaching relaxation time of the 0.1 Co:MAS sample under excitation of $^4A_2 \rightarrow ^4T_1(^4F)$ transition was measured using the following method. The Co:MAS sample was pumped by the 1.54-μm Er³⁺:glass laser pulses of 75 ns in duration and simultaneously probed with a 200-μs pulse at 0.57 μm extracted from a Xe flash lamp radiation. The temporal changes in the probe beam transmission was recorded with the fast photodiode and digital oscilloscope (the response time of the detecting system was 10 ns). The bleaching relaxation time τ is estimated using the formula:¹⁷

$$\ln[T(t)/T(0)] = \left[1 - e^{-t/\tau}\right] \ln[T(\infty)/T(0)] \quad (1)$$

where $T(t)$ – is a transmission of the sample for the time moment t after the pump pulse. The bleaching decay was monoexponential with a time constant of $\tau = (450 \pm 150)$ ns [Fig. 5(a)]. For the Co²⁺:MgAl₂O₄ single crystal the decay constant of the $^4A_2 \rightarrow ^4T_1(^4F)$ absorption bleaching was measured to be 200 ns⁵ and (350 ± 40) ns⁶ and was tentatively assigned to the lifetime of the $^4T_2(^4F)$ level of the tetrahedral Co²⁺ ion.⁶

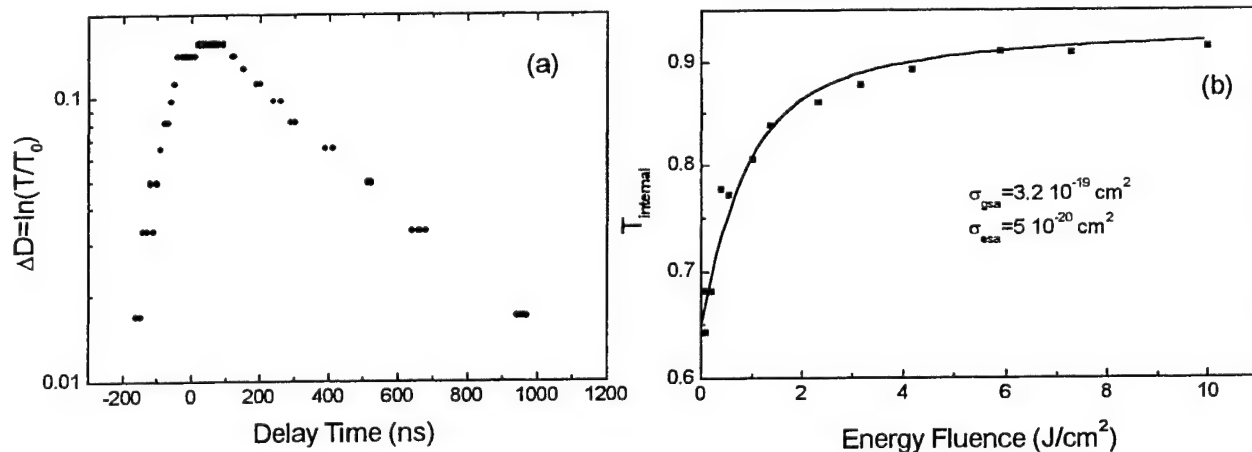
The absorption saturation measurement on the 0.1 Co:MAS sample was performed with the aid of passively Q-switched 1.54-μm Er³⁺:glass laser delivering pulses of 75 ns pulse widths. The transmission of the Co:MAS sample was measured with two photodetectors. The input energy of the pulses was varied with a set of filters. Figure 5(b) shows the transmission of the Co:MAS sample as a function of input energy fluence at wavelength of 1.54 μm, which corresponds to the $^4A_2 \rightarrow ^4T_1(^4F)$ transition. Bleaching from 62 up to 92% of transmission was observed. In view of the $^4A_2 \rightarrow ^4T_1(^4F)$ absorption bleaching relaxation time (~450 ns) is considerable longer than the experimental pulse duration (75 ns), the absorption saturation measurement data were analyzed within the framework of a slow-relaxing saturable absorber model.¹⁸

$$\frac{dE}{dz} = -hv[\ln(1/T_0)/(L\sigma_{GSA})](1 - \sigma_{ESA}/\sigma_{GSA})[1 - \exp(-\sigma_{GSA}E/hv)] - \ln(1/T_0)\sigma_{ESA}E/(L\sigma_{GSA}) \quad (2)$$

where T_0 is the small signal transmission, E is the input energy fluence, L is the length of the sample, σ_{GSA} and σ_{ESA} are ground state and excited state absorption cross-sections, respectively. We assumed that nonsaturable losses were negligible. The best fit to the experimental data was obtained with the values of $\sigma_{GSA} = (3.2 \pm 0.4) \times 10^{-19}$ cm² and $\sigma_{ESA}/\sigma_{GSA} = 0.16$ at 1.54 μm. These values are close to the values of $\sigma_{GSA} = (2.8 \pm 0.4) \times 10^{-19}$ cm² and $\sigma_{ESA}/\sigma_{GSA} = 0.07$ measured for the Co²⁺:MgAl₂O₄ single crystal.⁶

Using Co:MAS sample as the saturable absorber, passive Q-switching of 1.54-μm Er³⁺:glass laser was demonstrated. The Q-switching results are summarized in Table 1. The cavity of the 1.54-μm Er³⁺:glass flash-lamp pumped laser (Fig. 6) was 35 cm long and consisted of concave rear mirror M1 (radius-of-curvature, $r=100$ cm) and flat output mirror M2 (reflectivity at 1.54 μm, $R=78\%$). The Co:MAS saturable absorber was placed at Brewster angle between the rod of Er³⁺:glass (Ø3mm×50mm) and the output mirror M2. The Er:glass laser rod was Er:Yb:Cr:phosphate glass with the concentration of the Er³⁺ ion of 1.6×10^{-19} cm⁻³ and the emission cross section of 7×10^{-21} cm² at 1.54 μm. The Co:MAS sample was 0.36 mm thick without any antireflection coating. Its small-signal transmission at 1.54 μm was 78%. The repetition rate of the Q-switched Er:glass laser was 1 Hz. The Q-switched laser pulses of 80 ns in duration and up to 5.5 mJ in energy corresponding to 12% of

the free-running energy at the same pumping level were obtained. Using the mirror M2 with reflectivity $R=90\%$ the Q-switched pulses of also 80 ns in duration with energy of 3.5 mJ corresponding to 4.4% of the free-running output energy were observed. These results can be compared with the 75-ns, 2.7-mJ Q-switched pulses obtained from the 1.54- μm laser where the same laser rod as in our experiments was used with $\text{Co}^{2+}:\text{MgAl}_2\text{O}_4$ saturable absorber⁶ or with the 7 mJ in energy and less than 100 ns in duration Q-switched pulses obtained for Er:glass laser with transparent glass ceramic containing ZnAl_2O_4



spinel nanocrystals doped with Co^{2+} as the saturable absorber.¹²

Figure 5. (a) Kinetics of bleaching $\Delta D = \lg(T/T_0)$ for the 0.1 Co:MAS sample at probe wavelength of 0.57 μm under excitation at 1.54 μm with 75-ns duration laser pulses. The probe pulse width is $\sim 200 \mu\text{s}$. (b) Dependence of transmission of the 0.1 Co:MAS sample at the wavelengths of 1.54 μm on the input energy fluence. The pulse duration is 75 ns. Solid curve is the result of the fitting with the aid of Eq. (2).

Table 1. Passive Q-switch performance of the Co:MAS sample at 1.54 μm

Output coupler, R	Pulse energy, mJ	Pulse duration, ns	Q-switch. efficiency, %
90%	3.5	80	4.4
78%	5.5	80	12

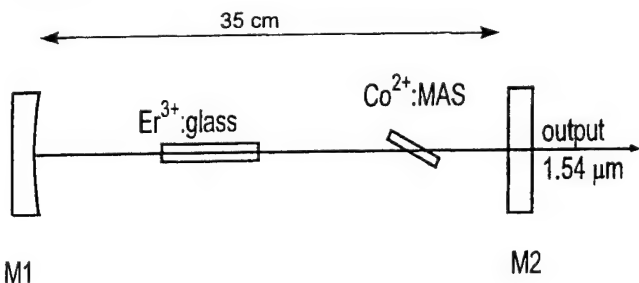


Figure 6. Schematic of the passively Q-switched 1.54- μm $\text{Er}^{3+}:\text{glass}$ laser cavity.

5. CONCLUSION

We present study of linear and nonlinear optical properties of different glass ceramics on the base of magnesium-aluminum, zink-aluminum, or lithium-aluminum spinel nanocrystallites doped with 0.1 or 0.3 wt. % of tetrahedrally coordinated Co^{2+} ions. Decay of luminescence of the ${}^4\text{T}_1({}^4\text{P}) \rightarrow {}^4\text{A}_2$ transition for the 0.1 Co:LAS, Co:MAS, Co:ZAS, and 0.3 Co:MAS samples has not monoexponential type and characteristics times of 28, 40, 200 and 32 ns, respectively. Luminescence decay showed shortening of the characteristic time with increase of Co ions concentration in the sample and no time dependence on the temperature of the second stage of heat treatment for all samples. The transparent glass ceramic containing magnesium-

aluminum spinel nanocrystallites doped with tetrahedrally coordinated Co^{2+} ions was used as the saturable absorber Q-switch for 1.54 μm Er:glass laser. Q-switched pulses of up to 5.5 mJ in energy and 80 ns in duration from 1.54 μm Er:glass flash-lamp pumped laser without intracavity focusing were achieved. The ground state and excited state absorption cross sections of the 0.1 Co:MAS sample at 1.54 μm were estimated to be $(3.2 \pm 0.4) \times 10^{-19} \text{ cm}^2$ and $(5.0 \pm 0.6) \times 10^{-20} \text{ cm}^2$, respectively. Relaxation time of the $^4\text{A}_2 \rightarrow ^4\text{T}_1(^4\text{F})$ transition bleaching was measured to be (450 ± 150) ns.

REFERENCES

1. B. Denker, G. Maksimova, V. Osiko, S. Sverchkov, Yu. Sverchkov, "Erbium glass lasers with passive Q-switching of the resonator by a component containing erbium", Sov. J. Quantum Electron, **21**, pp. 774-776, 1991.
2. R. Fluck, U. Keller, E. Gini, H. Melchior, "Eyesafe Pulsed Microchip Laser", in OSA TOPS on *Advanced Solid State Lasers*, **19**, pp. 146-149, 1998.
3. R. Wu, D. Rhonehouse, M. Myers, S. Hamlin, J. Myers, Y. Jiang, "Spectral bleaching and 1535 nm Q-switching of uranium glass", in OSA Proc. on *Advanced Solid State Lasers*, **24**, pp. 440-444, 1995.
4. M. B. Camargo, R. D. Stultz, M. Birnbaum, M. Kokta, "Co²⁺:YSGG saturable absorber Q switch for infrared erbium lasers", Optics Letters, **20**, pp. 339-341, 1995.
5. B. Denker, B. Galagan, E. Godovikova, M. Meilman, V. Osiko, S. Sverchkov, "The efficient saturable absorber for 1.54 μm Er glass lasers", in OSA TOPS on *Advanced Solid State Lasers*, **26**, pp. 618-621, 1999.
6. K. V. Yumashev, I. A. Denisov, N. N. Posnov, P. V. Prokoshin, V. P. Mikhailov, "Nonlinear absorption properties of Co²⁺:MgAl₂O₄ crystal", Appl. Phys. B, **70**, pp. 179-184, 2000.
7. K. V. Yumashev, I. A. Denisov, N. V. Kuleshov, "Co²⁺-doped spinels saturable absorber Q-switches for 1.3-1.6 μm solid state lasers", in OSA TOPS on *Advanced Solid State Lasers*, **27**, pp. 204-206, 2000.
8. K. V. Yumashev, I. A. Denisov, N. N. Posnov, V. P. Mikhailov, R. Moncorge, D. Vivien, B. Ferrand, Y. Guyot, "Nonlinear spectroscopy and passive Q-switching operation of a Co²⁺:LaMgAl₁₁O₁₉ crystal", JOSA B, **16**, pp. 2189-2194, 1999.
9. M. Birnbaum, M. Camargo, S. Lee, F. Unlu, R. Stultz, "Co:ZnSe saturable absorber Q-switch for the 1.54 μm Er:Yb glass laser", in OSA TOPS on *Advanced Solid State Lasers*, **10**, pp. 148-151, 1997.
10. A. V. Podlipensky, V. G. Shcherbitsky, N. V. Kuleshov, V. P. Mikhailov, V. I. Levchenko, V. N. Yakimovich, "Cr²⁺:ZnSe and Co²⁺:ZnSe saturable-absorbers Q switches for 1.54- μm Er:glass lasers", Optics Letters, **24**, pp. 960-962, 1999.
11. T.-Y. Tsai, M. Birnbaum, "Co²⁺:ZnS and Co²⁺:ZnSe saturable absorber Q switches", J. Appl. Phys., **87**, pp. 25-29, 2000.
12. R. Boiko, A. Okhrimchuk, A. Shestakov, "Glass ceramics Co²⁺ saturable absorber Q-switch for 1.3-1.6 μm spectral region" in OSA TOPS on *Advanced Solid State Lasers*, **19**, pp. 185-188, 1998.
13. V. Mikhailov, N. Kuleshov, "Picosecond spectroscopy of excited states in transition metal ion doped new laser materials", OSA Proc. on *Advanced Solid State Lasers*, **15**, pp. 320-323, 1993.
14. I. P. Alekseeva, V. V. Golubkov, T. I. Chuvaeva, Fiz. Khim. Stekla, **7**, pp. 47-53, 1981 (in Russian).
15. U. Kang, O. S. Dymshits, A. A. Zhilin, T. I. Chuvaeva, G. T. Petrovsky, "Structural states of Co(II) in β -eucryptite-based glass-ceramics nucleated with ZrO₂", J. Non-Cryst. Solids, **204**, pp. 151-157, 1996.
16. D. S. Baik, V. V. Golubkov, O. S. Dymshits, A. A. Zhilin, T. I. Chuvaeva, Glass Phys. Chemistry, **23**, pp. 259-264, 1997.
17. S. L. Shapiro (Ed.), *Ultrashort light pulses*, (Springer-Verlag, Berlin, 1977) p. 75.
18. Y. K. Kuo, M. F. Huang, M. Birnbaum, "Tunable Cr⁴⁺:YSO Q-switched Cr:LiCAF laser", IEEE J. Quant. Electronics, **31**, pp. 657-663, 1995.

Investigation of the Kerr-lens mode locking ability of Cr²⁺: ZnSe solid-state laser

V. L. Kalashnikov, I. G. Poloyko

International Laser Center, 65 Skorina Ave., Bldg. 17, Minsk, 220027 Belarus
tel./fax: (375-0172) 326-286, e-mail: vkal@ilc.unibel.by

ABSTRACT

The theoretical calculation for nonlinear refractive index n_2 in Cr²⁺: ZnSe - active medium predicts the strong defocusing cascaded second-order nonlinearity within 2 - 3 μm spectral range. On the basis of this result the optimal cavity configuration for Kerr-lens mode locking is proposed that allows to achieve a sub-100 fs pulse duration. The numerical simulations testify about strong destabilizing processes in the laser resulting from a strong self-phase modulation. The stabilization of the ultrashort pulse generation is possible due to spectral filtering that increases the pulse duration up to 300 fs.

Keywords: solid-state laser, Kerr-lens mode locking, ultrashort pulse, self-phase modulation

1. INTRODUCTION

The intensive investigations of the Cr²⁺-doped laser media testify about their high potential in the tunable generation in mid-IR between 2 - 5 μm . A special interest is connected with Cr²⁺: ZnSe - active medium due to its excellent material properties: high thermal conductivity which is close to that one of YAG, the absence of excited state absorption, and very broad gain band which allows for tunable generation in 2 - 3 μm range. The latter is very attractive for a lot of applications: remote sensing, spectroscopy, ophthalmology, and neurosurgery.

At this moment, the pulsed¹ and continuous-wave operation² in Cr²⁺: ZnSe lasers was demonstrated with InGaAs and Tm: YALO laser pumping, which demonstrated high efficiency and favorable lasing abilities of this active crystal.

A very interesting property of Cr²⁺: ZnSe is the high coefficient of the nonlinear refraction³ that results from the relatively small bandgap, i. e., in fact, from the semiconductor nature of the material. As it is known, the higher nonlinear refraction is favorable to self-starting of Kerr-lens mode locking⁴. The decrease of Kerr-lens mode locking threshold allows to simplify the laser configuration, to improve the ultrashort pulse stability, and to increase the lasing efficiency. Another advantage of Cr²⁺: ZnSe as media for ultrashort pulse laser is a very broad gain band, which can support the generation of 12 fs pulses.

However, high nonlinear refraction coefficient is the source of some shortcomings. As it was shown⁵, the Kerr-lens mode-locked lasers demonstrate a variety of unstable regimes that can destroy the ultrashort pulse and prevent from the pulse shortening.

Here, for first time to our knowledge we analyze the Kerr-lens mode locking abilities of Cr²⁺: ZnSe laser. The analysis of ZnSe nonlinear properties is presented that is necessary for an optimization of the laser design and for investigation of self-starting ability and ultrashort pulse stability in Cr²⁺: ZnSe laser.

2. NONLINEAR REFRACTION IN ACTIVE MEDIUM

As it is known³, the two-photon absorption, Raman scattering and Stark effect strongly contribute to nonlinear refractivity in semiconductors. The main parameter, which defines a value of nonlinear refraction coefficient n_2 , is the bandgap energy E_g :

$$n_2 [\text{esu}] = \frac{K \sqrt{E_p} G_2 (\hbar\omega / E_g)}{n_0 E_g^4}.$$

Here n_0 is the linear coefficient of refraction; $E_p = 21$ eV for the most of direct gap semiconductors; $K = 1.5 \cdot 10^{-8}$ is a material-independent constant; G_2 is the function depending only on the ratio of photon energy and the energy gap of the material. For ZnSe $E_g = 2.58$ eV. For G_2 we used the following approximation in the below bandgap region:

$G_2(x) = 0.01373 + \frac{0.656 \cdot 10^{-14}}{x^2} + \frac{0.1889 \cdot 10^{-37}}{x^6}$, which was obtained from experimental data presented in Ref. 3. In addition to dependence of G_2 on wavelength, we have to take into account the dispersion of n_0 . For ZnSe the next approximation is valid: $n_0 = 2.4215 + \frac{0.4995 \cdot 10^{-7}}{\lambda} - \frac{0.1747 \cdot 10^{-13}}{\lambda^2} + \frac{0.3429 \cdot 10^{-19}}{\lambda^3}$ (here λ is in meters). A resulting dependence of n_2 on wavelength is shown in Fig. 1. There is a strong Kerr nonlinearity producing self-focusing effect. The value of n_2 exceeds the typical values of the most of dielectric crystals by two orders of magnitude.

However, this is not sufficient for the estimation of the nonlinear properties of ZnSe. Despite the fact that ZnSe has

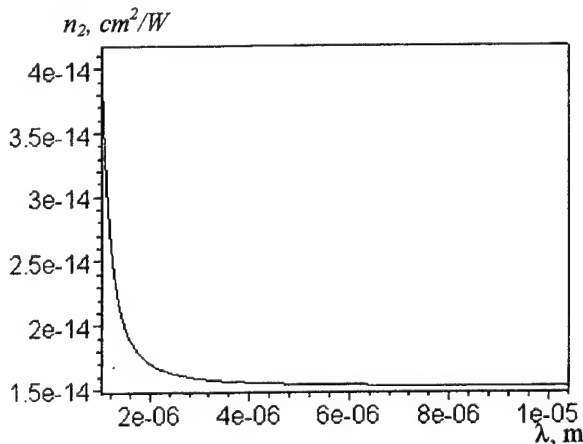


Fig. 1. The dependence of n_2 on wavelength in the case of third-order nonlinearity contribution.

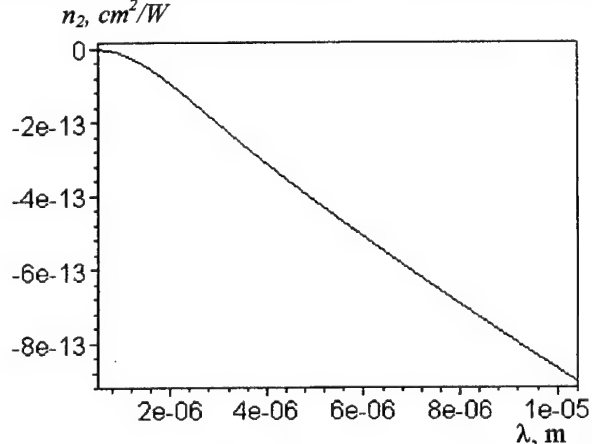


Fig. 2. The dependence of n_2 on wavelength in the case of second-order nonlinearity contribution.

cubical lattice, there is not center of inversion in crystal. As result, the medium possesses the second-order nonlinear properties. The corresponding nonlinear coefficient $d = 80 \text{ pm/V}^6$. Although there is no efficient frequency conversion, the existence of second-order nonlinearity can strongly contributes to the nonlinear refractivity due to so-called cascaded second-order nonlinearity, which can be used for Kerr-lens mode locking⁷. Usually, change of the index of refractivity has non-Kerr character, but the Kerr-like approximation $n = n_0 + n_2 I$ (where I is

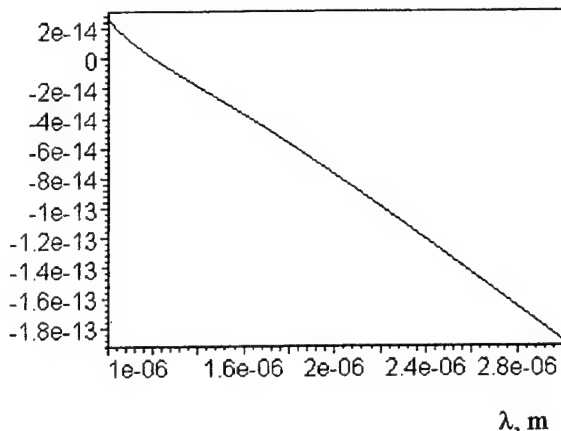


Fig. 3. Net-coefficient of nonlinear refraction in ZnSe

second-order nonlinearity is⁶:

$$n_2 = \frac{4\pi d^2}{\epsilon_0 n_0^2 n_{2\omega} c \lambda \Delta k}$$

Note, that in the case of the normal dispersion of n_0 the nonlinearity due to second-order nonlinearity has a defocusing nature. The dependence of n_2 on the wavelength is shown in Fig. 2. One can see, that the nonlinear refraction is very strong. As result of the joint contribution of third- and second-order nonlinearities, a net-coefficient of nonlinear refraction is shown in Fig. 3.

the field intensity) is valid if⁶ $\frac{(\Delta k/2\chi)^2}{I} \ll 1$, where

$$\chi = \frac{2\omega d}{\sqrt{2\epsilon_0 n_0^2 n_{2\omega} c^3}}; \Delta k = 2k_0 - k_{2\omega}; \omega, k_0$$
 are the fundamental

frequency and wave number, respectively; $n_{2\omega}, k_{2\omega}$ are the linear refractive index and wave number for the second harmonic. Our calculations showed, that the Kerr approximation for ZnSe is valid up to intensities of 2.2 TW/cm^2 at $2 \mu\text{m}$ and 600 GW/cm^2 at $3 \mu\text{m}$, and it is used throughout present work.

The nonlinear coefficient of refraction due to cascading

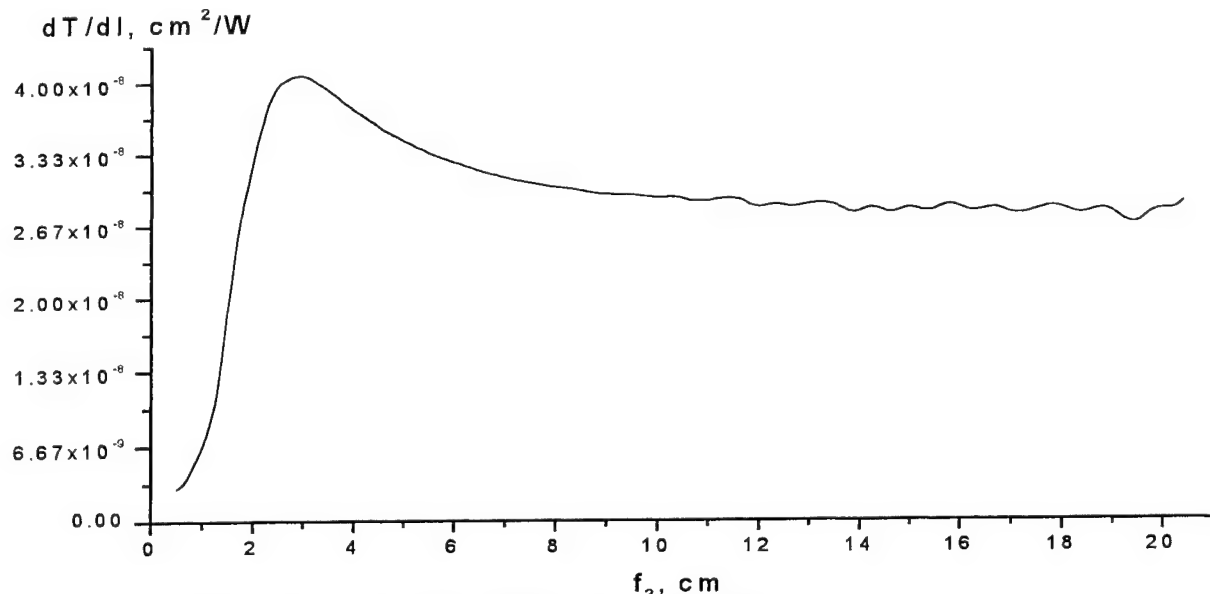


Fig. 4. Kerr-lens mode locking efficiency in ZnSe - laser

The nonlinearity is focusing up to 1.2 μm and defocusing in mid-IR range. An experimental value of n_2 measured at 1.06 μm demonstrates an excellent agreement with the corresponding value of calculated curve in Fig. 3.

3. LASER CONFIGURATION

The obtained value of n_2 enables us to estimate a mode locking efficiency due to Kerr-lensing. We have used the method presented in⁸: for each fixed value of the focal length of the mirror M_2 (see Fig. 5) we varied a folding distance and the position of active medium trying to maximize the value of $\frac{\partial T}{\partial I}$, where T is the effective transmission of the hard aperture.

This parameter defines the inverse saturation intensity of the efficient fast saturable absorber, induced by joint action of Kerr self-focusing in active medium and diffractive losses at aperture. For the common Kerr-lens mode-locked lasers $\frac{\partial T}{\partial I} \approx 10^{-10} - 10^{-12} \text{ cm}^2 / \text{W}$. In the case of ZnSe the modulation parameter is shown in Fig. 4. It is seen, that the Kerr-lensing efficiency in this case is higher by two orders of magnitude. It is interestingly, that the defocusing nature of the nonlinearity does not affect the process of the cavity optimization essentially: the change of the sign of n_2 only slightly affects the position of active medium and folding distance. The optimized cavity configuration is shown in Fig. 5.

4. ULTRASHORT PULSE STABILITY

Calculated values of $\frac{\partial T}{\partial I}$ suggest a good Kerr-lens mode locking ability of Cr^{2+} : ZnSe - laser. However, the strong self-phase modulation while being the positive factor facilitating self-focusing, can, on the other hand, destabilize an ultrashort pulse generation due to automodulational instability⁵. In order to estimate the mode locking stability in Cr^{2+} : ZnSe - laser we performed the numerical simulation on the basis of fluctuation model and distributed scheme of the laser generation. The master equation was:

$$\frac{\partial a}{\partial z} = \left(\alpha + (t_f + iD) \frac{\partial^2}{\partial t^2} - i\beta|a|^2 - \frac{\gamma}{1 + \sigma|a|^2} \right) a,$$

where a is the field, z is the longitudinal coordinate, α is the saturated by full field energy gain coefficient, t_f is the inverse bandwidth of the spectral filter, D is the net-group delay dispersion, $\beta = \frac{2\pi n_2 z_g}{\lambda n_0}$ is the self-phase modulation parameter, z_g is the active medium length, γ is the diffraction loss, defined from configuration of laser, $\sigma = \frac{\partial T}{\partial l}$.

The strong self-phase modulation and self-focusing dominate over the gain saturation. The last factor provides the negative feedback in laser that stabilizes ultrashort pulse. The critical parameter defining the ultrashort pulse dynamics is $\tau = \frac{t_f}{\beta E_s}$, where E_s is the gain saturation fluency. The decrease of this parameter worsens the pulse stability. To comparison, in ZnSe τ is ten times lower than in Ti: sapphire. Therefore, to obtain the stable pulse generation, we have to increase τ e.g. by increasing t_f . The stable pulses were obtained for $t_f=120$ fs. The pulse duration was about 300 fs for 800 mW absorbed pump power. An additional stabilization factor is the minimization (down to zero) of net-dispersion.

The character of the pulse destabilization needs some comments. The typical scenarios are shown in Figs. 6 – 8. The pulse behaviors presented here were calculated for the same set of the laser parameters but for different initial noise samples. There are the possibilities for multipulse generation (Fig. 6), generation of the breezer-like pulse and its subsequent disintegration (Fig. 7), and the collapse of the pulse into several pulses (Fig. 8). Note, that breezer-like pulse is formed without action of the soliton mechanism in laser because of net-dispersion in this case is close to 0. The regime depicted in Fig. 8 is characterized by low-frequency modulation of the generation spectrum that at last leads to the pulse collapse. It should be noted, that the generation of the stable single pulse is depended on the random noise sample, too.

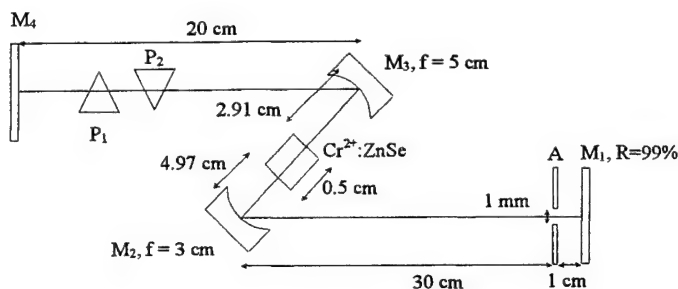


Fig. 5. Optimal cavity design for Kerr-lens mode locking

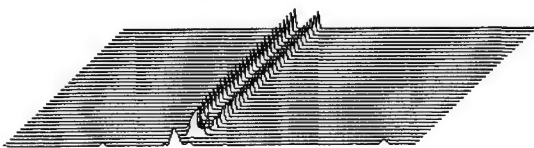


Fig. 7.

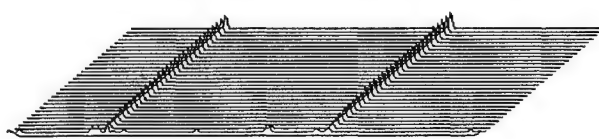


Fig. 6.

typical active media of femtosecond lasers. The optimal cavity configuration for Kerr-lens mode locking was found. But, as the analysis testifies, the main problem of the ultrashort pulse generation in Cr²⁺: ZnSe – laser is the pulse destabilization due to strong self-phase modulation. This requires to decrease the bandwidth of spectral filter. The last allows to generate 300 fs pulses. The self-start of Kerr lens mode locking has a statistical character, that is depended on the noise sample. The investigation of the pulse destabilization testifies about formation of the breezer-like pulses and pulse collapse due to low frequency perturbations.

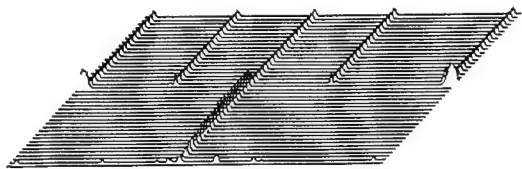


Fig. 8.

6. REFERENCES

1. R.H. Page, J.A. Skidmore, K.I. Schaffers, R. J. Beach, S. A. Payne, and W. F. Krupke, *OSA Trends in Optics and Photonics 1*, C. R. Pollock and W. R. Bosenberg, eds. (OSA, Washington, 1997).
2. G. J. Wagner, T. J. Carring, R. H. Page, K. I. Schaffers, J. Ndap, X. Ma, and A. Burger, *Opt. Lett.*, **24**, 19 (1999).
3. M. Sheik-Bahae, D. C. Hutchings, D. J. Hagan, and E. W. van Stryland, *IEEE J. Quantum Electr.*, **27**, 1296 (1991).
4. C. Radzewicz, G. W. Pearson, and J. S. Krasinski, *Optics. Commun.*, **102**, 464 (1993).
5. J. Jasapara, V. L. Kalashnikov, D. O. Krimer, I. G. Poloyko, M. Lenzner, W. Rudolph, *J. Opt. Soc. Am.*, **B 17**, 319 (2000).
6. R. L. Sutherland, *Handbook of nonlinear optics* (NY, 1996).
7. G. Cerullo, S. De Silvestry, A. Monguzzi, D. Segala, and V. Magni, *Opt. Letts.*, **20**, 746 (1995).
8. V. L. Kalashnikov, V. P. Kalosha, I. G. Poloyko, V. P. Mikhailov, *J. Opt. Soc. Am.*, **B 14**, 964 (1997).

KTiOPO₄ electro-optical devices with extinction ratio up to 1:1000

V.A.Rusov^a, Gorchakov A.V.^b, Belostotsky A.L.^b, Sapojsnikov V.K.^b,
Kaplun A.B. , Meshalkin A.B.^c, V.N.Shapovalov^d

^a Institute for Lasers Physics, St.-Petersburg, Russia, e-mail: rusov@ilph.spb.su

^bInstitute of Semiconductor Physics, Novosibirsk, Russia, e-mail: , gorchak@isp.nsc.ru

^cInstitute of Thermophysics, Novosibirsk, Russia, e-mail: kaplun@itp.nsc.ru

^dScimed Life Systems, Minneapolis, USA, e-mail: shapovav@bsci.com

ABSTRACT

We report on a complete technology ensuring fabrication of reliable electro-optical modulator employing Russian flux grown KTiOPO₄. The pilot units employing 2- crystals thermally compensated scheme, with aperture 4* 4 mm², operate at 1.064 mkm both at AC and DC mode and exhibit at half-wave voltage about 1500V an extinction ratio up to 1: 1000. No electrochromic damages were observed during multi hour testing.

Key words: KTiOPO₄, KTP, crystal, flux grown KTP, electro-optical modulator, EOM, , high contrast EOM, Q switch.

1. INTRODUCTION

The combination of good nonlinear-optical and electro-optical properties in the crystals of KTP family (KTP, KTA, RTP, RTA) is the basis for the constant interest to these media as the media, applicable for the creation of electro-optical devices for the control over high-power laser radiation. In particular, for KTP the specific half-wavelength voltage is about 7.5 kV, and the optical damage threshold at 1.06 μ m exceeds 1 GW/cm². The low (in comparison with LiNbO₃) value of dielectric permeability $\epsilon_{33}=(13-15)$ is convenient for the high-frequency matching, and the low value of the electro-mechanical matching coefficient results in the much-lower rate of “piezo-chime” under the pulsed control.

In spite of the obvious advantages of KTP crystals in comparison with the traditional electro-optics crystals (DKDP, LiNbO₃ and LiTaO₃), we know only several examples of creation of electro-optical modulators on the base of KTP crystal (for example, [1]) or RTP crystal (ISORAD/ZEBRA crystals (Israel) <http://www.raikol.com>). There are several factors, preventing the use of monocrystal of KTP in electro-optics. In the case of the hydrothermal grown KTP (USA, Airtron Litton SYNOPTICS - <http://www.cyberwirednc.com>) it is a relatively high cost - 5-8 \$/mm³ and small size of available crystals. The KTP crystals, grown by means of the traditional polyphosphate self-flux technology, reveal comparatively high specific conductivity $\sigma_z \sim 10^{-6}-10^{-8} \Omega^{-1} \times \text{cm}^{-1}$ [2] and the fast electrochrome degradation in the electric field, controlling the electro-optical modulator.

2. EXPERIMENTAL RESULTS AND DISCUSSION

The goal of our work was the directed modification of the main studies of technology of fabrication of the electro-optical modulators (EOM) on the base of KTP, namely of their growth, selection, processing and modeling of EOM. The specific

goal was to achieve the situation when the technology chain would guarantee the fabrication of high contrast (at least 1000) devices, which reveal stable performance under the constant and alternating control voltage. With this purpose we have modified the polyphosphate self-flux technology and developed the method of growing the high resistance monocrystals of KTP according to this technology. The growth was done according to the modified Chohralsky method - the growth in the gradient temperature field on the seeding crystal, oriented in the direction of the X-axis. The development of the technology of high resistance KTP crystal growth was preceded by the detailed study of the physical and chemical properties and of the crystallization process of the polyphosphate self-flux. The knowledge of reliable values of said parameters made it possible not only to enlarge the growth speed, but also to find the technology regimes, providing the specific resistance of KTP crystals of not more than $\sigma_z \sim (2-4) \times 10^{11} \Omega^{-1} \times \text{cm}^{-1}$ under the room temperature.

The grown up bulbs of KTP were shaped and polished in accordance with their crystallographic axes 16(X) x 30(Y) x 20(Z) mm³. The graphite electrodes were deposited onto the edges Z, and thus prepared specimens were subjected to the measurement of spatial distribution of the birefringence non-uniformity (contrast).

These testing has revealed the fact, that the defects of some definite type, which are important from the point of view of EOM performance, can not be revealed out by the usual procedure of measurement of the spatial distribution of contrast (without field). They become evident only in the electric field with the tension over some specific threshold. In the crystals of KTP, which we have studied, such a threshold corresponds to some 400 V/cm. The Fig.1 (E_z = 0 and E_z = 2000 V/cm) illustrates the character of variations in the distribution of the local contrast under the application of the voltage along the axis Z of the shaped bulb.

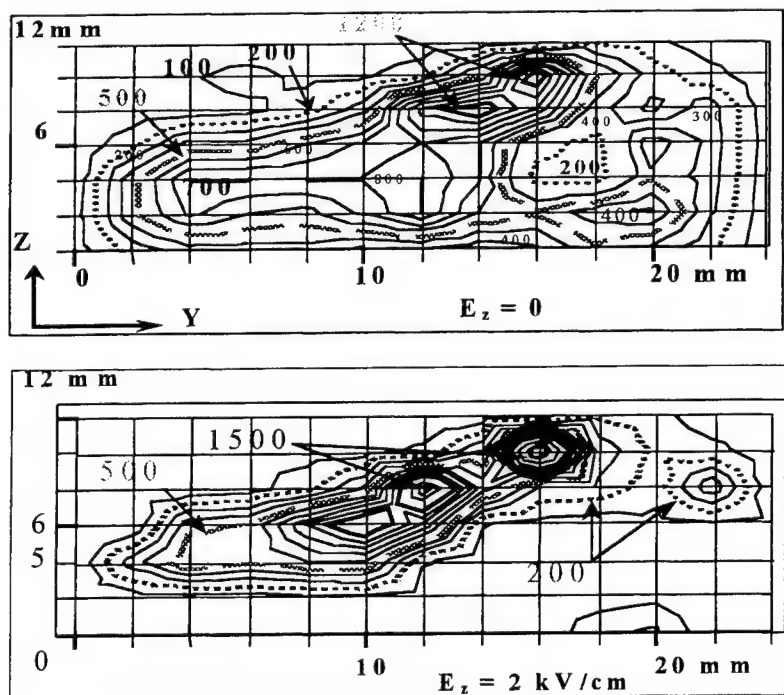


Fig.1. Map of contrastdistribution across the bulb of KTP crystal

The most reasonable explanation of these variations is the local heating of the "weak" zones of the bulb, which reveal the high conductivity.

The material for the high-contrast modulator was taken from the zones with the corresponding contrast level. The selected blanks were subjected to the mono-domain checking by measurement of spatial uniformity of piezo-response at the edges Z

and of half-wavelength voltage.

The measurements of the temperature dependence of conductivity of thus selected specimens has shown that in the temperature range 10-100°C and in the linear range of the Volt-Amper characteristics this dependence has the activation character $\sigma_z(T) \sim \sigma_0 \exp(-E_a/kT)$ with the activation energy $E_a \sim 0.85$ eV and $\sigma_0 \sim (2-4) \times 10^{-11} \Omega^{-1} \times \text{cm}^{-1}$. For the crystals, grown according to the traditional self-flux technology the activation energy is much lower - $E_a \sim 0.5$ eV, and the value of $\sigma_0 \sim (10^{-6}-10^{-8}) \Omega^{-1} \times \text{cm}^{-1}$.

We have said already, that the main limitations of KTP use in EOM are imposed by the electrochrome processes, leading to inducing the color centers $\text{Ti}^{4+} \rightarrow \text{Ti}^{3+}$ in the near-cathode zone under the current action. So it is very important to determine the admissible ranges of the applied field tension. In the KTP crystals, which we have grown up, the utmost admissible field tension is about 4.5 kV/cm under the room temperature, while for the KTP crystal, grown up according to the traditional self-flux technology the electrochrome effects begin develop fast at the much lower field tensions of some - 300 - 400 V/cm.

Our tests and results of measurements provide the basis for the definite recommendation of using the KTP crystals, grown up according to this technology, for fabrication of the EOM devices, working under the nearly room temperature (15-35)°C.

The crystals of KTP, grown up according to the novel technology, were used for fabrication of the "pilot" specimen of the amplitude modulator. This modulator was subjected to the preliminary testing inside the cavity of pulse-repetitive Nd:YAG laser. The modulator consisted of two crystals of X-cut with the size 5.1(Z) x 6.0(Y) x 20(X) mm³, mounted in the scheme of the birefringence compensation. The radiation was propagating along the X-axis, and the control voltage was applied along Z-axis. The quarter-wavelength voltage was equal 750 V. The laser was working in the Q-switch mode and has revealed the following parameters: pulse energy 20 mJ, pulse duration (FWHM) 20 ns, beam diameter 2.0 mm and pulse repetition rate 50 Hz. The experiments with this system has confirmed the good prospects of its use. However, the question of its application in the real laser systems requires yet some additional studies.

3. References

1. Ebbers Christofer A. A. Velsko Stefan P. High average power KTiOPO₄ electro-optic Q switch.
Appl.Phys. Lett. vol.67, N 5, pp. 593-595, 1995
2. Bierlein J.D., Arweiler C.B. Electro-optic and dielectric properties of KTiOPO₄
Appl.Phys.Lett. vol.49, N15, pp.917-919, 1986

Ion beam optical coatings for visible and near IR lasers

G. Kolodnyi, Yu. Golyaev, V. Azarova, M. Rasyov, and N. Tikhmenev

POLYUS Research & Development Institute, 3 Vvedensky St., Moscow, 117342,
Russian Federation

ABSTRACT

Ion beam optical coatings based on titanium, tantalum and silicon oxides find wide application in visible and near IR lasers since they allow production of mirrors with a high coefficient of reflection as well as provide high laser damage thresholds. This paper reports on development of the coatings with low absorption and scattering and high coefficient of reflection (99.98%) at 632 nm for circular polarization and an angle of beam incidence of 45° as well as on the protective antireflection coatings on BBO crystals and silicate glass at 1064 nm with high laser damage thresholds (15...20 J/cm²). Absorption, scattering and loss in the mirrors as well as laser damage thresholds of the protective antireflection coatings have been measured.

Keywords: Ion beam coatings. passive loss. absorption, scattering, laser damage.

1. INTRODUCTION

In recent years the technology for ion beam optical coatings for visible and near IR range has received a large development effort in the USA and Europe due to the fact that it has provided high quality and reliability of coatings when used in lasers^{1, 2}. The feature of ion beam coatings is a low value of passive loss due to a small value of absorption and scattering. Such coatings are necessary for precision low-power lasers such as ring gas laser gyros^{3, 4}, compact diode-pumped solid-state lasers, etc.

As shown in work⁵, the ion beam coatings can offer high laser damage thresholds in near IR region. These advantages of the ion beam coatings are due to more homogeneous microstructure of the coatings relative to the electron-beam coatings characterized in cross-section by specific column-shaped structure of layers with cavities, moisture traces and contamination of various foreign impurities⁶. This makes obtaining the coefficients of reflection more than 99.9% on electron-beam coatings difficult.

In this paper, the results of development of the ion beam mirrors for circular polarization and an angle of beam incidence of 45° with a coefficient of reflection of 99.98% at 632 nm for Zeeman laser gyros (ZLG) are presented⁷. Making the protective antireflection ion beam coatings on silicate glass, BaB₂O₄ (BBO) crystals and study of their laser damage thresholds are also reported. The BBO crystals are an excellent nonlinear material that is widely used to generate frequency harmonics of fundamental Nd:YAG lasers⁸. However the surface of the BBO crystals under usual laboratory conditions is damaged due to atmospheric moisture. So in this work the single-layers and two-layers protective antireflection coatings have been made that allow protection of the crystal surface without a great decrease of laser damage of crystal surface. The investigations of laser damage thresholds have shown that they are 15±3 J/cm² at 1064 nm in Q-switched operation.

We have studied the major optical characteristics of the single layers and two-layers coatings based on TiO₂-SiO₂ that allow making the 17...23-layer mirrors at 632 nm with an angle of beam incidence of 45°. The coatings based on Ta₂O₅-SiO₂ that allow making the protective antireflection coatings have been also studied. The results for integral scattering of the mirrors and its substrate surface polishing quality dependence are presented, the values of absorption of the coatings at 672 and 515 nm, the total absorption, scattering and transmission loss as well as the ellipsometric parameters of the mirrors have been measured.

In summary, the possible fields of application of the ion beam coatings for lasers of various types are discussed.

2. EXPERIMENTAL PART

2.1. VACUUM SYSTEM FOR PRODUCTION OF COATINGS

The scheme of the vacuum chamber is given in Fig. 1. It has the shape of a cube with a side about 400 mm. The cryogenic pump allows obtaining the residual pressure of $\sim 1 \times 10^{-6}$ mb. The substrate holder was manufactured as a flat planetarium holder, in the center of which there was the reference glass of the optical system for monitoring of the thickness of layers. The ion source made by PLATAR Ltd. was set on the top flange of the chamber. The ion source with beam diameter of 5 cm has the filamentary cathode, the filamentary cathode-neutralizer and the two-grid ion optics. High-purity argon was used as the working gas. To obtain stoichiometric oxides of titanium, tantalum and silicon, high-purity oxygen was inlet into the chamber. The targets of Ti and SiO_2 of a diameter of 150 mm and a purity of 99.99% and tantalum with a purity of 99.9% were used as the targets.

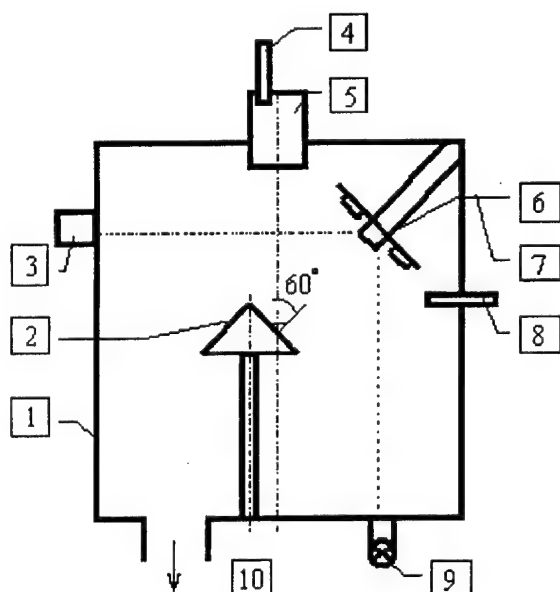


Fig. 1. Ion beam sputtering plant.

1. Vacuum chamber. 2. Target. 3. Receiver.
4. Working gas. 5. Ion source. 6. Substrate holder.
7. Reference glass holder. 8. Reactive gas. 9. Light source. 10. Cryo pump.

The mirror substrates for ZLG were made of CO 115M glass ceramic or KU1 fused silica, the working surfaces of which were well treated by the method of deep grinding and polishing. The RMS roughness of the mirror substrates was $\sigma=3.5\ldots10$ Å was measured by the differential light scattering technique using a light of the gas laser at 632nm⁹ as well as with the use of the atom force microscope¹⁰.

2.2. METHODS OF MEASUREMENT OF MIRROR ABSORPTION

The optimization of producing the mirrors having minimum absorption was carried out mainly by the laser modulated photothermal radiometry (LMPTR)⁴ at 672 nm. At the later stages several measurements of mirror absorption have been carried out at 515 nm by L.Escoubas by the photothermal deflection technique¹¹. The measurement by the photothermal deflection technique was produced at high local resolution over the surface since a diameter of probed beam was 0.1 mm, in this case the measurements were carried in 25 points near the central zone of the coating. The sensitivity of absorption measurement by this method was <10 ppm.

2.3. SCATTERING MEASUREMENT

The value of optical scattering of coatings is directly related to the microstructure of coatings which depends on the deposition process¹². The measurements of total integrated scattering (TIS) of coatings have been carried out. The system for TIS measurement was analogous to that in the work⁵ and included the integrating sphere of Ø150 mm, the stable single-mode He-Ne laser, the photoreceiver, and the synchronous detection amplifier. The inner surface of the sphere was coated with a material having a specific reflectivity. The mirror under measurement has been placed into the hole in the sphere surface. The angle of beam incidence was 4°, the diameter of the spot on the mirror surface was 0.5 mm. The mirror-reflected and transmitted beams came from the integrating sphere through the holes and were absorbed by the light traps. The system sensitivity was 10 ppm, the measurement error was about 15% and was determined by imperfection of calibration and by the influence of input and output holes in the sphere.

2.4. MEASUREMENT OF INTRACAVITY LOSS

To determine the intracavity loss, the bandwidth of the 4-mirror resonator was measured. This technique was described earlier¹³. These measurements have been carried out in circular polarization. Our measurement scheme is

shown in Fig. 2. As a source of light, the stable linear single-mode He-Ne laser has been used, the wavelength of which could be changed due to using the piezoelectric transducer mirror changing the resonator length. The linearly polarized laser emission has been directed into the 4-mirror resonator, one of the mirrors being spherical. The resonator has been assembled based on the ring laser gyro body. The resonator body has provided the nonplanar loop for propagation of circularly polarized emission.

The optical total loss L of the cavity is proportional to the bandwidth $\Delta\nu$ of the resonator¹³

$$\Delta\nu = cL/2\pi n\Lambda, \text{ where } n\Lambda \text{ is the optical length of the cavity, } c \text{ is the velocity of light.}$$

The measured resonator bandwidths have reached $\sim 30 \dots 300$ kHz for the high-reflection mirrors. This corresponded to the loss of 100...1000 ppm for the four mirrors. The mirrors under investigation have been taken from one deposition run and to a first approximation may be considered as having the same quality. To produce the loss value for one mirror, the measured value has been divided by 4. The sensitivity of this method was ~ 10 ppm.

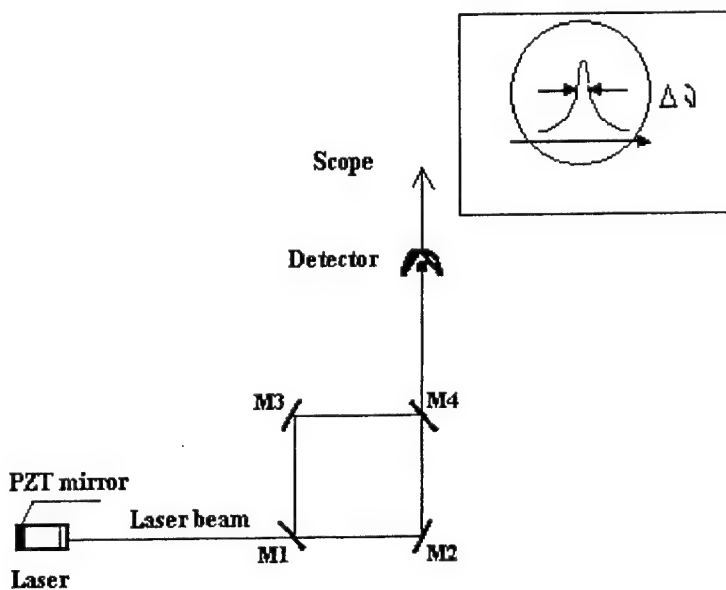


Fig. 2. Experimental set-up for measurement of mirror intracavity loss.

2.5. MEASUREMENT OF PHASE ANISOTROPY OF MIRRORS

In reflection of circularly polarized light from the ideal multilayer quarter-wave mirror, the layers of which are free of absorption, at the angles of incidence less than the Brewster angle, the s and p components in the reflected wave are opposite in phase to the incident wave.

In case of errors in the layer thickness the phase difference between the reflected and incident waves will be different from π . We have measured the mirror phase difference by the LEF 3M-1 ellipsometer at 632 nm, and the degree of deviation of the phase difference from π has been estimated. The phase difference of 0.01...0.05 rad was considered permissible.

2.6. LASER DAMAGE THRESHOLD MEASUREMENT

The laser damage threshold measurement of the coatings at 1064 nm was carried out by the method approaching the method¹⁴ by single-mode Nd:YAG laser with 10 ns pulse width, 12.5 Hz pulse repetition rate, 170 μm diameter of a laser beam on the surface of the sample. The number of the studied areas in the coating was no less than 30, the number of laser pulses acting on each area of the coating was no less than 100. When decreasing a laser power density on the coating surface to the specific level, damage occurred in none point of the coating. This value of power density was taken as a damage threshold.

3. MAIN RESULTS AND DISCUSSION

3.1. MULTILAYER MIRRORS FOR RLG WITH CIRCULAR POLARIZATION

As the investigations of the spectral characteristics of single-layer coatings within 300...900 nm have shown, the refractive indices of the TiO_2 , Ta_2O_5 and SiO_2 layers produced on the unheated substrate have been found to be 2.40 ± 0.02 , 2.12 ± 0.02 and 1.47 ± 0.02 at 630 nm. The investigations of the index of nonuniformity of the TiO_2 and Ta_2O_5 films in thickness have shown that Δn in thickness is low and does not exceed 0.01 for working thickness of the TiO_2 films.

As noted above, the substrates of $\sigma=3.5\text{...}10\text{ \AA}$ produced in different polishing processes have been used. Of much interest are the investigations of the dependence of TIS of mirrors produced on the substrates with a different value σ . We have carried out such investigations for 15...17-layer quarter-wave mirrors. The obtained dependence is shown in Fig. 3. It has been found that in the double log scale this dependence is of a linear behaviour.

These results show that TIS of ion beam mirrors is determined first of all not by a type of a substrate material, but depends on a roughness value, the roughness of the coating apparently repeating the roughness of the substrate. Thus at $\sigma=5\text{ \AA}$ the value of TIS was 100 ppm. The best results for integrated scattering value we have obtained were 50...70 ppm, that is, corresponded to $\sigma=3.5\text{...}4\text{ \AA}$ and depended slightly on the number of layers from 17 to 23.

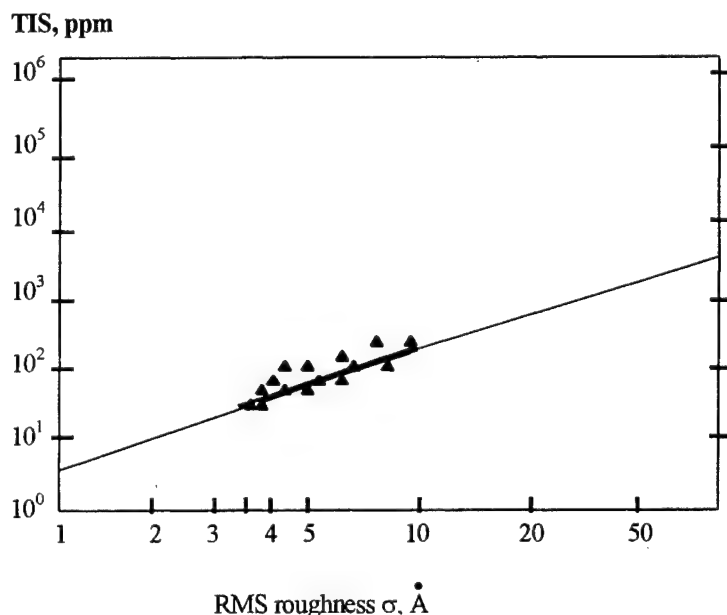


Fig.3. TIS of mirrors for different RMS roughness of the substrates.

on deposition of the single-layer coatings and control over the value of absorption have allowed the selection of the optimum parameters of the deposition processes.

The investigations of the single-layer films have made it possible to go to production of the multilayer mirrors with 17...23 layers. The value of absorption of such mirrors measured by the LMPTR method was about 100 ppm.

As already noted, to refine the value of absorption, a number of measurements has been carried out by the more precise method of photothermal deflection technique at 515 nm. For this purpose the special samples of coatings have been prepared that had the $5\lambda/4\text{TiO}_2 + \lambda/2\text{SiO}_2$ structure, where $\lambda=515\text{ nm}$. These coatings have been deposited on the substrate of KU-1 fused silica. Such coatings had similar reflection coefficients at 515 and 672 nm, and we could neglect the changes in the pattern of distribution of electric field in the individual layers of the coating at these wavelengths, which could influence the measurement results. Given below are the obtained absorption data for 25 points:

Mean value	30 ppm
Maximum value	70 ppm
Minimum value	2 ppm

The obtained results show that the value of absorption of the coatings is not high and does not exceed 70 ppm, although there are the areas of very low absorption (2 ppm).

Let us go to the results of the investigations of mirror absorption. As noted above, the main results have been obtained using the LMPTR method for the single-layer TiO_2 and SiO_2 films on the fused silica substrates. The value of absorption of the TiO_2 and SiO_2 films depended on the parameters of the deposition processes and the operation modes of the ion source. The determining factors were the O_2 partial pressure, the ion current of the ion source, the value of the anode voltage in the gas-discharge chamber, the voltage at the screen and accelerating grids, the cathode-neutralizer emission current as well as the accelerating grid current¹⁵. The experiments

It may be assumed that absorption of the TiO_2 and SiO_2 layers at 632 nm is no more than that measured at 515 nm. Since mainly the outer 5...7 layers of the coatings take part in absorption of multilayer quarter-wave mirrors, it may be considered that the measured absorption of the 6-layer coating ($5\lambda/4TiO_2 + \lambda/2SiO_2$) is close to the absorption of the mirror at 632 nm.

To make multilayer mirrors with minimum phase anisotropy, the theoretical estimation of the influence of coating layer thickness on the phase characteristics of the mirrors has been made. It has been determined that the most contribution to degradation of the phase characteristics of the mirrors is made by the outer 3...5 layers of the coating. To produce the phase anisotropy of the mirrors within 0.01...0.05 rad, it is necessary that the errors in thickness of the coating layers should not exceed 3...5% which is provided by the optical monitoring system.

In conclusion, when using the optimized modes, several lots of 23...25-layer mirrors for ring laser gyros at 632 nm and an angle of beam incidence of 45° has been made. The following parameters of the mirrors have been obtained:

absorption	30...70 ppm
scattering	50...70 ppm
circular polarization transmission	40...60 ppm
phase anisotropy of mirrors	0.01 rad.

So the sum of loss of the mirrors for circular polarization were 120...200 ppm. The total loss measured by the method 2.4. were 200...250 ppm, what is close to the value of sum of loss. The carried out measurements show that ion beam deposition provided obtaining a value $R=99.975...99.98\%$ at 632 nm and an angle of incidence of 45° for circular polarization. The estimation shows that this corresponds to a value $R\approx99.99\%$ for linear s polarization of an incident beam.

3.2. PROTECTIVE ANTIREFLECTION COATINGS ON SILICATE GLASS AND BBO CRYSTALS

To make the coatings on silicate glass and BBO crystals, the layers of Ta_2O_5 and SiO_2 were used. The parameters of the produced coatings are shown in the table.

Optical parameters of ion beam protective antireflection coatings

Substrate	Material of coating	Coefficient of reflection, %	Laser damage threshold at 1064 nm and $\tau=10$ ns, J/cm^2
Silicate glass	$Ta_2O_5-SiO_2$	0.2	20±5
BBO	-	-	15...20
BBO	$Ta_2O_5-SiO_2$	0.2	15±2
BBO	SiO_2	1.8	15±2

The analysis of this table shows that the ion beam coatings on glass have the high laser damage thresholds close to the ones of the electron-beam coatings. However the laser damage thresholds of the coatings on BBO crystals by 20...25% are less than the ones of the surface of BBO crystals. Nonetheless, these coatings having a high density and a small number of defects protect the crystal surface against ingress of moisture and stabilize the surface properties of the crystals.

4. CONCLUSION

The results of this work allow conclusion that the method of ion beam sputtering of metals and oxides with subsequent deposition is an universal method to make the various coatings for visible and near IR lasers. On the one hand, it allows making the multilayer mirrors with high coefficient of reflection for gas ring laser gyros. On the other hand, it allows making the coating with high laser damage threshold. A great extension of the fields of application of this

method is of interest to make the various types of the mirrors with small passive loss for Nd:YAG lasers, in particular, for diode-pumped green and blue lasers.

ACKNOWLEDGMENTS

The authors wish to thank L.Escoubas (Ecole Natl.Superieur de Phys, Marseille, France) for absorption measurement as well as A.Lyashenko for giving BBO crystals to make the coatings and carry out investigations.

5. REFERENCES

1. D. T. Wei, "Ion beam interference coating for ultralow optical loss", *Appl.Opt.* **28**, pp.2813-2816, 1989.
2. D.T. Wei, "Low-loss ion sputtered coatings in the Nineties", *SPIE* **2253**, pp.362-373, 1994.
3. A. Kalb, "Neutral ion beam sputter deposition of high-quality optical films", *Optics News*, August, pp.13-17, 1986.
4. G.Kolodnyi, V. Azarova, Yu. Golyaev, A. Melnikov, M. Rasyov, N. Tikhmenev, "Low-loss IBS mirrors for Zeeman laser gyros", *SPIE* **3738**, pp.446-452, 1999.
5. R. Henking, D. Ristau, E. Alvensleben, H. Welling, "Optical characteristics and damage threshold of low-loss mirrors", *SPIE* **2428**, pp.281-292, 1995.
6. D.T. Wei, H.R .Kaufman and C.C. Lee, "Ion beam sputtering in thin films for optical systems", ed by F.Flory (Marcel Dekker, New York, 1995).
7. V. Azarova, Yu. Golyaev, V. Dmitriev, A .Kazakov, G. Kolodnyi, A. Melnikov, M. Nazarenko, V. Svirin, and N. Tikhmenev, "Laser gyros with magnetic biasing: the ways of accuracy and operating property improvement", The 2nd Petersburg international conference on gyroscopic technology and navigation, pp.47-50, 1995.
8. Chen G., Wu B.Jiang A., "A new type ultraviolet SHG crystal - β -BaB₂O₄", *Scientia Sinica, Ser B.*, **28**, pp.235-243, 1985.
9. V. Azarova and N. Solovyeva, "Automatic optical device for roughness measurement based on differential scattering", *SPIE* **1711**, pp.191-193, 1992.
10. V. Azarova, I. Dronov, K. Malickiy, "Metrology of precision optical surfaces and laser mirrors", *SPIE*, v. **3739**, p.377, 1999.
11. M .Commandre and E. Pelletier, "Measurement of optical losses in TiO₂ by a collinear photo-thermal deflection technique", *Appl.Opt.* **29**, pp.4276-4283, 1990.
12. L. Mattsson, "Light scattering and characterization of thin films", *Proc.Soc.Photo.Opt.Instrum.Eng.* **652**, pp.215-220, 1986.
13. V. Azarova, V. Sharov, "Metrology of Precision Elements for Laser Gyros", "5th Saint Petersburg International Conference on Integrated Navigation Systems, pp.225, 1998.,
14. G. Kolodnyi, E. Levchuk, V. Novopashin and O.Sidoryuk, "Laser damage and passive loss multilayer thin-film coating in 1.5...1.6 μ m range", *Laser und Optoelektronik* **28**, pp.61-65, 1996.
15. H. Kaufman, "Broad-beam ion sources: present status and future directions", *J.Vac.Sci.Technol.* **A4**, pp.764-771, 1986.

Miniature optical parametric 1064/1573 nm converter.

Naumov V.L., Onischenko A.M.,
Podstavkin A.S., Shestakov A.V.

RDI "Polus", E.L.S. Co., 3 Vvedensky Street, Moscow 117342

ABSTRACT

High efficiency OPO has been designed for converting 1064 μm laser radiation into eye-safe region. Conversion efficiency 56.5% and threshold energy 2 mJ (0.06 J/sm²) have been achieved at repetition rate 12.5Hz. The divergence was less than 4 mrad up to 4 thresholds. With 180 mJ pump energy this converter can produce 70mJ output with efficiency 41% and low divergence at repetition rate 2.5 Hz.

Keywords: OPO, parametric, converter, eyesafe, KTP

INTRODUCTION

Optical parametric oscillators (OPOs) using KTP in noncritically phasematched configuration are known to provide efficient eyesafe wavelength conversion from 1 μm to 1.5 μm , operating in extracavity and intracavity configurations. Applications of KTP OPOs pumped by Q-switched Nd:YAG lasers have increased dramatically in different laser systems. Here we report design and experimental study of compact efficient single resonator KTP OPO pumped by single and multimode Q-switched Nd:YAG lasers operating in extracavity configuration.

DESIGN

KTP OPO optical scheme is shown in fig. 1. We have chosen 3-mirror ring resonator to simplify alignment procedure (as compared to 4-mirror resonator) and to make radiation field distribution more homogeneous (as compared to linear one). Homogeneous field pattern is obtained as a result of beam turnover. Resonator consists of flat mirrors – input mirror with AR for 1.06 μm and HR for 1.57 μm , interface mirror with HR for both, and output mirror with HR for 1.06 μm and 70% reflection for 1.57 μm coatings. Three flat faces KTP crystals are incorporated in the resonator. Dimensions of x-cut KTP crystals are as follows: cross section (y-z plane) is 4×4 mm, length along x-axis is 20 mm. Crystals was AR coated for 1.57 μm . Pump, signal and idler waves propagate along x axis. Pump and signal wave polarizations are directed along y-axis, idler wave polarization – along z one.

Signal wave output and depleted pump are separated in our resonator.

The OPO design is shown in fig. 2. Resonator mirrors and KTP crystals are packed in metal housing. At first stage mirrors are mounted, adjusted and then bonded. Each KTP crystal is mounted in its own holder (may be mounted individually), then it is mounted in metal housing. The precisely fabricated crystal can be easily mounted in the housing with little or no alignment. Designed converter is a simple and compact device.

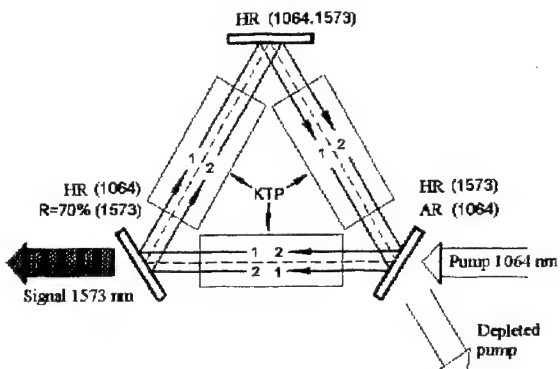


Fig. 1. OPO optical scheme

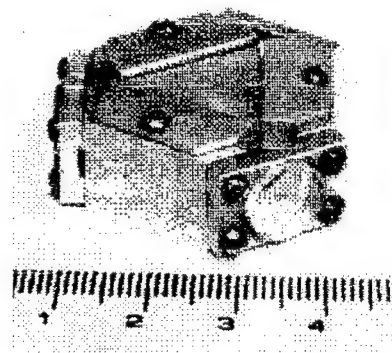


Fig. 2. OPO design.

EXPERIMENTS

We used single transversal mode and multimode Q-switched Nd:YAG lasers to pump developed converter. Input-output energy OPO dependences and signal wave divergences were studied with different pump lasers. To vary pump energy half-wave plate and polarizer were employed. To study converter beam energy divergence we used a lens with focal length 1000 mm and measured circular diameter that encompasses 86.5% of the total energy at its focus. For low-power multimode pump we used the laser that operates at 5 Hz repetition rate, has a 10 ns pulse width, and has a 2.5 mm beam diameter. Input-output energy dependence is shown in fig. 3a. As one can see, OPO has a 46% slope efficiency. By extending the linear curve fit to the x-axis, the threshold energy of OPO is estimated to be approximately 2.5 mJ, resulting in a threshold fluency of 120 mJ/cm². The beam divergence was approximately 3.5 mrad, so it didn't exceed four diffraction limits. For the low-power singlemode pump we used the laser that operates at 12.5-Hz repetition rate, has an 8 ns pulse width, and has a 1.6mm beam diameter. Input-output energy dependence is presented in fig. 3b. OPO has a 56.5% slope efficiency and 2 mJ threshold energy, resulting in a fluency of 60 mJ/cm². The measured beam divergence was approximately 4 mrad, so it also didn't exceed four diffraction limits.

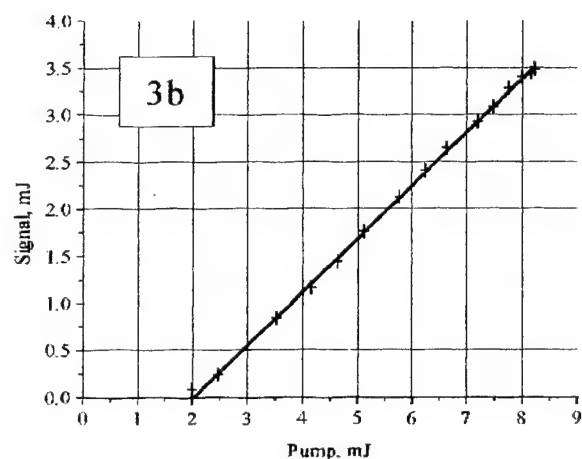
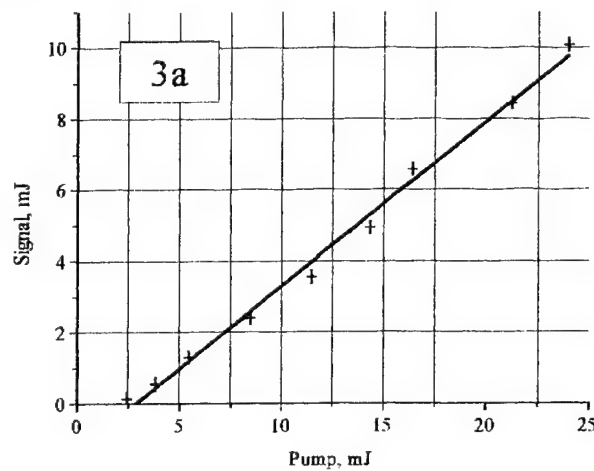


Fig. 3. Input-output energy curves: a - multimode pump, b - singlemode pump

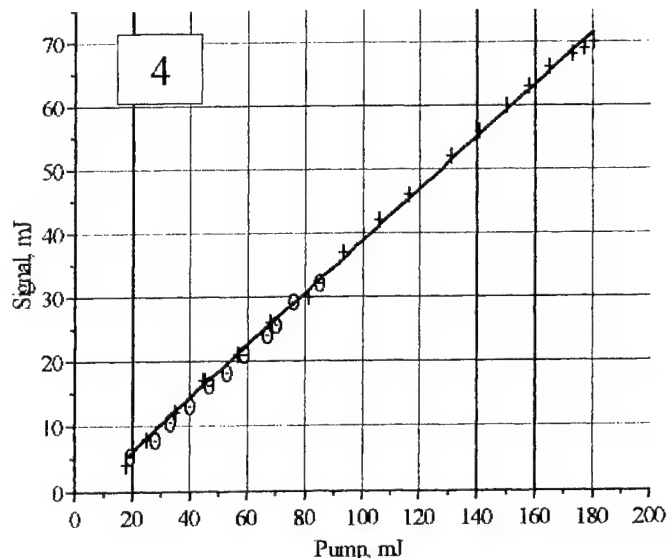


Fig. 4. Input-output energy dependence for high-energy pump

+ - 2.5 Hz repetition rate
 Θ - 20 Hz repetition rate

We investigated the developed OPO with high-energy pump laser source. For this experiment we used the multimode laser with pulse energy up to 180 mJ and repetition rate 20 Hz (for pump energies more than 80 mJ – 2.5 Hz). Pulse width was 15 ns and beam diameter was 3-mm. OPO input-output energy dependence is presented in fig. 4. The resulting slope efficiency was 40%, and the threshold energy was found to be approximately 5 mJ. No optical damage occurred. The measured divergence was less than 8 mrad within all pump interval. As one can see from the fig. 3c, OPO demonstrates stable generation with pump energies more than thirty times greater than threshold level. No OPO parameters degradation was found in our experiments.

CONCLUSIONS

A high-efficiency compact parametric converter has been developed for use in eyesafe laser devices. The results demonstrate that this OPO is an appropriate source for eyesafe radiation with high efficiency, low threshold and beam divergence. The significant reduction in threshold energy and beam divergence is because of long gain medium and triangle resonator concept. To exceed energy output and power the implementation of large-scale aperture KTP crystals is necessary.

Features of noncollinear parametric generation light in LiNbO_3 crystal pumped by the fundamental radiation of Nd:YAG laser

N. Kondratyuk^a, A. Shagov^b, V. Belyi^c, A. Mashchenko^c,
Yu. Bakhirkin^d, P. Philippow^d

^a Inter-Branch Institute of Advanced Training Byelorussian Politechnic Academy,
77, Partizansky av., Minsk, 220107, Belarus

^b SC "Solar LS" 77, Partizansky av., Minsk, 220107, Belarus

^c Institute of Physics of National Academy of Sciences of the Republic of Belarus,
70, Skorina av., Minsk, 220600, Belarus.

^d NII gazekonomika 20/8, Staraya Basmannaya str., Moscow, 107066, Russia

ABSTRACT

Theoretical and experimental studies the features of parametric generation light in LiNbO_3 with noncollinear phase matching from noncollinear angle i_{23} , i.e. angle between pump wave vector and resonant signal wave vector, are presented. It was shown that at the small angle $i_{23} < 0,3^\circ$ four nonlinear processes can simultaneously take place: these processes are noncollinear parametric conversion of the $1.0642 \mu\text{m}$ into the signal and an idler waves; second-harmonic generation of the signal; noncollinear difference-frequency mixing of the doubled signal and the idler; parametric conversion of the doubled signal into new pair: the signal and an idler waves.

It is shown that the maximum efficiency of noncollinear OPO takes place for tangential phase-matching at $i_{23} \approx 0,9^\circ$. Spectral broadening of the signal wave of LiNbO_3 noncollinear OPO was studied. Theoretically it is shown that the spectral bandwidth of the signal wave depends on the divergence of the signal wave.

Key words: optical parametric oscillator, LiNbO_3 crystal, noncollinear phase-matching conditions.

1. INTRODUCTION

The last few years have seen an increased number of scientific publications devoted to optical parametric oscillators (OPO) with noncollinear phase matching. This is due to the fact that at noncollinear phase matching for three-frequency parametric interactions, a marked change is possible in the shape of tuning curves, angular and spectral acceptance [1-3]. Detailed study of the peculiarities of $1.0642\text{-}\mu\text{m}$ pumped pulsed optical parametric oscillator of LiNbO_3 with noncollinear phase matching is an urgent problem which solution will make it possible to devise high-efficiency light sources generating radiation in the eye-safe range $1.5\text{-}1.8 \mu\text{m}$ as well as radiation for remote sensing of impurities in the atmosphere in the $2.8\text{-}3.5 \mu\text{m}$ range.

^a N.K.: e-mail:solarls@infonet.by

^b A.Sh.: e-mail:solarls@infonet.by

^c V.B., A.M. : e-mail: tol@dragon.bas-net.by

^d Yu.B. : e-mail:bakhirkin@chph.ras.ru

2. EXPERIMENTAL SET-UP

A type-I noncollinear phase matching LiNbO₃ OPO is schematically represented in Fig.1.

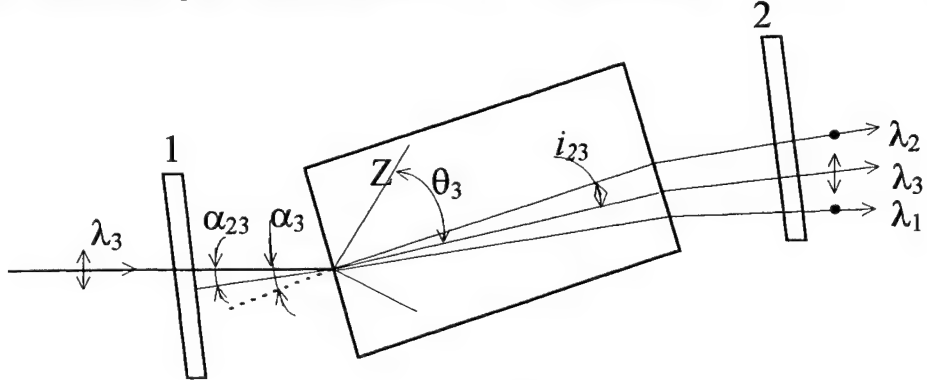


Fig.1

The LiNbO₃ crystal was cut at $\varphi=270^\circ$ and $\theta=45^\circ$ relative its optic axis and had dimensions 10mm×20mm×40mm. The OPO cavity consisted of two flat mirrors 1, 2 that reflected the signal wave in the range 1.5-1.7 μm . Both mirrors transmitted the pump and idler waves. The cavity length was 6.5 cm. The mirrors of the OPO resonator were set perpendicular to the YZ plane of the LiNbO₃ crystal. The optical axis of the cavity could be rotated with respect to the directions of the pump beam. In experiment the angle α_{23} between the optical axis of the cavity and the pump beam was varied over the range from 0.3° to 2° . Wavelength tuning of this OPO was realized by rotating the nonlinear crystal about the axis perpendicular to the YZ plane of the LiNbO₃ crystal. In the noncollinear OPO the idler wave radiation was directed toward a rift of the energy flux of the extraordinary pump wave. The OPO was pumped at $1.0642 \mu\text{m}$ by a 10 Hz repetition rate Q-switched multimode Nd:YAG laser (Solar LS, model LQ-727). The laser provided $\sim 240 \text{ mJ}$ of energy with pulselwidth $\sim 6 \text{ ns}$. The pump beam 5 mm in diameter had a divergence of $\sim 0.8 \text{ mrad}$. The spatial intensity profile of the pump beam polarized in a horizontal plane was close to a rectangular one. The pump radiation intensity was equal to $\sim 200 \text{ MW/cm}^2$. The pump radiation loss with allowance made for the reflection from the input face of the LiNbO₃ crystal was $\sim 30\%$.

3. EXPERIMENTAL RESULTS

We investigated the spectral characteristics of noncollinear OPO for the case where the angle α_{23} between the cavity axis and the pump beam was small and equal $\sim 0.3^\circ$. Initially, the LiNbO₃ crystal was positioned so that its faces were parallel to the cavity mirrors. In this case, the angle of incidence of the pump beam on the input face of the crystal $\alpha_3 \sim 0.3^\circ$ and OPO generated two waves: a signal $\lambda_2=1.943 \mu\text{m}$ and an idler $\lambda_1=2.353 \mu\text{m}$. When the angle α_3 was varied over the range from 0.43° to 0.86° , the OPO simultaneously generated four frequencies (Table):

α_3 , degree	λ_1 , μm	λ_2 , μm	λ_3 , μm	λ_4 , μm
0,43	2,380	1,925	0,9625	1,611
0,57	2,424	1,897	0,9485	1,560
0,72	2,450	1,881	0,9405	1,540
0,86	2,485	1,861	0,9305	1,527

When the angle α_3 was varied from 1° to 2° the OPO generated the two waves: the signal λ_2 and the idler λ_1 . Fig.2 shows the spectrum of OPO at angle $\alpha_3 \sim 0.55^\circ$ which generated the signal wave at $\lambda_2=1.917 \mu\text{m}$. As the reper line with $\lambda_r=1.598 \mu\text{m}$ shown in Fig.2, we used the third stokes component of the Raman frequency converter based on a Ba (NO₃)₂ crystal.

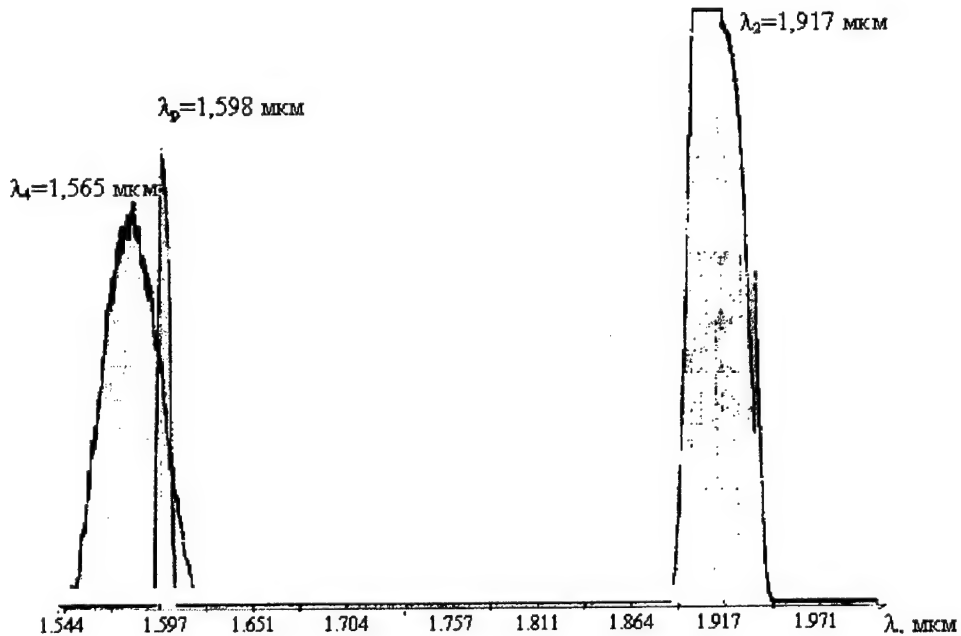


Fig.2

For various values of the angle α_{23} , measurements were made of the spectral linewidth of the signal wave at $\lambda_2=1.572 \mu\text{m}$. It has been found that as the angle α_{23} was increased from 0.3 to 2° , the spectral linewidth of the signal wave increased from 6 nm to 18 nm , respectively.

We investigated the OPO efficiency at $\lambda_1=3.294 \mu\text{m}$ and $\lambda_2=1.572 \mu\text{m}$ varying the angle α_{23} over the range from 1° to 2° . It has been found that at angles α_{23} in the range from 1.6° to 1.8° the OPO efficiency is maximum and the threshold pump energy is minimum.

4. DISCUSSION

To explain the experimentally observed peculiarities of noncollinear LiNbO₃ OPO we calculated the phase-matching angle-tuning curves

- for 1.0642 μm -pumped noncollinear OPO;
- for second-harmonic generation of the signal;
- for noncollinear difference-frequency mixing of the doubled signal and the idler and
- noncollinear OPO pumped by the second harmonic of the signal wave.

A vector diagram of vectors satisfying the phase-matching conditions for noncollinear parametric generation of two waves λ_1 and λ_2 is illustrated in Fig.3.

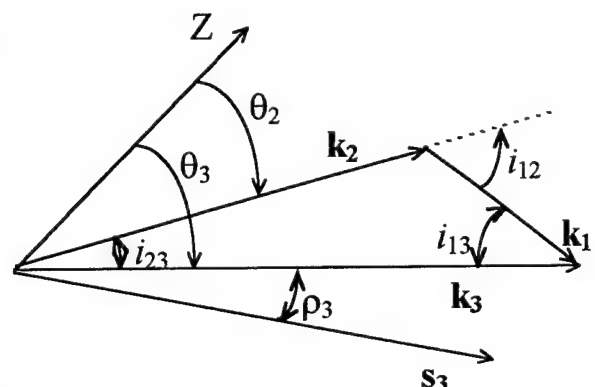


Fig.3

Here the following notations are used: i_{23} -angle between the wave vectors of the signal wave \mathbf{k}_2 and the pump wave \mathbf{k}_3 , i_{13} -angle between the wave vectors of the idler wave \mathbf{k}_1 and the pump wave \mathbf{k}_3 , i_{12} - angle between the wave vectors of the signal wave \mathbf{k}_2 and the idler wave \mathbf{k}_1 , ρ_3 -walk-off angle of an extraordinary polarized pump beam, θ_3 -angle between the vector \mathbf{k}_3 and the optical axis Z, θ_2 -angle between the vector \mathbf{k}_2 and the optical axis Z, \mathbf{s}_3 -Pointing vector of the extraordinary pump beam. The curves are calculated using the refractive indices by the Sellmeier dispersion equations for stoichiometric melt (mole ratio Li/Nb=1,000) LiNbO_3 [4].

The calculated phase-matching angle-tuning curves for 1.0642 μm -pumped noncollinear OPO and second-harmonic generation of the signal as a function of the wavelength of the signal in the 1.7-2.1 μm range are presented in Fig.4. The angle-tuning curves for the noncollinear OPO and the second-harmonic generation intersect in the range of angles i_{23} from 0° to 0.25° .

For example, at the angle $i_{23}=0.11^\circ$ in the direction of $\theta_2=44.73^\circ$ the simultaneous occurrence of two nonlinear processes:

- noncollinear parametric generation $1.0642 \mu\text{m} \rightarrow 1.897 \mu\text{m} \oplus 2.424 \mu\text{m}$ and
- second-harmonic generation $1.897 \mu\text{m} \rightarrow 0.9485 \mu\text{m}$.

The presence of the doubled signal may lead to the appearance of two new processes:

- noncollinear difference-frequency mixing $0.9485 \mu\text{m} - 2.424 \mu\text{m} \rightarrow 1.5582 \mu\text{m}$ and
- new parametric generation $0.9485 \mu\text{m} \rightarrow 1.560 \mu\text{m} \oplus 2.420 \mu\text{m}$.

Fig.5 shows the calculated phase-matching angle-tuning curves for 1.0642 μm -pumped noncollinear OPO and angle $i_{23}=0.11^\circ$ -1, and for 0.9485 μm -pumped noncollinear OPO and angle $i'_{23}=0.04^\circ$ -2. With the presence of the doubled signal the second noncollinear parametric process can in principle become possible.

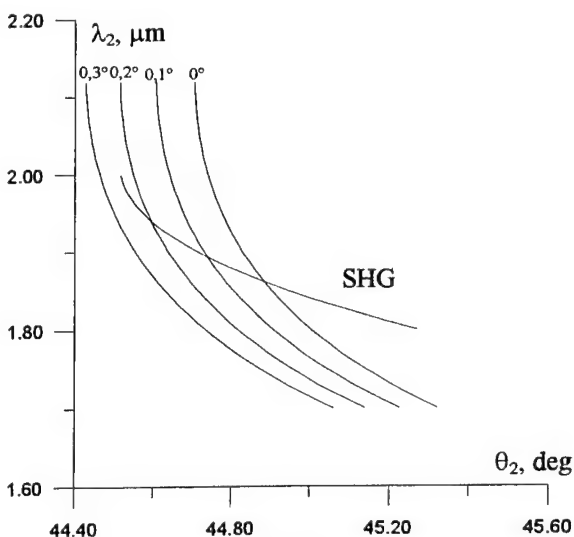


Fig.4

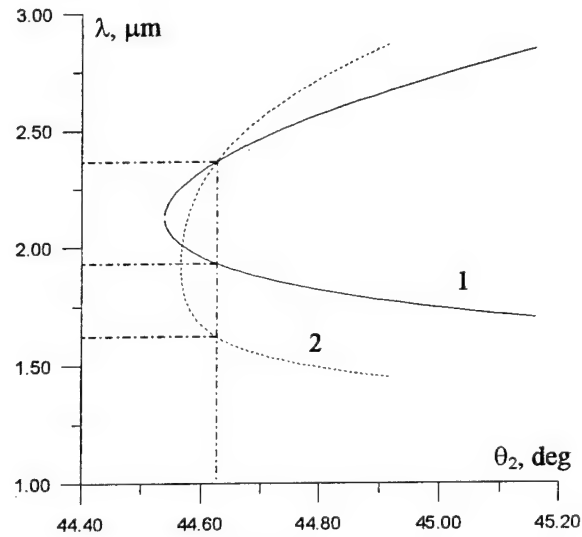


Fig.5

It should be noted that in [5] it is shown that for 1.0642 μm -pumped LiNbO_3 OPO there is a special case in which additional difference-frequency mixing of the doubled signal and the idler take place. The obtained results point to the possibility of simultaneous existence of four nonlinear processes.

The experimentally observed increase in the efficiency of OPO is due to the increase in the angular pump wave acceptance of the noncollinearly phase-matched type I OPO [6].

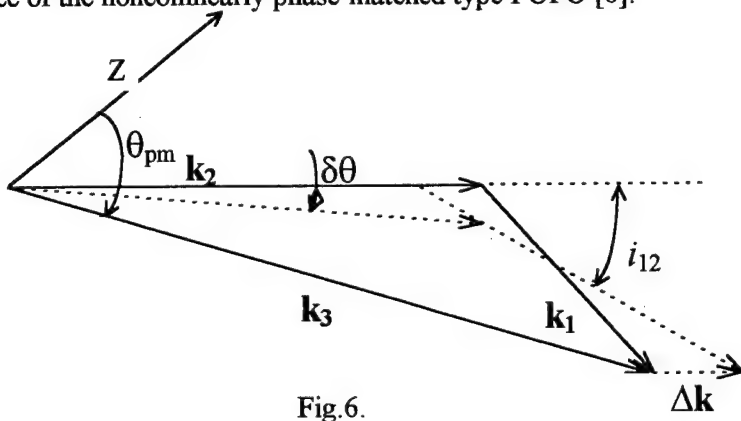


Fig. 6.

By using the vector diagram (Fig. 6) it is easy to obtain the expression for the angular acceptance $\Delta\theta_{pm}$:

$$\Delta\theta_{pm} = -\left|\frac{a}{b}\right| + \left[\left(\frac{a}{b}\right)^2 + \frac{1.772\lambda_3}{|b|L}\right]^{1/2}$$

$$\text{where } a = \frac{\partial n_3}{\partial \theta} (\cos i_{23} + \tan i_{12} \sin i_{23}) + n_3 (\cos i_{23} \tan i_{12} - \sin \alpha_{23}), \quad b = \frac{1}{2} \left(\frac{\partial^2 n_3}{\partial \theta^2} + \frac{\lambda_1 n_2 n_3 \cos i_{23}}{\lambda_2 n_1 \cos i_{12}} \right).$$

For small angles i_{12} and i_{23} and taking into account $\frac{\partial n_3}{\partial \theta} = -\rho_3 \cdot n_3$ expression $a \approx n_3 (i_{12} - i_{23} - \rho_3)$.

When $i_{12} = i_{23} + \rho_3$ and the Pointing vector s_3 of the extraordinary pump beam coincides with the wave vector \mathbf{k}_1 of the idler wave, coefficient a becomes zero and the angular acceptance $\Delta\theta_{pm}$ reaches its maximum

$$\Delta\theta_{pm}^{\max} = \left(\frac{1.772}{|b|} \frac{\lambda_3}{L} \right)^{1/2} \text{. The calculated curve of angular acceptance } \Delta\theta_{pm} \cdot L \text{ as a function of angle } i_{23} \text{ is}$$

shown in Fig. 7.

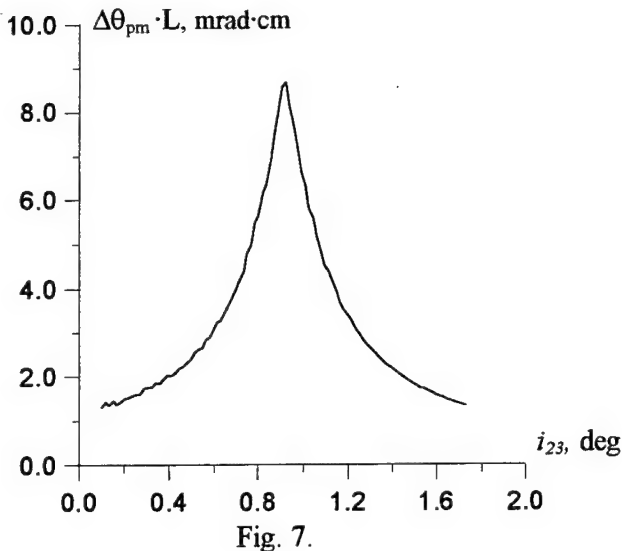


Fig. 7.

Tangential phase-matching increases the angular acceptance of the 1.0642 μm -pumped type I LiNbO_3 OPO from $\sim 1\text{mrad}\cdot\text{cm}$ (for collinear phase-matching) to $\sim 9\text{mrad}\cdot\text{cm}$.

Let us discuss the causes of the experimentally observed broadening of the spectral linewidth of the signal wave. It is known [7] that for collinear phase-matching OPO the spectral linewidth of the signal wave is due to both crystal dispersion $\Delta\nu' = 2\pi/(\beta_{21}L)$ and the pump beam divergence $\delta\theta_3$ $\Delta\nu'' = 2\rho_3\delta\theta_3/\beta_{21}$, where

$$\beta_{21} = \left| \frac{\partial(\omega_1 n_1)}{\partial\omega_1} - \frac{\partial(\omega_2 n_2)}{\partial\omega_2} \right|.$$

For LiNbO₃ OPO away from the degeneration point $\beta_{21} \approx 0.1$, estimation gives the following values of the spectral linewidth: $\Delta\nu' \approx 2 \text{ cm}^{-1}$ and $\Delta\nu'' \approx 6 \text{ cm}^{-1}$ per 1 mrad of the pump beam divergence [7], which are an order of magnitude smaller than the experimental ones. An increase in the spectral linewidth is due to the fact that at noncollinear phase-matching there appears an additional mechanism of broadening: the dependence of the spectral width $\Delta\nu'''$ from the signal beam divergence $\delta\theta_2$.

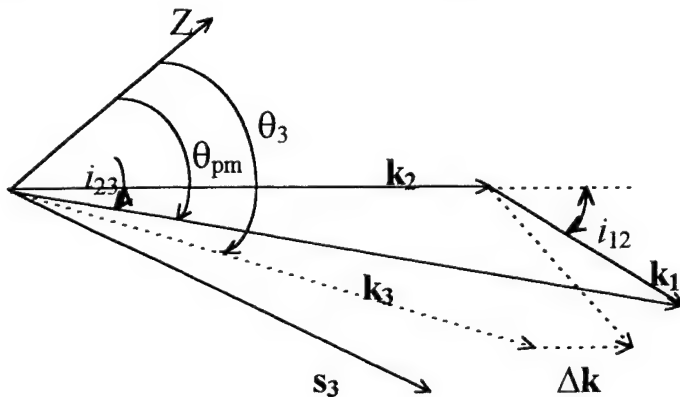


Fig. 8.

The signal beam divergence $\delta\theta_2$ leads to the appearance of additional phase detuning Δk_2 calculated on the basis of the vector diagram (Fig. 8):

$$\Delta k_2 = k_3(\theta) \cos i_{23} - k_1 \cos i_{12} - k_2 \cos(\delta\theta_2),$$

$$k_3 \sin i_{23} = k_1 \sin i_{12} + k_2 \sin(\delta\theta_2).$$

Since $k_3 = \text{const}$ and the wave vectors k_1 and k_2 change in both the direction and modulus, then differentiating with respect to w_1 , w_2 , i_{12} and $\delta\theta_2$, we obtain the following expression for the spectral linewidth $\Delta\nu'''$:

$$\Delta\nu''' = \frac{2k_2 k_3}{k_1} i_{23} \frac{\delta\theta_2}{g_{21}}, \text{ where } g_{21} = \beta_{21}.$$

For collinear phase-matching ($i_{23} = 0$), the broadening under consideration is absent.

For noncollinear phase-matching ($i_{23} = 1^\circ$) estimation gives $\Delta\nu''' \approx 65 \text{ cm}^{-1}$ per 1 mrad of the signal beam divergence. Thus, at the angle $i_{23} = 1^\circ$ spectral linewidth of the signal wave $\Delta\nu'''$, which is due to the signal beam divergence, is about an order of magnitude larger than the spectral width $\Delta\nu''$, which is due to the pump beam divergence.

5. CONCLUSION

It has been found that in a 1.0642 μm -pumped type I noncollinear LiNbO_3 OPO four nonlinear processes can simultaneously take place for a small angle between signal and pump beams. These processes are noncollinear parametric conversion of the 1.0642 μm into the signal and an idler waves; second-harmonic generation of the signal; noncollinear difference-frequency mixing of the doubled signal and the idler; parametric conversion of the doubled signal into new pair: the signal and an idler waves.

It is shown that the maximum efficiency of noncollinear OPO takes place for tangential phase-matching, when the Pointing vector of the extraordinary pump beam coincides with the wave vector of the nonresonant idler wave.

It has been found that in noncollinear OPO there appears an additional mechanism of broadening of spectral linewidth of the signal wave, which is due to the signal beam divergence.

REFERENCES

1. A.Oien, I.McKinnie, P.Jain, N.Russell, D.Warrington, L.Gloster, " Efficient, low-threshold collinear and noncollinear β -barium borate optical parametric oscillators", Optics Letters, **22**, pp. 859-861, 1997.
2. Sh.Huang, Ch.Hsu, D. Huang, C. Yang , " Retracing behaviors off the phase-matching angle in noncollinear phase-matched optical parametric oscillators ", J. Opt. Soc. Am. B, **15**, pp. 1375-1380, 1998.
3. R.Urshel, U.Bader, A.Borsutzky, R.Wallenstein, "Spectral properties and conversion efficiency of 355-nm-pumped pulsed optical parametric oscillators of β -barium borate with noncollinear phase matching", J. Opt. Soc. Am. B, **16**, pp. 565-579, 1999.
4. V.Dmitriev, G.Gurzadyan, D.Nikogosyan, " Handbook of nonlinear crystals", (Berlin, Springer-Verlag, 1997).
5. H.Bakker, P.Planken, L.Kuipers, A. Lagendijk, "Simultaneous phase matching of three second-order nonlinear optical processes in LiNbO_3 ", Optics Communications, **73**, pp. 398-402, 1989.
6. N.Barnes, V.Corcoran," Parametric generation processes: spectral bandwidth and acceptance angles", Applied Optics, **15**, pp. 696-699, 1976.
7. S.Brosnan, R.Byer, " Optical parametric oscillator threshold and linewidth studies", IEEE J. Quantum Electron. **15**, p. 415, 1979.

Gain saturation effects in BBO parametric amplifier

W.Hogervorst ^a, N.Kondratyuk ^b, A.Shagov ^b, V.Belyi ^c

^a Laser Centre Vrije Universiteit. De Boelelaan 1081, 1081 HV Amsterdam, The Netherlands.

^b SC "Solar LS" 77, Partizansky av., Minsk 220107, Belarus.

^c Institute of Physics of National Academy of Sciences of the Republic of Belarus,
70, Skorina av., Minsk, 220600, Belarus.

ABSTRACT

In the present work the gain saturation effects in type-I BBO optical parametric amplifier (OPA) pumped by the 3-rd harmonic of multimode Nd:YAG laser are investigated. The OPA gain was measured as a function of input idler energy at 1064 nm with a constant pump energy at 355 nm and a beam divergence 0,3 mrad. In the 9 mm BBO crystal at pump intensity $\sim 68 \text{ MW/cm}^2$ and input idler intensity $\sim 18 \text{ MW/cm}^2$ the efficiency of energy extraction in the saturated gain regime $\sim 31\%$ was obtained. The ways of increase the efficiency of energy extraction in the two-crystal OPA configuration are discussed.

Keywords: optical parametric amplifier, BBO crystal

1. INTRODUCTION

Significant successes now are achieved in the field of creation of narrow-band pulsed optical parametric oscillator (OPO) on BBO crystals pumped by the 3-rd harmonic of Nd:YAG lasers [1-3]. For increase of pulses energy of a single and an idler waves the optical parametric amplifier (OPA) containing one or several consistently located BBO crystals was used [3,4]. At collinear phase-matching the angular acceptance in BBO crystal is very small and it is equal $\sim 0,28 \text{ mrad}\cdot\text{cm}^{-1}$ [5]. In the present work the gain saturation effects in BBO parametric amplifier pumped by the 3-rd harmonic of Nd:YAG laser are investigated.

2. EXPERIMENT

We used a multimode Q-switched Nd:YAG laser with pulse energy up to 330 mJ, peak power density up to 250 MW/cm^2 and pulse width $\sim 5 \text{ ns}$ as a radiation source at 1064 nm. The output was multimode and had a flat-top intensity profile. For cascade third-harmonic generation (THG) we used a 3-mm-long type II KTP 1 crystal with AR coatings, cut at $\varphi_{\text{pm}} = 23,5^\circ$ and 20-mm-long type II DKDP 2 crystal, cut at $\theta = 59^\circ$. For space division of the fundamental and the third harmonics dichroic mirrors 4 and 5 were used. The diameters of the pump beam at 355 nm and the idler beam at 1064 nm were decreased by two hard apertures 4 mm in diameter. The divergence of the pump beam was $\sim 0,3 \text{ mrad}$. The pump energy in the input of the OPA was $\sim 43 \text{ mJ}$. The idler energy in the input of the OPA was attenuated from 0.2 mJ to 22 mJ using a waveplate 7 and two polarizers 6 and 8.

^a W.H.: e-mail: wh@nat.vu.nl

^b N.K., A.Sh.: e-mail: solarls@infonet.by

^c V.B.: e-mail: tol@dragon.bas-net.by

The OPA gain medium was a 9-mm-long type I BBO crystal, cut at $\theta = 29^\circ$ and coated with a protective AR coating. For space division of pump, signal and idler beams dichroic mirrors 4 and 5 were used.

The experimental set up is shown in Fig. 1.

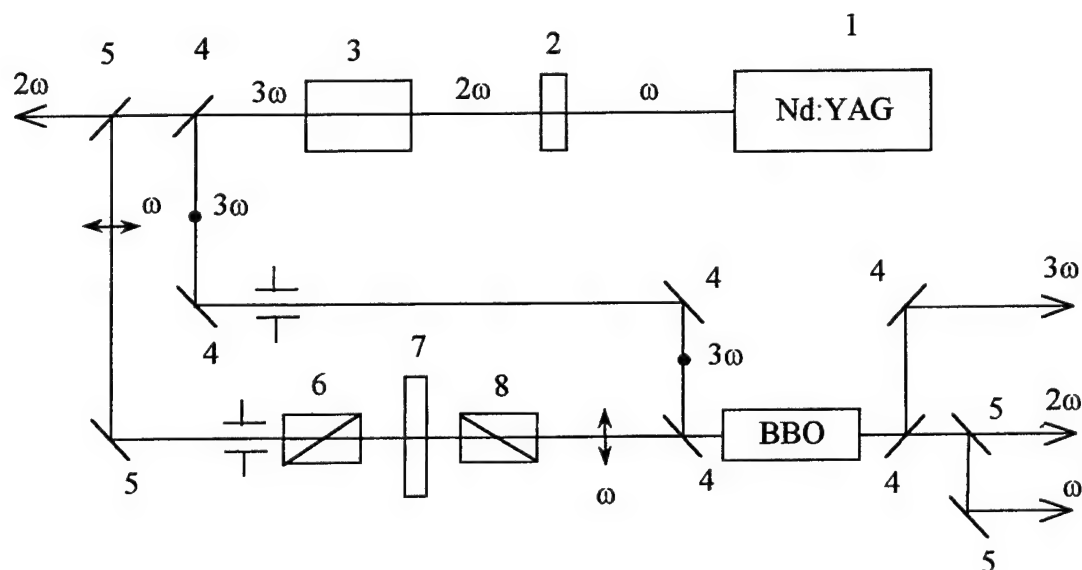


Fig.1 Experimental layout.

The experimentally obtained results of the OPA output energies with the input pump energy $W_{30} \sim 43$ mJ is shown in Fig.2. It can be seen that the maximal extraction efficiency and the gain saturation effects were obtained at input idler energy $W_{10} > 8$ mJ. The OPA output energies of the signal and the pump waves were constant when input idler energy was varied from 8 mJ to 22 mJ.

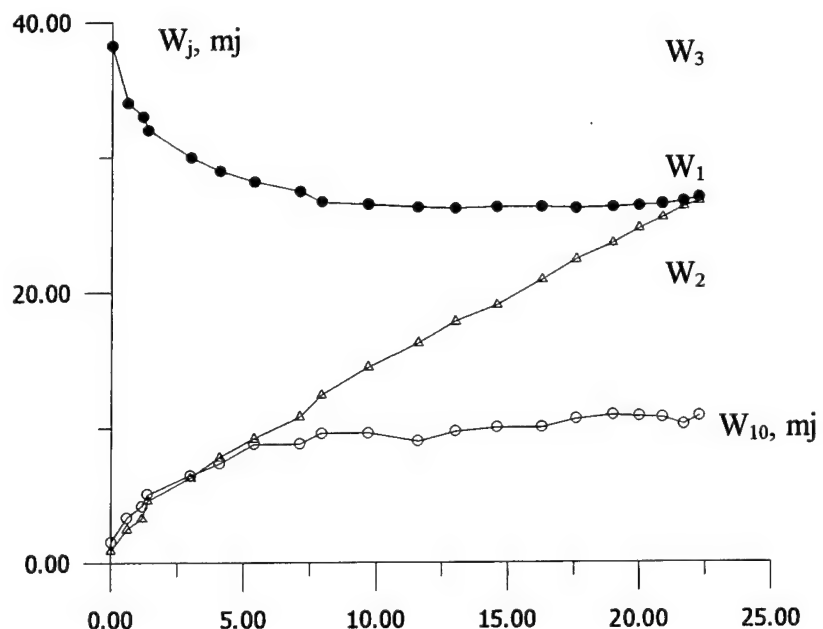


Fig.2. The OPA output pulse energies at λ_1 , λ_2 and λ_3 with the constant input pump energy $W_{30} \sim 43$ mJ versus input idler energy at λ_1 .

From the Fig.2 the following characteristics of the OPA can be seen:

- the output energies of pulses

at 355 nm - $W_3 \sim 26,5$ mJ,

at 532 nm - $W_2 \sim 10,0$ mJ,

at 1064 nm - $W_1 \sim 11,5$ mJ,

- the efficiency of OPA at the signal $\eta_2 \approx \frac{W_2}{W_{30}} \approx 0,23$,

- the efficiency of OPA at the idler $\eta_1 \approx \frac{W_1 - W_{10}}{W_{30}} \approx 0,08$,

- the total OPA efficiency $\eta_1 \approx \eta_2 + \eta_1 \approx 0,31$

We investigated the gain saturation effects when the input pump energy OPA was decreased down to ~ 29.3 mJ. The results are shown in Fig.3.

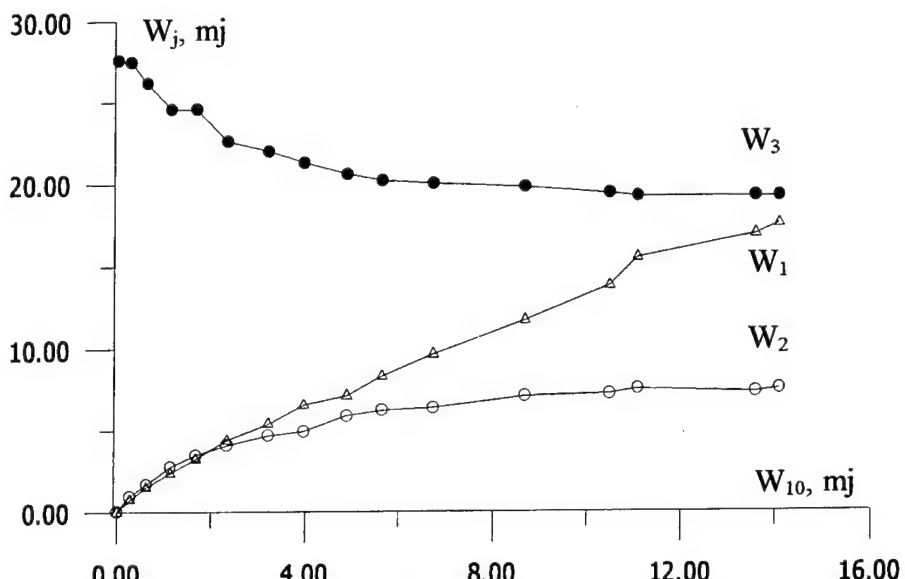


Fig.3. The OPA output pulse energies at λ_1 , λ_2 and λ_3 with the constant input pump energy $W_{30} \sim 29.3$ mJ versus input idler energy at λ_1 .

In this case the maximal extraction efficiency and the gain saturation effects were obtained at input idler energy $W_{10} > 5$ mJ which is less than in the previous case.

On the base of the obtained experimental data the OPO scheme consisting 2 consistently located BBO crystals with a mirror between them with a high reflection coefficient for signal wave and a high transmission for the pump and idler waves is proposed. In the two-crystal OPA configuration efficient energy extraction may be increased. In this case both of the BBO crystals work in the gain saturation regime and:

- the crystal-1 provides the maximum signal gain,
- the crystal-2 provides the maximum idler gain.

Comparing the measured values of OPA output energies (Fig. 2, Fig.3) it is possible to make an estimation of extraction energy efficiency in the two-crystal OPA configuration:

- for crystal-1: input $W'_{10} = 4\text{mJ}$, $W'_{30} = 43\text{mJ}$
output $W'_1 = 6,8\text{mJ}$, $W'_2 = 7,5\text{mJ}$, $W'_3 = 29\text{mJ}$;
- for crystal-2: input $W''_{10} = 6,8\text{mJ}$, $W''_{30} = 29\text{mJ}$
output $W''_1 = 8,4\text{mJ}$, $W''_2 = 6,3\text{mJ}$, $W''_3 = 20\text{mJ}$
- total OPA efficiency at signal $W_2 = W'_2 + W''_2 = 13,8\text{mJ}$ ($\eta_2 = 0,32$);
- total OPA efficiency at idler $\Delta W_1 = W''_1 - W'_{10} = 4,4\text{mJ}$ ($\eta_1 = 0,10$);
- total OPA efficiency $\eta_1 \approx \eta_2 + \eta_1 \approx 0,42$

3. CONCLUSION

Gain saturation effects were studied using a constant pump intensity and variable input idler intensity. In the one-crystal OPA configuration at pump intensity $\sim 68 \text{ MW/cm}^2$ and input idler intensity $\sim 18 \text{ MW/cm}^2$ the efficiency of energy extraction in the saturated gain regime $\sim 31\%$ was obtained. On the basis of experimental data we made the conclusion, that in the two-crystal OPA configuration with the same input parameters the efficiency of energy extraction up to 42% is possible.

4. REFERENCES

1. J.M.Boon-Engering, L.A.W.Gloster, W.E.van der Veer, I.T.McKinnie, T.A.King, W.Hogervorst, "Highly efficient single-longitudinal-mode $\beta\text{-BaB}_2\text{O}_4$ optical parametric oscillator with a new cavity design ", Optics Letters, **20**, pp. 2087 -2089, 1995.
2. J.M.Boon-Engering, W.E.van der Veer, E.A.J.M.Bente, W.Hogervorst, " Scanning and locking of a single longitudinal mode $\beta\text{-BaB}_2\text{O}_4$ OPO in grasing incidence configuration" , Optics Communications, **136**, pp. 261-266, 1997.
3. A.Umbrasas, J.Jacob, " Widely tunable stable single longitudinal mode BBO OPO ", OSA TOPS on Advanced Solid State Lasers, **10**, pp. 86-89, 1997.
4. S.Wu, V.Kapinus, G.Blake, " A nanosecond optical parametric generator/amplifier seeded by an external cavity diode laser", Optics Communications, **159**, pp. 74-79, 1999.
5. V.Dmitriev, G. Gurzadyan, D.Nikogosyan , "Handbook of Nonlinear Optical crystals" (Berlin: Springer-Verlag, 1997).

Optical quality and efficiency of non-linear laser crystals

P.N.Afanasyev^b, N.D.Baiborodova^a, A.A.Dashtoyan^a, E.M.Dianov^a,
V.F.Lebedev^{*a}, V.V.Lobachev^b, M.Ya.Shchelev^c

^aFiber Optics Research Center at the General Physics Institute of the Russian Academy of Sciences,
38, Vavilova St., Moscow 117756, Russia

^bInstitute of Laser Technique and Technology of Baltic State Technical University,
1, 1-st Krasnoarmeyskaya St., St. Petersburg 198005, Russia

^cGeneral Physics Institute of the Russian Academy of Sciences,
38, Vavilova St., Moscow 117756, Russia

ABSTRACT

Correlation between non-linear properties and optical quality of KTP crystals is investigated. Optical quality is investigated by the schlieren method. The distribution of the mean-root-square refractive index gradient has been obtained along the radiation propagation direction. A comparison of optical quality of a crystal and the conversion efficiency is made. For the first time, the possibility of domain structure imaging in a crystal by using only an optical method is shown.

1. INTRODUCTION

It is known that the term "optical quality" of a crystal is determined by defects, such as scattering sites, strain and refractive index variation. The schlieren method is well known as a simple and sensitive optical method to determine the level of transparent solid and gaseous medium^a. However, this method is known as a method for qualitative analysis, not for quantitative analysis. In the literature it was mentioned only that an optical method was applied to evaluate the optical quality of a KTP crystal², but the schlieren images were not included in the paper. It is possible to use a digital CCD-camera with a high dynamic range and spatial resolution for adequate quantitative analysis. It is possible to visualize such defects, which are usually registered by the high-sensitivity method of second harmonic generation^{3,4}. Moreover, to provide a purely optical method to imaging the domain structure of a crystal, it is reasonable to use an optical method in combination with cooling to the cryogenic temperature. It is very important because it is known that high quality KTP crystal must be single domain only³. The purpose of this paper is demonstration of the capabilities of the schlieren method for optical quality evaluation of a KTP crystal.

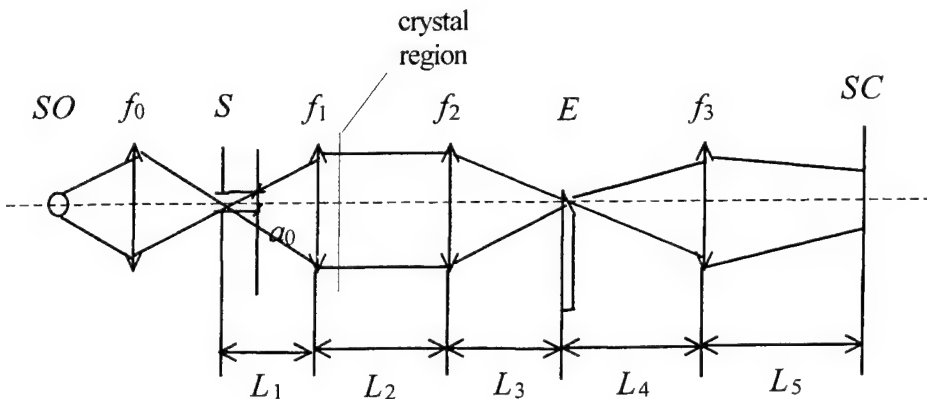


Fig.1. SO - light source (halogen lamp), S - slit a_0 , E - optical knife, SC -screen,
 f_0, f_1, f_2, f_3 - lens focuses,

* Correspondence: E-mail: vfleb@fo.gpi.ac.ru; WWW: <http://www.forc.gpi.ru/homepages/vfleb/vfleb.html>

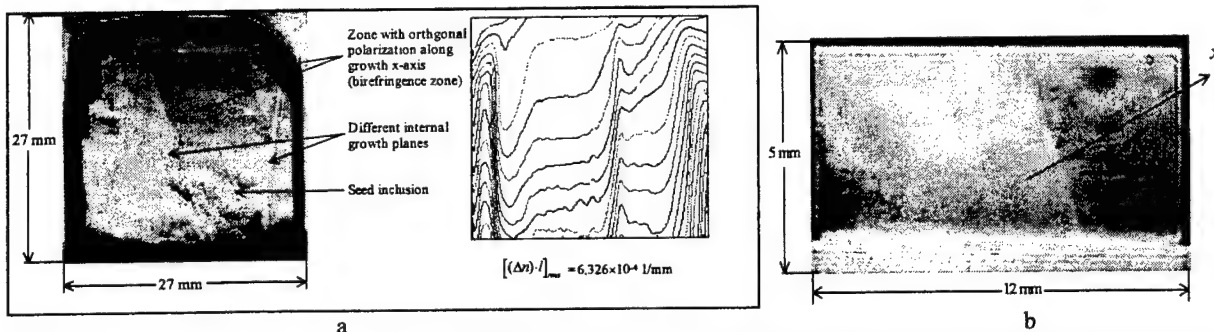


Fig.2. Different inhomogeneities and structure of faults in crystals; a – II-type phase-matching plane and reconstructed structure of Δn , b – zone of orthogonal polarization along the growth x-axis (birefringence zone, z-plane)

2. EXPERIMENTAL SET UP

KTP crystal flux grown along x-axis (at a temperature above 935 C) was studied. The schlieren method (Fig.1) was applied to quantitative evaluation of the optical quality of the crystals. The distribution of the mean-integrated refractive index gradient along the diagnostic direction was obtained. The angle ε of deflection of the beam on an optical inhomogeneity (in our case, on refractive index gradient) and refractive index gradient producing this deflection are calculated from expressions

$$\varepsilon = -\frac{2a \cdot I - I_0}{f_1 \cdot I_{00}}, \quad \varepsilon \sim I \cdot \frac{dn}{dx},$$

where a – is the slit size, f_1 – is the lens focus, I – is the intensity in the screen plane in the case of a crystal and a knife, I_0 – is the intensity in the screen plane without a crystal, but with a knife, I_{00} – is the intensity in the screen plane without a crystal and without a knife, l – is the crystal thickness, dn/dx – is the refractive index gradient along the x axis.

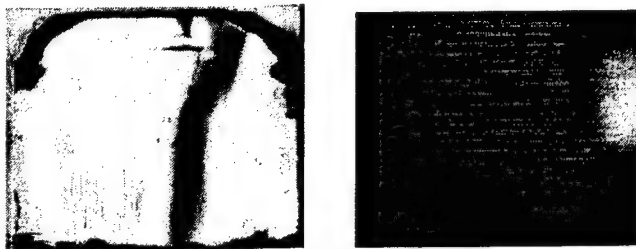


Fig.3. Schlieren picture (on left) and SHG image (on right) of 27x27x7 mm KTP crystal; II-type phase-matching plane

Hamamatsu digital camera C4742-95 (sensitive area 1024×1024 pixels, pixel size $6.7 \times 6.7 \mu\text{m}^2$) was used for capture of images. The minimal spatial resolution was $10 \mu\text{m}$. The absolute value of Δn will be determined more accurately after additional calibration of the schlieren method.

The output beam from a Q-switched Nd-YAG laser (Quantronix 116) was collimated to a spot, ~ 2 cm in diameter, and the test crystal was placed in the beam. The digital camera connected to a computer recorded the SHG beam.

A cryostat was used to investigate the crystal after cooling to the liquid nitrogen temperature. The test part of the cryostat was made in the form of a metal cube, where the interior volume was evacuated. The crystal has been installed in the cryostat on

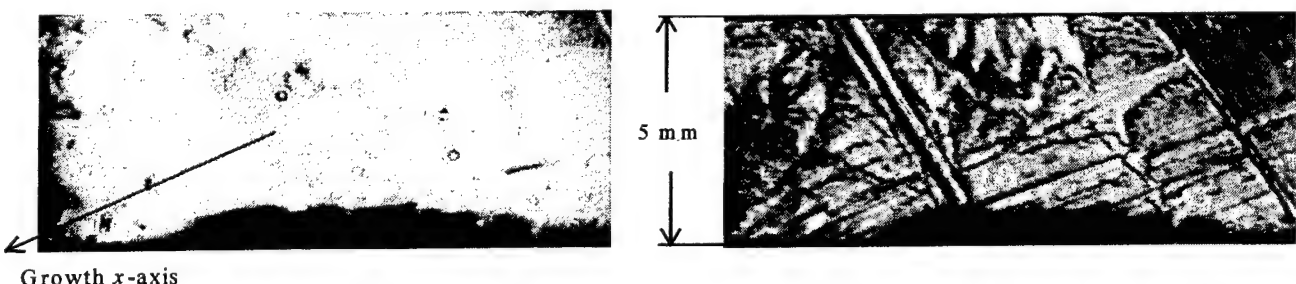


Fig.4. Schlieren images of a z-plane 5x5x12 mm crystal at 300 K (left) and 77 K (right).

cooling wall. During the cooling process, from room temperature to the liquid nitrogen temperature, the schlieren pictures are processed by the computer.

The z-slice investigated by the schlieren method was then exposed to selective etching. The etching was applied as a well-known method to visualize of ferroelectrics domain structure⁵.

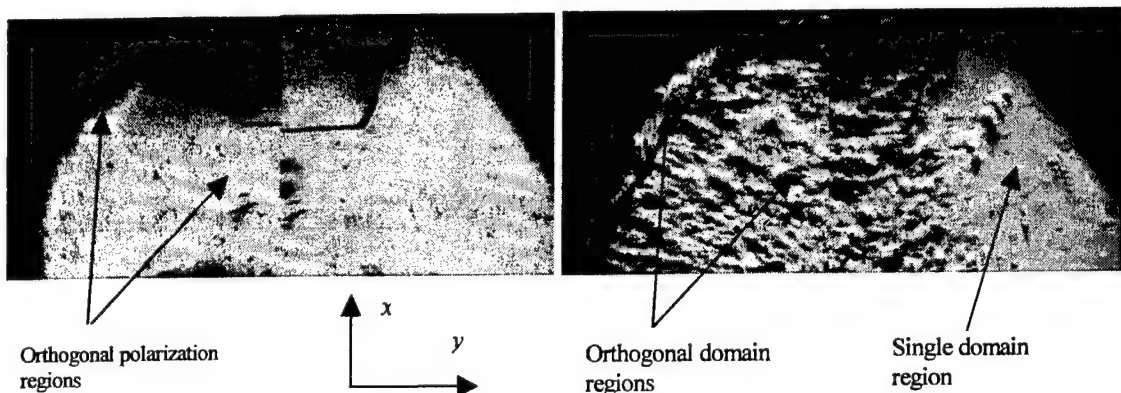


Fig.5. Schlieren images of z-slice of a KTP at 300 K (left) and 77 K (right)

3. RESULTS AND DISCUSSION

Various inhomogeneities, the structure of faults in a type II phase-matching plane crystal, and the reconstructed refractive index distribution are shown in Fig.2. There are seed inclusion, various internal growth planes, and zones with orthogonal polarization along the growth x-axis (birefringence zones). A comparison of crystal quality and SHG efficiency is shown in Fig.3. A correlation of the schlieren and SHG images can be seen.

To detect ferroelectrics domains by using only the optical method, the samples were cooled in a cryostat (Fig.4,5). Previously cooling was used to study the ferroelectrics domain structure of KTP⁵, but visualization of the domain structure was made with the help of a special carbon submicron powder, which consisted of charged microparticles. During the cooling process, spontaneous polarization will be increasing to cause the appearance of charges on the z-surfaces of crystal⁶.

To detect the domain structure optically a cryostat with a crystal was installed in the schlieren device. The schlieren images evolution under cooling during some minutes from 300 K (left picture) to 77 K (right picture) is shown on Fig.4. At 77 K there are added internal growth planes. Images will be reverse after reverse heating from 77 K to 300 K. The schlieren images of the z-slice (thickness is about 1 mm) of the crystal at different temperatures are shown in Fig.5. Ferroelectrics nature of the domains is confirmed by selective etching of z-surfaces of the KTP (see Fig.6).

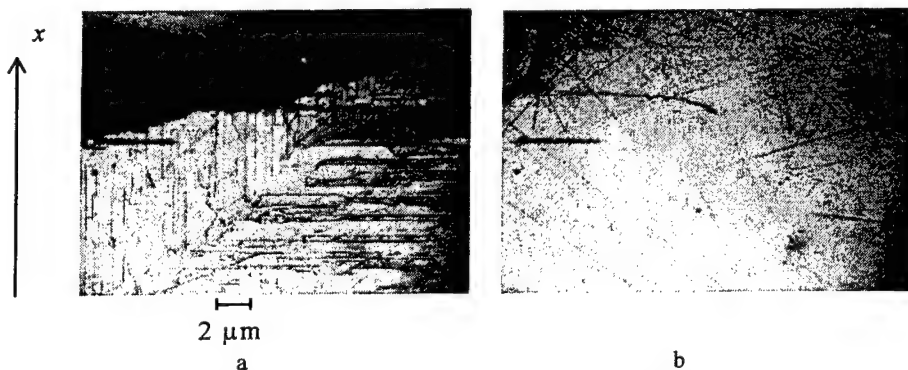


Fig.6. Z-slice of a KTP after etching; orthogonal domain – (a) and homogeneous region (single domain) – (b) of a KTP sample of Fig.5

4. SUMMARY

The schlieren method can be used to visualize the structure of crystal optical quality. This paper is the first demonstration of the possibility to measure Δn distributions in KTP by the schlieren method. For the first time, a purely optical method was used to visualize the domain structure in a KTP crystal. After increasing spatial resolution up to unit of microns, the nondestructive optical method can be used to visualize quality, for example, of grid in a periodically poled KTP, which is made by the ferroelectrics domains reversal technique⁵.

REFERENCES

1. H. Wolter, "Schlieren-, Phasenkontrast- und Lichtschnittverfahren, in "Hand-buch der Physik", **B 24**, Springer, Berlin, 1956, S.555-641.
2. G.E.Tsvetkov, "Segnetoelectricheskie domeny v kristallakh titanil-fosfata kaliya, vyrashchennykh is rastvora- rasplava metodom TSSG", Kristallografia **43** (1), pp.64-70, 1998.
3. G.M. Loiacono, and R.A. Stolzenberger, "Observation of complex domain walls in KTiOPO₄", Appl. Phys. Lett. **53**(16), pp. 1498-1499, 1988.
4. R.A. Stolzenberger, "Nonlinear optical properties of flux growth KTiOPO₄", Applied Optics **27** (18), pp. 3883-3886, 1988.
5. F. Laurell, M.G. Roelofs, W. Bindloss, H. Hsiung, A. Suna, and J.D. Bierlein, "Detection of ferroelectric domain reversal in KTiOPO₄ waveguides", J. Appl. Phys. **71** (10), pp. 4664-4670, 1992.
6. J. Mangin, G. Jeandel, and G. Marnier "Temperature dependence of polarization in KTiOPO₄ single crystals", Phys. Status Solid A **117**, pp. 319-323, 1990.

GENERAL PROPERTIES OF HARMONIC GENERATION SUSCEPTIBILITIES

F. Bassani and V. Lucarini

Scuola Normale Superiore, P.zza dei Cavalieri 7, 56100 Pisa, Italy

and

Istituto Nazionale di Fisica della Materia, Italy

ABSTRACT

We derive the asymptotic behaviour of the n^{th} order harmonic generation susceptibility using the Kubo response function formalism: it is characterized by a ω^{-2n-2} dependence and a coefficient proportional to the trace of the $(n+1)^{\text{th}}$ derivative of the potential energy on the equilibrium density matrix. Using this result and the analytical properties of the susceptibility considered we derive new Kramers-Krönig relations and sum rules. The general properties obtained show a strict correspondence with those already obtained with the classical anharmonic oscillator model.

P.A.C.S.

42.65 -k *Nonlinear Optics*

42.65 An *Optical susceptibility, hyperpolarizability*

42.65 Ky *Harmonic generation, frequency conversion*

78.20 -e *Optical properties of bulk materials and thin films*

78.20 Ci *Optical Constants (including refractive index, complex dielectric constant, absorption, reflection and transmission coefficient, emissivity)*

32.80 -t *Photon interactions with atoms*

33.80.-b *Photon interactions with molecules*

1. INTRODUCTION

The theoretical and experimental study of harmonic generation processes is one of the most important branches of nonlinear optics^{1,2}. Since the pioneering work in the 60's^{1,3}, a continuous development in this field has produced experimental and theoretical analyses of harmonic generation in solids^{4,5,6,7}, molecules⁸ and atoms^{9,10}, up to very high orders^{11,12} in the last case.

In nonlinear optics the use of integral properties is not as common as in linear optics, where they are tools of fundamental importance for the interpretation of optical data^{13,14,15,16}. After the first theoretical analyses of the 60's and of the 70's¹⁷, only in the last years relevant efforts towards the establishment of a general theory of the integral properties of nonlinear susceptibilities have been done^{18,19,20,21}.

The purpose of this paper is to determine the asymptotic behaviour of harmonic generation susceptibilities of every order and to establish Kramers-Krönig relations and sum rules for insulators, semiconductors and conductors, thus extending the results already obtained for the second²² and third²³ harmonics. The general quantum theory of Kubo optical response function²⁴ is used. We also discuss the problem of the introduction of the local field correction.

In section II we define the harmonic generation susceptibilities and give their explicit expressions. In section III we analyse their asymptotic behaviours and obtain K.K. relations and sum rules to all orders. In section IV we draw our conclusions.

2. QUANTUM EXPRESSION FOR THE HARMONIC GENERATION SUSCEPTIBILITY $\chi_{ij_1j_2\dots j_n}^{(n)}(n\omega; \omega, \dots, \omega)$

We consider N electrons in a volume V which interact with an external static potential $V(\vec{r})$ and which repel each other with Coulomb interaction, and we study the effect of their coupling with the electromagnetic field of the incident radiation. The total Hamiltonian of the system is given by the sum of two terms: the first term H_0 represents the unperturbed Hamiltonian:

$$H_0 = \sum_{\alpha=1}^N \frac{p_{\alpha}^2}{2m} + \sum_{\alpha=1}^N V(\vec{r}_{\alpha}) + \frac{1}{2} \sum_{\alpha \neq \beta=1}^N \frac{e^2}{|\vec{r}_{\alpha} - \vec{r}_{\beta}|} ; \quad (1)$$

the second term H' is given by the interaction of the electrons with the electromagnetic field, which we express in the velocity gauge²⁵ adopting the dipolar approximation:

$$H' = \sum_{\alpha=1}^N \left(e \frac{p_j^\alpha A_j(t)}{mc} + \frac{A_j(t) A_j(t)}{2mc^2} \right) , \quad (2)$$

Using the usual definition of the polarization vector $\bar{P}(t)$:

$$P_i(t) \equiv -\frac{e}{V} \text{Tr} \left\{ \sum_{\alpha=1}^N r_i^\alpha \rho(t) \right\} ; \quad (3)$$

where $\rho(t)$ is the density matrix of the electronic system evaluated at the time t , we obtain with the usual perturbation theory² that the n^{th} order polarization vector is:

$$P_i^{(n)}(t) = -\frac{e^{n+1}}{V(-i\hbar mc)^n} \text{Tr} \left\{ \int_{-\infty}^{+\infty} d\tau_1 d\tau_2 \dots d\tau_n \theta(\tau_1) \theta(\tau_2 - \tau_1) \dots \theta(\tau_n - \tau_{n-1}) \times \right. \\ \left. \times A_{j_1}(t - \tau_1) \dots A_{j_n}(t - \tau_n) \left[\sum_{\alpha=1}^N p_{j_n}^\alpha(-\tau_n) \dots \left[\sum_{\alpha=1}^N p_{j_2}^\alpha(-\tau_2), \left[\sum_{\alpha=1}^N p_{j_1}^\alpha(-\tau_1), \sum_{\alpha=1}^N r_i^\alpha \right] \dots \right] \right] \rho(0) \right\} , \quad (4)$$

Taking into account a monochromatic incident field of frequency ω and using the constitutive relation between the electric field $\bar{E}(t)$ and the vector potential $\bar{A}(t)$ ²⁵, we obtain that the $n\omega$ frequency component of the induced nonlinear polarization $P_i^{(n)}(t)$, which is proportional to $e^{-in\omega t}$, can be expressed as:

$$P_i^{(n)}(t)_{n\omega} = \chi_{ij_1 \dots j_n}^{(n)} \left(n\omega; \underbrace{\omega, \dots, \omega}_{n \text{ times}} \right) E_{j_1} \dots E_{j_n} e^{-in\omega t} , \quad (5)$$

where the n^{th} order harmonic generation susceptibility is:

$$\begin{aligned} \chi_{ij_1 \dots j_n}^{(n)} \left(n\omega, \underbrace{\omega, \dots, \omega}_{n \text{ times}} \right) &= -\frac{e^{n+1}}{V(\hbar m)^n \omega^n} \int_{-\infty}^{+\infty} d\tau_1 \dots d\tau_n \theta(\tau_1) \theta(\tau_2 - \tau_1) \dots \theta(\tau_n - \tau_{n-1}) \times \\ &\times e^{i\omega\tau_1} e^{i\omega\tau_2} \dots e^{i\omega\tau_n} Tr \left\{ \left[\sum_{\alpha=1}^N p_{j_n}^{\alpha}(-\tau_n), \dots, \left[\sum_{\alpha=1}^N p_{j_2}^{\alpha}(-\tau_2), \left[\sum_{\alpha=1}^N p_{j_1}^{\alpha}(-\tau_1), \sum_{\alpha=1}^N r_i^{\alpha} \right] \dots \right] \right] \rho(0) \right\} \quad . \quad (6) \end{aligned}$$

Applying Scandolo's theorem¹⁹ we obtain that for every n the function $\chi_{ij_1 j_2 \dots j_n}^{(n)}(n\omega; \omega, \dots, \omega)$ is holomorphic in the upper complex ω -plane.

With a long and cumbersome analysis of the expression of the susceptibility it is possible to derive that for high values of the frequency ω we have:

$$\begin{aligned} \chi_{ij_1 \dots j_n}^{(n)} \left(n\omega, \underbrace{\omega, \dots, \omega}_{n \text{ times}} \right) &= \frac{(-1)^n}{n^2 n!} \frac{e^{n+1}}{m^{n+1}} \frac{1}{V} Tr \left\{ \sum_{\alpha=1}^N \frac{\partial^{n+1} V(\vec{r}_{\alpha})}{\partial r_{j_n}^{\alpha} \dots \partial r_{j_2}^{\alpha} \partial r_{j_1}^{\alpha} \partial r_i^{\alpha}} \rho(0) \right\} \frac{1}{\omega^{n+2}} + o(\omega^{-2n-2}) = \\ &= \frac{(-1)^n}{n^2 n!} \frac{e^{n+1}}{m^{n+1}} \frac{N}{V} Tr \left\{ \frac{\partial^{n+1} V(\vec{r}_{\alpha})}{\partial r_{j_n}^{\alpha} \dots \partial r_{j_2}^{\alpha} \partial r_{j_1}^{\alpha} \partial r_i^{\alpha}} \rho(0) \right\} \frac{1}{\omega^{2n+2}} + o(\omega^{-2n-2}) \quad (7) \end{aligned}$$

where $o(\omega^{-2n-2})$ represents all the terms with an asymptotic behaviour faster than ω^{-2n-2} .

Planck's constant \hbar doesn't appear in the asymptotically dominant term of the susceptibility formula (7) and the quantum aspect of the expression we have obtained appears only in the definition of expectation value of the derivatives of the potential energy on the equilibrium density matrix of the system. These results have a clear correspondence with the ones we derived from the anharmonic oscillator model^{1,29,30,31}, once we consider the expectation value of the derivatives of the potential energy as the quantum analogue of the same derivatives of the classical potential energy evaluated at the equilibrium position. Therefore the asymptotic behaviours of the harmonic generation susceptibilities and consequently their integral properties do not essentially depend on the microscopic treatment of the interaction between light and matter, but are connected to the validity of the causality principle in physical systems.

3. K.K. RELATIONS AND SUM RULES FOR THE

$$\chi_{ij_1 j_2 \dots j_n}^{(n)}(n\omega; \omega, \dots, \omega)$$

In the case of insulators and semiconductors the knowledge of the asymptotic behaviour of the $\chi_{ij_1j_2..j_n}^{(n)}(n\omega; \omega, \dots, \omega)$ and its properties of holomorphicity in the upper complex ω plane already discussed allow us to write the following set of $2n+2$ K.K. type equations for the nonlinear harmonic susceptibilities:

$$\left\{ \omega^{2\alpha} \Re(\chi_{ij_1j_2..j_n}^{(k)}(n\omega; \omega, \dots, \omega)) = \frac{2}{\pi} \int_0^\infty d\omega' \frac{\omega'^{2\alpha+1} \Im(\chi_{ij_1j_2..j_n}^{(n)}(n\omega'; \omega', \dots, \omega'))}{\omega'^2 - \omega^2} \right. \quad (8a)$$

$$\left. \omega^{2\alpha-1} \Im(\chi_{ij_1j_2..j_n}^{(n)}(n\omega; \omega, \dots, \omega)) = -\frac{2}{\pi} \int_0^\infty d\omega' \frac{\omega'^{2\alpha} \Re(\chi_{ij_1j_2..j_n}^{(n)}(n\omega'; \omega', \dots, \omega'))}{\omega'^2 - \omega^2} \right. \quad (8b)$$

$$\text{with } 0 \leq \alpha \leq n \quad ,$$

where α is an integer such that the asymptotic decrease of the d^h moment of the harmonic susceptibility considered is at least as fast as ω^{-2} .

We can see that the number of independent K.K. relations grows with the order of the process of harmonic generation considered. The relations (8a) and (8b) generalize to all orders the results previously obtained for the second²² and third²³ harmonic susceptibilities.

These relations have been verified for the third harmonic process in the case $\alpha=0$ by Kishida, Hasegawa *et al.*²⁶ and have been used for theoretical calculations of the second and third harmonic generation processes in solids by Moss, Sipe, Ghahramani *et al.*²⁷.

Applying the superconvergence theorem²⁸ to the K.K. relations (8a-8b) and considering the asymptotic behaviour (7) we obtain the following set of sum rules:

$$\int_0^\infty d\omega' \omega'^{2\alpha} \Re(\chi_{ij_1j_2..j_n}^{(n)}(n\omega', \omega', \dots, \omega')) = 0 \quad \text{with } 0 \leq \alpha \leq n \quad (9a)$$

$$\int_0^\infty d\omega' \omega'^{2\alpha+1} \Im(\chi_{ij_1j_2..j_n}^{(n)}(n\omega', \omega', \dots, \omega')) = 0 \quad \text{with } 0 \leq \alpha \leq n-1 \quad (9b)$$

$$\begin{aligned} \int_0^\infty d\omega' \omega'^{2n+1} \Im(\chi_{ij_1j_2..j_n}^{(n)}(n\omega', \omega', \dots, \omega')) &= \frac{\pi}{2} \frac{(-1)^{n+1}}{n^2 n!} \frac{e^{n+1}}{m^{n+1}} \frac{1}{V} \text{Tr} \left\{ \sum_{\alpha=1}^N \frac{\partial^{n+1} V(\vec{r}_\alpha)}{\partial r_{j_n}^\alpha \dots \partial r_{j_2}^\alpha \partial r_{j_1}^\alpha \partial r_i^\alpha} \rho(0) \right\} = \\ &= \frac{\pi}{2} \frac{(-1)^{n+1}}{n^2 n!} \frac{e^{n+1}}{m^{n+1}} \frac{N}{V} \text{Tr} \left\{ \frac{\partial^{n+1} V(\vec{r}_\alpha)}{\partial r_{j_n}^\alpha \dots \partial r_{j_2}^\alpha \partial r_{j_1}^\alpha \partial r_i^\alpha} \rho(0) \right\} \end{aligned} \quad (9c)$$

All the moments of the susceptibility vanish except the one of order $(2n+1)$ of the imaginary part of $\chi_{ij_1j_2..j_n}^{(n)}(n\omega, \omega, \dots, \omega)$, which relates the nonlinearity of the potential energy of the system to the measurements of the imaginary part of the $\chi_{ij_1j_2..j_n}^{(n)}(n\omega, \omega, \dots, \omega)$. Up to now we do not have knowledge of experimental results related to the sum rules of harmonic generation processes.

The results obtained display a strict analogy with those previously derived²⁹ with the classical anharmonic oscillator model^{1,30,31}, thus demonstrating its relevance to the theory of nonlinear susceptibilities, as assumed by Peiponen²¹.

We would like to point out that other nonlinear sum rules have been used for the interpretation of experimental data, as in the case of pump and probe sum rules^{32,33}, which have been used to explain the results of an E.I.T. experiment³⁴ and in other cases mentioned in the review paper by Sheik-Bahae³⁵.

In the case of conductors we have to consider that the presence of a static nonvanishing nonlinear real conductivity changes the integral properties of their n^{th} order harmonic generation susceptibilities, since it introduces another pole in the susceptibility function at the origin of the ω plane, as can be deduced from the fact that the susceptibility can always be expressed in terms of the conductivity:

$$\chi_{ij_1j_2..j_n}^{(n)}(n\omega; \omega, \dots, \omega) = i \frac{\sigma_{ij_1j_2..j_n}^{(n)}(n\omega; \omega, \dots, \omega)}{n\omega} , \quad (10)$$

The presence of this pole changes the second one of the K.K. relations (8b) in the case $\alpha=0$:

$$P \int_0^\infty d\omega' \frac{\Re(\chi_{ij_1j_2..j_n}^{(n)}(n\omega'; \omega', \dots, \omega'))}{\omega'^2 - \omega^2} = -\frac{\pi}{2\omega} \Im(\chi_{ij_1j_2..j_n}^{(n)}(n\omega; \omega, \dots, \omega)) + \frac{\pi}{2} \frac{\sigma_{ij_1j_2..j_n}^{(n)}(0)}{n\omega^2} \quad (11)$$

and the related sum rule (9a):

$$P \int_0^\infty d\omega' \Re(\chi_{ij_1j_2..j_n}^{(n)}(n\omega'; \omega', \dots, \omega')) = -\frac{\pi}{2n} \sigma_{ij_1j_2..j_n}^{(n)}(0) , \quad (12)$$

where $\sigma_{ij_1j_2\dots j_n}^{(n)}(0)$ is the nonvanishing real tensor of nonlinear static conductivity of order n .

They extend to the nonlinear case the well-known results of linear optics, which have been experimentally verified^{36,37,38,39}.

The K.K. relations and related sum rules we obtain in the nonlinear case setting $1 \leq \alpha \leq n$ remain unchanged for metallic matter because the moments of the susceptibilities $\omega^{2\alpha} \chi_{ij_1j_2\dots j_n}^{(n)}(n\omega, \omega, \dots, \omega)$ don't have poles at the origin.

In all the applications to solid material we have considered the Maxwell average electromagnetic field as external perturbation. If strongly localized states have to be taken into account we should consider for those transitions the local field corrections, and our expression for the n^{th} order harmonic generation susceptibility should be multiplied by the n^{th} power of:

$$\frac{E_{\text{loc}}(\omega)}{E(\omega)} = \frac{n_{\text{lin}}^2(\omega) + 2}{3} \quad (13)$$

This factor doesn't change the analytical properties and the asymptotic behaviour of the harmonic generation susceptibilities since the linear refractive index $n_{\text{lin}}(\omega)$ is analytical in the upper complex ω plane and the asymptotic limit of expression (13) as $\omega \rightarrow +\infty$ is 1. Therefore the K.K. relations and the sum rules are not affected by the inclusion of the local field corrections. Modifications to the susceptibilities considered occur in the individual transitions.

4. CONCLUSIONS

We summarize the main results we have obtained in this paper.

With a rigorous quantum mechanical perturbative treatment we have derived general integral properties of the $\chi_{ij_1j_2\dots j_n}^{(n)}(n\omega, \omega, \dots, \omega)$, in particular $2n+2$ new K.K. type relations and sum rules.

They impose many stringent constraints which must be verified by all experimental data and must be obeyed by any detailed theory regarding harmonic generation processes. We have also shown that these results do not change even including local field corrections to macroscopic Maxwell fields.

The above results display a clear correspondence with those previously obtained from the anharmonic oscillator model²⁹, the reason being that the temporal causality is the only basic ingredient determining the integral properties of the susceptibility.

We have also analysed the particular case of conductors and have presented the modifications appearing order by order in one K.K. relation and in its related sum rule because of the nonvanishing of the static nonlinear conductivity.

We conclude that the general results here presented can be useful tools for the interpretation of experimental data in all materials, and for the elaboration of approximate models, as done in the case of second^{22,40} and third²³ harmonics. The basic factor which distinguishes different systems is the trace of the directional derivatives of the potential energy on the equilibrium density matrix.

ACKNOLEDGEMENTS

This research is based on work supported in part by C.N.R. under agreement with Scuola Normale Superiore and by M.U.R.S.T. (Italian Ministry). We wish to thank Giuseppe La Rocca, Iacopo Carusotto and Sandro Scandolo for useful discussions.

REFERENCES

¹ N. Bloembergen, *Nonlinear Optics* (Benjamin, New York, 1965 and subsequent editions);

² R.W. Boyd, *Nonlinear Optics* (Academic Press, New York, 1992)

³ P.A. Franken, A.E. Hill, C. W. Peters, G. Weinreich, *Phys. Rev. Lett.* **7**, 118 (1961)

⁴ V. Pellegrini, A. Parlangeli, M. Börger, R.D. Atanasov, F. Beltram, *Phys. Rev. B* **52**, 5527 (1994)

⁵ J. Miragliotta and D. K. Wickenden, *Phys. Rev. B* **50**, 14960 (1994)

⁶ C. Sirtori, F. Capasso, D. L. Sivco, A. Y. Cho, *Phys. Rev. Lett.* **68**, 1010-1013 (1992)

⁷ A. Mathy, K. Ueberhofen, R. Schenk, H. Gregorius, R. Garay, K. Müllen, and C. Bubeck *Phys. Rev. B* **53**, 4367 (1996)

⁸ D. J. Fraser, M. H. R. Hutchinson, J. P. Marangos, Y. L. Shao, J. W. G. Tisch, M. Castillejo, *J. Phys. B: At. Mol. Opt. Phys.* **28**, L739 (1995)

⁹ J. Reintjes, R.C. Eckardt, C.V. She, N.E. Karangelen, R.C. Elton e R.A. Andrews, *Phys. Rev. Lett.* **37**, 1540 (1976)

¹⁰ M. Bellini, C. Lyngå, A. Tozzi, M.B. Gaarde, T.W. Hänsch, A. L'Huillier, and C.-G. Wahlström, *Phys. Rev. Lett.* **81**, 297 (1998)

¹¹ C.-G. Wahlström, *Phys. Script.* **49**, 201 (1994)

¹² A. L'Huillier, L.A. Lomprè, G. Mainfray, C. Manus, *High Order Harmonic Generation in Rare Gases*, pp 139-207, in *Atoms in Intense Laser Fields*, ed. M. Gavrila, (Academic Press, New York, 1991)

¹³ F. Bassani e M. Altarelli, *Interaction of radiation with condensed matter*, from *Handbook on synchrotron radiation*, pp. 463-605, ed. by E.E. Koch (North Holland, Amsterdam, 1983)

¹⁴ D.L. Greenaway and G. Harbeke, *Optical Properties and Band Structures of Semiconductors* (Pergamon Press, Oxford, 1968)

¹⁵ H.M. Nussenzveig, *Causality and Dispersion Relations* (Academic Press, New York, 1972)

¹⁶ J.S. Toll, *Phys. Rev.* **104**, 1760 (1956)

¹⁷ Sh. M. Kogan, *Zh. Eksp. Teor. Fiz.* **43**, 304 (1962) [*Sov. Phys. JETP* **16**, 217 (1963)]; P.J. Price, *Phys. Rev.* **130**, 1792 (1963); F. L. Ridener, Jr. and R. H. Good, Jr., *Phys. Rev. B* **10**, 4980 (1974); F. L. Ridener, Jr. and R. H. Good, Jr., *Phys. Rev. B* **11**, 2768 (1975).

¹⁸ K.-E. Peiponen, *J. Phys. C* **20**, 2785 (1987) and K.-E. Peiponen, *Phys. Rev. B* **37**, 6463 (1988)

¹⁹ F. Bassani and S. Scandolo, *Phys. Rev. B*, **44**, 8446 (1991); F. Bassani and S. Scandolo, *Phys. Stat. Sol. (b)* **173**, 263 (1992)

²⁰ D.C. Hutchings, M. Sheik-Bahae, D.J. Hagan, E.W. Stryland, *Opt. Quantum. Electron.* **24**, 1 (1992)

²¹ K.E. Peiponen, E.M. Vartiainen, T. Asakura, *Dispersion, Complex Analysis and Optical Spectroscopy*, (Springer, 1999)

²² S. Scandolo, F. Bassani, *Phys. Rev. B* **51**, 6925 (1995)

²³ N.P. Rapapa and S. Scandolo, *Jou. of Phys.: Condensed Matter* **8**, 6997 (1996)

²⁴ R. Kubo, *J. Phys. Soc. Jpn.* **12**, 570 (1957)

²⁵ J. Jackson, *Classical electrodynamics* (Wiley and sons, New York, 1975)

²⁶ H. Kishida, T. Hasegawa, Y. Iwasa, T. Koda, Y. Tokura, *Phys. Rev. Lett.* **70**, 3724 (1993);

²⁷ D. J. Moss, J. E. Sipe, and H. M. Van Driel, *Phys. Rev. B* **36**, 9708 (1987); E. Ghahramani, E. Sipe, *Phys. Rev. B* **43**, 9700 (1991); E. Sipe and E. Ghahramani, *Phys. Rev. B* **48**, 11705-11722 (1993).

²⁸ M. Altarelli, D.L. Dexter, H.M. Nussenzwieg, D.Y. Smith, *Phys. Rev. B* **6**, 4502 (1972)

²⁹ F. Bassani and V. Lucarini, *Il Nuovo Cimento D* **20**, 1117 (1998)

³⁰ C.G.B. Garrett, F.N.G. Robinson, *IEEE J. Quantum Electron.* **QE-2**, 328 (1966)

³¹ S.S. Iha, N. Bloembergen, *Phys. Rev. B* **41**, 1542 (1968)

³² S. Scandolo and F. Bassani, *Phys. Rev. B* **45**, 13257 (1992)

³³ F. Bassani, V. Lucarini, *Eur. Phys. Jou. B* **12**, 323 (1999)

³⁴ F.S. Cataliotti, C. Fort, T.W. Hänsch, M. Inguscio, and M. Prevedelli, *Phys. Rev. A* **56**, 2221 (1997)

³⁵ M. Sheik-Bahae, *Nonlinear Optics of Bound Electrons in Solids*, pp. 205-224 in *Nonlinear Optical Materials*, ed. By J.V. Moloney (Springer, New York, 1998)

³⁶ M Altarelli, D.Y. Smith, *Phys. Rev. B* **9**, 1290 (1974)

³⁷ E. Shiles, T. Sasaki, M. Inokuti, D.Y. Smith, *Phys. Rev. B* **22**, 1612 (1980)

³⁸ B. J. Kowalski, A. Sarem, and B. A. Orowski, *Phys. Rev. B* **42**, 5159 (1990)

³⁹ D. Miller and P. L. Richards, *Phys. Rev. B* **47**, 12308 (1993)

⁴⁰ S. Scandolo, F. Bassani, *Phys. Rev. B* **51**, 6928 (1995)

Frequency doubling in the Čerenkov regime utilising an abnormal reflecting mirror structure

I.F. Salakhutdinov^{a,c}, L. Kotačka^{b,c}, H.J.W.M. Hoekstra^c, J. Čtyroký^b,
H. van Wolferen^c, V.A. Sychugov^a, O. Parriaux^d

^a General Physics Institute, Moscow, Russia; ^b Institute of Radio Engineering and Electronics, Prague, The Czech Republic; ^c MESA Research Institute, University of Twente, Enschede, The Netherlands;
^d Laboratoire TSI, Université Jean Monnet, St. Etienne, France

ABSTRACT

Abnormal reflecting mirror (ARM) structures, consisting of a corrugated optical waveguiding structure, can serve as a narrow band reflection filter in which strong field enhancement may occur by excitation of the guided mode. The latter is quite interest for SHG. We report experimental results of a first prototype, which exhibits ČSHG in the ARM structure.

1. INTRODUCTION

The growing importance of short-wavelength coherent sources (green/blue light) has proved that the SHG in so-called Čerenkov regime (ČSHG) is still very attractive [1-6]. It was shown by Asai [4] for the first time, that the conversion efficiency of ČSHG exhibits only a few very sharp maxima as a function of the wavelength and the layer thickness (see also [6]). The origin of this feature was discussed in [5,6]. It was shown theoretically [6] that more degrees of freedom, with respect to the wavelengths corresponding to such peaks, are introduced by using three and four layer systems. It was also shown both, theoretically [4] and experimentally [2,3], that the peak conversion efficiency is just a transition point between ČSHG and the SHG of a guided mode. A normalised conversion efficiency of about 1000%/Wcm² was reported in [3]. In this work we used an ARM (Abnormal Reflecting Mirror) structure for ČSHG.

2. THEORY OF THE ČERENKOV SHG

This section briefly describes basic properties of the Čerenkov SHG (ČSHG). First of all only relevant expressions from theory are extracted and adapted. Further more, only the $TE^\omega - TE^{2\omega}$ conversion is considered because the results relating to the TM modes may be deduced similarly as corresponding results for the TE modes. The conversion of fundamental TE^ω guided mode to second harmonic $TE^{2\omega}$ radiation mode is analysed using the coupled mode analysis in the configuration of a three-layer slab optical waveguide.

A typical arrangement of the ČSHG is presented in Fig. 1. A waveguiding high-refractive index layer made from an optically linear material is deposited onto a non-linear substrate and covered by a lower-index superstrate.

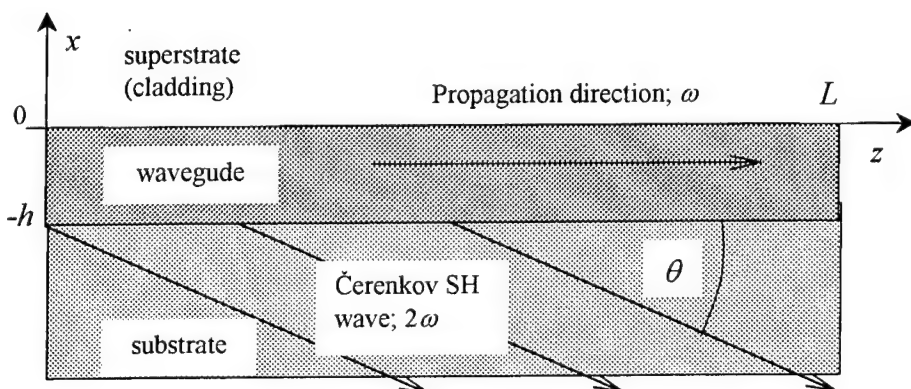


Fig. 1: The geometry of a non-linear optical waveguide under study.

If the Tamada's procedure [1] is followed then the distribution of the guided fundamental (ω) field in the substrate, i.e. for $x < -h$, obeys the relation

$$E_y^\omega = A_g \left[\cos(\kappa h) + \frac{\delta}{\kappa} \sin(\kappa h) \right] \exp[\gamma(x+h)] \quad (1)$$

where $\kappa = k(n_{g,\omega}^2 - N_\omega^2)^{1/2}$, $\gamma = k(N_\omega^2 - n_{s,\omega}^2)^{1/2}$, $\delta = k(N_\omega^2 - n_{c,\omega}^2)^{1/2}$, with $k = 2\pi/\lambda$. The subscripts g , s , c relate to a guide, a substrate, and a cladding, respectively. N_ω is the effective refractive index of the guided pump wave. The normalisation constant A_g is given by

$$A_g = \left(\frac{4\omega\mu_0\kappa^2}{\beta_\omega(\kappa^2 + \delta^2)(h + \gamma^{-1} + \delta^{-1})} \right)^{1/2} \quad (2)$$

to fulfil the condition $\int_{-\infty}^{\infty} |E_y^\omega|^2 dx = 1$ [W/m]. The second harmonic field is expressed as a radiation mode. Thus,

$$E_y^{2\omega} = A_r \left\{ \left[\cos(\sigma x) + \frac{\Delta}{\sigma} \sin(\sigma x) \right] \cos[\rho(x+h)] + \frac{\sigma}{\rho} \left[\sin(\sigma x) - \frac{\Delta}{\sigma} \sin(\sigma x) \right] \sin[\rho(x+h)] \right\}, \quad (3)$$

where $\sigma = 2k(n_{g,2\omega}^2 - N_\omega^2)^{1/2}$, $\rho = 2k(n_{s,2\omega}^2 - N_\omega^2)^{1/2}$, $\delta = 2k(N_\omega^2 - n_{c,2\omega}^2)^{1/2}$, with $k = 2\pi/\lambda$. The normalisation constant A_r is given as follows

$$A_r = \left(\frac{8\omega\mu_0\sigma^2\rho^2}{\pi\beta_\omega \{ \sigma^2[\sigma \sin(\sigma h) - \Delta \cos(\sigma h)]^2 + \rho^2[\sigma \cos(\sigma h) + \Delta \sin(\sigma h)]^2 \}} \right)^{1/2}. \quad (4)$$

As the next point the wave equation with a perturbed polarisation vector is to be solved (for any detail see e.g. [1]). Because the solution is quite complicated it is, for the sake of brevity, omitted here.

The solution of the wave equation leads to the following expression describing the generated second harmonic power $P_{2\omega}$ as the function of the pump power P_ω and the interaction length L

$$P_{2\omega} = \eta L P_\omega^2. \quad (5)$$

The quantity η is the so-called normalised conversion efficiency given by

$$\eta = \frac{\pi}{2} d_{33}^2 \omega^2 \epsilon_0^2 |I|^2 \cot\theta, \quad (6)$$

where ω is the frequency of the fundamental radiation, ϵ_0 is the permittivity of the vacuum, and d_{33} is a pertinent nonlinear coefficient (i.e. d_{33} plays an essential role in the configuration exploiting the KTP for the $TE^\omega - TE^{2\omega}$ conversion). Last two terms in (6) are explained in detail bellow because they have appeared to be crucial for the conversion efficiency.

The first one, the so-called overlap integral I , is defined by

$$I = \int_{-\infty}^{-h} E_{y,\omega}^2 E_{y,2\omega} dx. \quad (7)$$

Substituting from Eqs. (1) and (3), the overlap integral yields

$$I = A_g^2 A_r^2 \int_{-\infty}^{-h} \exp[2\gamma(x+h)] \left\{ B \cos[\rho(x+h)] + C \frac{\sigma}{\rho} \sin[\rho(x+h)] \right\} dx, \quad (8)$$

With $A = \cos(\kappa h) + (\delta/\kappa) \sin(\kappa h)$, $B = \cos(\sigma h) + (\Delta/\sigma) \sin(\sigma h)$, $C = \sin(\sigma h) - (\Delta/\sigma) \cos(\sigma h)$. Hence, a simple integration gives

$$I = A_g^2 A_r A^2 \left[\frac{2B\gamma - C\sigma}{4\gamma^2 - \rho^2} \right]. \quad (9)$$

The second term - $\cot\theta$ - needs an explanation of its origin. The angle θ is the so-called Čerenkov angle defined in the theory leading to Eq. (6). This angle is represented by $\cot\theta = 2N_\omega k / \rho$ and determines the slope of the generated second harmonic radiation (see Fig. 1). The main role of the Čerenkov angle is given by the matching condition in Čerenkov regime (see also Fig. 2)

$$2kn_{s,2\omega} \cos\theta = 2\beta_\omega = \beta_{2\omega}. \quad (10)$$

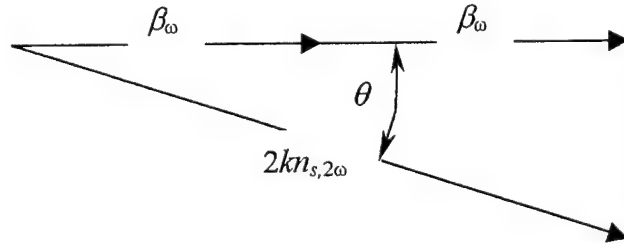


Fig. 2: Scheme of the phase-match condition in the Čerenkov regime.

Fig. 2 explains the existence of an effective conversion efficiency in Čerenkov regime in a wide interval of fundamental wavelengths. One can simply say that the phase-matching condition is automatically satisfied in the Čerenkov regime at a particular angle θ (see Fig. 2). Introducing the so-called “wavelength - guide thickness” (λ -t) diagram (see Fig. 3), the ČSHG has non-zero conversion efficiency in fairly broad area of the diagram. The Čerenkov regime is defined by the condition $\theta = 0^\circ$ or $N_\omega = n_{s,2\omega}$. The right side (determined by $\theta = 0^\circ$ and the right side of this curve in Fig. 3) of the λ -t diagram belongs to the pure GSHG.

The curve given by $\theta = 0^\circ$ appeared to be very important especially for SHG in waveguides, because this curve contains a transition point of the maximum of the conversion efficiency between ČSHG and GSHG. In general, the behaviour of ČSHG and GSHG at the close vicinity of that curve was not completely well recently understood yet [5, 6]. The explanation of the conversion efficiency behaviour for small Čerenkov angles has just been given in [7]. Thus, the efficiency for such case obeys the expression

$$P_{2\omega} = \eta_p L^{3/2} P_\omega^2, \quad (11)$$

The conversion efficiency from Eq. (6), used with (9), may be rewritten in the form of

$$\eta = F \frac{A_r(\rho)}{\rho} \left[\frac{2B\gamma - C\sigma}{4\gamma^2 - \rho^2} \right], \quad (12)$$

with $F = \pi d_{33}^2 \omega^2 \epsilon_0^2 A_g^2 A^2$. As was said, $\rho \rightarrow 0$ for $\theta \rightarrow 0^\circ$. Thus, an easy inspection of Eq. (12) given in [6] exhibits sharply peaked conversion efficiency at the close vicinity of a point obeying the condition

$$\sigma \sin(\sigma h) - \Delta \cos(\sigma h) = 0, \quad (13)$$

which produces the modified dispersion relation giving the efficiency as follows

$$\frac{\arctan(\delta/\kappa) + \arctan(\gamma/\kappa)}{\kappa} - \frac{\arctan(\Delta/\sigma) + \pi}{\sigma} = 0. \quad (14)$$

The existence of the peaked efficiency was for the first time reported by Asai *et al* [4] who only declared that the expression (6) (derived by Tamada in [1]) is accurate enough for $\rho \gg L^{-1}$, because the expression diverges. On the other hand, the theory is sufficiently valid for Čerenkov angles $\theta > 0.1^\circ$. Thus, a value of the peaked efficiency has to be corrected by Eq. (11).

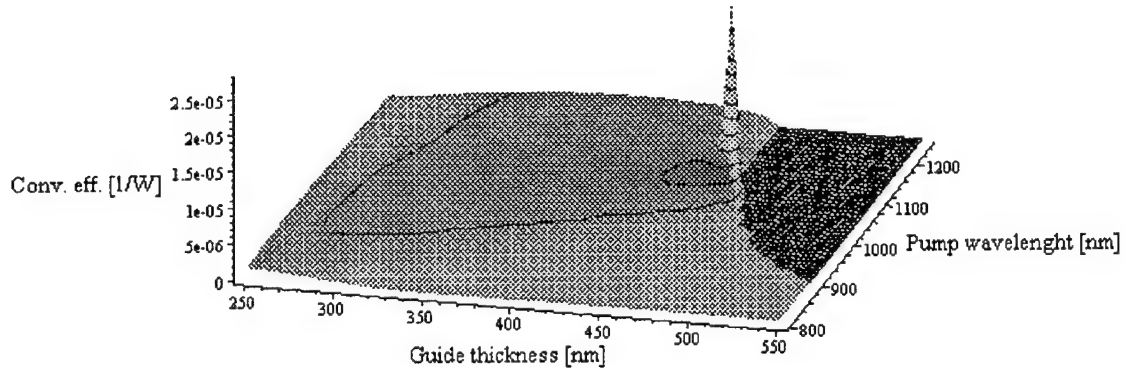


Fig. 3: SHG conversion efficiency as a function of the guide thickness and the pump wavelength. In the dark area at the right corner of the graph, there would have been depicted pure guided-guided SHG conversion efficiency (which was omitted for the sake of brevity).

Solving the modified dispersion relation (14) one can find that there is only one suitable wavelength which can be converted with the highest conversion efficiency for given refractive indices. This can be done only for a particular thickness of the guiding layer, namely that given by the explicit expression $h = [\arctan(\delta/\kappa) + \arctan(\gamma/\kappa)]/\kappa$. Similar remarks hold for four-material systems, which is the matter of our study (a grating may be understood as an extra layer of specific properties).

Finally, the peak exhibits rather narrow FWHM (see Fig. 3) similar to the guided-guided SHG behaviour. This causes certain hurdles in a device fabrication (e.g., an accuracy of the guide thickness ± 0.2 nm is needed). These strict requirements are further more complicated together with the demands necessary for an ordinary working ARM (see the text below). But, it still leads to a promising offer to exploit the Čerenkov regime apart from its peaked conversion efficiency, because of the “automatically” satisfies phase matching. However, a reasonable connection of the highest conversion efficiency together with the ARM phenomenon is currently being studied.

3. ABNORMAL LIGHT REFLECTION FROM CORRUGATED WAVEGUIDE

Mashev and Popov discovered theoretically the effect of abnormal light reflection from the surface of corrugated waveguide structure in [8]. It was confirmed experimentally in [9,10]. It was found later that this structure can be used for a wide variety of applications including narrow-band reflection filter [11], semiconductor waveguide gratings [12] as well as for excitation of long-range surface plasmons in corrugated metal films [13]. In this work we used an ARM for ČSHG structure.

The effect of abnormal light reflection consists in a following. Let us consider three-layer waveguide structure consisting from air ($n_c=1$) as a cover medium, waveguide layer with n_c and substrate with n_s (Fig.1) We can choose waveguide parameters when light can radiate both in cover and substrate media. For the several conditions we can $\sin(\theta) \approx n^* \cdot \lambda / \Lambda$, $D\alpha \gg 1$, $\alpha_{rad} \gg \alpha_{dis}$

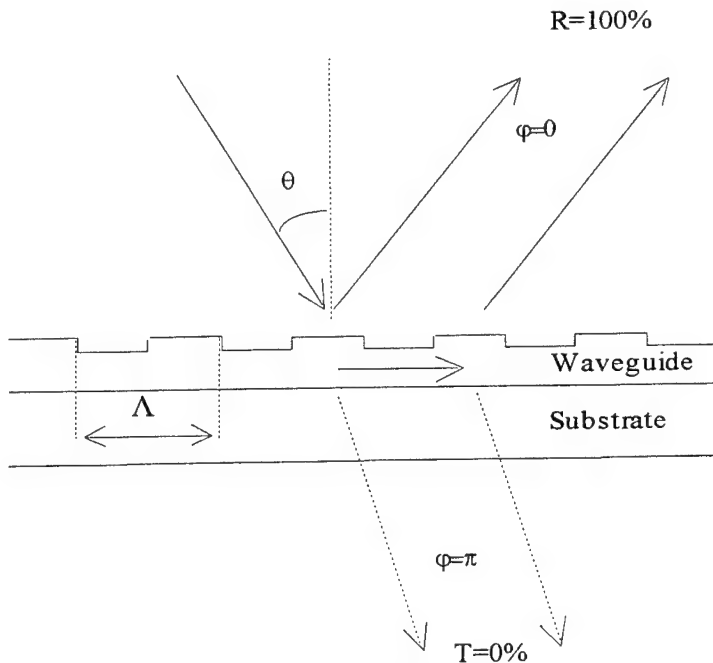


Fig. 4: The drawing shows, as an example, a case in which the reflection coefficient (R) is almost equal to 100% (reflected beam and re-radiated beam are in the case of constructive interference) and so the transmission coefficient (T) is almost equal to 0% (transmitted beam and re-radiated beam are in the case of destructive interference).

The necessary condition for obtaining this reflection effect is the excitation of a guided wave and the occurrence of light radiation into both media adjacent to the guiding layer.

4. TECHNOLOGY

Technology is a key component for investigation of ČSHG in waveguide geometry due to strong requirements to waveguide parameters. For example accuracy of n_g value must be not less than 0.001. Requirements for waveguide layer thickness is also very critical – its value must be made with accuracy about 0.1 nm.

Si_3N_4 layers were made by PECVD (plasma-enhanced chemical vapour deposition) method. Chemical vapor deposition is based on surface chemical reaction of one or more processing gases. The gas reactants flow to the surface of the substrate where they will react. As a result the growth of a thin layer of the desired material could be obtained.

Parameters of technological process were following:

Pressure - 650 mTorr. Temperature of annealing – 300÷400° C. Annealing gas – N_2 . Deposit flow: SiH_4 - 1000÷2000 sccm and NH_3 - 3÷7 sccm.

Obtained n_c varied from 1.9501 to 1.9911.

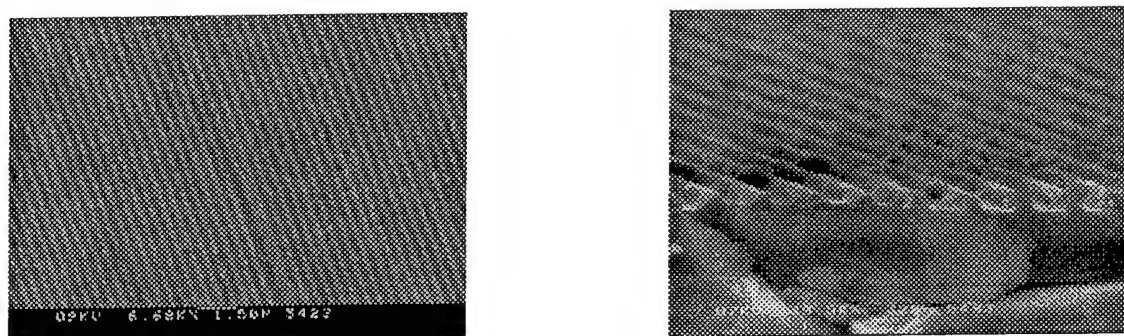


Fig. 5: Photographs of gratings used in experiment.

The gratings were made by standard holographic exposure (with a Ar laser), followed by ion beam etching for the transfer of the grating from the resist film into the substrate. The pictures of obtained gratings are presented in Fig. 5.

5. EXPERIMENT

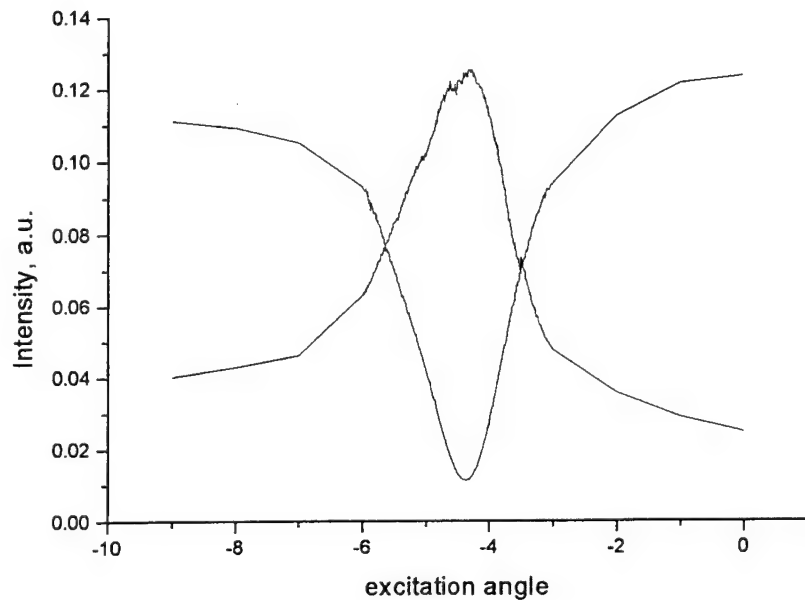


Fig. 6: Reflection and transmission curves for linear ARM.

As a first step of investigation the ARM structure on the base Si_3N_4 film was made. The parameters of the structure were following: cover layer – air ($n_c=1$), waveguide layer - Si_3N_4 layer ($n_g=1.97$). The Fig. 6 presents experiment results for transmission and reflection. The maximum reflection coefficient 0.92 was obtained.

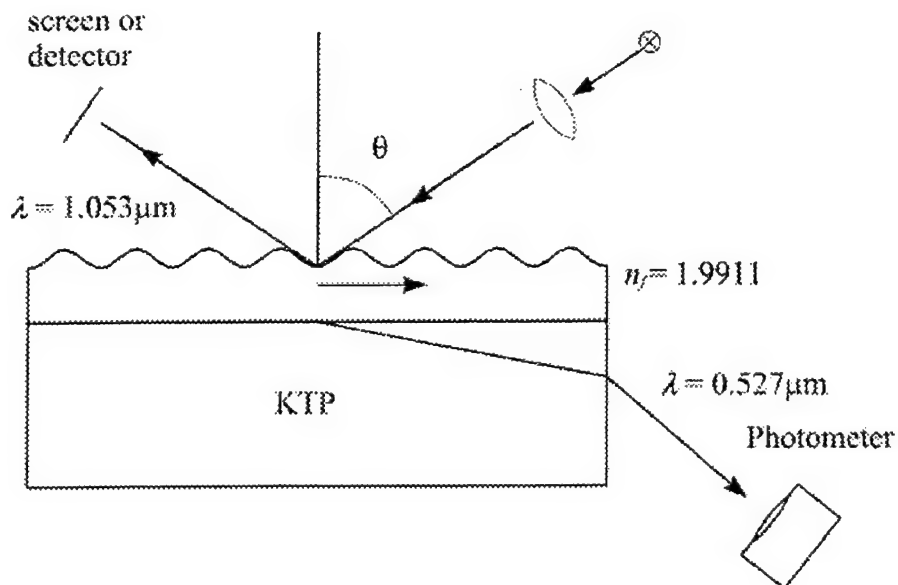


Fig. 7: The scheme of the experimental set-up for CSHG.

The connection of the SHG phenomena with the waveguide gratings was studied. This research resulted in a not yet fully optimised prototype. The first specimen consisted of KTP as a substrate, Si_3N_4 as a medium constituting both - the guide layer (the thickness varied from 470 to 518 nm) and the regularly corrugated region (grating period was 440 nm and the corrugation depth was about 200 nm). The experiment scheme is presented in Fig. 7. The cladding consisted of the air. As a result we obtained more than $30\mu\text{W}$ green light with 2 W pump CW power ($\lambda = 1053$ nm) for the structure with $n=1.9911$ (at 633 nm).

6. DISCUSSION AND CONCLUSIONS

Thus high conversion efficiency of the main radiation into SH signal was obtained. From our point of view it is a result of ČSHG peak conditions obtained in the experiment. This result confirms theory predictions given in Part II.

However from the point of view of using of this result in laser physics we must be very careful. From the point of view of laser cavity for solid-state laser ARM structure is a source of additional losses. Of course $R=0.92$ could be increased by optimisation of technological conditions. However there are two main problems. Firstly, obtaining of ARM with reflection close to 100% requires additional technological improvements (that not easy from the point of view of technological possibilities of MESA⁺ Institute of Twente University). These efforts could increase price of obtained ARM structures. Secondly, from the practical point of view it is very hard to obtain ARM with $R=0.97$ and more is very difficult. However from point of view of cavity of solid-state laser these losses are extremely high. Probably the best results could be obtained for using of ARM structures for semiconductor laser due to high efficiency of these lasers.

We can note one additional mechanism of increasing of SH. It is well known effect of SH signal enhancement due to coupling of signal from the rough surface [14]. This effect plays important role for short-pulse radiation as well as for the case of high-power CW radiation. In our case we can speak about enhanced SH from the rough surface of "dielectric layer – non-linear crystal" boundary. This radiation could be collected due to resonance character of waveguide-grating structure.

7. ACKNOWLEDGMENSTS

This work was supported by EC Inco-Copernicus 960194, NWO 047.006.014 and RFBR 98-02-17355 projects.

8. REFERENCES

1. Tamada H., *IEEE J. Quant. Electron.* **27**, (1991), 502.
2. Doumuki T., Tamada H., Saitoh M., *Appl. Phys. Lett.* **64**, (1994), 3533.
3. Doumuki T., Tamada H., Saitoh M., *Appl. Phys. Lett.* **65**, (1994), 2519.
4. Asai N., Tamada H., Fujiwara I., Seto J., *J. Appl. Phys.* **72**, (1992), 4521.
5. Chang R.-S., Shaw S.-Y., *J. Mod. Opt.* **45**, (1998), 103.
6. Kotačka L., Čtyroký J., Hoekstra H. J. W. M., in: *OSA Technical Digest - NLGW'99*, OSA, Washington DC 1999, 380.
7. Čtyroký J., Kotačka L., *Opt. and Quant. Electron.* **32** (2000), 799.
8. Mashev L., Popov E., *Opt. Commun.* **51**, (1984), 131.
9. Golubenko G.A. et al., *Sov. J. Quant. Electron.* **15**, (1985), 886.
10. Mashev L., Popov E., *Opt. Commun.* **55**, (1985), 377.
11. Magnusson R., Wang S.S., *Appl. Phys. Lett.* **61**, (1992), 1022.
12. Sharon A., Rosenblatt D., Friesem A.A., *J. Opt. Soc. Am. A* **14**, (1997), 2985.
13. Salakhutdinov I.F. et al, *IEEE J. Quant. Electron.* **34**, (1998), 1054.
14. Raether H., *Surface plasmons on smooth and rough surfaces and on gratings*. Springer-Verlag, Berlin, Heidelberg 1988.

Laser Detection of the Parameters of Small Solid Particle Located in Air

Alexander Andreev^{1,2}, Toshitsugu Ueda¹, Muneaki Wakamatsu¹, Anatoly Golub²

1. Yokogawa Electric Corporation, 2-9-32 Nakacho, Musashino-shi, Tokyo, 180-8750 Japan.
2. Institute for Laser Physics, St.Petersburg 193232, Russia

ABSTRACT

The problem of small particle size and material detection is important for industrial and environmental applications. Previous investigations have shown the possibility of using the laser breakdown method to achieve first goal; the sensitivity of this method is a thousand times higher than that of conventional methods. However, for small particle sizes, the damage threshold of the solid target in this case is very close to the breakdown point of pure air. After breakdown, there is a small volume of dense hot plasma that emits radiation. We analyzed this radiation especially at late stage using an analytical model and simulation code as well as by experiment, and found that the emission intensity varied depending on the laser type and plasma parameters including initial particle size.

Keywords: laser pulse, small solid particle size, laser breakdown in air, laser plasma line emission

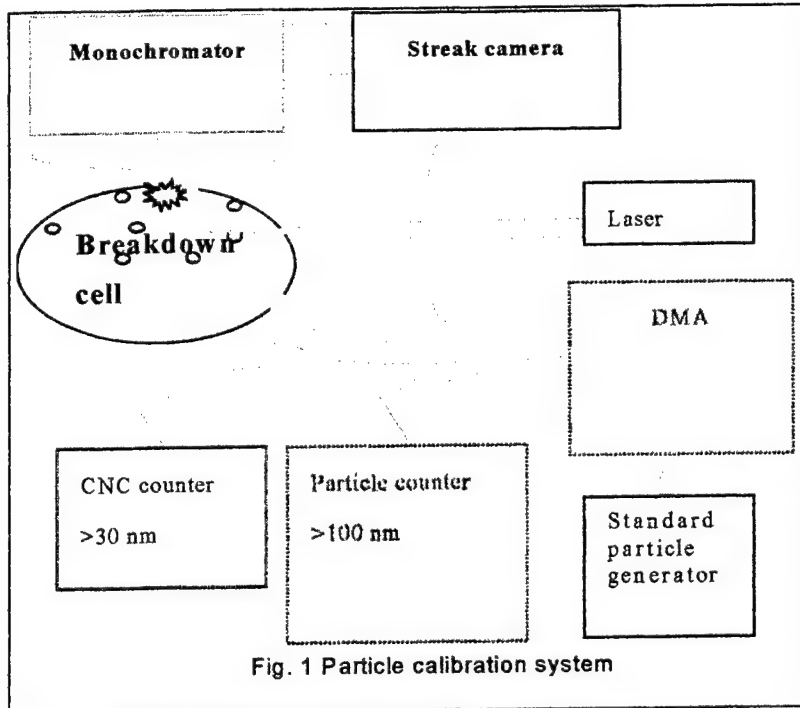
1. INTRODUCTION

Laser-induced breakdown (LIB) of gas has been the subject of a number of studies for plasma generation. It has been observed in many studies that the threshold for generating shielding plasma in the presence of a solid is significantly lower than the threshold for clean gases (see for example [1,2]). First, the dependence of aerosol breakdown on its size was predicted [1] and then developed [3]. The particle breakdown threshold value is greatly influenced by particle material, particle diameter, laser wavelength, intensity and pulse duration.

The problem of SSP size detection is important for industrial and environmental applications. Previous investigations have shown the possibility of using the laser breakdown method for such detection. The sensitivity of this method is a thousand times higher than that of conventional methods such as ICP and MIT [4]. However, for a particle size of less than 0.1 μm , the damage threshold of the solid target in this case is very close to the breakdown point of pure air. After breakdown, there is a small volume of dense hot plasma that emits radiation in lines and continuum. This study set out to determine the threshold intensity required to generate dense plasma when interacting with a small solid particle (SSP) suspended in air and its emission. We analyzed this radiation using an analytical model and simulation code as well as by experiment, and found that the emission intensity varied depending on the laser type and plasma parameters including initial particle size.

2. EXPERIMENTAL SET-UP

Figure 1 shows a block diagram of the prototype particle calibration system [5]. The commercially available flash-lamp excitation Nd:YAG laser was used in the system. The maximum repeated frequency of the laser is about 100 Hz with pulse duration of 5.8 ns and with 10 - 50 mJ/pulse energy. We used a 50-mm focal length lens to focus the laser. Furthermore, we used a commercially available generation device for uniformly distributing particles in the atmosphere without condensing them. Standard particles generated by the particle generation device were led through a pipe to the breakdown cell. The pulse laser light was focused in this cell and generated LIB. The light generated by breakdown was led to a monochromator and recorded by a streak camera with timesharing spectrum. The data in the streak camera was read by a computer and processed. The resolution of time in the streak camera was less than 10 ps.



3. Breakdown of pure air by laser pulse and light emission of a spark

In this part of our investigations we consider a breakdown process of clean air. Theoretical analysis has shown that there are two mechanisms responsible for a laser air breakdown: avalanche or cascade ionisation and multi-photon ionisation. Each mechanism is responsible for a breakdown at certain conditions of laser-air experiment. By decreasing the pressure of the gas, the mean free path of the free electron increases and breakdown threshold increases too, making the cascade collision ionisation process less effective; thus, the multi-photon absorption process plays a more dominative role. Also the increasing of laser frequency decreases threshold of multi-photon process very much.

If we take into account inelastic and multi-photon processes as well which produce an initial number of electrons in the laser focal volume, we obtain breakdown threshold [6]:

$$I_{th} \approx \mu \frac{\omega^2 + v_{en}^2}{\omega^2} \frac{J_a}{mc^2} \left(\frac{N_0 - N(\omega)}{\tau_p v_{en}} + \frac{v^*}{v_m} \delta \frac{J_a}{J^*} + \beta \frac{D}{r^2 v_{en}} \right) \propto \omega [J_a/h] (1/v_m \tau_p) \ln(\omega^2 J_a / \omega_{Nd}^2 I_{12}) \quad (1)$$

here $v^* = N_a v^*$ σ^* is the frequency of excitation by electrons whose energy lies in the range $J^* < E_e < J_a$; σ^* and v^* are the average values of excitation cross section of atoms and of electron velocity in the same energy range, J^* - excitation potential; $\delta = 0$ for $E_e < J^*$ and $\delta = 1$ for $E_e > J^*$; $N(\omega) = \ln(n_a V_f w \tau_p)$, D - diffusion coefficient, v_{en} - frequency of electron atom collisions. There is saturation level in (1) from pressure dependence, because v^* depends from pressure approximately as v_m from p_R . We calculated breakdown laser intensities for a different gases by this formula and the results of simulations are close to the experimental data.

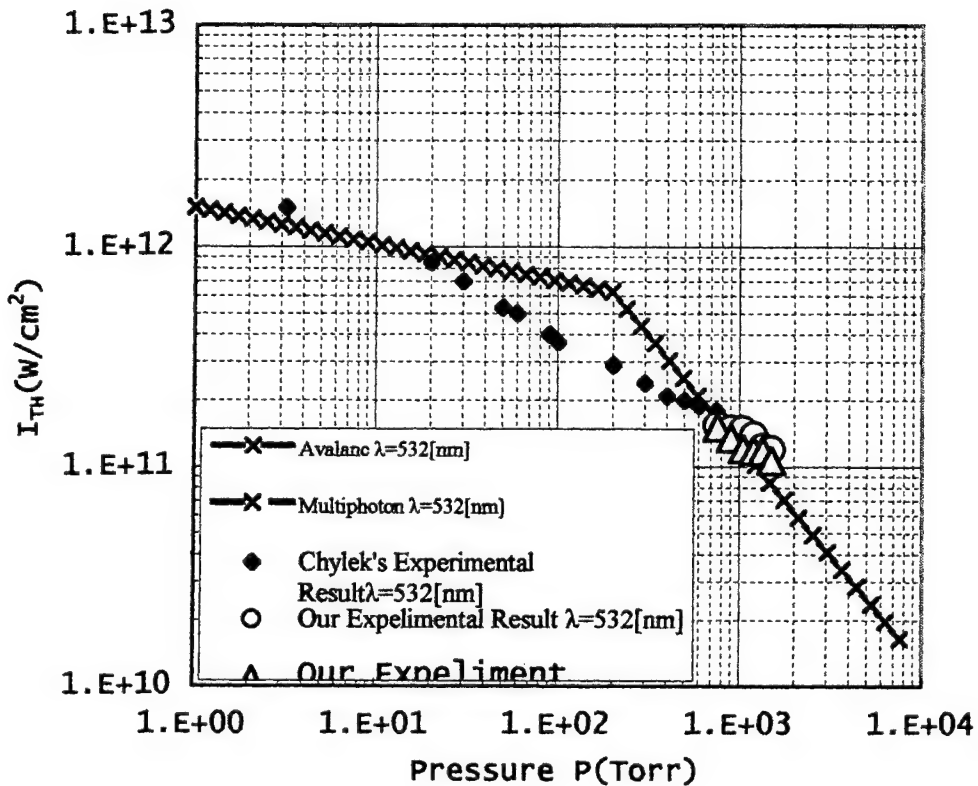


Fig.2 Breakdown threshold intensity at laser wavelength 0.53 mkm for clean air.

On Fig.2 the experimental data [7], for the second harmonic of Nd laser, have shown by blue \diamond . Here we have strong influence of multi-photon process at low atmospheric pressure on breakdown air threshold. Line, denotes by black - x, shows the theoretical dependence for multi-photon process and by pink - x is also theory prediction by avalanche process. The combination of these two processes from (1) gives result close to experimental data.

3.1 Breakdown air plasma emission

Laser spark appears in air if laser intensity exceeds breakdown threshold. Let's estimate the power P emitted by spark area from the model of black body radiation at adiabatic plasma temperature decreasing:

$$I = \sigma T^4, P = I 4\pi R^2 \approx 4\pi\sigma T_0^4 (c_{s0}t/R_0)^{-10\beta(2+\beta)} = 4\pi\sigma T_0^4 R_0^2 (c_{s0}t/R_0)^{2-10\beta(2+\beta)}$$

From these expressions we see that at our spark parameters $R_0 \approx 100$ mkm and $c_{s0} \approx 10^6$ cm/s we can obtain the decreasing of the plasma power emission in 2 times for the moment $t = 100$ ns if $\gamma = 1.197$. It is coexisted with air γ for this range of hydro parameters [8] and experimental results.

From our experiments we have some cut-off in plasma emission time dependence and this cut-off time increases at laser energy increasing (see Fig.3). Let's estimate total power emitted by plasma from the next formula: $P \approx 4\pi\sigma T_0^4 R_0^2 (c_{s0}t/R_0)^{0.3}$, then emitted energy:

$$E = \int P dt \approx 6\pi\sigma T_0^4 R_0^2 (c_{s0}t_f/R_0)^{0.7},$$

We suppose that light emission from plasma is finished at the moment (cut-off time t_f) then plasma temperature is equal to air ionisation potential $T = J_{air}$. So, we get next expression for cut off time:

$$t_f \approx (R_0/c_{s0}t_f) (T_0/J_{air})^{(2+\beta)\gamma\beta} \propto E_{abs}^{3.8} \quad (2)$$

From (2) we see that cut-off time t_f strongly depend from laser energy as in experiment (see Fig.3)

where theoretical prediction has shown by solid line and simulation results by dashed line and the experimental results by open cycle).

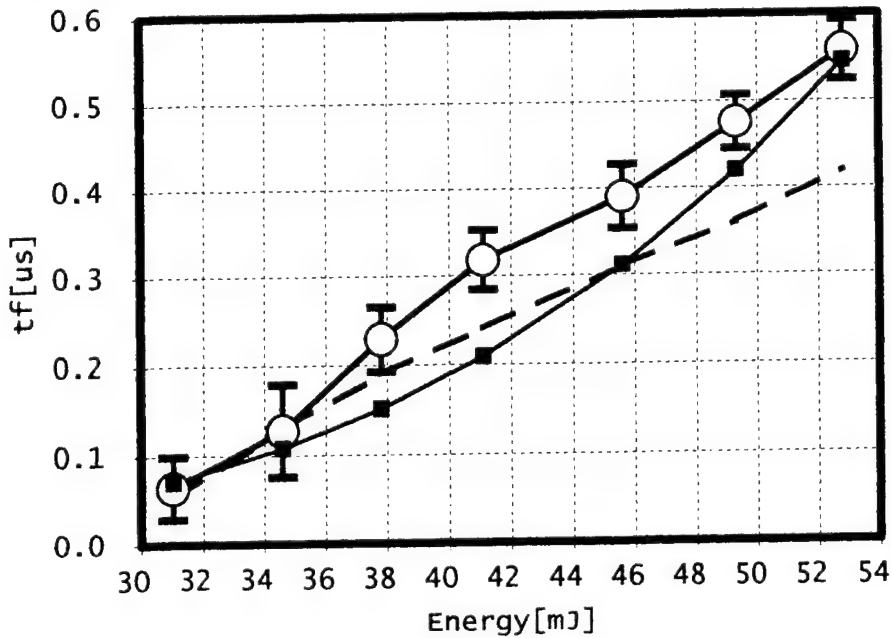


Fig.3 Dependence of breakdown cut-off time from laser energy.

As in experiment, we measured emitted energy ΔE in some spectral range $[x_1, x_2]$, let's calculate it now from Planck's law. For energy emitted in spectral range $[x_1, x_2]$ we have the next expression

$$\Delta E = \int_{t_0}^{t_f} \Delta I 4\pi R^2 dt \approx \sigma T_0^4 4\pi R_0^2 \frac{R_0}{c_{so}} \left(\frac{h\nu_1}{k_B T_0} \right)^3 \left(\frac{c_{so} t_0}{R_0} \right)^{3/2} \exp\left(-\frac{h\nu_1}{k_B T_0} \sqrt{\frac{c_{so} t_0}{R_0}}\right) \propto \sqrt{T_0} \exp(-h\nu_1/k_B T_0) \quad (3)$$

here $t_f \gg t_0$ and $\Delta E = \Delta E(E_L)$. We take $t_0 \approx (R_0/c_{so})$ because after breakdown for the time $t_B \approx 0.1$ ns, near breakdown threshold $t_B \propto (E_0/E_L)$, plasma volume heated thermal wave until this time and temperature does not changes in space along plasma sphere
The strong changing of $\Delta E = \Delta E(E_L)$ is possible as in the experiment because we have linear dependence of plasma temperature $T_0 \propto E_L$ and for $E_L = E_{L0} + \Delta E_L$, where according to experiment $\Delta E_L / E_{L0} \approx 0.3$, we obtain $\Delta E(E_L)/\Delta E(E_{L0}) \approx 5$ and it is near the experimental data.

4. Computer code and numerical simulations

The developed simulation code includes the next physical processes: propagation of a heat wave inside matter, hydrodynamics of gas atmosphere and plasma by two temperature approximation, thermo heating, absorption of laser radiation, thermal radiation emission and absorption by gas and plasma. On first stage of simulations we suppose that absorbed laser energy puts in air volume uniform in its volume at initial time moment $t = 0$. At $t > 0$ we consider heated gas matter expansions in surrounded air together with thermal radiation of this matter. The task is solved in two temperatures one fluid hydrodynamic approximation. We consider gas matter which consists from two subsystems: first the subsystem of heavy particles (molecules, atoms and ions) and electron-oscillator subsystem which consists from thermal energy of electrons, molecular energy of oscillation and dissociation and energy of electron excitation and ionisation of atoms and ions. We suppose that at any moment each subsystem is in equilibrium determined by own temperature (T_e for electrons and T_i for another particles) and gas density ρ . The energy of heavy particles is the energy of movement and rotation its components according to T_i . The systems change by energy through collisions of electrons with heavy particles and between movement and rotation channels. Beside we take into account electron thermo-conductivity

and energy transformation by radiation emission and absorption of electron oscillation subsystem. In this case our gas is in thermodynamical equilibrium at T_e and ρ . It permits to use table data for equilibrium thermodynamic and optics properties of the gas. We solve our task by the next set of equations:

$$\rho r^2 \frac{\partial r}{\partial m} = -I, \quad \frac{\partial u}{\partial t} = -r^2 \frac{\partial(p + p_e)}{\partial m},$$

$$\frac{\partial U_e}{\partial t} + p_e \frac{\partial}{\partial m} (r^2 u) + \frac{\partial}{\partial m} (F_e + F_r) = -Q_e - Q_v,$$

$$\frac{\partial U}{\partial t} + p \frac{\partial}{\partial m} (r^2 u) = Q_e + Q_v,$$

$$F_e = k_e r^2 \frac{\partial T_e}{\partial r},$$

$$Q_e = \frac{1}{\rho} \sum_i \frac{3v_{ei} n_e m_e k (T_e - T)}{M_i},$$

$$Q_v = \frac{1}{\rho} \sum_v \frac{n_v \epsilon_v}{\tau_v} \left(\frac{1}{[\exp(\epsilon_v / kT_e) - 1]} - \frac{1}{[\exp(\epsilon_v / kT) - 1]} \right),$$

$$U = \frac{3}{2} \frac{kT}{\rho} \sum_i n_i + \frac{kT}{2\rho} \sum_m n_m g_m,$$

$$p = kT \sum_i n_i, \quad p_e = kT_e n_e,$$

$$U_e(T_e, \rho), \quad v_{ei}(T_e, \rho), \quad k_e(T_e, \rho), \quad \tau_v(\epsilon_v, T, T_e, \rho), \quad n_e(T_e, \rho), \quad n_j(T_e, \rho), \quad j = i, m, v.$$

Here: t - time, m - Lagrange mass coordinate, $m \leq 0$ - air, $m > 0$ - initial matter, r - radius, ρ - density, u - velocity, U_e - energy of electron oscillated subsystem per gas mass unit, T_e - electron oscillated temperature, U и T - thermal energy and temperature of heavy gas particle subsystem, p и p_e - pressures, F_e и F_r - energy flows of electron conductivity and thermal radiation, k_e - coefficient of electron conductivity, Q_e - energy change velocity between subsystem at elastic collisions of gas particles, Q_v - energy change velocity between subsystem at oscillation relaxation, n_e - concentration of free electrons, n_j - concentration of j -sort particles, v_{ei} - elastic collision frequency of electrons with i -sort particles, M_i и m_e - mass of i -sort particles and mass of electron, g_m - number of rotation rate per one m -sort molecule, n_v - concentration of oscillators at energy of oscillation quanta ϵ_v , τ_v - time of oscillation relaxation, k - Boltzmann constant.

Field of non-equilibrium thermal radiation describes by next equation: $\frac{\partial I_e^\pm}{\partial s} = K_e (I_{ep} - I_e^\pm)$

Here ds - length element along ray, $I_e^\pm(\epsilon, \phi, r, t)$ - radiation intensity for the photons with energy ϵ at positive (+) and negative (-) directions of axis m , ϕ - angle between ray and radius r , $\mu = \cos\phi \geq 0$, $I_{ep}(T_e)$ - equilibrium radiation intensity, $K_e(T_e, \rho)$ - spectrum absorption coefficient.

Flow F_r and flow density q_r of thermal radiation represented through spectral intensity I_e^\pm :

$$q_r^\pm = 2\pi \int_0^\infty d\epsilon \int_0^1 I_e^\pm \mu d\mu, \quad q_r = q_r^+ - q_r^-, \quad F_r = r^2 q_r.$$

Equations describe gas movement and transfer of radiation before shock wave front and behind as well.

If dissociation and ionization processes did not finish in the heated layer before shock wave, these processes can be in the front at heavy particles collisions between each other. We approximately describe these processes according to reactions with participation of molecules and atoms of O and N by the next way: reaction does not begin if temperature T less than $(2/3)E_k$, where E_k - threshold energy of k -sort reaction; reaction begin "immediately" if $T = (2/3)E_k$, at this process the energy of electron oscillation subsystem increases on the value equal energy which spend by heavy particle

subsystem for dissociation and ionization.

The next initial conditions are using:

we give density ρ_c and radius of initially heated gas volume r_c ; at $0 \leq r \leq r_c$ we have $u=0, \rho=\rho_c, T=T_e=T_c$, where T_c – initial temperature according to the energy absorbed this; at $r > r_c$ we have un-perturbated air at density $\rho=\rho_{a0}$, temperature $T=T_e=T_{a0}$ and velocity $u=0$. We use the next boundary conditions:

at $r=0$ we have $u=0, I_e^- = I_e^+$; at $r=\infty$ there are $\rho=\rho_{a0}, T=T_e=T_{a0}, u=0, I_e^+ = I_{ep}(T_{a0})$.

Numerical solution is doing by methods of [9,10]. Simulations have shown the next main points of LIB in air: the focal volume air is quickly ionized if laser intensity exceeds the breakdown threshold; the air plasma (AP) absorbs E_L while laser pulse continues and T rises, T descends slowly after the pulse.

5. BREAKDOWN OF SSP IN AIR

In our paper [12] we considered the main processes of SSP LIB. The first step of laser pulse interaction with SSP is particle heating and evaporation by laser radiation. For a small spherical particle with radius r we obtained the laser intensity required to heat and vaporize this particle. The breakdown threshold laser intensity is given by[12]:

$$I_{bd} \approx \mu \frac{\omega^2 + v_n^2}{\omega^2} \frac{I_a}{mc^2} \left(\frac{40}{\tau_p v_n} + \beta \frac{D}{r^2 v_n} \right), \text{ for C and } \tau_p = 10\text{ns}: I_{bd} \approx 2 \cdot 10^{10} \left(\frac{\lambda_{Nd}}{r} \right)^2 \left[\frac{W}{cm^2} \right] \quad (4)$$

where, $\mu = 10^{18} \text{ W/cm}^2$ and $\beta \geq 1$.

As our particle is located in air, we cannot exceed the breakdown threshold of pure air (see p. 3). We checked this formula by our and another experimental data. The experiment was done using PSL particles, but simulation of the values was calculated using carbon particles and we obtained coexistence between experimental and theoretical results [12].

6. PARTICLE PLASMA ABSORPTION

After LIB we obtain a plasma sphere and now analyze its absorption. We can neglect the ionization energy of SSP to produce plasma particle (PP). At first laser pulse generates the avalanche and then produces fast ionization of the entire SSP volume, so we obtain high density PP. The plasma skin layer length is $l_{sn} \approx c/\omega_p \approx 10^{-5} \text{ cm}$ and for SSP with a diameter of less than l_{sn} , the laser field penetrates PP totally.

In the analytical model of laser pulse interaction with a small sphere of dense plasma, we use the following assumptions:

The initial plasma temperature is taken from our evaporation model [13] where is $T = \text{const}(r)$ inside PP because the time of electron thermal wave propagation is small compared to another characteristic time scale; the Debye radius is small compared to other characteristic lengths; initial density is determined from the vapor of our model, and the density inside PP is homogeneous during laser heating and expansion.

During laser breakdown (and after if the duration of the laser pulse is longer than the breakdown time), the electron concentration in the particle vapor rises rapidly and at some point in time the plasma frequency can reach and even exceed the laser frequency at some distance from the particle center (at $\omega_{pe} = \omega, n_e = n_c$). In this case we should use a local absorption coefficient of the form:

$$K_p = k \frac{v}{\omega} \frac{\eta}{\left(\frac{\eta-3}{3} \right)^2 + \left(\frac{v}{\omega} \right)^2} \quad (5)$$

where, $v = \max\{v_{ei}, v_{en}\}$; $v_{ei} = \sqrt{2\pi} Z^2 e^4 n_i / (m_e^{1/2} T_e^{3/2})$, $v_{en} \approx \sqrt{2\pi} Z^2 e^4 n_n / (m_e^{1/2} I_a^{3/2})$ are electron-ion and electron-atom collision frequencies and $\eta = n_e / n_c$.

From our expression for absorption coefficient, at $n_e / n_c = 3$ there is a resonant point and the absorption coefficient increases greatly at $v/\omega < 1$. The maximum absorption coefficient is given by $3 kr / (v/\omega)$.

We consider absorption of laser intensity I_L by a small plasma sphere with volume V from the next set

of equations:

$$T_e N_e \frac{3}{r} \frac{\partial r}{\partial t} = -\frac{3}{2} N_e k_B \frac{\partial T_e}{\partial t} + V K_p I_L; \quad V = \frac{4}{3} \pi r^3$$

$$\frac{\partial^2 r}{\partial t^2} = \frac{3P_e}{n_i m_i} \frac{1}{r} = \frac{3ZT_e}{m_i r}; \quad n_e = Zn_i = Z \frac{N_i}{V} = Zn_{i0} \left(\frac{r_0}{r}\right)^3; \quad Z \approx \frac{2}{3} (AT_e)^{1/3}$$

If we will calculate this system very roughly, suppose $r \approx r_0 + c_s t$, sound velocity $c_s = (3ZT_e/m_i)^{1/2}$ and $v \approx 0.4 \cdot 10^{-4} Z n_e T_e^{3/2}$ we obtain for temperature next expression:

$$T_e \approx 0.3 \frac{1}{N_e r_0} \left(\frac{r}{r_0}\right)^3 K_p r_0 I_L(t) \pi r_0^2 t \quad (6)$$

Where is maximum of temperature at $\eta = 3$, because where is max of absorption coefficient. It will be at the moment when $n_e/n_c = 3$:

$$t_r \approx \frac{r_0}{c_{s0}} \left[\left(\frac{Zn_{i0}}{3n_c}\right)^{1/3} - 1 \right]$$

Next we estimate the particle lifetime t_{pl} . We suppose that t_{pl} is the time taken for PP density to decrease to air density. If we take into account c_s dependence from T_e , we obtain: $t_{pl} \approx 0.25 (n_0/n_{air})^{2/3} (r_0/c_{s0})$. As an example, if $r_0 \approx 10^{-5} \text{ cm}^3$, $n_0 = 10^{23} \text{ cm}^{-3}$, $n_{air} = 10^{19} \text{ cm}^{-3}$ and $T_e \approx 10 \text{ eV}$ we obtain $t_{pl} \approx 1 \text{ ns}$. So laser pulse τ_p should be close to this time for optimal interaction, but a shorter pulse duration is preferable because for large classical absorption of the laser pulse by PP we should have: absorption coefficient $A \approx 10 (v_{ei}/\omega) (c_s t_{pl}) \approx 1$, and from this condition and our parameters the optimal $\tau_p \approx 0.1 \text{ ns}$.

7. PLASMA EMISSION

As seen from the above, there are two possible variants of SSP size detection by its PP radiation after LIB:

In the first case at $r_0 < \lambda$, $\tau_p < 10 \text{ ns}$, $\lambda = 1 \text{ mkm}$ and $I > 10^{11} \text{ W/cm}^2$ the entire focal volume of the gas and particle breaks down and we must consider radiation from this complex area. From the large initial SSP density, its radiation will be more than air radiation initially, but due to the huge volume difference the Bremsstrahlung radiation of air will increase very fast after the radius of PP has doubled. In this case, we should analyze the line emission of elements other than those of air.

In the second case at $r_0 < \lambda$, $\tau_p < 10 \text{ ns}$, and $I \approx 10^{11} \text{ W/cm}^2$ we can take laser radiation with $\lambda \leq 0.5 \text{ mkm}$ and air pressure of less than atmospheric pressure because the damage threshold of air increases at λ and air pressure decrease as well, thus helping to prevent the breakdown of air instead of SSP. This case was considered in [13]. We therefore focus on the first case and will consider the late stage of the process when emission from SSP plasma exceeds air plasma emission.

To calculate plasma emission of SSP and air we are using the code which was described in paragraph 4. Additionally we include the processes of vaporization of SSP and absorption of laser radiation.

Vaporization wave we describe by next set of equations:

$$\rho_c \cdot u_c = \rho_w \cdot (u_c + u_w) = D_w, \quad q_w = D_w \cdot \left(Q_v + H_w + \frac{(u_c + u_w)^2}{2} \right),$$

$$p_w = p_v(T_w), \quad \frac{dm_w}{dt} = r_w \cdot D_w, \quad \frac{dr_c}{dt} = -u_c, \quad r_c = r_w,$$

where Q_v - vaporization energy, p_v - vapour pressure, q_w - intensity at vaporization wave, u_c -

velocity of vaporization wave, ρ_c - solid density, u_w , ρ_w , T_w , p_w , H_w - parameters after, D_w - расход массы паров через волну, m_w - vapour mass, r_w - coordinate of wave, r_c - SSP radius, $u_w < 0$.

These equations at a wave of vaporization are the boundary (at $m=m_w$) for the set of gas dynamic equations (see p.4). Its describe self consistent propagation of vaporization wave and gas. For Juge conditions $u_c + u_w = c_w$, where c_w - sound velocity behind vaporization wave.

Transport of laser radiation outside and inside focal volume we describe by the next equations:

$$\frac{\partial F_L^\mp}{\partial r} = \pm k_L \cdot F_L^\mp, \quad F_L^\mp = r^2 \cdot q_L^\mp \quad \text{at } r \geq r_f - \text{radius of focal spot.}$$

$$\frac{\partial q_L^\mp}{\partial r} = \pm k_L \cdot q_L^\mp \quad \text{at } r < r_f.$$

Here r - radius, F_L^\mp и q_L^\mp - flow and intensity of laser radiation in negative (-) and positive (+) direction of axis r , $k_L(\rho, T_e)$ - absorption coefficient, ρ - density, T_e - electron temperature. On critical point ($\hbar \omega_p = \epsilon_L$, ω_p - electron plasma frequency, ϵ_L - laser quanta energy) $q_L^+ = c_L \cdot q_L^-$, where c_L - reflection coefficient.

Boundary condition: $F_L^- = r_f^2 \cdot q_{Lf}$ at $r = +\infty$, $q_{Lf}(t)$ - laser intensity in focus without absorption, t - time.

Simulations have shown the following points regarding LIB SSP in air:

Evaporation through laser irradiation starts from the surface of SSP and the volume increases.

The evaporated material is quickly ionized if laser intensity exceeds the breakdown threshold.

The PP absorbs E_L while the laser pulse continues and T rises; T then descends slowly after the pulse.

Absorption is decided first by absorption of the solid and at that moment the gas is transparent. The PP size is close to that of SSP, and has resonance. There is sufficient growth in absorption if T_e is high enough.

Figure 4 shows the dependence of rate $K_r = E_r / E_a$ on initial particle size r_0 , where E_r is total energy emitted in the line spectral range and integrated in space at the moment $t = 100$ ns divided by laser absorbed energy E_a . This dependence is approximately linear and allows us to determine the particle size from the plasma emission after LIB.

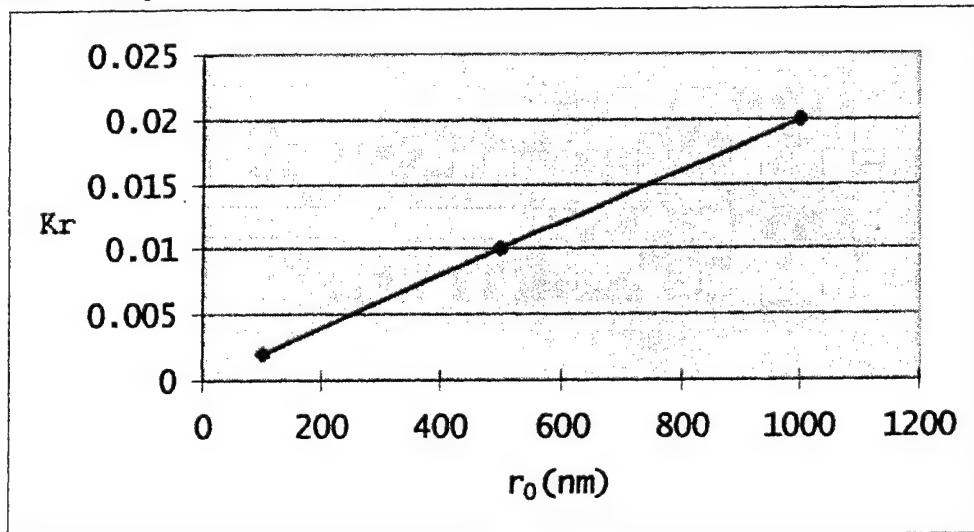
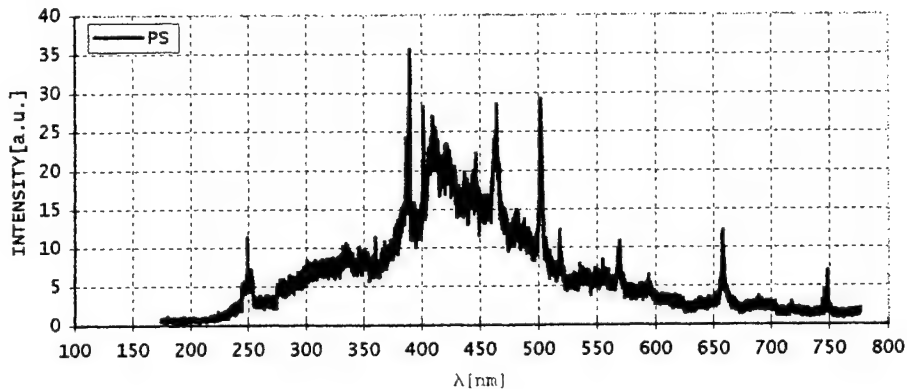


Fig. 4 Dependence of $K_r = E_r / E_a$ on initial particle size

The experimental spectrum of plasma emission integrated in time have show on Fig. 5



6. CONCLUSION

A basic experiment on particle measurement was performed with a standard particle of polystyrene latex. Operation of the system was confirmed by using part of the standard particle generator and a measurement device. We experimented with the breakdown of 55 nm and 100 nm particles of polystyrene latex using this system. From the obtained dependence of LIB threshold on particle size, it is clear that particle sizes of less than 1 mkm can be measured by a conventional laser pulse.

We developed the simulation code to calculate laser pulse interaction with small solid particle in gas atmosphere. The temporal dynamics of plasma parameters showed a large rise of electron temperature and emitted light up to hard ultraviolet photon energy at the moment of resonant conditions, even for small laser intensity. At the moment surrounded particle air is ionized by particle plasma radiation and absorbs laser light very much. After this moment the total light emission from air exceeds an emission from plasma particle from a big air radiated volume, but the line emission from particle plasma permits to detect target material on the late stage of the process.

The increased dependence of SSP plasma line emission rate on initial particle size permits this method to be used for measuring particle size for particle diameters of less than 0.1 mkm.

We have shown that jet propulsion of SSP from laser vaporization permits to clean atmosphere from a dust.

Developed model can be used for investigation of cluster monochromatic radiation.

ACKNOWLEDGEMENTS

This work was supported by the R&D Institute for Photonics Engineering, the Manufacturing Science and Technology Center, and the New Energy and Industrial Technology Development Organization.

REFERENCES

1. Yu. P. Raizer, *Laser-induced discharge phenomena: "Studies in Soviet Science,"* NY, 1977.
2. T. Kitamori, K. Yokose, K. Suzuki, T. Sawada, *Jpn. J. Applied Physics*, **27**, No. 6, pp. L983-L985, 1988, S.I. Anisimov, *Sov. Phys. – JETP*, **27**, p. 182, 1968.
3. G.H. Canavan and P.E. Nielsen, *Appl. Phys. Lett.*, **22**, p. 40, 1973.
4. D.C. Smith, *Journal of Applied Physics*, **48**, No. 6, p. 2217, 1977.
5. H. Hayashi, T. Ueda, *SICE '99*, p. 645, July 1999.
6. T. Ueda, H. Hayashi, A.A. Andreev, M. Wakamatsu, H. Kudou, T. Sugiyama, *The 4rd Symposium on Advanced Photon Processing and Measurement Technologies*, p.142, 2000.
7. Cheleck ?H. Takahara, et al. *IEEE I&M*, **44**, No. 3, p. 819, 1995
8. Ya.B. Zel'dovich and Yu.Raizer *Physics of Shock Waves and High Temperature Phenomena*, M. 1966.

9. A.A. Andreev, A.N. Semakin and V.V. Akulinichev, *Probl. Nauchn. Priborostr.* **3**, 884 1993.
10. A.A. Samarskii and V.G. Popov "Numerical schemes of gas dynamics", M., 1975
11. A.P. Golub, *Journal Calculation Math. And Math. Phys.*, v.23., p.142-151, 1983.
12. T. Ueda, H. Hayashi, A.A. Andreev, M. Wakamatsu, H. Kudou, T. Sugiyama, *The 3rd Symposium on Advanced Photon Processing and Measurement Technologies*, p.142, 1999.
13. A. Andreev, T. Ueda, M. Wakamatsu, "Investigation of Laser Plasma Radiation from Small Solid Particle in Gas Atmosphere" *International Conference "Photonics West"*, San Jose, January 2000.

Application of femtosecond lasers for the frequency synthesis in radio-optical ranges and for the creation of an optical clock

S.N. Bagayev, S.V. Chepurov, V.M. Klementyev, D.B. Kolker, S.A. Kuznetsov, Yu.A. Matyugin,
V.S. Pivtsov, V.F. Zakharyash

Institute of Laser Physics, Siberian Branch, Russian Academy of Sciences,
Pr. Lavrentyev 13/3, 630090 Novosibirsk, Russia,
E-mail: clock@laser.nsc.ru

ABSTRACT

The spectral characteristics and stability of a frequency of intermode beats of a femtosecond Ti:S laser are investigated. An active method is used to obtain high stability. The frequency stability of intermode beats not lower than $5.8 \cdot 10^{-14}$ rms in 100s is achieved. Possible applications of the setup, such as measurement of large frequency intervals in the optical range, creation of optical frequency synthesizers, etc. are proposed. The physical principles for the creation of an optical clock of a new type using highly stable femtosecond Ti:S laser are considered.

PACS: 42.62.Eh; 07.60.Ly; 06.30.Ft

Keywords: Laser stabilization; Mode-locked laser; Optical synthesizer; Optical frequency clock

1. INTRODUCTION

Recently there appeared new applications of ultrashort light pulses in addition to the traditional ones (i.e., ultrafast spectroscopy, ultrastrong optical fields). These applications are based on the operational characteristics of mode-locked lasers, such as the wide radiation spectrum of equidistant modes and the regular sequence of short high-power light pulses in output radiation^{1,2}. Lasers of this type can be used to construct optical standards of frequency, length and time, in the Fourier spectroscopy, high-precision measurements of large frequency intervals in the optical range, etc. In all cases the parameters of light pulses, especially their repetition frequency, i.e., the frequency of intermode beats, must be highly stable.

The present paper is the experimental investigation of the stability and spectrum of the frequency of intermode beats of a femtosecond Ti:S laser and their improvement by an active method. In this method, the frequency of intermode beats of the laser is phase-locked to the frequency of a highly stable radio frequency oscillator. We tested this method using a He-Ne laser in 1992, and it turned out to be highly efficient³.

2. EXPERIMENTAL SETUP

A schematic diagram of the experimental setup is shown in Fig.1. An argon-ion pump laser operated on all lines in the visible region of the spectrum. It is characterized by radiation power pulsations of $\sim 0.5\%$. The cavity of a Ti:S laser had a Z-shaped configuration with arms of unequal length. The curvature radius of the spherical mirrors was 125 mm. The Ti:S rod was 12.5 mm long. A mirror of the Ti:S laser was mounted on the piezoelectric transducer to stabilize the frequency of intermode beats. The sensitivity of this transducer was $\sim 1 \text{ Hz/V}$ at the frequency ν_1 of beats between the adjacent modes. The stable generation of femtosecond pulses was achieved without an intracavity aperture. It was obtained by the gain modulation resulting from a change in the overlap of the laser output with the pump radiation beams (soft aperture). The output power of the Ti:S laser ($\lambda \sim 800 \text{ nm}$) operating in the self-mode-locked regime was $\sim 300 \text{ mW}$ at a pump power of 7 W. The cavity components were placed on a massive cast-iron plate.

The radiation spectrum was recorded by an optical multichannel analyzer, the pulse duration was determined by an intensity autocorrelator, and the power was measured by a power meter. Photodiodes (PD1, PD2) were used as receivers of the signal of intermode beats. A radio-frequency synthesizer (RS2) served as a reference oscillator of a phase offset lock

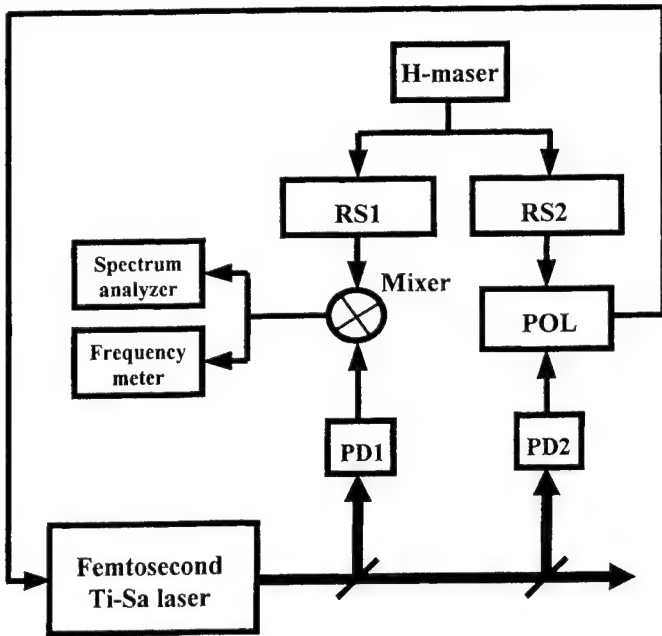


Fig. 1. Schematic diagram of the experimental setup. H-maser, hydrogen frequency standard; RS1, RS2, radio-frequency synthesizers; POL, phase offset lock; PD1, PD2, photodiodes.

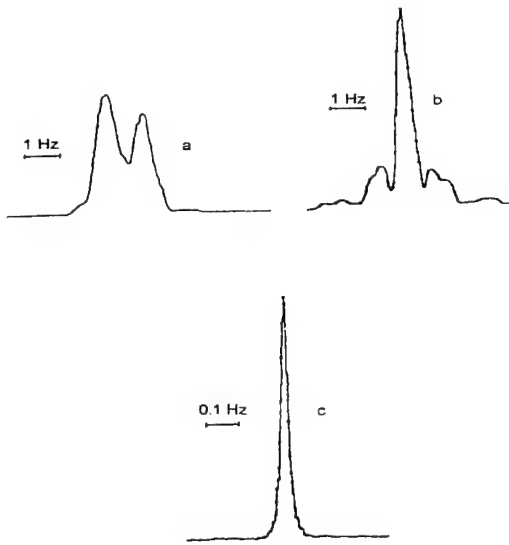


Fig. 2. Spectra of the beats frequency ν_1 between the adjacent modes obtained without (a, b) and with phase locking of ν_1 to the frequency of an external highly stable oscillator (c). The scale is linear.

system (POL). The error signal produced by POL was transferred to the piezotransducer to stabilize the beats frequency of adjacent modes. The difference between intermode beats frequency and the RS1 frequency obtained from the output of a mixer was recorded by a spectrum analyzer. The reference frequency was transferred to the synthesizers RS1 and RS2 from a hydrogen frequency standard (H-maser). In accordance with our measurements, this guarantees the frequency stability of the synthesizers not lower than $1 \cdot 10^{-13}$ in 50 s and the spectrum width not more than 0.02 Hz. Therefore, up to the described limits, the stability and the spectrum width of the frequency ν_1 can be measured using similar characteristics of the difference frequency. The frequency ν_1 was matched to 99 ± 0.001 MHz by changing the cavity length. Then the frequency of RS2, i.e., the reference frequency for POL, was tuned precisely to the phase-locking interval of ν_1 .

3. RESULTS

Fig. 2a,b shows two typical spectra of the beats frequency between the adjacent modes obtained without the phase locking to the frequency of an external highly stable oscillator. The spectrum was characterized by fast time changes, within several hertz, and slow frequency drift. The radiation spectrum width was ~ 10 nm, and the pulse duration did not exceed 120 fs.

Under the phase locking of the beats frequency to the frequency of synthesizer RF2, the spectrum became stabilized over time and frequency (Fig. 2c). The spectrum with a full width at half maximum was 0.02 Hz for the averaging time of 100 s. It was limited by the resolution of a spectrum analyzer.

The frequency of the signal from the mixer was measured by a frequency meter (Fig. 1) to determine the frequency stability of intermode beats. For the averaging time of 10 s and 100 s the relative frequency stability of intermode beats was $\approx 2.3 \cdot 10^{-12}$ and $5.8 \cdot 10^{-14}$ respectively.

4. MEASUREMENT OF FREQUENCY INTERVAL IN ANY OPTICAL DOMAIN

A laser with such characteristics can be used for high-precision measurements of large frequency intervals. Similar experiments were performed by some groups^{4,5}. Frequency intervals were measured up to approximately 300 THz. The radiation frequencies of the lasers or their harmonics entered the generation domain of a femtosecond Ti:S laser. If this condition is not fulfilled, other schemes should be used. We have developed some schemes for this.

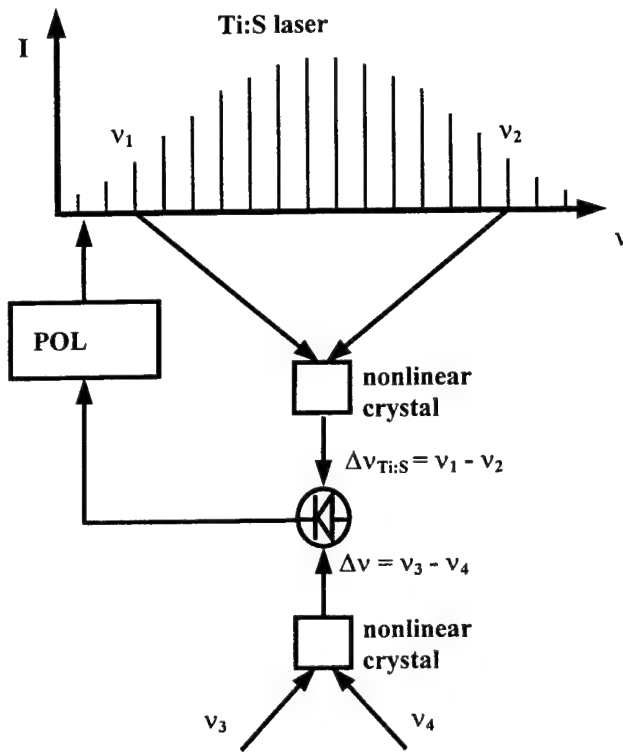


Fig. 3. Scheme of measurement of frequency intervals in any optical domain.
POL, phase offset lock.

Fig. 3 shows a scheme of measurement of frequency intervals in any optical domain. It is necessary to measure the interval between v_1 and v_2 . For this, we obtain a difference frequency $v_1 - v_2$ and $v_3 - v_4$ in a nonlinear crystal, perform the phase locking of $v_{Ti:S}$ to Δv , and measure the frequency of intermode beats. Nonlinear crystals are used to obtain an optical radiation at difference frequencies $v_1 - v_2$ and $v_3 - v_4$. A radiation frequency $\Delta v_{Ti:S}$ is phase locked to Δv frequency. Measuring the frequency of intermode beats and a number of the intermode intervals in $\Delta v_{Ti:S}$ gap of a Ti:S laser radiation one can calculate $v_3 - v_4$. In another case $\Delta v_{Ti:S}$ is phase locked not to Δv but to the frequency of an external high stable radio oscillator, i.e., the frequency of intermode beats is stabilized. Beats frequency between $\Delta v_{Ti:S}$ and Δv is measured.

5. MEASUREMENT OF ABSOLUTE FREQUENCIES AND CREATION OF A OPTICAL CLOCK

A similar scheme (Fig. 4) can also be used to measure the absolute frequency of the laser up to several THz (a) and higher (b). There is no nonlinear crystal in the scheme (a). A Schottky barrier diode is used as a mixer. An error signal from its output is led to POL. On the basis of this principle one can measure absolute frequencies from radio range up to visible with the help of a femtosecond Ti:S laser.

The scheme (4a) is modified to an optical clock when the frequency of a laser standard is used as a measured and the intermode beats are used as an output signal.

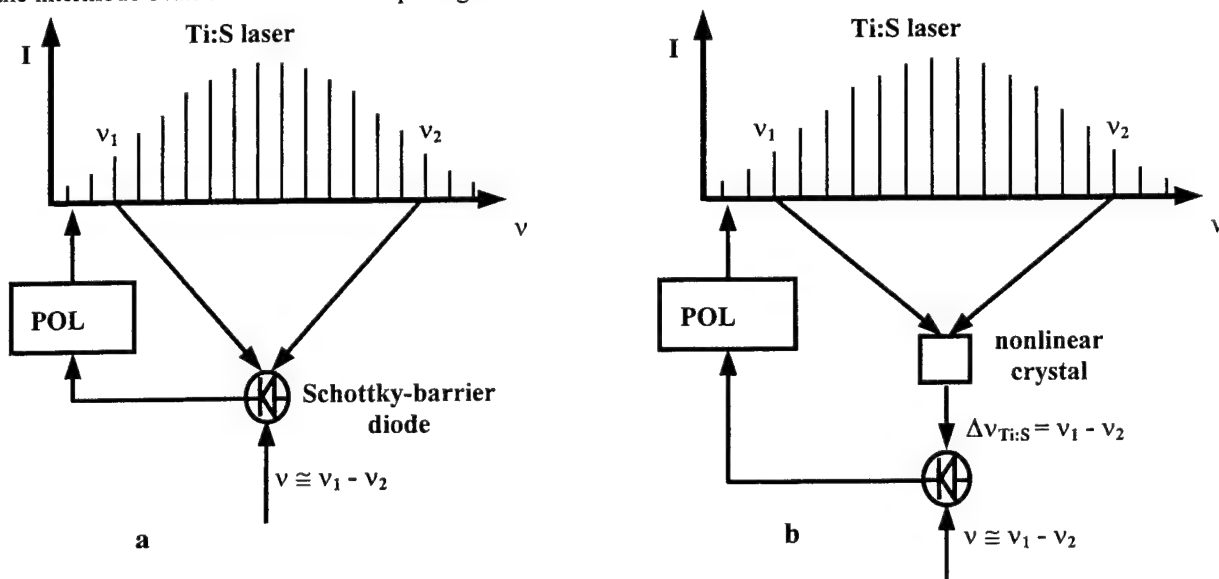


Fig. 4. Scheme of measurement of absolute frequencies of the lasers up to several THz (a) and higher (b).

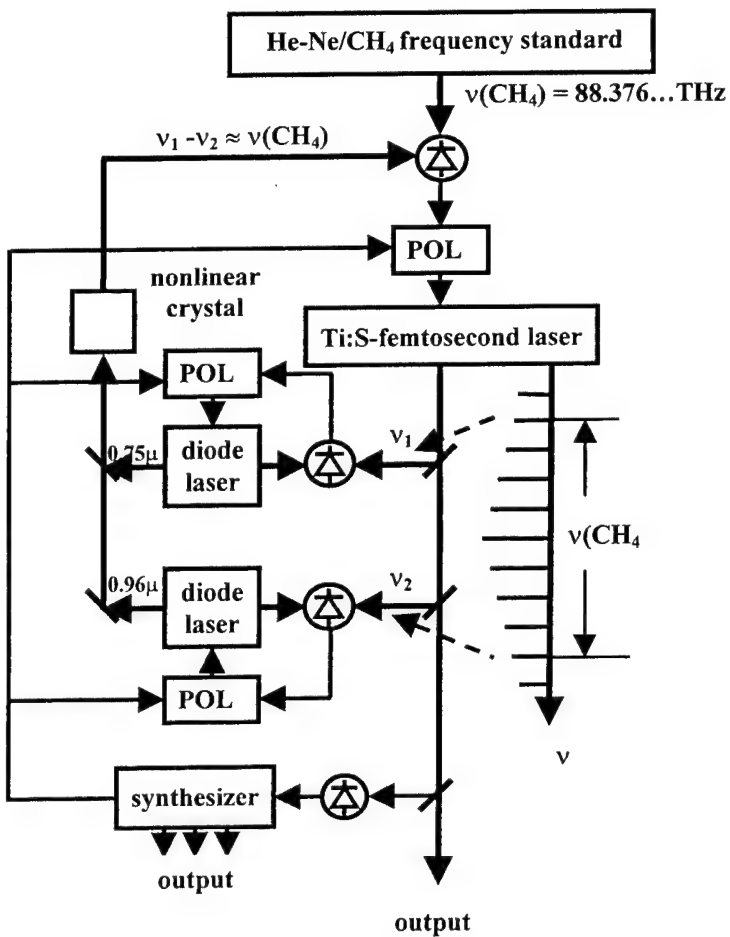


Fig.5. Setup of the femtosecond optical clock

In the Fig. 5 a scheme of an optical clock with the He-Ne/CH₄ laser standard based on the principle described above is presented. Laser diodes are used as power amplifiers of modes of a femtosecond Ti:S laser at the frequencies v_1 and v_2 . The frequency characteristics of the He-Ne/CH₄ standard are transmitted into the radio range without intermediate steps. The scheme is self-contained, i.e., it does not require introduction of reference frequencies from outside. Using beat frequencies of distant and adjacent modes one can obtain a comb of stable radio and optical frequencies, i.e., a radio and optical frequencies synthesizer. If it is necessary, a spectrum width of a Ti:S laser output radiation can be sufficiently broaden with the help of a single mode optical fiber.

6. REFERENCES

1. J.N.Eckstein, A.I.Ferguson, and T.W.Haensch, "High-Resolution Two-Photon Spectroscopy with Picosecond Light Pulses", Phys. Rev. Lett., Vol. 40, pp. 847 – 850, March 1978.
2. S.N.Bagayev, V.P.Chebotayev, V.M.Klementyev, O.I.Pyltsin, "Time Fourier Super-High Resolution Spectroscopy", Proc. of 10th Int. Conf. on Laser Spectroscopy, p.91 – 98, Font-Romeu, France, June 17 – 21, 1991.
3. V.P.Chebotayev, V.M.Klementyev, O.I.Pyltsin, V.F.Zakhariash, "Optical-Pulse Frequency Stabilization of Self-Mode-Locked He-Ne Lasers", Appl. Phys., Vol. B 54, 98 – 99, 1992.
4. S.A.Diddams, D.J.Jones, L.-Sh.Ma, S.T.Cundiff, and J.L.Hall, "Optical Frequency Measurement Across a 104-THz Gap with a Femtosecond Laser Frequency Comb", Opt. Lett., Vol. 25, pp. 186 – 188, Feb. 2000.
5. S.A.Diddams, D.J.Jones, J.Ye, S.T.Cundiff, J.L.Hall, J.K.Ranka, R.S.Windeler, R.Holzwarth, T.Udem, T.W.Haensch, "Direct Link Microwave and Optical Frequencies with a 300 THz Femtosecond Laser Comb", Phys. Rev. Lett., Vol. 84, pp. 5102 – 5105, May 2000.

Doubled Yag laser stabilized on iodine as length/frequency standard at 532 nm

Yves P. Millerioux and Patrick Juncar

Bureau National de Metrologie-INM/CNAM
292 rue Saint Martin 75141 Paris Cedex 03 France

ABSTRACT

We describe our doubled Yag laser stabilized on the hyperfine structure of molecular iodine 127. We present the results in terms of stability and reproducibility and we will give a scheme of the scheduled absolute frequency measurement.

Keywords: Stabilized lasers, iodine spectroscopy, length standard, optical frequency.

1. INTRODUCTION

Nine new lines of molecular iodine transitions have been recommanded by the comite international des poids et mesures in 1997 for the practical realization of the metre near 532 nm.[1]. The hyperfines structures were studied and the frequencies measured [2]. Due to the properties of solid state lasers and strong iodine transitions, doubled Yag lasers stabilized on these transitions are good candidates for length standards in the green.

2. EXPERIMENTAL SET-UP

We have built a simple system of saturated absorption with a 3f demodulation. Our base is a commercial lighwave 140 model laser and we act directly on the piezoelement glued on the crystal to modulate and stabilize the frequency. A power of more than 50 mW is available over the thermal scanning range of the laser. We take a part of this power to send 3.2 mW of pump beam power and 600 μ W of counterpropagating probe beam power in a 50 cm long iodine cell with a cold point at -13°C . We modulate at $f = 5.555$ kHz with a modulation depth of 2 MHz peak to peak.

3. RESULTS

We make comparisons with BIPM A and B lasers. The relative standard deviation in terms of Allan variance is $2.6 \tau^{-1/2}$ until 1000s. For longer integration times we get a plateau or a positive slope due to mechanical and thermal instabilities. The reproducibility is better than 1kHz over days and the difference $V_{INM} - V_{BIPM} = -5.2$ kHz with these parameters and cell. We measure a shift of - 6.5 kHz per MHz of modulation depth and - 680 Hz per degree at -13°C. Improvements can be made by using more stable mechanics and by controling the geometry of the beam inside the iodine cell. The present beam is elliptical and diverging. An anamorphoser and a beam expander will provide a circular and more parallel beam of 3-4 mm in diameter. The use of crossed polarisations for probe and pump beams will increase the S/N ratio.

4. FREQUENCY MEASUREMENT

There is some dispersion in the frequency measurement results [2],[3]. A frequency measurement is scheduled in collaboration with the BNM-LPTF(Laboratoire Primaire du Temps et des Frequences). Their chain is based on two standards: A CO₂/OsO₄ standard accurate at 4 Hz (1.3 10-13) over a period of one year and the two photons in Rb standard accurate at 1 kHz (3 10-12) [4],[5]. The gap of 611 GHz will be filled at 1,06 μ m with a FIR (Far Infrared) laser.

5. CONCLUSION

We have built a simple system which give a good stability of $2.6 \tau^{-1/2}$ and a reproducibility of 1 kHz . Its frequency will be measured at BNM-LPTF laboratory.

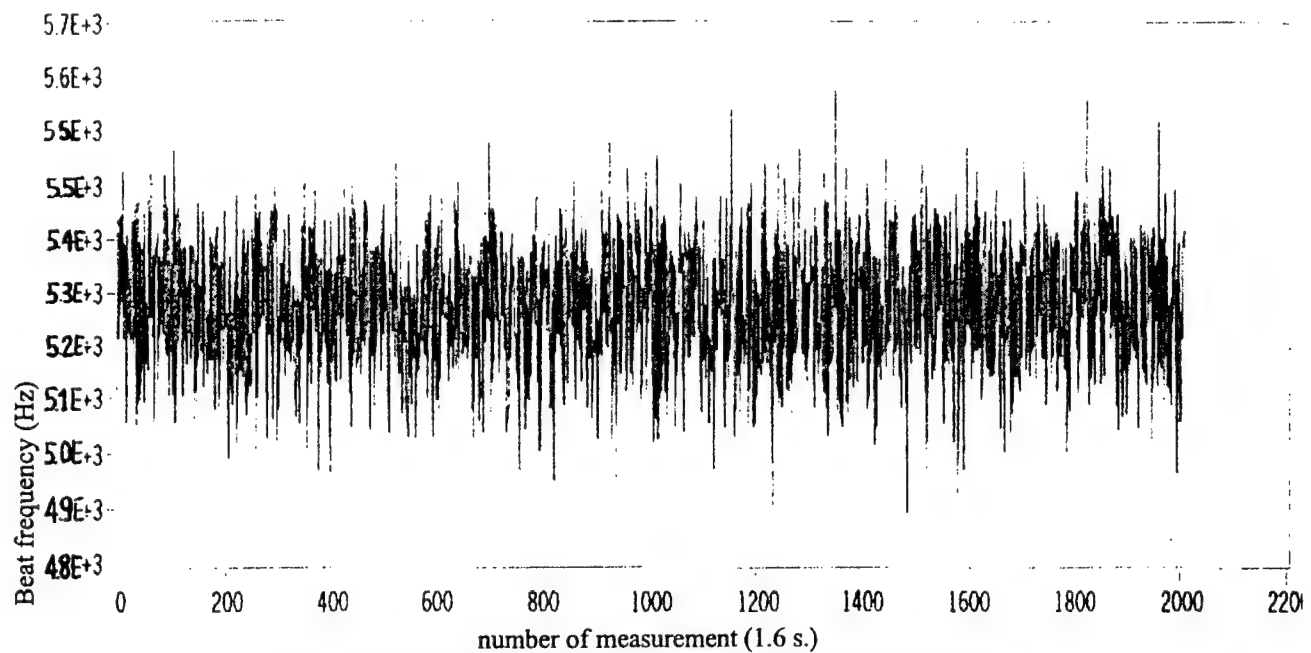


fig. 1 Beat measurements between BNM-INM and BIPM A lasers

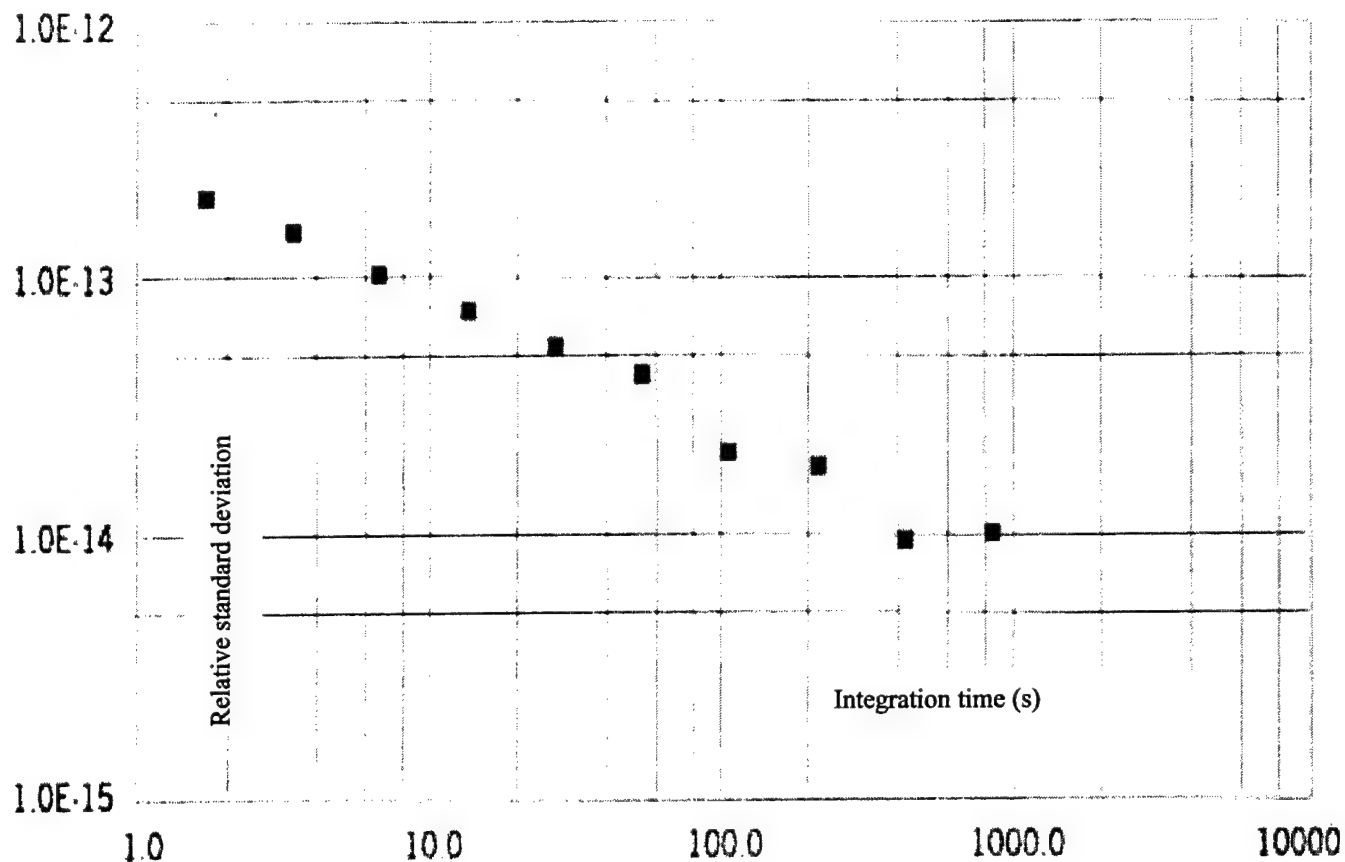


fig.2 Relative standard deviation from Allan variance analysis.

6. ACKNOWLEDGMENTS

The BNM-LPTF frequency chain for this measurement is especially run by F. Ducos, Y. Hadjar, G.D. Rovera and O. Acef. And we thank the BIPM laser team for fruitful collaboration.

7. REFERENCES

1. T.J.Quinn "practical realization of the definition of the metre (1997) " *Metrologia* **36**, pp.211-244, 1999
2. P. Junger, M.L. Eickhoff,S.D. Swarz, Yun Ye, J.L. Hall, S. Waltman "Stability and absolute frequency of molecular iodine transitions near 532 nm" *Laser frequency stabilization and noise reduction*, SPIE, **2378** pp.22-34, 1995
3. S.A. Diddams, D.J. Jones, L.S. Ma, S.T. Cundiff and J.L. Hall "Optical frequency measurement across a 104 THz gap with a femtosecond laser frequency comb" *Optics Letters*, **25**, n°3 pp.186-188, 2000
4. F. Ducos, G.D Rovera , C; Daussy and O. Acef "Performances of Os O₂ stabilized CO₂ lasers as optical frequency standards near 29 THz "in Proceedings of the 1999 Joint Meeting of the European Frequency and Time Forum and the IEEE International Frequency control Symposium Vol 2 pp 714 – 717 , 1999
5. D. Touahri , O Acef , A Clairon , J.J Zondy , R Felder , L Hilico , B de Beauvoir , F Nez and F Biraben , "Frequency measurement of the 5S_{1/2} – 5D_{5/2} two photon transition in rubidium " *Optics Comm.*,vol **133** pp 471 ,1997 .

Large scale laser gravitational interferometer with suspended mirrors for fundamental geodynamics

Valentin N. Rudenko^a, Victor V. Kulagin^a, Sergei L. Pasynok^a and Andrei V. Serdobolskii^a

^aSternberg Astronomical Institute of Moscow State University,
Universitetsky prosp. 13, Moscow, 119899, Russia

ABSTRACT

A Fabry-Perot-Michelson gravitational free mass interferometer is considered for a registration of the low frequency Earth gravity gradients. A variation of the Earth gravity force vector cause the corresponding misalignment of the interferometer mirrors thus providing information about the Earth gravity field. Gravitational interferometer with suspended mirrors provides a unique possibility to measure a relative angle variations between two "plumb lines" (gravity force vectors) separated by the large distance $3 \div 4$ km. So at very low frequencies the set up presents a long based angular gravity gradiometer for registering global geodynamics through the surface gravity gradient. A possibility of measuring the geophysical phenomena resulted in gravity field variations (core movements, Earth free oscillations, tidal harmonics, Earth rotation variations, etc.) is discussed and technical requirements for the set up optical elements are formulated. Comparison with conventional geophysical devices is carried out. Estimates of the basic instrumental and seismic noises limiting the sensitivity at low frequency (in the quasi-static regime) are discussed briefly. These estimates show that there is a hope for measurement of the gravitational angular perturbation of the mirrors at the level of $10^{-12} \div 10^{-13}$ rad for the observation time about several hours. The possibility of arm signals reconstruction in the presence of recycling mirror is demonstrated. The auxilliary optical system for precise justification between up-down movements and tilts of the end spherical mirrors is considered. The requirements on the stability of laser system are discussed.

Keywords: Long base laser gravitational interferometers, geodynamical processes, Earth gravity gradients

1. INTRODUCTION

Large base gravitational laser interferometers having a fundamental purpose of the direct detection of gravitational waves emitted by various astrophysical sources leads to the construction of large scale opto-mechanical set up which accumulates best achievements of modern technology and state of the art in many branches of experimental physics.¹⁻⁴ This extraordinary instrumentation besides its main destiny could serve also the other very important aim providing a unique information concerning the geodynamical processes in the deep Earth interior.^{5,6} In this case the gravitational interferometer appears as a meter of low frequency variations of the gravity gradient on Earth surface. A permanent monitoring of such gravity dynamics with an accuracy sufficient for a controlling the inner core movements could bring a new light to the nature of Earth magnetic dynamo, rotational irregularities and other effects.

Besides the fundamental physical applications the new method of large scale monitoring of the gravity gradients promises to open an additional way for earthquake forecast so as it is believed that namely the surface gravity gradient perturbations could play a role of earthquake precursors.

2. LASER GRAVITATIONAL ANTENNA AS GRAVITY FIELD GRADIOMETER

2.1. Idea of geo-gravity measurements

The gravitational laser interferometric detector as a device is the gravity gradiometer responding the gradient of the gravity field along its arms. The main object of the laser gravitational detector is a registering the gradient induced by gravity waves that come to the Earth from astrophysical sources. A small variations of the distance (arm's length)

Further author information: (Send correspondence to V.N.Rudenko.)

V.N.R.: E-mail: rvn@sai.msu.ru

V.V.K.: E-mail: kul@sai.msu.ru

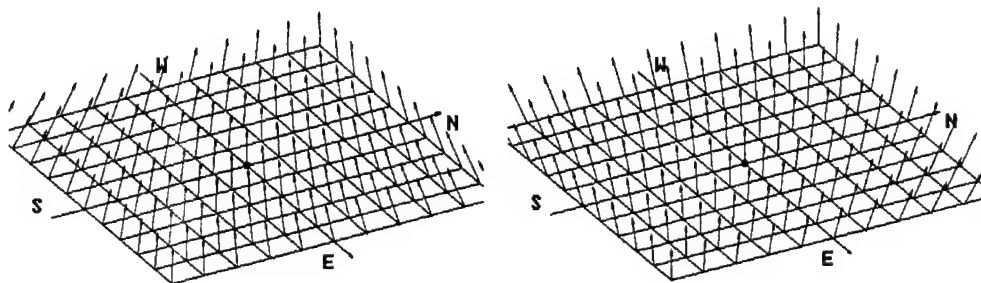


Figure 1. Deformation of the surface and plumb lines for different phases shifted by π .

between test mass-mirrors result in the optical phase shift which finally has to be measured. A frequency range is supposed to be from $10 \div 100 \text{ Hz}$ to $\sim 10^3 \text{ Hz}$, the lower limit depends on the technical ability in providing the device vibration isolation. In the process of operation the interferometer will undergo different perturbations of the geophysical nature so special efforts have to be undertaken to keep interferometer mirrors in the proper positions.

Could the gravitational wave interferometer be used also for measurement of a very low frequency gravity gradient of the Earth field variations? A frequency range in this case a priori can be defined as $f < 0,1 \text{ Hz}$ i.e. this region lies much below the resonant frequency of the mirror's pendulum mode.

An answer to this question can be found only as a result of the proper "signal-noise analysis" of geophysical effects and instrumental characteristics of the device. The idea of "geophysical application" can not be rejected simply on the reason of large noises at low frequencies because effects for measurement (geodynamical variations of surface gravity gradient) also are much greater than the gravitational wave perturbations ($10^{-11} \div 10^{-13}$ instead of $10^{-21} \div 10^{-23}$).

From the instrumental point of view the gravitational interferometer can be considered as a new type of geophysical set up different from conventional geophysical devices. Interferometer with suspended mirrors provides a unique possibility to measure a relative angle variations between two "plumb lines" (gravity force vectors) separated by the large distance $3 \div 4 \text{ km}$. If a source of light is also suspended close to the input mirrors (or beam-splitter) then such interferometer becomes sensitive only to the gravity field perturbations and does not react on variations of the local normal to the surface which suffers from different deformations. Thus at very low frequencies the set up presents a long based angular gravity gradiometer for registering global geodynamics through the surface gravity gradient.

As for the sensitivity one might hope to have a decreased level of "instrumental noises" (including intrinsic and technical sources) with respect to conventional devices because all optical and mechanical parameters of gravitational interferometers are very close to the ultimate technological limit at present.

2.2. Simple gravity field dynamics

Now we describe a simulation of the gravity field time evolution in the very simple model which includes only two geophysical phenomena: the semidiurnal tidal gravity changes and inner core polar oscillations. Our goal is to demonstrate on the qualitative level a picture of the "plumb lines dynamics" in the area considered as a site for free mass gravitational interferometer. Such picture has to give a clear presentation of the "subject for measurement" - relative angular perturbations of the plumb lines separated in space which also undergo deformations.

Let consider only one geodynamical effect - the motion of the inner core at the background of the tides. A gravity amplitude of the "inner core effect" (corresponding to the core oscillation amplitude $r_0 = 1 \text{ m}$) is approximately by 300-400 times smaller than the tidal amplitude. To observe both effects simultaneously in the same simulation run one has to increase the inner core effect artificially. In our simulation we used the amplification factor 100; then the core effect remained to be 3 times smaller the tidal one but it was possible to present both on the same plot (fig. 1). So the geodynamical variations of relative distances and gravity force angles are very complex: there are unisotropic oscillations of surface scales and precession of plumb lines.

2.3. Comparison with conventional geophysical devices

There are four principal classes of measuring instruments in experimental geophysics, they are seismometers, gravimeters, strain and tilt meters. Ideally a seismometer measures noninertial dragings in the Lab (at frequencies much higher than its eigenfrequency); a gravimeter measures vertical variation of gravity force (below eigenfrequency); a strain and tilt meter measure land deformations (longitudinal expansions and inclinations). In general a free mass interferometer on the Earth surface is coupled with all mentioned fields - inertial, gravitational and deformational. However the strongest effect is provided by the gravity. Suspended mirrors follow the gravity force vector ("plumb line") so the free mass interferometer operates as a long based gravity gradiometer measuring mutual angle variations between separated "plumb lines" which is proportional to the variations of the gravity gradient along the Earth surface. So the gravitational interferometer is a large scale gradiometer capable to measure a global geodynamical gravity variations. It is important to remark here that such measurement could not be realized through an expanded net of tiltmeters or gravimeters (these ideas were discussed time by time in the geophysical literature).

A differential signal of two tiltmeters located in separated places could provide an information about relative angle between their "plumb lines" only under supposition of identical behaviour of normals in both places. In reality the larger the distance between two normal vectors to the surface the more different motion they perform. Generally it is impossible to exclude an effect of normal variations from the differential signal if the separation is as large as one kilometer or more.

A differential signal of two gravimeters also suffers from individual geophysical interferences but besides it would provide in the best case a gradient of vertical components of the gravity force; in this case a reconstruction of the relative angle variations between gravity force vectors at the device's places is a very "ill posed" problem.

3. GEOPHYSICAL EFFECTS TO BE MEASURED

3.1. Earth tides

The gravitational interferometer will sense the tide due to a land deformation and plumb line deflection. By the order of value these effects have magnitudes defined by the relative gravity variations, i.e. $\Delta L/L \simeq \delta\alpha \simeq \Delta g/g$. Taking into account the depressing factor $(L/R_e) \simeq 5 \cdot 10^{-4}$ (L - base length, R_e - Earth radius) due to a differential character of the device one can estimate the "tidal angular signal" as $\delta\alpha_t = (\Delta g_t/g)(L/R_e) \simeq 3 \cdot 10^{-11}$ rad for the largest harmonic M_2 .

In the set of tidal harmonics higher frequency components are $M_3(\tau_0 = 8 \text{ hours}; \Delta g = 0.8 \mu\text{Gal})$ and $M_4(\tau_0 = 4 \text{ hours}; \Delta g = 0.03 \mu\text{Gal})$. These forced "luni-solar" oscillations attract special interest because they have periods about $3 \div 10$ hours and for this reason they have to be studied and controlled very carefully. In the case of gravitational interferometric gradiometer an observation of such fine effects would require the sensitivity level better than $\delta\alpha = (2 \div 3) \cdot 10^{-13} \text{ rad}$ for the 10^5 sec of measurement time.

3.2. Earth free oscillations

An experimental knowledge of the Earth free (eigen) oscillations spectrum plays a principal role for creating an adequate model of the Earth interior. Thus the experimental measurement of high frequency Earth harmonics is very interesting for a more precise definition of the Earth interior structure.

Observations of the free Earth oscillations are available after large earthquakes which serve as sources of excitation. The high frequency harmonics registered after large earthquakes had the order of magnitudes about $\Delta g \sim 0.1 \mu\text{Gal}$ that for gravitational interferometer could be recalculated as $\delta\alpha = 5 \cdot 10^{-14} \text{ rad}$.

3.3. Earth core oscillations

There are so called "core oscillations" in the region of periods exceeding the period of fundamental mode ${}_0S_2 \simeq 57 \text{ min}$. Their specifics is a concentration of most part of displacements in the central zone of the globe with relatively small amplitudes on the surface. According to modern notions the group of core movements has to exist with characteristic times between 100 min and 10 h which can not be explained as ordinary elastic oscillations; an essential role belongs to the gravitation. One of them is the polar mode (or Slichter mode) in which the inner ("hard") core (the central region with radius $r \simeq 1200 \text{ km}$) oscillates along the Earth rotation axis in the outer ("liquid") core. For the gravitational interferometer with $L = 3 \text{ km}$ and oscillating amplitude $r_0 = 1 \text{ m}$ an expected value of the effect is $\delta\alpha \simeq 4 \cdot 10^{-14} \text{ rad}$. The other possible modes are quadrupole oscillations of the inner core and

angular oscillations of the inner core axis with respect to the Earth rotation axis. By the order of value both could produce in the best case the same angular effect $\delta\alpha \simeq 5 \cdot 10^{-14}$ rad. All this estimates are approximate because of the unknown magnitude of the initial excitation and badly defined core's characteristics.

3.4. Earth rotation variations

There are three type of variations of Earth rotation parameters which are the subjects of research. These are a nutation (precession), polar motion of the rotation axis and also spin-rate variation. For gravitational interferometer as a two coordinate gravity gradiometer the more attractive goal would be a searching for correlation between the Earth's core oscillations and spin rate changes. A search for the "gravity-rotation coupling" effect looks reasonable starting from the level $\delta\alpha \leq 10^{-13}$ rad.

3.5. Summary of geophysical effects

The presented brief analysis of geophysical phenomena resulted in gravity field variations gives us only rough presentation (the order of value) of the effects which could be subjects of measurement for gravitational interferometer at very low frequencies. It is difficult to calculate their values more precisely due to an uncertainty in models, initial conditions, etc. Nevertheless these estimations permit to formulate majorant requirements for sensitivity of the gravitational detector as angular gradiometer at the Earth's surface. In the frequency range $10^{-4} \div 10^{-5}$ Hz one could admit the noise with spectral density 10^{-12} rad/Hz $^{1/2}$; then the effect on the level of 10^{-14} rad can be registered for $\tau = 10^4$ sec.

4. GRAVITATIONAL NEWTONIAN NOISES

In this section we estimate roughly mirror's angular perturbations associated with gravitational noises of technogenic and natural origin. In that number first of all are the so called "newtonian fluctuations" i.e. stochastic variations of the gravitational acceleration produced by local mass dynamics, which can be associated with human activity or some geophysical processes. Then it is "geometrical noises" caused by plumb line vector variations depending on changes of suspension point position due to tidal, temperature or tectonic deformations of interferometer arms and some other noises.

4.1. Movements of local bodies

A first trivial reason of the test mass-mirror's perturbations is a direct gravitational attraction generated by movements of local bodies in the close environment. It is easy to estimate an angle deflection of the mirror produced by some mass m at the distance r from mirror's tower. In the typical situation $m \simeq 10^3$ kg that corresponds to the mean car mass. Having in mind the value of measurable geophysical effects $\Delta\alpha \simeq 10^{-13}$ rad one finds a critical distance for car approaching as $r \leq 100$ m. If a car comes more closely it can be controlled (a duty car monitoring) and excluded.

4.2. Natural newtonian fluctuations

4.2.1. Seismic surface waves

The model of seismic surface waves supposes that the gravitational acceleration on the Earth surface is produced by the seismic stochastic field under the surface. The stationary gravity field surface gradient is perturbed by seismic density variations. A correspondent varying component of the gravity gradient is proportional to the amplitude of seismic spectrum but depressed by the factor of ratio of the arm's length and Rayleigh wave length. Then the angular noise standard is expected to be at the level $\langle |\Delta\alpha|^2 \rangle^{1/2} \simeq [5 \cdot 10^{-15}/f] \text{ Hz}^{-1/2}$. At the frequency of our special interest $f = 10^{-4}$ Hz ($\tau_0 = 3$ hours) one could collect the noise level $\langle \Delta\alpha \rangle \simeq 10^{-11} \text{ Hz}^{-1/2}$ which allows a registration of the effect at order of $5 \cdot 10^{-14}$ rad for a measurement time equal to 10 characteristic periods of inner core oscillations.

4.2.2. Atmospheric fluctuations

A next source of the "newtonian noises" are dynamical atmospheric processes. A stochastic density variations and transportation of large air masses gives some contribution into the gravity force at the Earth surface. Almost all such kind of processes are coupled with correspondent pressure changes and so could be controlled through the pressure monitoring. It is well known from the theory of gravimetry that effects of atmospheric pressure upon the gravity consist of direct attraction of atmospheric mass and crustal deformation due to atmospheric loading. The both effects have the same order of value but the loading effect as a rule is less then direct attraction by two-five times. The expected angular noise for atmospheric fluctuations is $\langle \delta\alpha \rangle \simeq 5 \cdot 10^{-13} \sqrt{\Delta f}$ rad. This estimation looks satisfactory: for the time 10^4 sec - three periods of the polar oscillations of the inner core - a detectable angular signal would achieve $5 \cdot 10^{-15}$ rad. A correction for the "gravity atmospheric noise" can be introduced if one controls precisely pressure variations at the place of the "front" and "end" mirrors of gravitational interferometer.

4.2.3. Ground water variations

The next serious source of newtonian noise is variations of ground water level around the experimental site. It is difficult to describe this phenomenon in details: a distribution and flow pattern of ground waters is complex and its level affected by precipitation and local geology. Nevertheless some rough general evaluation can be done in the frame of a simplified model in which a homogeneous medium with porosity p filled up by the water with density ρ is located under the Earth surface. Then the following numerical evaluation (for $p=0.3$) of the ground water effect is valid $\delta\alpha h \leq 2.5 \cdot 10^{-14}$ rad, h is the variations (in meters) of the water level. Moreover a spectral density of the "water effect" is concentrated mainly at very low frequencies: typical times are months. As it was demonstrated by measurements the maximum of spectrum lies in the range $10^{-7} \div 10^{-6}$ Hz. For the region of our interest $10^{-4} \div 10^{-5}$ Hz a spectrum amplitude falls down at least by two orders of value; so the number above is the majorant value. At last a correction for the "gravity ground water effect" can be introduced if a permanent monitoring of the ground water level through a system of wells covering the interferometer site will be foreseen.

4.2.4. Slow gravity drifts

There are several geophysical phenomena that result in slow variations (drifts) of the gravity acceleration on the Earth surface. Between them are the tectonic plate motion, mantle convection, Earth rotation irregularities, glacial rebound and some others. We do not need to make a detail analysis of them having in mind relatively high frequency processes of our interest with typical times 1 – 10 hours. Nevertheless it is usefull to present here rough majorant estimations of the mentioned effects because some of them could be also "a subject of investigation" during of a long operational time of the gravitational interferometer. A standard deviation of the plumb line is evaluated for these phenomena as $\Delta\alpha \leq 3.4 \cdot 10^{-13}$ rad and looks as acceptable value having in mind the majorant character of our estimations.

4.3. Geometrical position noise

Due to the curvature of the Earth a plumb line direction is a function of the suspension point position. It means that any change of the interferometer arm length must be accompanied by variation of relative angle between filaments of the "front" and "end" mirrors. These variations can have nothing common with interior Earth dynamics but reflects only some surface geometry. Arm's deformations contain both a regular (tides) and stochastic component produced by complex of geophysical and climatic phenomena so that the correspondent relative plumb line deflections could be much larger than the measurable effects of our interest. We will use the term a "geometrical noise" for these angular perturbations. For example tidal deformations having the amplitude $\Delta L/L \simeq 10^{-8}$ result in the geometrical angular noise amplitude $\delta\alpha_{gm} = \Delta L/R_e = (L/R_e)(\Delta L/L) = 5 \cdot 10^{-4} \cdot 10^{-8} = 5 \cdot 10^{-12}$ rad that is two orders of value larger than the inner core oscillations effect. Temperature land expansion in turn could exceed the tides by two orders of value etc.

Certainly it is useful to appeal to the frequency discrimination for to overcome this kind of noise. But a more effective method exists: if the arm length variation ΔL is known with high enough accuracy then the geometrical plumb line deflections can be easily calculated and subtracted from a total data of angle measurements. Let α_0 be an observed angle variation through a direct angle measurement and ΔL is the measured independently arm's change, then a corrected value of the measured angle effect $\alpha_c = \alpha_0 - (L/R_e)(\Delta L/L)$ will have an accuracy at least $\delta\alpha = (L/R_e)(\Delta L_m/L)$. For $\Delta L_m = 1\mu m$ the error of correction will be $\delta\alpha \simeq 2 \cdot 10^{-13}$ rad. It is the level of effects of our interest and some improvement of the length measurement accuracy is desirable at least by one order of value.

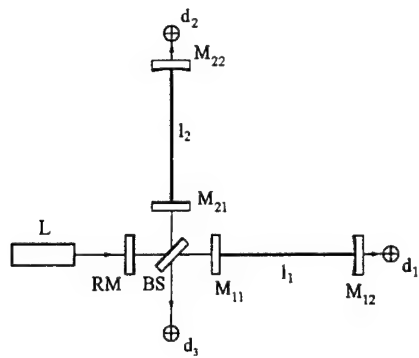


Figure 2. The principal scheme of gravitational interferometer.

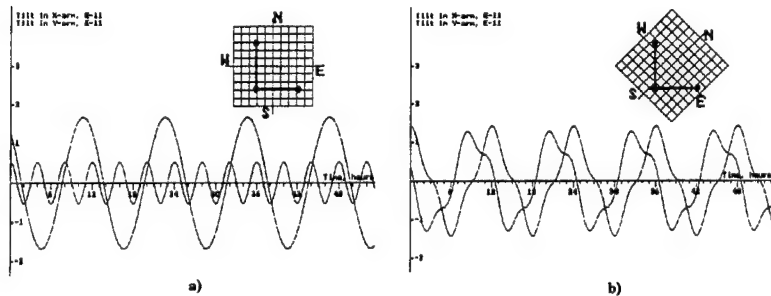


Figure 3. Core movement (arm SN) and tide (arm WE) for "meridian-parallel" (a) and "45°" (b) orientations.

4.4. Summary of newtonian noises

One can conclude that prior estimations of the newtonian stochastic background do not forbid a measurement of relative angular deflections of the suspended gravitational interferometer mirrors at the level of 10^{-13} rad during of few hours measurement time. It looks satisfactory for the main purpose of "geophysical applications" of the gravitational interferometer - a registration of the Earth core oscillations.

5. GRAVITATIONAL INTERFEROMETER IN THE EARTH GRAVITY FIELD

The principal scheme of gravitational interferometer is presented at fig. 2. For free mass interferometer it was supposed that a filament of suspended mirror must be directed along the gravity vector and its deflection produces a correspondent inclination of the mirror's surface, i.e. the mirror tilts together with the filament. A reciprocal tilt of arm's mirrors has to depend on the interferometer orientation with respect to the "gravity field map". In general some mixture of the tidal and core harmonics is typical for each arm but it degenerates to the picture of complete separation of harmonics between two arms when the interferometer arms stretch along the meridians and parallels (fig. 3a, 3b).

Practically there is no difference between tilts in the close group of elements: laser (mode cleaner), beam-splitter, front (input) mirrors (more exactly: such differences have a higher order of value and can be neglected). With respect to this group only the far "end mirror" in each interferometer arm has considerable angular deflection.

A registration of the end mirror deflections can be performed through the circuits of the interferometer alignment system that react to perturbations of optical field in the arm's cavities caused by deviations of Fabry-Perot resonator cavity axis from the optical beam. A tilt $\delta\alpha$ of the end spherical mirror is perceived by this system as a lateral shift of the resonator axis $R\delta\alpha$ (R is the mirror's curvature radius) and appears in the output voltage of the phase

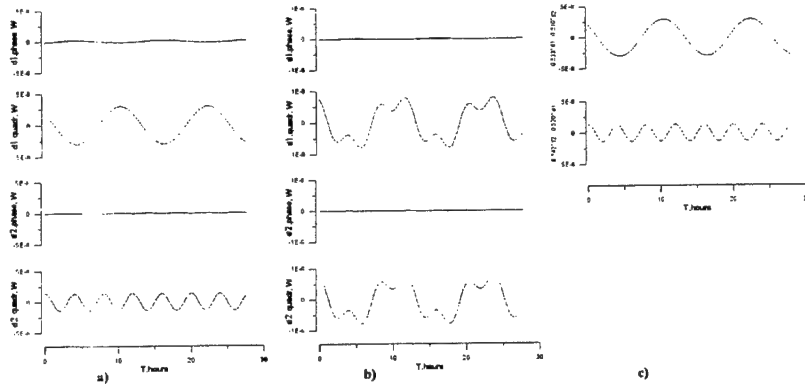


Figure 4. Output arm signals for interferometer in "meridian-parallel" orientation: a - without recycling mirror, b with recycling mirror, c - reconstructed signals.

sensitive quadrant photodiode behind the end mirror (d1 or d2) in one of its quadrature component. This signal presents the interferometer response to the gravity field.

The output signals of end arms photodetectors for the "meridian-parallel" set up is presented at fig. 4a and 4b. The fig. 4a presents output signals for interferometer without recycling. One can see a clear separation of the tidal and core signals distributed between two arms according to fig. 3. An inclusion of recycling mixes arm signals, makes them completely identical and increase the amplitudes by two orders of value (fig. 4b). Then one can find a liner combination of the arm's outputs (d1 and d2) and reconstruct the initial signals in the arms (fig. 4c). Analogous procedure can be fulfilled for other interferometer orientation.

6. SENSITIVITY OF THE ALIGNMENT SYSTEM AND INSTRUMENTAL NOISES

6.1. Measurement of mirrors tilts (shot noise sensitivity)

One of the possible way to infer the alignment error signals in the gravitational interferometer is to use an optical heterodyne technique. Phase modulation side bands are applied to the laser beam at the frequencies separating the first-order off-axis mode from the fundamental.

An optical resonator has a complete set of spatial transverse electromagnetic modes (TEM), which can be represented in the paraxial beam approximation by the Hermite-Gaussian functions $U_{mn}(x, y)$ of the transverse coordinates x and y .⁷ In the gravitational interferometer the source laser operates in the longitudinal mode producing a Gaussian beam that is aligned and mode matched to the optical resonator. Alignment errors correspond either to lateral displacements of the input beam waist relative to that of the cavity or to angular tilts between the planes of the two waists. For small misalignments in the x direction the following expression is valid

$$\Psi(x) = C_{00}U_0(x) + C_{10}U_1(x) \quad (1)$$

where C_{10} is the coupling coefficient to the respective off-axis mode. The input beam consists mainly of the fundamental mode at the carrier frequency so the coupling coefficient $C_{00} \approx 1$. For C_{10} in the case of small angle of the tilt α and lateral displacement of the beam a in the x direction one has

$$C_{10} = i\alpha/\alpha_x + a/w_x \quad (2)$$

where $\alpha_x = \lambda/(\pi w_x)$ is the far-field divergence of the beam, w_x is the waist size in the x direction and λ is the wavelength of the laser. Below we consider only the effect of mirror tilt.

The field amplitude for the beam of phase modulated light at the optical frequency ω has the following form

$$E = E_0 \left[\sum_{k=0}^{\infty} J_k(m) \exp(i(\omega + k\omega_m)t) + \sum_{k=1}^{\infty} (-1)^k J_k(m) \exp(i(\omega - k\omega_m)t) \right] \quad (3)$$

where ω_m is the modulation frequency, E_0 is a constant real vector, $J_k(m)$ is the Bessel function of the order k and phase modulation index m . When the index of modulation m is not very large only the lower sidebands will be present in the field decomposition

$$E = E_0[J_0(m) \exp(i\omega t) + J_1(m) \exp(i(\omega + \omega_m)t) - J_1(m) \exp(i(\omega - \omega_m)t)]. \quad (4)$$

The frequency of the carrier is locked to the fundamental mode frequency of Fabry-Perot resonators. When the resonators are aligned properly then only this mode can be transmitted by the cavity. However in the case of small misalignments the lowest orders of off-axis modes can be excited. If the frequency of phase modulation is equal to the separation between the first-order off-axis mode and the fundamental one then the first upper sideband is also at the cavity resonance and can be transmitted.⁸ Then the field amplitude of the transmitted field is approximated by the following expression

$$E_t \approx E_0 t_c [C_{00} J_0(m) \exp(i\omega t) U_0(x) + C_{10} J_1(m) \exp(i(\omega + \omega_m)t) U_1(x)] \quad (5)$$

where the nonresonant fields and weak coupling to the higher-order terms are neglected, t_c is the transmittivity of the cavity on the fundamental mode resonance. The resulting transmitted intensity has the following form ($T_c = |t_c|^2$)

$$I_t(x) = |E_t|^2 = T_c E_0^2 [|C_{00}|^2 J_0^2(m) U_0^2(x) + |C_{10}|^2 J_1^2(m) U_1^2(x) - 2 J_0(m) J_1(m) U_0(x) U_1(x) \alpha / \alpha_x \cdot \sin \omega_m t] \quad (6)$$

For a nearly aligned system, the first term is a large constant term, the second is constant but small and therefore can be neglected. The third term represents the amplitude modulation of the transmitted beam at the modulation frequency and is proportional to the misalignments of the resonator.

The Hermite-Gaussian functions are mutually orthogonal when integrated over the whole space. Therefore the detection by two elements followed by electronic subtraction of the photocurrents is necessary. In this case the output signal has the following form

$$i_{pd} = e\eta/(\hbar\omega) \left\{ \int_0^\infty I_t(x) dx - \int_{-\infty}^0 I_t(x) dx \right\} = -(2/\pi)^{1/2} (2e\eta/(\hbar\omega)) P_0 T_c J_0(m) J_1(m) \alpha / \alpha_x \sin \omega_m t \quad (7)$$

where P_0 is the laser power incident on the resonator, η is the quantum efficiency of the detector and e is the charge of the electron. This equation shows that the intensity modulation in the quadrature signal is proportional to the angular alignment error.

Detection sensitivity to the misalignments is theoretically limited by the short noise of the photocurrent. Then for the effective noise angle of the mirror tilt one has $\alpha_n(\omega) = \alpha_x \cdot (\pi \hbar \omega / (4\eta P_0 T_c J_1^2(m)))^{1/2}$ and the minimal measurable tilt angle has the following form

$$\alpha_{\min} = \alpha_x \cdot (\pi \hbar \omega \Delta f / (4\eta P_0 T_c J_1^2(m)))^{1/2} \quad (8)$$

where Δf is the bandwidth of the measurement. For usual parameters of gravitational interferometer one has: $\eta = 0.9$, $\lambda = 1.06 \mu m$, $P_0 = 10^3 \text{ Wt}$ (the power inside the recycling resonator), $T_c = 1.6 \cdot 10^{-3}$ (evaluated for the input mirror with $R = 0.88$ and end mirror with $R = 0.99995$), $m = 0.2$, $w_x = 2 \text{ cm}$. Then the effective spectral amplitude of angle is $\alpha_n = 1.2 \cdot 10^{-13} \text{ rad/Hz}^{1/2}$ and the minimal measurable tilt of the mirror for the value of Δf about 10^{-5} s^{-1} is $\alpha_{\min} = 4 \cdot 10^{-16} \text{ rad}$.

This value is far below the goals of the geophysical application of laser gravitational detector. However it is necessary to mention that the noises at such low frequencies is not investigated yet. If we assume that the real noise is larger than the photon noise by the factor A then the increase in the measurable tilt angle will be in $A^{1/2}$. So even for the $A = 10^4$ the minimal measurable angle will be about $4 \cdot 10^{-14} \text{ rad}$ that is also high enough.

In Ref. 9 an experimental noise power spectral density is estimated for the alignment system. For parameters used in Ref. 9 the overall noise at frequency 0.1 Hz was 2 db larger than a shot noise level. Supposing the flicker type of noise below 0.1 Hz one can estimate the parameter A as $0.1/f$ that gives for the frequency $f \sim 10^{-5} \text{ Hz}$ the value about 10^4 so the error in alignment system can be about $4 \cdot 10^{-14} \text{ rad}$. Further increase in sensitivity can be expected for increased pump power of gravitational interferometer.

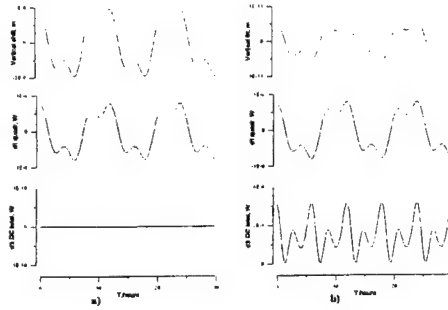


Figure 5. Output signals from d1 and d3 photodiodes for vertical shift (a) and tilt (b) of the end mirror.

6.2. Filtering of coherent deformation interferences

The principal idea of the gravity gradient measurements using the interferometers with suspended mirrors supposes that output signals can be initiated only by gravity perturbations and do not depend on the deformations of the base line. This supposition is valid if one could distinguish between mirror's mutual tilts and mirror's lateral (vertical) displacements. Such condition is certainly fulfilled for the Fabry-Perot-Michelson interferometer with flat mirrors. However in reality end mirrors of the gravitational interferometer are curved ones: they have a small sphericity with a curvature radius $R \approx 3$ km. A tilt α_0 of a spherical mirror in the first order of value is not accepted by the "alignment readout" as a tilt. It appears in the certain quadrature as an error signal corresponding to the equivalent lateral displacement of the mirror's center by the value $\Delta x \approx \alpha_0 R$. This fact means that one cannot distinguish between the tilts and the vertical shifts of the end mirrors. At the same moment vertical movements of the interferometer mirrors depend on deformations of the Earth surface which can be much larger than gravitational effects.

One solution to this problem bases on the fact that a tilt of the mirror's filament due to variations of the "plumb line" direction is accompanied by the longitudinal shift of the mirror. Such shift detunes the Fabry-Perot resonators in the arms and the whole FPM interferometer as well. On the other hand a lateral (vertical) displacement of the end mirror does not change the arm's length in the first order of value. Thus one could detect gravitational perturbations (or end mirror's tilts) selecting "misalignment signals" which simultaneously accompanied by the error signals in the "longitudinal adjustment control circuits".

The main output signal of the FPM interferometer registered by the photodiode d₃ (fig. 2) is used to form the longitudinal adjustment error signal. A time structure of the gravitational perturbation has been taken in the same model of "simple gravity field dynamics" as in section 2. The interferometer's orientation corresponds to the case of "45° setup". Results of vertical shifts and tilts simulation are illustrated in fig. 5a and 5b.

Fig. 5a demonstrates a time varying vertical shift of the end mirror correspondent to the quadrature output of the photodiode d₁ (misalignment signal) and an absence of any reaction in the main interferometer output from photodiode d₃. Fig 5b presents an equivalent end mirror's tilt, quadrature output from d₁ and a presence of nonzero perturbation from photodiode d₃. The quality of such tilt and shift separation depends on a ratio of the effective amplitudes. In the case considered above the tidal deformation amplitude (relative vertical shift of the end mirror) is three orders of value larger than the gravitational tilt signal of inner core oscillations. A modern digital filtration technique permits a reduction of known interferences with residuals on the level of 10^{-5} , so in principle a compensation of the tidal kind of deformation background is possible.

6.3. Thermal noises of mirror suspension at infra-low frequency

For analysis of the oscillations of the suspension for infra-low frequency range one can use the simplest one-dimensional model and consider this devise as the equivalent mechanical system with N degrees of freedom (antiseismic filter and mirror). Let suppose that the last stage of this system (mirror) has a mass m_N and length l_N , besides the deviation of the mass from a vertical line is ϕ_N . To determine the thermal fluctuations of ϕ_N one has to find according to the fluctuation dissipation theorem the equivalent displacement of the mass (ϕ_N) caused by an external force (torque) Q_N . A spectral density of the thermal force will be determined by an imaginary part of transfer function connecting ϕ_N and Q_N . Using this method and the typical values of gravitational interferometer parameters - the length of the

suspension $l \approx 1$ m, the masses of the mirrors ≈ 10 kg, the quality factor of mirrors suspension $Q \approx (10^6 \div 10^8)$ - one can obtain for the value of thermal noise spectral density $\sqrt{\langle |\alpha_{\omega,0}(j\omega)|^2 \rangle} \approx 7 \times (10^{-16} \div 10^{-17})$ rad/Hz $^{1/2}$ that is smaller than the expected useful effects.

For nonelastic intrinsic dissipation (creep) the coefficient of friction depends on running frequency ω . Taking into account the nonelastic dissipation, one can obtain the following estimate for spectral density of the thermal noises: $\sqrt{\langle |\alpha_{\omega,1}(j\omega)|^2 \rangle} \approx (10^{-12} \div 10^{-13})$ rad/Hz $^{1/2}$ for $f = \omega/(2\pi) \approx 3 \times 10^{-5}$ Hz.

6.4. Temperature gradients and suspension assymetry

The final stage of mirrors suspensions consists of two wires supporting the probe mass with mirror. Let the length l of the wires is equal in balance. When the temperature of the wires changes then the angle of mirror tilt $\Delta\varphi$ will be proportional to the difference in the wire length. So the angle tilt of the mirror can only be produced if the temperatures of two wires are different, for equal temperatures the mirror will only have the vertical displacement.

There are three mechanisms of heat transfer from the surrounding world (e.g., walls of the vacuum camera) to the wire: heat transfer due to the black body radiation inside the camera, heat transfer through the ends of the wires and heat transfer through the lateral surface of the wire from the residual gas in the camera.

Taking into account the parameters of suspensions and vacuum cameras one can estimate the temperature variations inside the vacuum camera at the frequency 3 - 4 hours as about $10^{-6} \div 10^{-8}$ degree. These values corresponds to the amplitudes of the angle fluctuations of the mirrors about $10^{-12} \div 10^{-14}$ rad that is not dangerous for registration of the signal from Earth core oscillation. For the registration of oscillations with smaller frequencies one have to use some kind of temperature stabilization scheme. For example if one have to measure the change of mirror angles near the frequency 24 hours then the stabilization of temperature inside the vacuum camera building have to be higher than $10^{-4} \div 10^{-5}$ degree.

6.5. Magnetic field variations

Control magnets are mounted at the the last stage of the antiseismic filter to adjust the mirrors orientation therefore external fluctuating magnetic field can cause the angular displacement of the mirror. Estimating tilts due to the magnetic field of the Earth one can conclude that the maximum angular displacement of the mirrors filament is $\varphi \cong 10^{-15}$ rad therefore the influence of the fluctuating magnetic field of the Earth is inessential.

6.6. Radiometric noises

The mirror has a form of cylinder made of quartz with one end coated with dielectric layers. This end is included into the Fabry-Perot resonator. Therefore the laser light falling on it can be partially absorbed and the temperature of this end can be higher than the temperature of the other end. Therefore due to the interaction with the residual gas the force along the cylinder axes can arise. For the deviation of the angle one has $\Delta\alpha = \Delta x/l = F_y/(Mg) \approx 2 \cdot 10^{-18}$ rad. Therefore this source of fluctuations is also not important for the geodynamical application.

6.7. Summary

Potential sensitivity of the alignment system of gravitational interferometer is high enough to measure the geodynamical signals considered in section 3. The main instrumental noises also do not forbide such measurements. For reliable operation one has to take care in temperature stability of the mirror suspension system or use an additional device measuring the temperature variation inside the tower and compensating it in the output of alignment system.

7. GRAVITATIONAL INTERFEROMETER IMPROVEMENTS

7.1. Auxiliary interferometer

To increase the sensitivity of gravitational installation to the angular displacement of the mirrors at low frequency one can use an auxiliary interferometer. Let suppose that the additional interferometer is Michelson type device with Fabry-Perot interferometers in the parallel arms. One arm of this device is formed by the mirrors attached to the test masses of an arm of gravitational interferometer (or it mirrors) and the other arm is formed by the mirrors attached to the last stage of antiseismic filters (cf. fig. 6). Let suppose that the distance between two antiseismic filters is L_r , and the distance between free masses in this arm (between two mirrors) is L . Then the output signal

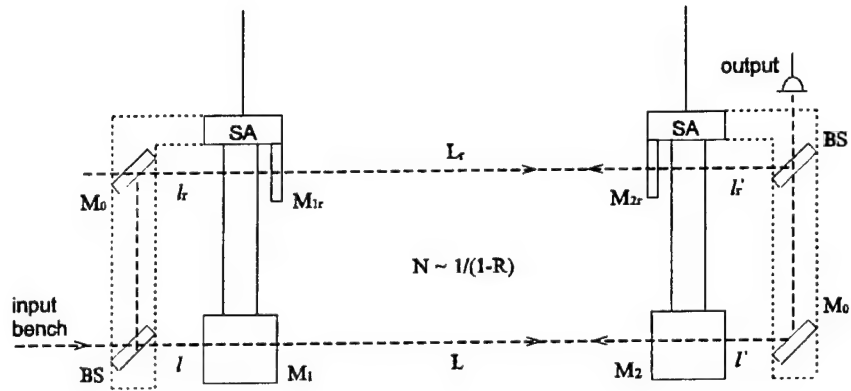


Figure 6. The principal scheme of auxiliary interferometer.

is proportional to the difference $L_r - L$. For the known length of mirror suspension l_s , one can easily calculate the angle deviation as $\delta\alpha \approx (L_r - L)/l_s$.

An expected frequency range for the output signal of such auxiliary interferometer is not larger than $\sim 10^{-3} \div 10^{-4}$ Hz therefore one can use the mirrors with very high reflectivity (large finesse) and a relaxation time will be also large allowing to accumulate the signal during a long interval. In this case the sensitivity can be large enough to register the required geophysical effects for considerably small pump power of auxiliary interferometer. Approximate estimation of the sensitivity to angular perturbations gives the value $2 \cdot 10^{-18}$ rad that is high enough for the geodynamical applications.

Such scheme is completely differential therefore the common mode hindrances can be in principle almost fully compensated. The advantages of this scheme are the following:

- geophysical, seismic and other mechanical perturbations of the suspensions can be compensated automatically;
- the output signal is proportional only to the differential angular deflection of the suspension, synchronous (unidirectional) movements have to give a zero signal to the output;
- beam walks and jitter are not important;
- laser frequency fluctuations are unimportant.

For additional interferometer of the Michelson type it can be hard to maintain the equality of two arms. In this case one can use the additional interferometer of the Mach-Zender type working with the transmitted beams (fig. 6) instead of reflected beams for the Michelson type additional interferometer. For such device the optical scheme can be highly symmetrical providing a good isolation from an undesirable dependence on perturbations of different optical elements.

7.2 Additional flat mirror for discrimination between tilts and up-down movements

The end mirrors in gravitational interferometers are planed to be spherical. For such end mirrors the Anderson technique of alignment cannot give explicit information about the type of mirror movement - tilt or up-down motion.

For the geophysical application it is necessary to obtain the signal containing information on the tilt of the end mirrors. Such signal can be easily produced if an additional flat mirror (or beamsplitter) can be suspended after the end mirror (fig. 7). This is just the output for the alignment with end photodetectors. Then a part of the beam exiting from the end mirror can be passed through the beamsplitter and entered the end photodetector (as is supposed for the alignment system) and the other part of the exiting beam can be deflected by the beamsplitter to the additional lens system and quadrant photodetector. The beamsplitter can be suspended at the last stage of the seismic attenuation system. Then in the gravity field of the Earth this mirror will be tilted therefore the beam reflected from it will be tilted also. Using the lens system one can focus this beam in such a way that the position of the focal spot will be defined by the angle of the beam tilt. Then using the quadrant photodetector one can extract from the differenced photocurrent the information about the tilt angle of the end mirror. The methods of extracting can be different including those utilizing the Anderson technique or others with modulated

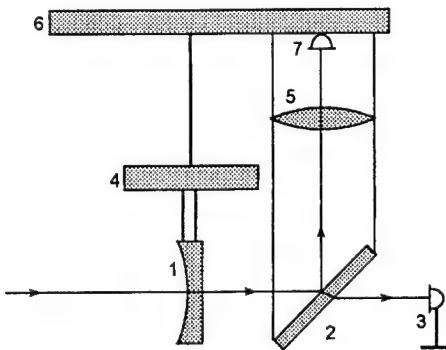


Figure 7. Additional flat mirror for discrimination between tilts and up-down movements of the arm end mirror.

light beam and AC signal output. For the simple positional method with DC output one can estimate the sensitivity as $\alpha_{\min} \geq \alpha_0 \cdot \pi(2\hbar\omega/(\eta P))^{1/2}$ where α_0 is the diffraction divergence of the beam of power P . So one can conclude that the sensitivity of this method can be not worse than that of the Anderson alignment method. Note that the principal (shot noise) sensitivity of the Anderson method, for example, for the tilt of a flat mirror is about (P_{total} is the total power of the beam available at the photodetector)

$$(\alpha_{\min})_{\text{Anderson}} \approx \alpha_0 \cdot (\pi\hbar\omega/(\eta P_{\text{total}}))^{1/2} \quad (9)$$

and is not dependent on the length and finesse of interferometer resonator.

It is worth to note that the signal of the additional photodetector is proportional to the tilt of the end mirror. The output of the end alignment photodetector is proportional to both tilts and up-down displacements of the end mirror. So combining in an appropriate way the output signals from two photodetectors one can reconstruct the signal proportional only to the up-down movements of the end mirror.

8. CONCLUSIONS

The above consideration allow to conclude that laser long base gravitational interferometer is capable of measuring the low frequency Earth gravity gradients. By elaboration of relatively simple additional devices (such as auxiliary interferometer, temperature stabilization system etc.) one can increase the sensitivity of geophysical measurements and give the possibility to detect the signature of very interesting geodynamical processes.

REFERENCES

1. *VIRGO Final design report, issue 1*, CNRS, INFN (VIRGO project documents), 1997.
2. A. Abramovici, W. Althouse, J. Camp et. al, "Improved sensitivity in a gravitational wave interferometer and implications for LIGO", *Phys. Lett. A*, **218**, pp. 157-163, 1996.
3. K. Danzmann, H. Luck, A. Rudiger et.al, "Proposal for a 600 m laser-interferometric gravitational wave antenna, Max-Planck-Institut für Quantenoptik Report 190, Garching, Germany, 1994.
4. K. Tsubono, "300-m laser interferometer gravitational wave detector (TAMA300) in Japan", in *Proc. of the First E. Amaldi Conf.: Gravitational Wave Experiments*, pp. 112-114, World Scientific, Singapore, 1995.
5. V. N. Rudenko, "Gravitational free mass antenna as an angular gravity gradiometer", *Phys. Lett. A*, **223**, pp. 421-429, (1996).
6. A. V. Kopaev, V. N. Rudenko, "Spectroscopy of Earth oscillations with the help of gravitational wave interferometers", *JETP Letters*, **59**, pp. 630-633, 1994.
7. H. Kogelnik, T. Li, "Laser beams and resonators", *Appl. Opt.*, **5**, pp. 1550-1567, 1966.
8. D. Z. Anderson, "Alignment of resonant optical cavities", *Appl. Opt.*, **23**, pp. 2944-2949, 1984.
9. N. M. Sampas, D. Z. Anderson, "Stabilization of laser beam alignment to an optical resonator by heterodyne detection of off-axis modes", *Appl. Opt.*, **29**, pp. 394-403, 1990.

Optical fiber characterization by use of Laser Scanning Microscopy

Hassan Fatemi EG

Physics Dept., Faculty of Science, Shahid Bahonar Univ. of Kerman, Kerman, Iran

Abstract

In this report, an interferometric method for measuring the parameters of the emitted light from a Step-Index Single-Mode optical fiber is introduced. A mirror oriented normal to the optical fiber axis is axially scanned in front of the fiber emitting face. The intensity of the resultant coupled back into the fiber interference is then detected. Interference fringes are used, as a tool, to determine the emitted light modal radius. Knowing the beam waist, the values of other parameters of the beam can be calculated.

2. INTRODUCTION

There are applications in which the laser light that is transmitted by a single-mode optical fiber is used as a measuring tool. In these cases, the Near-Field Radius(or Mode-Field Radius) and the divergence of the light emitted from a well-cleaved fiber tip are two important factors to be, practically, considered. Some times technical information released by the manufacturers of these optical fibers are not very reliable, and due to fluctuation in these parameters, it is better to measure them at the time of using these fibers. The fluctuations penetrate during fabrication of the single-mode optical fiber. Core radius may randomly changes and/or a small diffusion at the core-cladding interface can produce an appreciable profiling effect. It alters the theoretically expected intensity distribution of the light emanating from the fiber.

Different people have proposed various methods for measuring the MFR of Step-Index Single-Mode(S-I S-M) optical fiber and the light eminent divergence of the propagation. There are, traditionally, two techniques reported. These techniques may be grouped as direct and indirect optical fiber characterizations. As an examples of direct characterization techniques we may refer to Butler et al² and of indirect characterization we may mention Parton². A summarization of these methods is given by Anderson and Philen³. In present report, one application of the Fiber Probe Interferometric Microscopy(FPIM) technique⁴ for S-I S-M optical fiber characterization is introduced. It is actually a different method, in comparison to the others.

3. THEORY

In FPIM technique, the light emitted from a S-I S-M optical fiber is coupled back into the same fiber by using a mirror which is located in front of the fiber. Interference between coupled light to the fiber and that part which is reflected from the fiber tip is the measuring device for the characterization.

As transverse cross-sectional amplitude distribution of the light emanating from the S-I S-M optical fiber can be closely approximated by a Gaussian function, similar to that is assumed by Deschamps⁵, a complex form may be considered for beam propagation in the cavity;

$$U(r, \text{at } z) = (1 + iz/2z_*)^{-1} e^{ikz} e^{(-r^2/2\omega(z)^2)} e^{\left(-ikr^2/2(z + 4z_*^2/z)\right)} \quad (1)$$

$$\approx (1 + iz/2z_*)^{-1} e^{ikz} e^{(-r^2/2\omega(z)^2)}$$

in which $U(r, \text{at } z)$ is the Gaussian function amplitude at the axial, z , and the radial, r , coordinates. $\omega(z)$ is the beam radius at z , and z_* is the confocal length of the optical fiber eminence. The end surface of the fiber and the sample reflecting surface constitute a Fabry-Perot resonator which causes multiple reflection of the light. As the resonator gap is increased, the intensity of the light coupled back into the fiber decreases, whereas, its interference with the light reflected from the fiber end surface creates a fluctuation in intensity. The normalized interference intensity resulting from the interference of the multiple reflections coupled back into the fiber and the light reflected from the optical fiber end surface at any point in the beam propagation medium, I_{nor} , can be expressed as

$$I_{\text{nor}} = \left| r_0 - \frac{(1 - r_0^2)}{r_0} \sum_j (-r_0 r)^j (1 + iju)^{-1} \text{Exp}((ik^2 \omega_0^2)u) \right|^2 \quad (2)$$

where u is the normalized cavity gap size and is defined as $\left(\equiv \frac{z}{z_*} \right)$. r and r_0 are the amplitude reflection coefficients of the reflecting object surface and the optical fiber end surface at normal incidence, respectively. j represents the number of successive reflections in this cavity that couples into the fiber. ω_0 is the mode-field radius of the Gaussian beam for which the mode-field waist is located at the fiber tip.

According to the equation (2), the interference intensity is a periodic function of the normalized sample displacement, u , and Mode-Field Radius, ω_0 . Figure 1 demonstrate periodic variation of the interference intensity, as a function of u , for four different S-I S-M optical fibers. The sample is assumed to have an amplitude reflection coefficient of 0.95 and the wavelength of the light launched into the fiber, λ , is considered to be $0.633 \mu\text{m}$.

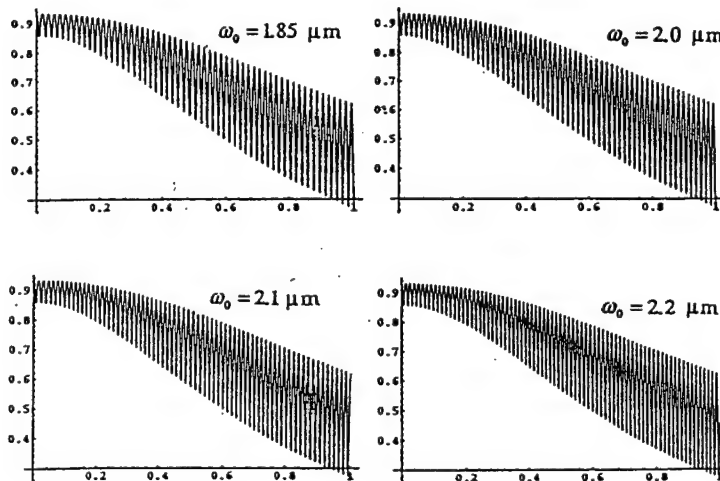


Figure 1. Interference intensity variation as a function of the sample normalized displacement, for four different optical fibers.

The main difference between the graphs, shown in Figure 1, is their value of the spatial frequency of the interference intensity. This frequency, f , for an optical fiber, with a certain value of ω_0 , that is emitting a light with wavelength of λ is,

$$f = 2\pi \left(\frac{\omega_0}{\lambda} \right)^2. \quad (3)$$

Also, by definition, the spatial frequency in a $I(u)$ - u domain is $f = \frac{N}{\delta u}$. Otherwise, N is the number of fringes within a certain δu . Comparing this relation with equation (3), may results the below equation

$$\ln \omega_0 = \frac{1}{2} \ln \left(\frac{N}{\delta u} \right) + c \quad (4)$$

in which c is a constant related to the source of illumination and is equal to $c = \frac{1}{2} \ln \left(\frac{\lambda^2}{2\pi} \right)$. Figure 2 indicates the linear relation given in equation (4). According to these relations, the value of the MFR of the S-I S-M optical fiber can be extracted if the spatial frequency of the interference intensity is known.

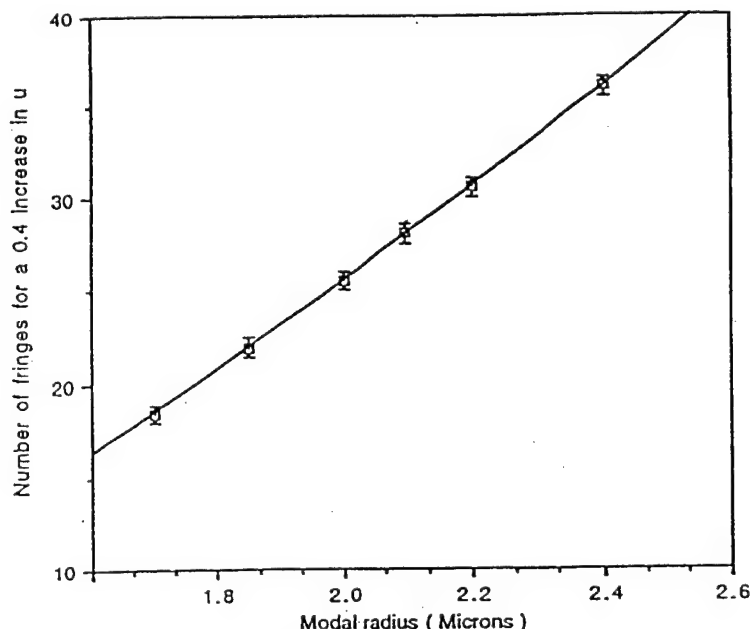


Figure 2. Number of interference fringes, for a 0.4 increase in u , as a function of ω_0 .

4. EXPERIMENTAL

In a Fiber Probe Interferometric Microscopy(FPIM) set-up, a highly reflecting flat mirror is scanned, axially, in front of a S-I S-M optical fiber. The intensity of the interfered light is transmitted to the other side of the fiber, which is mechanically joint to one of the 2×2 optical fiber coupler ports of the FPIM. In FPIM set-up, the interfered intensity is detected, accumulated by the computer, and then plotted against the mirror normalized displacement, u . One of the experimental plots is shown in Figure 3. Counting number of fringes within a certain

amount of intensity reduction of the lower picks is used to find the value of ω_0 of the eminent light of the optical fiber. This value is found to be equal to $4.2 \mu\text{m}$, that is within the range of the value given by the manufacturer ($3.7 \mu\text{m} \pm 0.5 \mu\text{m}$).

Knowing the value of ω_0 makes it possible to find the value of other parameters of emission, such as confocal length, z_0 , which is calculated to be equal to $22 \mu\text{m}$. The far field angle of divergence is approximated to 5.5° .

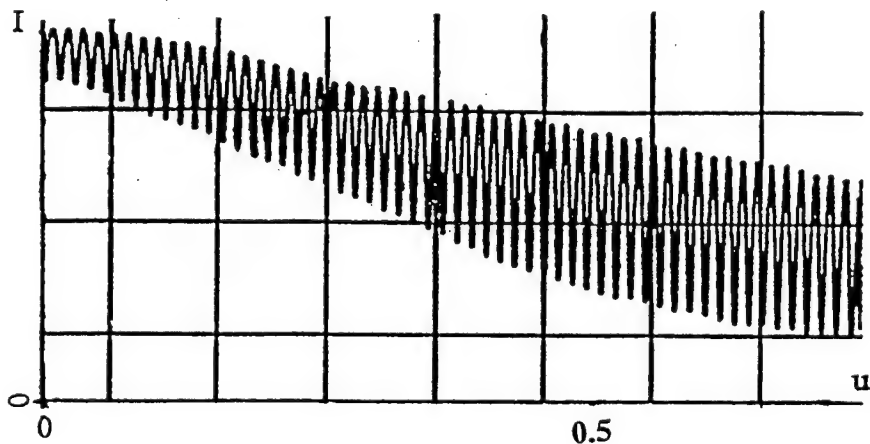


Figure 3. Experimental interference changes, for a certain S-I S-M optical fiber, as a function of the sample translation.

5. CONCLUSION

In this report one of applications of FPIM is introduced. It is a technique to find information concerning the near-field modal distribution of the S-I S-M optical fibers. The advantage of this technique in optical fiber scanning microscopes is that fiber probe characterization can be done easily in the same microscope set-up, without the need of removing the fiber probe and using any other equipment. Thus, the FPIM technique can be considered as a new way of optical fiber characterization.

6. REFERENCES

1. D. J. Butler, K. A. Nugent, and A. Roberts, "Application of Near-field scanning Optical Microscopy to Optical Fibers," *Proc. of Aust. Conf. on Opt. Lasers and Spectr.*, 46 (1994).
2. J. R. Parton, "Improvements to the Variable Aperture Method for Measuring the Mode-Field Diameter of Dispersion-Shifted Fibers," *Journal of Lightwave Technology* 7 1158-1161, (1989).
3. W. T. Anderson, and D. L Philen, "Spot Size Measurements for Single-Mode Fibre; A Comparison of Four Techniques," *Journal of Lightwave Technology* LT-1, 20-26. (1983).
4. H. Fatemi EG, " Scanning Optical Interferometry, using Optical Fiber Probe," *Proc. of SPIE* 3573, 247-251 (1998).
5. G. A. Deschamps, " Gaussian Beam as a Bundle of Complex Rays," *Electronics Letters* 7, 684-685 (1971).

Theoretical Backgrounds of Methods of Angle-Resolved and Total Integral Scattering for Precise Dielectric Surfaces.

Malitski K.

Moscow Institute of Physics and Technology,

Institutskiy per. 9, Dolgoprudny, Moscow region, 141700, Russia

ABSTRACT.

Theoretical models of light scattering methods are considered for precise dielectric surfaces. By use of microscopic treatment it is shown, that polarization of near-surface medium in the presence of roughness differs from that in the volume of medium. Simple theoretical model of near-surface polarization dependence due to effective field difference is presented for the case of s-polarized incident light. Corresponding light scattering is calculated by use of quasi-microscopic approach. It is shown that the intensity of scattering decreases noticeably for very smooth surfaces, which height deviations are compared with interatomic distance ($\sim 5 \text{ \AA}^0$ for SiO_2). Therefore the differences of power spectral density functions measured by angle-resolved scattering and atomic force microscopy methods may be qualitatively explained.

Keywords: surface roughness, light scattering, angle-resolved scattering, total integral scattering.

1. INTRODUCTION.

The measurements of light scattering due to surface roughness are widely used for quality investigation of precise dielectric surfaces¹, particularly for gyro mirrors and substrates. Method of angle-resolved scattering (ARS) allows to determine power spectral density (PSD) function of surface roughness, that is very informative characteristic of roughness statistics. Method of total integral scattering (TIS) yields the effective mean-square roughness (rms) height, that is useful characteristic of surface quality. The interpretation of experimental ARS and TIS data requires the adequate theory of roughness light scattering, that gives the relation between scattering characteristics and roughness statistic properties.

The so-called “vector scattering theory”² or Rayleigh-Rice theory is frequently used for interpretation of ARS measurements. Scalar theory³, that is the particular case of vector theory in the limit of normal incidence and small scattering angles, is often used in calculations of effective rms height from TIS data and is also used in ARS measurements⁴. Both scalar and vector theories are intrinsically macroscopic. That means that the optical properties of surface material are described by macroscopic quantities, i.e. the dielectric constant or refractive index. That implies that the polarization amplitude is constant anywhere in medium under the surface. In microscopic view it means that induced dipole moments of atoms at and near boundary coincide with the volume ones.

If it is not so, there exists thin near-surface layer, in which the polarization is changed (thin layer is the layer, which thickness is much less than wavelength of light). The existence of such layer were considered only for ideal plane boundaries of discrete and continuous media in the theory of transitional layers⁵. We performed the calculation of near-boundary polarization of ideal cubic medium irradiated by s-polarized incident field according to this theory and obtained that only polarization of first layer atoms differs from volume polarization and the relative magnitude of such difference is about 1.5%. Therefore the first layer almost totally screened the incident field. That means that for ideal plane surfaces the assumption that the polarization amplitude is constant anywhere in medium is well-grounded. But it is not the same if the boundary is rough. In our consideration we want to show that the surface roughness effects the polarization of atoms, that it consists of, and in that way influence on the scattering. As the characteristic thickness of transitional layer is of about interatomic distance, it is evident, that the effect of roughness influence on polarization would be significant only for very precise surfaces with rms height compared with interatomic distance. As the value of mean interatomic distance for SiO_2 is $\sim 5 \text{ \AA}^0$ and the measured effective rms heights goes to 2 \AA^0 and less, it is obvious that our consideration is of great importance in ARS and TIS data interpretation for precise surfaces.

Our consideration is confined to the case of s-polarized incident light because it's clearly shows how the effect of roughness influence on polarization changes the scattering. The case of p-polarized scattering is more complicated because the anisotropy must be taken in account.

In the next section we introduce simple quasi-microscopic model of atomic polarization of surface roughness area that satisfies general assumptions of effective field behavior near the boundary. In third section we calculate surface roughness scattering according to considered model. Then we discuss the difference in scattered field amplitude and intensity between standard macroscopic scattering theories and our model for the case of precise quartz surface.

2. THEORETICAL MODEL OF POLARIZATION OF NEAR-BOUNDARY MEDIUM IN THE PRESENCE OF ROUGHNESS.

Let the height of the surface above xy plane be described by the profile function $z = f(x,y)$, $\langle f(x,y) \rangle = 0$. Above the boundary is vacuum ($z > f(x,y)$), and the medium occupies the space below it ($z < f(x,y)$). The medium is characterized by a dielectric constant $\varepsilon(\omega)$, which is real, isotropic and constant in medium far from its surface. Plane wave s-polarized light of wavelength λ irradiates the surface at an incident angle of θ_0 . The plane of incidence is xz . Surface roughness is assumed to be small, that means that the deviations of surface height is much less than λ .

In the presence of incident field the stationary state of polarization is formed in medium. According to the quasi-microscopic treatment this state is described by continuous atomic polarization that is the dipole moments of atoms, averaged by physically small areas. In our case averaging is performed through the area of radius that is much bigger than the mean interatomic distance a and much less than λ .

In stationary state atomic polarization of amplitude $p(\mathbf{R})$ may be expressed as follows:

$$p(\mathbf{R}) = \hat{\alpha}(\mathbf{R}) \mathbf{E}'(\mathbf{R}), \quad (1)$$

where α is atomic polarizability, \mathbf{E}' is effective field amplitude, that acts on the appropriate atom from the induced dipole moments of all other atoms. Phase dependencies of both atomic polarization and effective field are described by $\exp\{i\mathbf{k}_t \mathbf{R} - i\omega t\}$, where $\mathbf{k}_t = \frac{2\pi}{\lambda}(\sin \theta_t, 0, \cos \theta_t)$ is wave vector of refracted wave, θ_t is angle of refraction. The treatment is not fully microscopic because the atomic polarization is described by continuous distribution, but it may be used for calculations of fields in far zone $z \gg \lambda$, which is the case of practical interest.

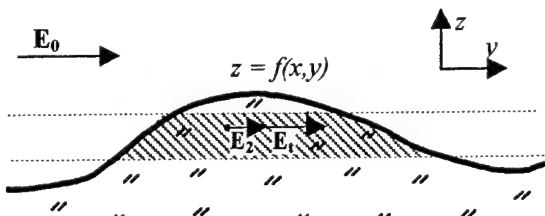
As it may be seen from (1), the polarization of medium near boundary may change because of two reasons, that are: 1). the difference of atomic polarizability of near-boundary atoms from volume ones and 2). the difference of effective field that acts on near-boundary atoms. Furthermore, the difference of polarizability near surface may be caused by the number of reasons such as the change of distance between atoms, the presence of surface electronic states, subsurface structural defects, and other. The effective field near surface is changed because the near-boundary geometry differs from volume one and because of the reasons mentioned above for the case of polarizability. In present report we consider only the second reason of polarization difference near boundary, i.e. we assume that surface roughness effects the polarization of atoms it consists of because of the difference of effective field \mathbf{E}' . Therefore we assume that the polarizability is constant $\alpha(\mathbf{R}) = \alpha$.

Amplitude of polarization wave in medium on the distances $|z| \gg a$ according to our assumptions is constant $p(\mathbf{R}) = p_v$, and direction of polarization coincides with that of mean electric field of refracted wave \mathbf{E}_t . In this case according to Lorentz-Lorenz equation the relation between effective field and refracted field is

$$\mathbf{E}'_v = \mathbf{E}_t + \frac{4\pi}{3} N p_v. \quad (2)$$

We want to show that in the presence of roughness the relation (2) is not valid for near-boundary atoms, and therefore the polarization near surface differs

from the volume one p_v . For this aim let consider the slot of width a that is cut in the area of roughness by the planes $z = \text{const}$ (Pict. 1). The effective field, that acts on any atom in the slot, is composed of the incident field \mathbf{E}_0 , of field of all atoms that lie behind the slot \mathbf{E}_1 , and the field of all atoms that lie in slot except the considered one \mathbf{E}_2 . Now we use the following result of theory of transitional layers⁵ for the case of electric field parallel to the axis $y = 0$ (our case



Picture 1. Effective field in the roughness area (see discussion).

of s-polarized incident field) : if we neglected small unhomogeneous components of dipole waves, the sum of incident field \mathbf{E}_0 and field \mathbf{E}_1 of atoms, that lie behind the slot, is equal to the mean electric field in medium or refracted field $\mathbf{E}_t \approx \mathbf{E}_0 + \mathbf{E}_1$. Therefore from equation (2) we derive, that the additional contribution to the effective field is associated with the field \mathbf{E}_2 of dipoles of atoms that lie in the slot. In volume this contribution is $\mathbf{E}_2 \approx \frac{4\pi}{3} \mathbf{p}N$. But the number of atoms that lie in the slot that is cut in the area of roughness is not constant

but decreases if the slot is cut closer to the upper boundary of roughness. Consequently the additional contribution to the effective field \mathbf{E}_2 associated with these atoms becomes smaller. In the limit of upper boundary of surface roughness there are no atoms in the slot, and the effective field coincides with the mean electric field in medium $\mathbf{E}' \approx \mathbf{E}_t$. Also it may be seen that the effective field in plane $z = \text{const}$ increases for the atoms, that lie farther from sides of roughness.

Now we introduce the simple model, that satisfies the above conclusions about effective field behavior in the roughness area. Let us consider the following non-linear coordinate transformation (application of such non-linear transformation for scattering problem is discussed in detail in⁶)

$$u_1 = x, \quad u_2 = y, \quad u_3 = z - f(x, y) \exp\left\{\frac{u_3}{\Delta_{\max}}\right\}, \quad (3)$$

where Δ_{\max} is the maximum deviation of surface height from mean plane.

The first assumption of our model is that the polarization amplitude is constant on the coordinate surfaces $u_3 = \text{const} \leq 0$. Such selection of surfaces of constant amplitude is done because the additional contribution to effective field is associated with atoms, that lie in the same plane $z = \text{const}$, that's why, if we move off the upper boundary plane of roughness $z = \Delta_{\max}$, the roughness influence on polarization must smooth out. The second assumption of the model is that we accept the following approach for the polarization amplitude on the surfaces $u_3 = \text{const} \leq 0$:

$$\mathbf{p}(\mathbf{U}) = \mathbf{p}_v + (\mathbf{p}_0 - \mathbf{p}_v) \exp\left\{\frac{u_3}{\Delta_{scr}}\right\}, \quad u_3 \leq 0, \quad (4)$$

where $\mathbf{p}_0 \approx \alpha \mathbf{E}_t$ is the polarization on the boundary, Δ_{scr} is the characteristic screen depth, that correspond to the depth, at which the above lying atoms screen the incident field.

Picture 2 shows the coordinate surfaces $u_3 = \text{const}$ for roughness with $\Delta_{\max} = 50 \text{ \AA}^0$ ($\sigma = 20 \text{ \AA}^0$)

(a) and $\Delta_{\max} = 15 \text{ \AA}^0$ ($\sigma = 7 \text{ \AA}^0$) (b), that correspond to constant polarization amplitudes $\mathbf{p}_v + C(\mathbf{p}_0 - \mathbf{p}_v)$, $C = 0.5, 0.25, 0.1, 0.05$, according to (4) with characteristic screen depth $\Delta_{scr} = 5 \text{ \AA}^0$. It may be seen, that as the deviations of surface height become smaller, the smoothing of roughness influence on polarization becomes more significant.

3. LIGHT SCATTERING CALCULATIONS.

Now we use the simple model of polarization of atoms of roughness area, that was considered in above section, for calculation of light scattering. We apply the general method of quasi-microscopic theory for such calculations. According to our model we assume that polarization amplitude is constant in the layers confined by surfaces $u_3 = \text{const}$, (3). We denote these amplitudes through $\mathbf{p}_0, \mathbf{p}_1 \dots \mathbf{p}_n$, each of them defined according to (4). Let then substitute the polarization wave (1) with the following system of polarization waves of constant amplitudes, that are propagating in media with different boundaries⁵:

$$\begin{aligned} \mathbf{p}_0 \exp\{i\mathbf{k}_t \mathbf{R} - i\omega t\}, \quad u_3 < 0; \\ (\mathbf{p}_1 - \mathbf{p}_0) \exp\{i\mathbf{k}_t \mathbf{R} - i\omega t\}, \quad u_3 < h; \\ \dots \\ (\mathbf{p}_j - \mathbf{p}_{j-1}) \exp\{i\mathbf{k}_t \mathbf{R} - i\omega t\}, \quad u_3 < jh, \quad j = 0..N, \end{aligned} \quad (5)$$

where h is the average thickness of layers, N is the number of layers.

Every j - polarization wave of constant amplitude in (5) is equivalent to the medium with constant polarization $\mathbf{p}_j - \mathbf{p}_{j-1}$ with rough boundary $u_3 = jh$ or according to (3) $z = jh + f(x, y) \exp\{-\frac{jh}{\Delta_{\max}}\}$. Scattering by medium of constant polarization in the presence of boundary roughness is the problem that is solved by usual (i.e. macroscopic) scalar or vector theories of surface scattering. Therefore we see that each "subproblem" in (5) is solved and we must only summarize the appropriate solutions to find our result.

Let write the macroscopic scattering theory result in form $\mathbf{E}_m^{(s)}(\mathbf{R}) = A\tilde{f}(x, y)\mathbf{F}(\mathbf{R}, \lambda, \epsilon, \theta_0, \theta_s, \phi_s)$, where A is the amplitude of incident field, $\tilde{f}(x, y)$ is surface profile function, \mathbf{F} – vector function, that describe dependency on wavelength, dielectric constant, incident angle, scattering angles θ_s, ϕ_s and polarization (expression for it depends on theory, that is used, e.g. scalar or vector). Then let use continuous distribution instead of discrete (5) : $jh \rightarrow u_3$, $\mathbf{p}_j \rightarrow \mathbf{p}(u_3)$, $\mathbf{p}_j - \mathbf{p}_{j-1} \rightarrow d\mathbf{p}(u_3) = \mathbf{p}'(u_3)du_3$. Therefore performing integration we obtain the following expression for field scattered on the surface of medium which polarization in roughness area is described by model (3) – (4) :

$$\mathbf{E}^{(s)}(\mathbf{R}) = f(x, y) \frac{1}{p_v} \left[\mathbf{p}_0 + (\mathbf{p}_v - \mathbf{p}_0) \frac{\Delta_{\max}}{\Delta_{\max} + \Delta_{scr}} \right] \mathbf{F}(\mathbf{R}). \quad (6)$$

In obtaining the above expression we neglected the phase dependency of field on z -coordinate $\exp\{ik_z z\}$ because the surface height deviations are much less the wavelength of light.

For the case of surface roughness, which height deviations is much bigger than the screen depth, $\Delta_{\max} \gg \Delta_{scr}$, we obtain using (6), that scattering is described by usual macroscopic scattering theory:

$$\mathbf{E}^{(s)}(\mathbf{R}) \approx \mathbf{E}_m^{(s)}(\mathbf{R}).$$

For the case of surface roughness, which height deviations is of order of the screen depth, $\Delta_{\max} \sim \Delta_{scr}$, from (6) it follows, that scattering becomes smaller, being compared with that described by macroscopic theory. The relative decrease of scattering field amplitude is given by the following equation:

$$\frac{\Delta E^{(s)}}{E_m^{(s)}} = \frac{E_m^{(s)} - E^{(s)}}{E_m^{(s)}} = \frac{(p_v - p_0)}{p_v} \frac{\Delta_{scr}}{\Delta_{\max} + \Delta_{scr}} . \quad (7)$$

Therefore the relative decrease of scattering field intensity can be find:

$$\frac{\Delta I^{(s)}}{I_m^{(s)}} = \frac{E_m^{(s)2} - E^{(s)2}}{E_m^{(s)2}} = \left(\frac{\Delta E^{(s)}}{E_m^{(s)}} \right)^2 - 2 \frac{\Delta E^{(s)}}{E_m^{(s)}} . \quad (8)$$

We obtained expressions, that give difference in scattering field amplitude and intensity due to polarization model (3) – (4), that takes into account the influence of roughness on the polarization of near-boundary area. In the next section we discuss the differences in scattering for fused silica substrates.

4. DISCUSSION.

For numerical evaluation of the effect of roughness influence on polarization we consider light scattering from polished surfaces of fused silica substrates (SiO_2).

As it was noted above in section 1 the first layer of ideal crystalline medium practically totally screened the incident field. Therefore we assume that the characteristic screen depth is equal to the interatomic distance, $\Delta_{scr} = a$. Polarizability of SiO_2 may be obtained according to Lorentz-Lorenz equation:

$$\alpha = (3a^3 / 4\pi)(n^2 - 1)/(n^2 + 2) \approx 8 \text{ \AA}^3 . \text{ We next find from (2) and (4): } \frac{p_v - p_0}{p_v} = \frac{4\pi}{3a^3} \alpha \approx 0.27 .$$

Picture 3 shows the relative differences of scattering field amplitude and intensity as the function of maximum surface height deviation Δ_{\max} , according to (7) and (8).

For evaluations we may consider, that the value of Δ_{\max} is two times larger than the rms height σ . Therefore for the SiO_2 surface with $\sigma = 10 \text{ \AA}^0$ we obtain that the relative decrease of intensity is about 10%. For the surface with $\sigma = 4 \text{ \AA}^0$ we obtain the relative decrease of intensity about 20%. Also we see that the maximum relative decrease of scattering intensity don't exceed 50%.

The result of above evaluation is that the difference in polarization due to presence of roughness have relatively small influence on scattering intensity. This conclusion may be seen from the following qualitative consideration. The effective electric field, that acts on atoms of roughness, according to our model is always bigger or equal than the mean electric field in medium. The additional contribution to effective field in medium volume is equal $\frac{4\pi}{3} pN$ and its value is more than three times less than the value of mean field. Therefore the presence of roughness changes only the small contribution in effective field and polarization of atoms induced

by effective field in roughness area don't differ significantly from the volume polarization.

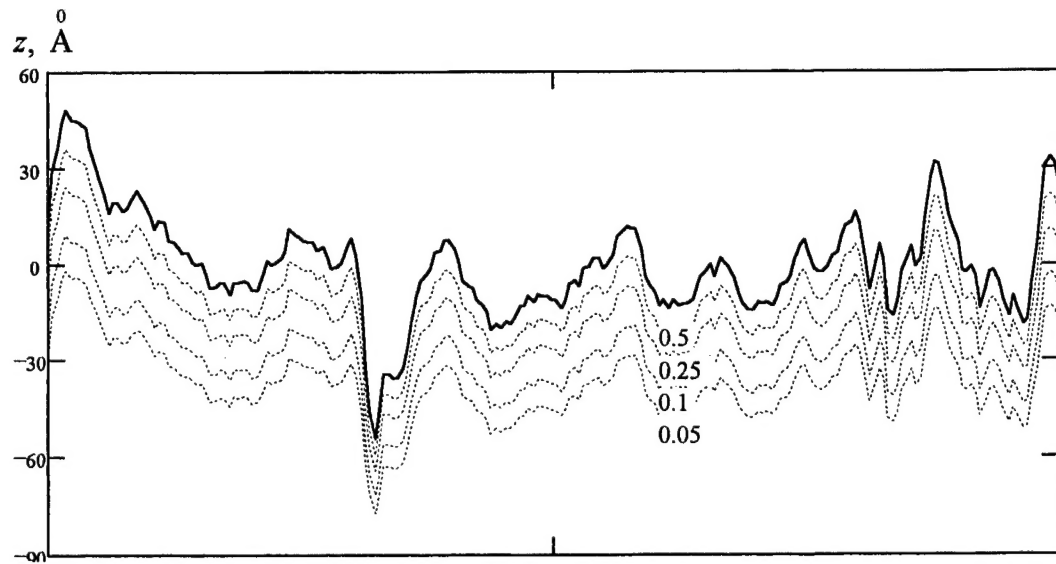
Our consideration may be used in common light scattering methods. We will apply our results for the ARS and TIS measurement interpretation. ARS methods are often used for roughness PSD function determination. As it follows from our consideration the intensity of scattering for very smooth surfaces becomes smaller than it follows from standard vector scattering theory. As the result if we calculate roughness PSD function according to standard theory it will be lower than the real one. The discrepancy will be larger as the surface becomes more smooth. This conclusion is in qualitative agreement with following experimental results of meas-

6. ACKNOWLEDGMENTS.

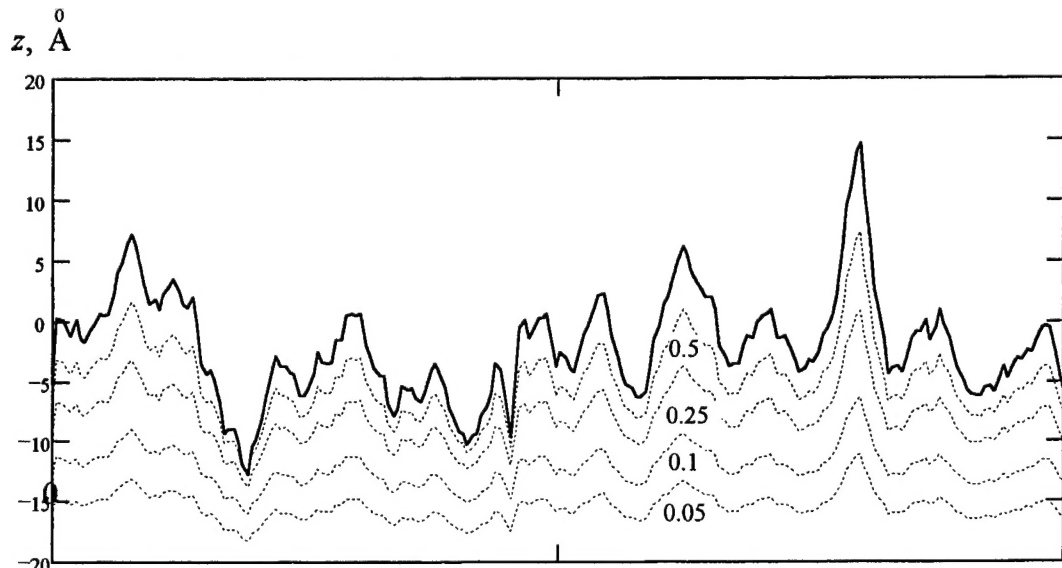
The author is very grateful to professors V.G.Dmitriev, Yu.N.Devyatko, V.V.Azarova and Yu.N.Lokhov for useful discussions and interest in the present work.

7. REFERENCES.

1. J.M.Bennett, L.Mattsson, *Introduction to Surface Roughness and Scattering*, Optical Society of America, Washington DC, 1989.
2. J.M.Elson, J.M.Bennett, "Vector Scattering Theory", *Opt. Eng.*, **18**, 116 (1979).
3. P.Beckmann, A.Spizzichino, *The Scattering of Electromagnetic Waves from Rough Surfaces*, Pergamon Press, London, 1963.
4. V.V.Azarova, N.Solovieva, *Proc. SPIE*, **1711**, 191-194 (1992).
5. D.V.Sivukhin, "Molecular Theory of Reflection and Refraction of Light", *Zh.Eksp.Teor.Fiz.* **30**, 374 (1956) (in Russian).
6. V.V.Azarova, V.G.Dmitriev, Yu.N.Lokhov, K.N.Malitski, "Angle-Resolved and Total Integral Scattering Theory of Laser Radiation by a Precise Dielectric Surface", *QE*, **30**, N4, (2000).
7. S.Gliech, A.Duparre, R.Recknagel, "Wide-scale Surface Characterization by Combination of Scanning Force Microscopy, White Light Interferometry and Light Scattering" , *Proc. SPIE*, **3739**, 355-362 (1998).

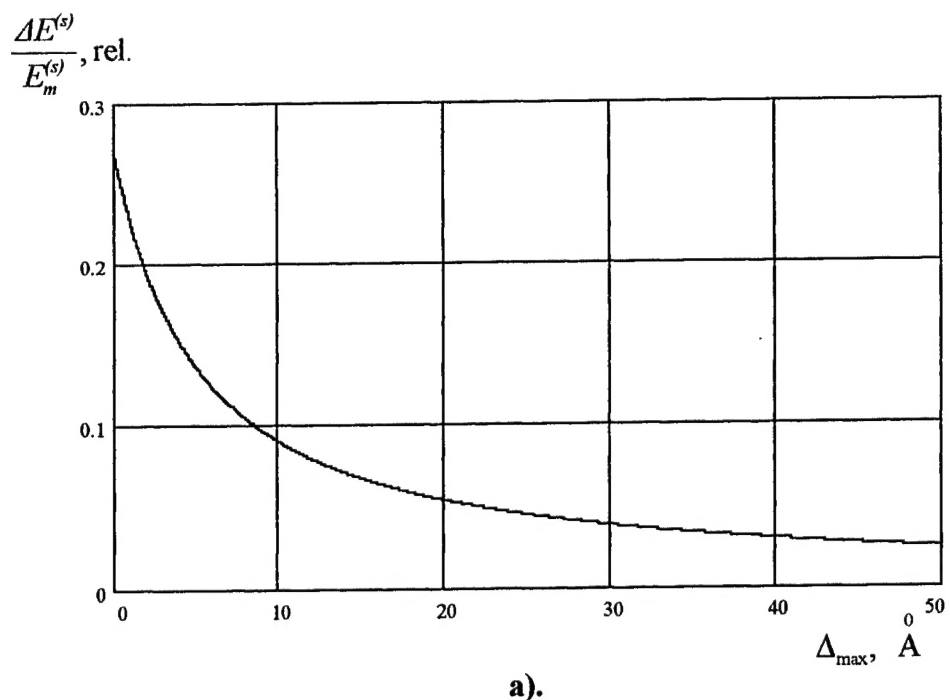


a).

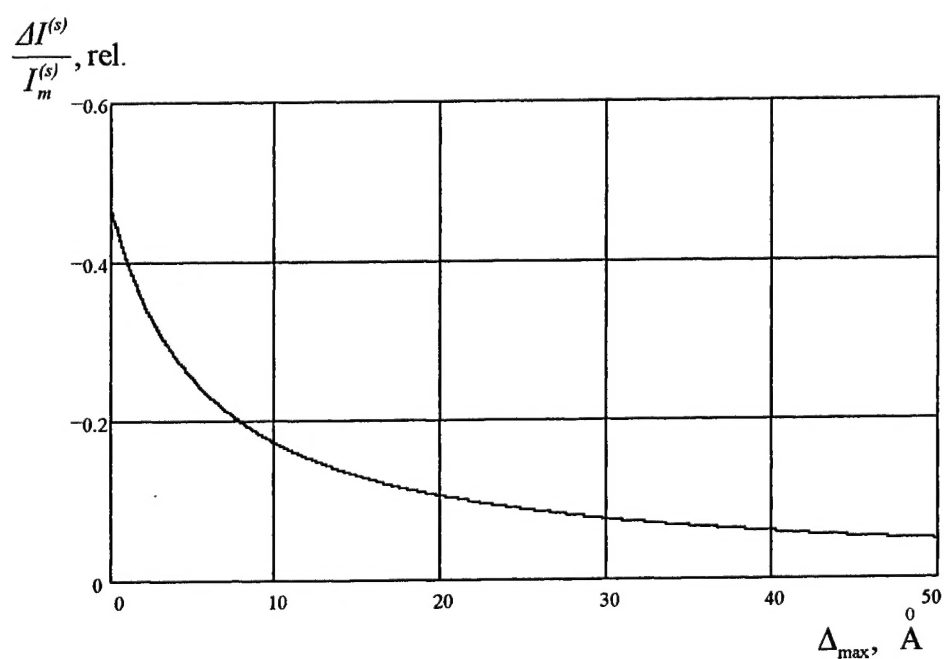


b).

Picture 2. Coordinate surfaces $u_3 = \text{const}$ for roughness with $\Delta_{\max}^0 = 50 \text{ \AA}^0$ ($\sigma = 20 \text{ \AA}^0$) (a) and $\Delta_{\max}^0 = 15 \text{ \AA}^0$ ($\sigma = 7 \text{ \AA}^0$) (b), that correspond to constant amplitudes of polarization $p_v + C(p_0 - p_v)$, $C = 0.5, 0.25, 0.1, 0.05$, characteristic screen depth is $\Delta_{scr}^0 = 5 \text{ \AA}^0$.



a).



b).

Picture 3. Relative difference of scattering electric field amplitude (a) and intensity (b) due to roughness influence on polarization of near-boundary atoms as the function of maximum height deviation Δ_{\max} . The calculation is performed for fused silica surface, characteristic screen depth is $\Delta_{scr} = 5 \text{ \AA}^0$.

Author Index

Abazadze, A. J., 25
Adachi, H., 90
Afanashev, P. N., 140
Alimpiev, A. I., 68
Andreev, Alexander A., 161
Antipov, Oleg L., 9
Azarova, Valentina V., 120
Bagayev, Sergei N., 171
Baiborodova, N. D., 140
Bakhirkin, Yu. A., 129
Bassani, F., 144
Belostotsky, A. L., 117
Belyi, V. N., 129, 136
Berenberg, Vladimir A., 50
Chausov, Dmitry V., 9
Chepurov, S. V., 171
Chuvaeva, Tamara I., 106
Čtyroký, Jiri, 154
Dashtoyan, A. A., 140
Denisov, Igor A., 106
Dianov, Eugeni M., 140
Dymshits, Olga S., 106
Edelmann, Martin, 81
Fatemi, Hassan, 190
Fujimura, K., 90
Gapontsev, V. P., 75, 81
Golub, Anatoly, 161
Golyaev, Yu. D., 120
Gorchakov, A. V., 117
Graf, Thomas, 1
Gulin, Alexander V., 36
Hoekstra, Hugo J. W. M., 154
Hogervorst, W., 136
Ishii, T., 90
Izyneev, Anatoly A., 62
Juncar, Patrick, 175
Kalashnikov, Vladimir L., 112
Kaplun, A. B., 117
Karpukhin, S. N., 39, 50
Kirpichnikov, A. V., 68
Klementyev, V. M., 171
Kolbatskov, J. M., 25
Kolker, D. B., 171
Kolodnyi, George, 120
Kondratyuk, N., 129, 136
Kotačka, Libor, 154
Kulagin, Victor V., 178
Kuratev, Ivan I., 17
Kuzhelev, Alexander S., 9
Kuznetsov, S. A., 171
Lebedev, V. F., 140
Lipovskii, Andrey A., 32
Lobachev, Vitaly V., 140
Lucarini, V., 144
Malitskl, K., 194
Malyarevich, Alexander M., 32, 106
Malyshov, A. V., 75
Mashchenko, A., 129
Matyugin, Yu. A., 171
Meshalkin, A. B., 117
Milleroux, Yves P., 175
Mironov, I. A., 81
Mirzaeva, A. A., 75
Naumov, S., 99
Naumov, V. L., 126
Novikov, Georgii E., 75, 81
Ogasawara, K., 90
Okhrimchuk, A. G., 99
Onischenko, A. M., 126
Onushchenko, Alexei A., 106
Orlov, O. A., 75, 81
Parriaux, Olivier M., 154
Pashkov, V. A., 36
Pasynok, Sergei L., 178
Pavlovitch, Vladimir L., 25
Pestryakov, Efim V., 68
Petrov, V. V., 68
Philippov, P., 129
Pivtsov, V. S., 171
Podstavkin, A. S., 126
Pohl, H.-J., 81
Poloyko, Igor G., 112
Prokoshin, P. V., 32
Rasyov, M., 120
Razumova, Irene K., 75
Reiterov, V. M., 81
Rudenko, Valentin N., 178
Rusov, Vladimir A., 117
Sadovski, P. I., 62
Salakhutdinov, Ildar F., 154
Sapožnikov, V. K., 117
Savitski, V. G., 32
Serdobolskii, Andrei V., 178
Shagov, A. A., 129, 136
Shapovalov, Vitaly N., 117
Shchelev, M. Ya., 140
Shestakov, Alexander V., 126
Sorokin, E., 99
Sorokina, I. T., 99
Steiner, Rudolf W., 81
Sychugov, Vladimir A., 154
Tanaka, I., 90
Tikhmenev, N., 120
Tkachuk, Alexandra M., 75, 81
Trunov, V. I., 68
Ueda, Toshitsugu, 161
Ustimenko, Nikolai S., 36
van Wolferen, H., 154
Wakamatsu, Muneaki, 161
Weber, Heinz P., 1

Yumashev, Konstantin V., 32, 106

Zakharyash, V. F., 171

Zhilin, Alexander A., 106

Zinov'ev, Andrey P., 9

Zverev, Georgiy M., 17, 25